The University Of Sheffield.

The Investigation of Self-excited Thermoacoustics in a Rijke Tube Burner

Xuanqi Liu

A thesis submitted in partial fulfilment of the requirements for the degree of Doctor of Philosophy

The University of Sheffield
Faculty of Engineering
Department of Mechanical Engineering

Submission Date
Spring 2023

Declaration

I, the author, hereby declare that this thesis is my original work and has not been submitted for the award of any other degree at University of Sheffield or any other university or institution.

Acknowledgements

I would like to show my deepest gratitude to my parents, Prof. Yanwei Liu and Ms Xiaodong Li. Thank you for your unconditional love, which has unwaveringly supported me. The encouragement, guidance and sacrifices from them makes it become possible for me to achieve countless milestones of my life. Your love will always be my source of strength to encourage me to keep going forward. If possible, I truly wish to gift such to you, and I will always do all I can to to make you proud in the future.

I am deeply grateful to my supervisor, Prof. Yang Zhang for the guidance and patience provided by him. He offered me continuous support and the greatest help over my whole PhD over these four years. I could not make any academic achievement without his consistent encouragements and helps. I am also grateful to my second supervisor, Prof. Shuisheng He for his help and support during my study.

I would like to express my special gratitude to my colleagues, Dr Hangxu Zhou, Dr Yufeng Lai, and Dr Muyi Pan for their generous support and guidance throughout my PhD journey. They provided me with unwavering assistance, not just with respect to research, but also in navigating my daily life. I will forever cherish the bond of friendship that we have forged.

I would also be so thankful to my girlfriend, Dr Jing Wu for her love and great encouragements which encourages me to be brave in my PhD study, especially over my depressed emotion. She makes my life full of happiness and brightness.

I would also like to extend my gratitude to all the colleagues from Combustion and Flow Diagnostics Research Group, Dr Houshi Jiang, Dr Xiao Wang, Dr Jing Zhang, Dr Yuchen Zhang, Dr Ahmad Albadi, Mr Huanrong Lei, Mr Haibo Zhou, Mr Xiangfei Meng, Mr Hugo Wong, Mr Haoting Wu and Mr Ahmed Aboalhamayie. I really enjoy working with them.

Publications

[1] **X. Liu**, H. Zhou, Y. Lai and Y. Zhang, Equivalence ratio independence and dependence ranges of system responses for a nonlinear thermoacoustic oscillation in a Rijke tube, *Journal of Sound and Vibration*, 2023.

[2] **X. Liu**, H. Zhou, Y. Lai and Y. Zhang, Characterisations of self-excited nonlinear oscillations at varied system parameters in a Rijke tube with a premixed laminar flame, *Experimental Thermal and Fluid Science*, 2023.

[3] **X. Liu**, Y. Lai, H. Zhou, C. Fisk, J. Willmott and Y. Zhang, Experimental investigation on the effect of the mesh at the downstream region on the self-excited thermoacoustic oscillation in a combustion driven Rijke tube, *Journal of Sound and Vibration*, 2023 (*Submitted*)

[4] Y. Lai, **X. Liu***, C. Fisk, M. Davies, Y. Wang, J. Yang, C. Plessis, L. Cotton, Y. Zhang and J. Willmott, Combustion inhibition of biomass charcoal using slaked lime and dolime slurries, *Fire Safety Journal*, 2023.

[5] Y. Lai, **X. Liu***, Y. Li, E. Leonidas, C. Fisk, J. Yang, Y. Zhang and J. Willmott, Investigating the Fire-Retardant Efficiency of Intumescent Coatings on Inclined Timber: A Study on Application Strategies and Heat Transfer Mechanisms, *Construction and Building Materials*, 2023. (*Submitted*)

[6] Y. Lai, A. Albadi, **X. Liu**, M. Davies, M. Hobbs, J. Willmott, Y. Zhang, Investigation of forced flow orientations on the burning behaviours of wooden rods using a synchronised multi-imaging system, *Proceedings of the Combustion Institute*, 2022.

[7] H. Yang, Y. Lai, **X. Liu**, H. Jiang and J. Yang, Equivalence Ratio Modelling of Premixed Propane Flame by Multiple Linear Regression Using Flame Color and Spatial Characteristics, *Measurement Science Review*, 2023.

[8] H. Yang, Y. Lai, **X. Liu**, M. Davies, J. Willmott, Y. Zhang and J. Yang, Experimental and Simulated Study of the Relationship Between Color Camera Imaging and Color-Modeled Equivalence Ratio Measurement, *IEEE Transactions on Instrumentation and Measurement*, 2023.

[9] H. Yang, Y. Lai, **X. Liu**, X. Yang, J. Willmott, Y. Zhang and J. Yang, Premixed flame equivalence ratio measurement and modelling based on combustion noise using a data-driven methodology, *Thermal Science and Engineering Progress*, 2022. *(Revision in progress)*

Abstract

Self-excited thermoacoustic instabilities in combustion systems have been a major concern and remain a challenging industry problem over decades since they are usually undesirable in combustion systems. Complex interactions between heat release and pressure fluctuations are usually involved, which can generate nonlinear thermoacoustic oscillations with high amplitudes and frequencies in a combustion chamber. The nonlinear oscillation can be intense enough to cause combustion problems and severe structural damage. Therefore, it is necessary to study the system response under different conditions from various aspects and reveal the characteristics of thermoacoustic systems.

In this study, a Rijke tube system with a premixed methane-air laminar flame was utilised to trigger the self-excited oscillations. The system responses to various system parameter changes have been focused on, including the equivalence ratio (Φ), burner position, methane flow rate and tube inner diameter, due to their crucial roles in characterising system oscillations. The effects of mesh in the downstream region on characterising the thermoacoustic oscillation also have been investigated due to the sensitivity of thermoacoustic oscillation to downstream heat and flow conditions. Several time-domain analysis methods, including phase space reconstruction, Wayland translation error, Recurrence plot and Recurrence quantification analysis, have been applied to qualitatively identify and quantify the system nonlinear dynamical properties. A novel calculation of internal phase difference between different harmonic modes has been developed for investigating the characteristics of changes in time-evolution of pressure fluctuations, which was utilised in studying the effects of Φ on the system. The Φ-independence and Φ-dependence ranges of the system response to Φ have been discovered. Meanwhile, it also has been found that the nonlinear dynamical properties of system can be significantly influenced by the system parameter changes. The effects of mesh in the downstream region on suppressing oscillations and changing system behaviours also have been investigated.

Focusing on the thermoacoustic system behaviours under various conditions, the gained insights from this study can be helpful for improving the understanding of nonlinear thermoacoustic oscillation and thus may contribute to evaluating and controlling the thermoacoustic instabilities in industrial combustion systems.

Content

List of Figures

List of Tables

Nomenclature

Abbreviations & Symbols

$\Delta h_{combust}$	Enthalpy of combustion (J/kg)
$h_{reactant}/h_{product}$	Standardised enthalpy of the product/ reactant (J/kg)
$u_{reactant}/u_{product}$	Internal energy of reactant/ product (J/kg)
T_0	Initial temperature of the reactant (K)
T_{ad}	Adiabatic flame temperature (K)
P	Pressure (Pa)
P_0	Initial pressure (Pa)
P_{final}	Final pressure (Pa)
C	Carbon (atom)
O	Oxygen atom
H	Hydrogen atom
N	Nitrogen atom
CH_4	Methane
O_2	Oxygen
H_2O	Water
CO_2	Carbon dioxide
F/A	Fuel-to-air ratio
Φ	Equivalence ratio
m_f/m_a	Mass of fuel/air
n_f/n_a	Number of moles of fuel/air
ϕ	Normalised form of equivalence ratio
S_L	Laminar flame speed (m/s)

T_u/T_d	Upstream/downstream temperature (K)
l_R^O	Thickness of reaction region (m)
l_D^O	Thickness of transport region (m)
CH^*	CH radical chemiluminescence
C_2^*	C_2^* radical chemiluminescence
OH^*	OH^* radical chemiluminescence
Le	Lewis number
α_t	Thermal diffusivity (m^2/s)
$\mathfrak{D}$	Molecular diffusivity (m^2/s)
κ	Thermal conductivity (W/m·K)
$\mathfrak{d}$	Diffusion coefficient (m^2/s)
c_p	Constant-pressure heat capacity (J/kg·K)
Re	Reynolds number
u	Flow velocity (m/s)
$\mathcal{L}$	Characteristic linear dimension (m)
ν	Kinematic viscosity (m^2/s)
μ	dynamic viscosity (Pa.s)
p_{sound}	Acoustic pressure (Pa)
P_{Total}	Ambient pressure after being disturbed (Pa)
P_{static}	Static ambient pressure (Pa)
SPL	Sound pressure level (dB)
p_e	Effective acoustic pressure (Pa)
p_{ref}	Auditory threshold (Pa)
s	Displacement of the particle away from neutral position (m)
x_l	Longitudinal position (m)
t	Time (sec)

c	Sound speed (wave speed) (m/s)
ω	Angular frequency (rad/sec)
f	Frequency (Hz)
L	Medium length (tube/string length) (m)
λ	Wavelength (m)
$\triangle e$	End correction (m)
d	Hydraulic diameter (m)
$\dot{p}(t)/\dot{q}(t)$	Oscillating components of the pressure/heat (Pa, J)
$\theta_{Heat-Pressure}$	Phase difference between heat and pressure fluctuations (rad)
RI	Rayleight index
T	Period of one oscillation cycle (s)
χ	Position (m)
f_{1st}	Fundamental harmonic frequency (Hz)
f_{2nd}	Second harmonic frequency (Hz)
τ	Time delay
$p(t)$	Pressure fluctuation time series
Fs	Sampling rate (Hz)
N_p	Length of $p(t)$
D	Embedding dimension
$\mathbf{P}_{\mathrm{t}}(\mathrm{D})$	D-dimensional space vector
$\mathrm{R}_{\mathrm{pp}}(\tau_c)$	Autocorrelation function with time delay of τ_c
$I(\tau_c)$	Mutual correction
$P[A]$	Probability density of A
FNN	False nearest neighbour
$S_k(D)$	Distance in D-dimensional phase space
$\widehat{\mathbf{P}}_{\mathrm{t}_k}(\mathrm{D})$	Nearest neighbour of $\mathbf{P}_{\mathrm{t}_k}(\mathrm{D})$

σ	Standard deviation
$\mathbb{P}_0$	Image of $\mathbf{P}_0$
$\mathbf{v}_{\text{trans}}(i)$	Translation vector
$\bar{\mathbf{v}}_{\text{trans}}(i)$	Average $\mathbf{v}_{\text{trans}}(i)$
e_{trans}	Translation error
$\|.\|$	Euclidean length
$\mathbf{R}_{\text{i,j}}$	Recurrence matrix
LOI	Line of identity
ε	Recurrence threshold
$\mathbb{R}^*$	Positive real number
Θ	Heaviside function
RR	Recurrence rate
N	Length of data for recurrence analysis
DET	Determinism
l	Diagonal line length
L_{max}	Longest diagonal line
$P(l)$	Histogram of the diagonal lines with length of l
DIV	Divergence
ADL	Average diagonal line length
$\wp(l)$	Probability distribution of diagonal line with length l
v	Vertical line length
E_{upper}/E_{lower}	Upper/Lower envelope
$V_{10\ Pa}$	Voltage for 10 Pa acoustic signal (V)
$V_{p(t)}$	Raw acoustic data in volt (V)
φ_{ref}^{α}	Local reference phase at α-th cycle (rad)
y	Sinusoidal signal

M_f^{α}	Local maximum point at α-th cycle
$\varphi_{f,2}^{\alpha}$	Local phase difference between fundamental and second harmonic mode (rad)
$\overline{\varphi_{f,2}}$	Mean $\varphi_{f,2}^{\alpha}$ (rad)
f_{eigen}	Oscillation dominant eigenfrequency (Hz)
P_{rms}	Root mean square amplitude (Pa)
$\dot{\mathrm{m}}_{\mathrm{CH_4}}$	Methane flowrate (L/min)
ID	Inner diameter (mm)
$\mathbf{P}^*{}_{\mathrm{t}}(\mathrm{D})$, $p^*(t)$	Normalised form of $p(t)$ and $\mathbf{P}_{\mathrm{t}}(\mathrm{D})$
c_{avg}	Average sound speed (m/s)
l_u/l_d	Upstream/Downstream region length (m)
η	Ratio of upstream region length to the tube length
T_u/T_d	Upstream/Downstream temperature (K)
γ_u/γ_d	Upstream/Downstream adiabatic index
LWIR	Long wavelength infrared
SWIR	Short wavelength infrared
$\mathrm{T}_{\mathrm{mesh}}^{\mathrm{mean}}$	Mean mesh temperature (K)
$E_{RMS}^{upper}/E_{RMS}^{lower}$	Upper and Lower root mean square envelope (Pa)
$\bar{T}_{mesh}$	Time-averaged $\mathrm{T}_{\mathrm{mesh}}^{\mathrm{mean}}$ (K)

Chapter 1 Introduction

1.1 Background and Motivation

Nowadays, energy and environmental protection issue have globally drawn attention due to global environmental deterioration and energy shortage. Many countries have started to seek possible solutions, such as clean energy. However, the requirement for the energy provided by combustion remains the largest by the industry (especially in the space and aviation industry), transportation and etc. [1]. It indicates the central role of combustion in the development of human beings. Under such situation, minimising the exhaust of pollutants and green house gas, and increasing efficiency would be one of the best ways to ease the shortage of energy and the concern of environmental deterioration. Therefore, it is vital to deepen the understanding of combustion and the phenomena that are caused by combustion.

According to current research, methane can be considered to be one of the 'most clean' energy source since it has the lowest amount of carbon per molecule among all the hydrocarbons. For example, carbon dioxide emission is 25% less than petrol, 30% less than Diesel and 16% less than liquefied petroleum gas. In industry and daily life, methane is most used in the form of natural gas, whose composition is 70%~90% of methane, along with other types of hydrocarbons, nitrogen, alkanes and etc. Even though, burning methane still may lead to several unexpected pollutants after the combustion due to the impurity. The pollutants produced could lead to severe air pollution. For example, burning of natural gas can produce pollutant emissions at relatively high peak temperatures, including NOx, SOx, which are extremely harmful to human bodies. To seek the ways for overcoming this, both the fuel-lean and fuel-rich techniques have been utilised in some combustion systems due to their relatively low combustion temperature. However, combustion instabilities are potentially triggered in these systems.

Combustion instabilities can lead to a worse result by decreasing combustion efficiency and increasing pollutant emissions. Since the unsteady heat release along the combustion process, thermoacoustic instabilities are highly possible to be triggered. Although thermoacoustic phenomena can be utilised to drive the thermoacoustic engine, unexpected and undesirable thermoacoustic instabilities can negatively affect the combustion systems. The thermoacoustic instabilities are mainly caused by the coupling effect between the fluctuation of heat release and the acoustic properties of the chamber. In a combustion system, the flame can act as an acoustic actuator. Once the flame is ignited, the feedback loop would be established if the fluctuation of the heat release rate released by the flame responds to the fluctuations of both pressure and flow velocity [2,3], as shown in Fig. 1.1. A feedback loop between the system acoustics and heat release can destabilise the system. Under these circumstances, the high amplitude pressure pulsation could be generated due to this coupling effect. The pressure pulsation can potentially further trigger the intense oscillations of the structure. Several problems can result from the unexcepted oscillation, such as decreased combustion efficiency and enhanced combustion noise. In some extreme cases, it could damage the key sections of the engine and even destroy the whole system [4], as shown in Fig. 1.2.

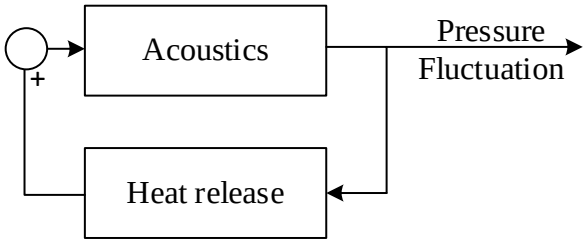

Fig. 1.1. Feedback loop of the thermoacoustic system between the acoustics and unsteady heat release [2].

Fig. 1.2. Destroyed combustor structure due to the unexpected thermoacoustic oscillations [4].

The studies of thermoacoustic instabilities have been developed over a century. In 1777, this phenomenon was first observed and recorded by Higgins, and named as ‘singing flame’ [5]. Thermoacoustic instabilities were able to be triggered in some relatively simple systems, usually with sufficient temperature gradients. The temperature gradient can be either provided by the heat or cold source [6]. The convective flow caused by the temperature gradients or the forced flow passing through the source can result in unsteady heat release, further leading to pressure perturbations. Rijke developed an experimental setup to trigger thermoacoustic instabilities in 1859 [7], and this setup was known as the ‘Rijke tube’, which is used as a typical experimental setup for the investigation of thermoacoustic instabilities, as shown in Fig. 1.3. It consists of a tube and a heated gauze located at the lower half of the tube. Once the gauze is heated, the air will be drawn from the bottom end of the tube, forming an upwards convective flow due to the natural convection. The sound can then be produced through the heat directly conducted from the heated gauze to the gaseous medium in the tube [6]. For a Rijke-type combustor, the heating elements are mostly in the form of premixed flame with a flame holder [6,8]. By comparing the complex system, such simple systems provide a relatively simple, effective, and direct way to study thermoacoustic instabilities. In 1878, Lord Rayleigh gave a general explanation of the thermoacoustic phenomena based on the relationship between acoustic wave excitation and unsteady heat transfer, which is known as Rayleigh criterion [9]. It states that the oscillation would be encouraged when the heat fluctuation and pressure fluctuation are in phase. Putnam [10] and Culick [11] further developed the criterion and proposed the mathematical expressions for the criterion by integrating the heat release fluctuation and the pressure fluctuations.

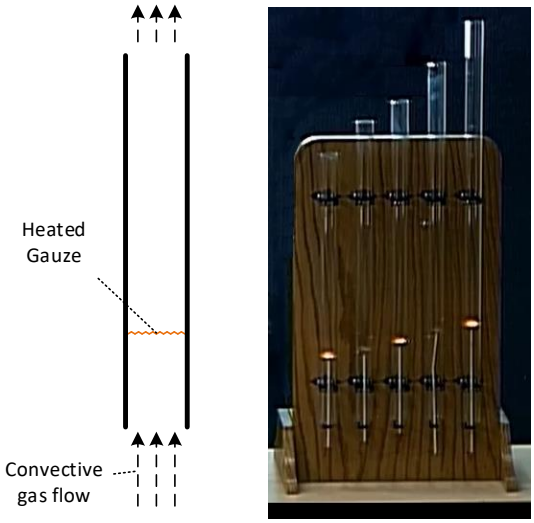

Fig. 1.3. Original Rijke tube with a heat source in the form of heated gauze [12].

However, it needs to be noted that the thermoacoustic instabilities can also be a positive phenomenon with considering the intense pressure oscillation. Some studies have mentioned that the prime movers and refrigerator thermoacoustic engines can provide considerable power output [13–16]. The basic concept for a thermoacoustic engine is the temperature difference within the system. The greater temperature gradient in a stack of the prime mover in a thermoacoustic engine can lead to the conversion of acoustic energy to other forms of energy [3,13,16]. The refrigerator thermoacoustic engines have moderate temperature gradients. With the help of external acoustic excitation, the refrigerating effect that the heat transfer from the low-temperature source to high-temperature area can be caused.

In recent decades, many studies have experimentally and theoretically investigated the characteristics of thermoacoustic instabilities. It has been found that the thermoacoustic system can be highly nonlinear, and the system states can be strongly affected by the experimental conditions and have significant time-variant natures [3,8,17–24]. The way about how the system responds to the parameter changes still remains unclear due to the high complexity of a nonlinear system. Therefore, in order to minimise the negative influence of the unexpected thermoacoustic instabilities, it is vital to investigate the system characteristics and deepen the understanding of thermoacoustic instabilities.

1.2 Aim and Objectives

This study aims to reveal the characteristics of the self-excited thermoacoustic oscillation in a Rijke tube with a premixed methane flame under different conditions based on system response and system dynamics. It has been reported that the self-excited thermoacoustic oscillation driven by the flame can be affected by the various system parameters, such as equivalence ratio, fuel flow rates, flame position and etc. [8,25–28]. The system response (frequency and amplitude) and the system nonlinear dynamical properties have been found to be nonlinearly related to the system parameters [8]. According to the system response to parameter changes, both active and passive control of the oscillation and aeroacoustic noise can be obtained [29–31]. However, the comprehensive study on investigating the nonlinear relationship between characteristics of the system and system parameters remain insufficient. Thus, in this study, the investigation of the system response and the system dynamics under the various system parameters were conducted. This study can be helpful for the prediction and control of thermoacoustic instabilities in the real internal combustion engine. To achieve this aim, several objectives need to be obtained, as listed below:

- To establish a Rijke tube type burner driven by a laminar premixed methane flame for triggering the self-excited nonlinear thermoacoustic oscillations.

- To develop and apply the appropriate methods for analysing the system response and the dynamical system properties of self-excited nonlinear thermoacoustic oscillations under different conditions.

- To establish a thermal and schlieren imaging system to achieve the temperature measurement and the visualisation of the flow field with density gradients.

Case studies:

- To investigate the equivalence ratio effect on the self-excited thermoacoustic system in terms of system eigenfrequency, amplitude, and the internal phase difference between harmonic modes and system dynamics for a combustion-driven Rijke tube burner.

- To determine the effects of burner position, fuel flow rate and tube inner diameter on characterising the system responses, system deterministic natures and dynamical properties of the self-excited oscillations.

- Investigation about the effects of woven mesh in the downstream region, including the existence of woven mesh, the changes in mesh number and the positions of the mesh, on suppressing the self-excited oscillation and influencing both system response and dynamical properties.

1.3 Thesis outline

This thesis is comprised of seven chapters. The three main parts are 1) introducing the relevant background knowledge of combustion, literature of thermoacoustic instabilities and the methodology of nonlinear analysis (Chapter 1-3); 2) applying analysis methods for investigating the characteristics of the thermoacoustic systems under different parameters based on the experimental results (Chapter 4-6); 3) presenting the main conclusions of this thesis (Chapter 7). Each chapter about the research results (Chapter 4-6) consists of its own structure, including a separate introduction, methodology, results and discussion, and conclusions. The outlines of each chapter are listed below:

Chapter 1 highlights motivation and background of this thesis, and outlines aim and objectives of this research.

Chapter 2 introduces the relevant background knowledge and reviews the literature related to this research. The literature review consists of three main parts: (1) the fundamental background theory of combustion; (2) the introduction of thermoacoustic instabilities with the basic definition of acoustics; (3) the introduction of analysis for nonlinear systems.

Chapter 3 presents the general methodology of this research, including the general experimental setup, data processing methods and analysis methods. The brief explanations for the analysis method are discussed in this chapter. Besides, key

parameters of the phase space reconstruction and the recurrence analysis are also explained in the meantime.

Chapter 4 investigates the effects of equivalence ratio on characteristics of self-excited thermoacoustic oscillation, from the perspectives including system frequency response, the phase difference between the harmonic modes, and the system dynamical properties. The system dynamical properties are obtained from the recurrence analysis of the system states. The equivalence ratio independence and dependence ranges are determined based on the system response to the equivalence ratio changes.

Chapter 5 studies the system response to the changes of the burner position, fuel flow rate and tube inner diameters from the aspects of oscillation eigenfrequency, system deterministic natures and system nonlinear dynamics via phase space analysis and the recurrence analysis. The simplified model for explaining the eigenfrequency change are developed based on the downstream temperature.

Chapter 6 shows the experimental study about the self-excited oscillation response to the addition of woven mesh in the downstream region and the changes in mesh properties. The oscillation eigenfrequency, amplitude and the system dynamics properties are determined. Thermal and schlieren imaging systems are applied to obtain the mesh temperature and the downstream flow conditions at the tube top end, by which the mechanisms of the mesh effect then are revealed.

Chapter 7 concludes the main findings of the studies. Besides, the further works suggested to be carried out in the future are presented.

Chapter 2 Literature review and background knowledge

In this chapter, the background knowledge for this thesis and the related research are introduced and reviewed in detail. There are three main sections in the chapter:

Section 2.1 introduces the background knowledge of combustion theory, including the definition of combustion, flame classification, equivalence ratio and basic hydrocarbon combustion.

Section 2.2 mainly presents the reviews of the thermoacoustic instabilities research, along with some basic acoustic knowledge. The basic introduction of the thermoacoustic phenomenon, classic setup for thermoacoustic instabilities study (such as Rijke tube, Sondhauss tube), mechanisms of thermoacoustic instabilities and the nonlinearities of the thermoacoustic system are reviewed in this section. Besides, an introduction of the basic knowledge for nonlinear system is also presented.

Section 2.3 introduces the analysis methods for analysing the nonlinear system and reviews the application of these methods. The analysis method utilised in this study, such as the phase space analysis and the recurrence analysis, are discussed in detail.

This chapter provides an overview of the studies about thermoacoustic instabilities, and the introduction of general knowledge related. The academic gaps in current research and the contribution of corresponding work are discussed in the corresponding chapters.

2.1 Combustion

2.1.1 Definitions of combustion

Combustion is usually defined as a rapid oxidation process with heat release or heat release and light emission simultaneously [32]. Some types of combustion can have slow oxidation processes with small amounts of heat release without light emission.

The combustion discussed in this study only focuses on the type with rapid oxidation process. In most combustion reactions, the reactant could be roughly divided into two types, which are the oxidant and reductant (fuel). Therefore, the combustion process of the pure substance can be generally considered to be the chemical reactions between fuel and oxidant, and the oxidant oxidises the fuel during the reaction. The combustion product is determined by the elements involved in the fuel and oxidant according to the element conservation. For example, the global hydrogen combustion equation can be written as below:

$$2H_2 + O_2 \rightarrow 2H_2O \qquad \textbf{2.1}$$

In 2.1, it can be seen that only two elements exist in the reactants, which are hydrogen (H) and oxygen (O). Thus, the final product of a complete hydrogen and oxygen combustion reaction is water since no other elements are involved. As another example, the combustion of hydrocarbon involves carbon, hydrogen, and oxygen in the reactants, and the final products of a complete hydrocarbon combustion are carbon dioxide and water, as $C_xH_yO_z + O_2 \Rightarrow CO_2 + H_2O$. A detailed introduction to the combustion process and the elementary reactions are discussed in the following sections.

Generally, there are several different ways to categorise combustion. As one of the classic categories, combustion can be divided into complete combustion and incomplete combustion based on the completeness of the combustion. Complete combustion usually occurs when the oxidant is sufficient, whereas insufficient oxidant may cause incomplete combustion. For the combustion of carbonaceous substance, its incomplete combustion is usually with soot and smoke. Fig. 2.1 shows the typical examples of incomplete and complete combustion. The products of incomplete combustion of carbonaceous substances can have more complex compositions than the products of complete combustion. For instance, unburnt fuel with partially oxidised species can be produced, which can be harmful to the environment and human beings. For gaseous fuels, one of the main methods for increasing the completeness of combustion is premixing fuel with air at a certain mixing ratio before the combustion. This will be discussed in Section 2.1.3 during the introduction of equivalence ratio.

Fig. 2.1. Incomplete (left) and complete (right) Combustion [33,34]

As another important category, combustion can be divided into flame and nonflame modes based on the existence of flame [32]. Nonflame mode, which is defined as the combustion without visible or invisible flame, is uncommon in a combustion system. The flame mode, as the most common combustion mode, is focused on in this study. The flame mode is defined as the combustion with the presence of flame, either visible or invisible, depending on the reactants, during the combustion process. As an example, the studies of the hydrogen flame emission spectrum show that the spectrum intensity of the hydrogen flame in the infrared range (greater than 760nm) and ultraviolet range is significantly greater than the visible range [35,36].

2.1.2 Heat and enthalpy of combustion

The heat release during the combustion process is one of the most significant characteristics of combustion [32]. The amount of heat released includes the energy consumed due to phase change and the difference in energy between the breaking and reforming of the chemical bonds. In most cases, the released heat is mainly from the energy converted from parts of the energy stored in chemical bonds. The standardised enthalpy of species is introduced to describe the energy transfer during this process. It is a sum of the enthalpy of formation, which is the net change in enthalpy due to the breaking and formation of chemical bonds, and the sensible enthalpy change, which is only related to the temperature [32,37,38].

The enthalpy of combustion ($\Delta h_{combust}$) can represent the energy change of the combustion reaction. For a combustion reaction that the fuel is completely consumed,

the $\Delta h_{combust}$ can be determined based on the difference between the standardised enthalpy of the product ($h_{product}$) and reactant ($h_{reactant}$) under the certain condition, as shown below:

$$\Delta h_{combust} = h_{product} - h_{reactant} \quad \textbf{Eq. 2.2}$$

The heat of combustion has the same absolute value with the $h_{product}$ but with an opposite sign. Based on the phase of products, two types of the heat of combustion can be defined. The higher heating value is defined as the heat of combustion when all generated water condenses to the liquid phase, because massive energy is released during this condensing process [39]. In contrast, the lower heat value indicates the value when there is no phase change of generated water from the gas to the liquid phase. The heat produced is then utilised to raise the temperature of the product mixture to the adiabatic flame temperature. The adiabatic flame temperature is defined as the final temperature of the products when the equilibrium is established. Depending on the reaction conditions, two types of adiabatic flame temperature can be defined: constant-pressure and constant-volume adiabatic flame temperature [37,39]. For the combustion under the constant-pressure adiabatic condition, the initial standardised enthalpy of the reactant should be the same as the final standardised enthalpy of the product. Therefore, the adiabatic flame temperature (T_{ad}) under the constant-pressure condition can be defined as below:

$$h_{reactant}(T_0, P) = h_{product}(T_{ad}, P) \quad \textbf{2.3}$$

where T_0 denotes the initial temperature of the reactant mixture, and *P* denote the pressure. Similarly, the constant-volume adiabatic flame temperature can be defined based on the internal energy (u) of the reactant and product, as shown below:

$$u_{reactant}(T_0, P_0) = u_{product}(T_{ad}, P_{final}) \quad \textbf{2.4}$$

where P_0 denotes the initial pressure and P_{final} denotes the pressure at the final state.

2.1.3 Stoichiometry and Equivalence ratio

The relative concentration of fuel and oxidiser is one of the most critical factors in combustion intensity [39]. The combustion reaction with a chemically correct fuel-to-oxidiser ratio can be approximated to the highest intensity since all reactants are completely consumed. This combustion mode is defined as stoichiometric combustion. The stoichiometric quantity of oxidant is the amount of the oxidant that can consume fuel completely in a reaction. For example, the net reaction of the combustion of methane can be expressed in the following form:

$$CH_4 + 2O_2 \rightarrow 2H_2O + CO_2 \quad \textbf{2.5}$$

In this reaction, all reactants can be consumed completely, which means the reaction is stoichiometrically balanced. Based on the relative concentrations of fuel and oxidiser, the mixture and the combustion could be categorised into fuel-rich, stoichiometry and fuel-lean types. In detail, fuel-rich indicates the exceeding amount of fuel to oxidant, possibly resulting in incomplete combustion and partially premixed flame. Secondary combustion can exist if fuel-rich combustion happens in an environment with sufficient oxidant. Oppositely, the fuel-lean indicates an exceeding amount of oxidant, which leads to complete combustion in most cases since the fuel can be completely consumed.

The fuel-to-oxidiser ratio represents the amount ratio of the fuel over oxidiser. For most combustion processes, the oxygen in the air is mostly used as the oxidiser. Thus, a common practice for combustion study is to use a fuel-to-air ratio. However, the fuel-to-air ratio (F/A) is not able to indicate whether the combustion is under fuel-rich, stoichiometry or fuel-lean conditions. Therefore, a dimensionless parameter, equivalence ratio (Φ), is usually utilised to quantitatively define the richness of the fuel in a combustible gas mixture based on the stoichiometric fuel-to-air ratio. Φ is defined as:

$$\Phi = \frac{F/A}{(F/A)_{Stoichiometric}} = \frac{m_f/m_a}{(m_f/m_a)_{Stoic}} = \frac{n_f/n_a}{(n_f/n_a)_{Stoic}} \quad \textbf{2.6}$$

where m is the mass, n is the number of moles for the reactants, and the subscript f and a denotes fuel and air, respectively. Subscript $stoic$ represents the stoichiometric state. Based on 2.6, the combustion condition can be determined as: $\Phi = 1$, which indicates the stoichiometric balanced mixing ratio; $\Phi > 1$ and $\Phi < 1$ as the fuel-rich and fuel-lean mixture or combustion, respectively. A symmetrical and normalised form of equivalence ratio is defined by Law [39] to emlimate the range's asymmetricity of the original form of equivalence ratio, as expressed below:

$$\phi = \frac{\Phi}{1 + \Phi} \quad \textbf{2.7}$$

where ϕ is a symmetrical and normalised equivalence ratio. By this definition, ϕ is symmetrical with $\phi = 0.5$, which indicates a stoichiometric mixture. For those $\phi \in (0.5, 1)$ indicate the fuel-rich condition, whereas $\phi \in (0, 0.5)$ for the fuel-lean condition.

The definition of the global Φ is based on the evenly mixed mixture, which means the Φ is spatial homogenous and independent on time. However, the equivalence ratio can present spatial inhomogeneity and fluctuate with time for the combustion with a partially mixed mixture and the existence of combustion instabilities. Meanwhile, the equivalence ratio is strongly related to the heat release of a combustion process. Thus, some studies introduce the local equivalence ratio for investigating flame dynamics, flame structure and local heat release [40–44]. Besides, the local equivalence ratio can also be applied to describe the characteristics of diffusion flame and thus indicate its species profiles and structural properties [45,46].

2.1.4 Flame classification

A flame is defined as a self-sustaining combustion zone that is able to propagate at subsonic speeds [32]. There are several different classifications of flame based on different criteria. Generally, the most common classifications are based on combustion and flow properties. Based on the existence of oxidisers in supplying gas before the

combustion, the flame could be categorised into non-premixed (also called diffusion) and premixed flame [32]. The behaviours of combustion and flame can strongly depend on whether the fuel and oxidiser are premixed or not [39]. From the aspects of flow properties, the flame can be categorised into laminar and turbulent flame. Therefore, if taking both properties into consideration, there are four different types of flame: laminar premixed, laminar diffusion, turbulent premixed and turbulent diffusion flame. The following sections are organised based on the classification of diffusion and premixed flames, as shown in Fig. 2.3.

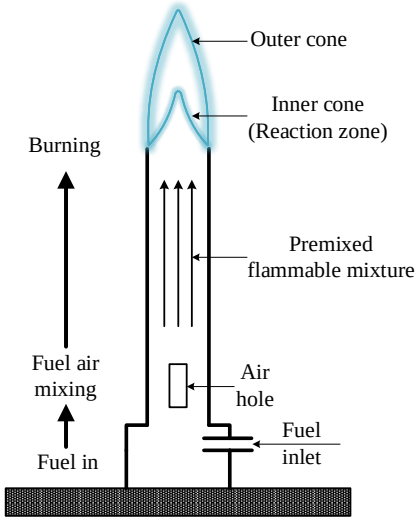

Fig. 2.2. Schematic figure of Bunsen burner.

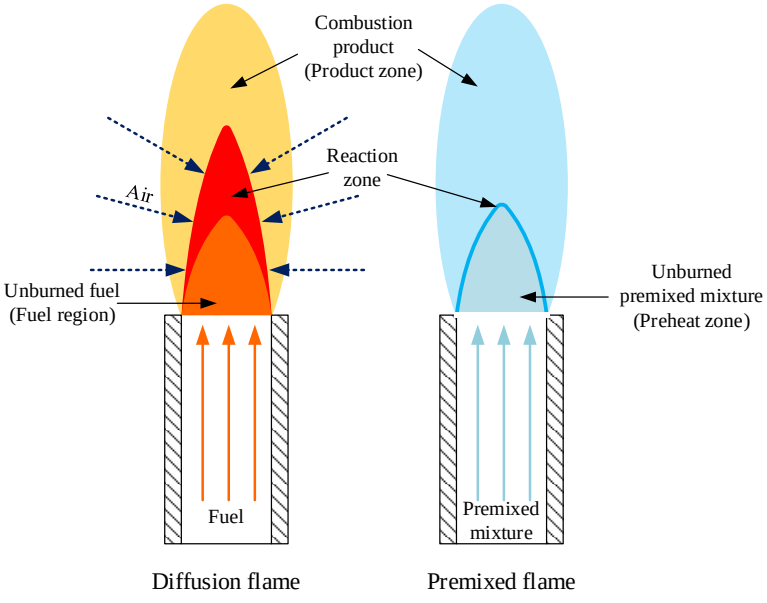

Fig. 2.3. Laminar diffusion and premixed Bunsen flame

Bunsen burner is one of the common devices for the combustion of gaseous fuels. Both premixed and diffusion flame can be produced by a Bunsen burner. A schematic of a typical Bunsen burner is shown in Fig. 2.2. A single or several air holes are located at the bottom of the burner tube, which allows air to flow into the tube and then mix with upward fuel flow. Thus, the premixed flame can be produced by keeping the air holes open. If the air holes are closed, no air can be drawn, and only the fuel can be consumed for combustion, producing a diffusion flame instead.

2.1.4.1 Diffusion flame

A diffusion flame is a flame in which the fuel and oxidant are separated before the reaction initiates. Under this circumstance, the fuel jet first injects into the oxidant directly. Consider the simplest case that the fuel flow stream jets to an infinite container which consists of quiescent oxidant. The diffusion of the fuel and the convective motion takes place, making the fuel mix with the surrounding oxidiser and eventually reach the position where the mixing and reaction can take place subsequently. For the diffusion flame with an infinite mixing rate, the area where local $\Phi = 1$ is defined as the flame surface or flame front [32]. However, the reaction rate at stoichiometric reaction is far higher than the mixing rate of fuel and oxidiser, leading to the leakage of the reactants at the flame surface, which further results in a reaction zone rather than a reaction sheet [39]. Law [39] provides a typical structure of the laminar diffusion flame, as shown in Fig. 2.4. The heat released from reaction and combustion products rapidly diffuses inward (to the fuel region) and outward (to the oxidiser zone) once they are formed at the reaction zone.

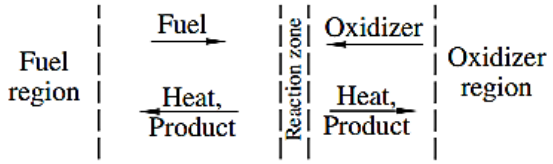

Fig. 2.4. Structure of laminar diffusion flame [39]

For the diffusion combustion of hydrocarbon fuel, soot is frequently generated during combustion. The soot particles are generated in the reaction zone near the fuel region, and these particles are oxidised and consumed as they move to the oxidiser region. The

temperature of soot particles can be generally high, resulting in the diffusion flame appearing in a yellow-orange colour due to the blackbody radiation.

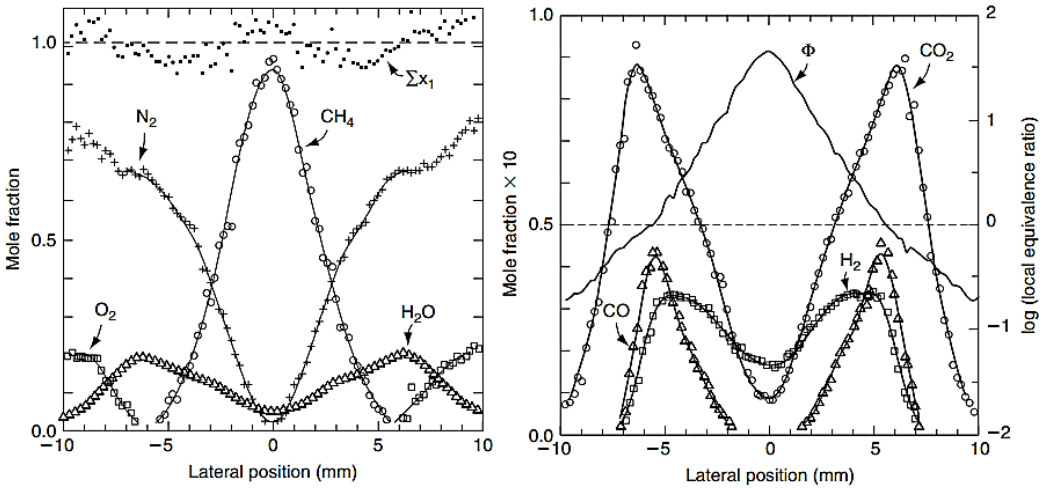

Fig. 2.5. Profile of species and local equivalence ratio of methane-air flame [45]

Smyth et al. [45] summarised a methane-air laminar diffusion conical flame, including the species mole fraction and local equivalence ratio, as shown in Fig. 2.5. It can be seen that the mole fraction of methane decreases when moving away from the centre (fuel jet location, lateral position = 0). The species profile shown in the left panel of Fig. 2.5 evidence the presence of diffusion of the fuel, air and product (water). The reaction zone can be clearly indicated by the region where the mole fractions of oxygen and methane reach approximately zero. At the position slightly prior to this region, the products of the elementary reactions, including carbon monoxide and hydrogen, reach their peak mole fraction values. The final products, including water and carbon dioxide, achieve their peak values at positions subsequent to the peaks of carbon monoxide and hydrogen. Combined with the curve of local Φ, the diffusion of the fuel from the fuel region to the oxidiser region can be clearly indicated.

2.1.4.2 Premixed flame

Different from the diffusion flame, the fuel and oxidiser of a typical premixed flame are premixed evenly in a certain ratio before they enter the area where the reaction occurs [32,37,39]. The mixing process is prior to the reaction initiating. Therefore, the premixed flame has a different structure and different properties from the diffusion flame, since less intense diffusive motions for the mixing occurred between the fuel flow stream and oxidiser. For the premixed combustion that happens in a confined

space full filled with premixed combustible gas, the premixed flame tends to propagate to consume all the combustible premixed mixtures once the combustion process is initiated under the condition without the restraint of aerodynamics, which means the flame front of a premixed flame is not stationary. The free movement speed of the premixed flame front is defined as the propagation speed (S_L), also called the laminar flame speed [32,39]. Therefore, a stationary premixed laminar flame can be obtained when the equilibrium between S_L and the velocity of upstream unburned gas at perpendicular direction to the flame front is achieved. The burned gases (products of combustion) are heated to a temperature significantly greater than unburned gas, resulting in a lower density of downstream burned gases. Therefore, the equilibrium can be obtained when the velocity of burned gases is greater than unburned gases. Besides, the flame temperature is related to Φ of the mixture, leading to changes in the velocity of burned gases, thereby changing the flame front position. A typical laminar premixed Bunsen burner flame (laboratory flame) is shown in Fig. 2.3. Generally, three regions can be categorised as: unburned gases region, reaction region and product region.

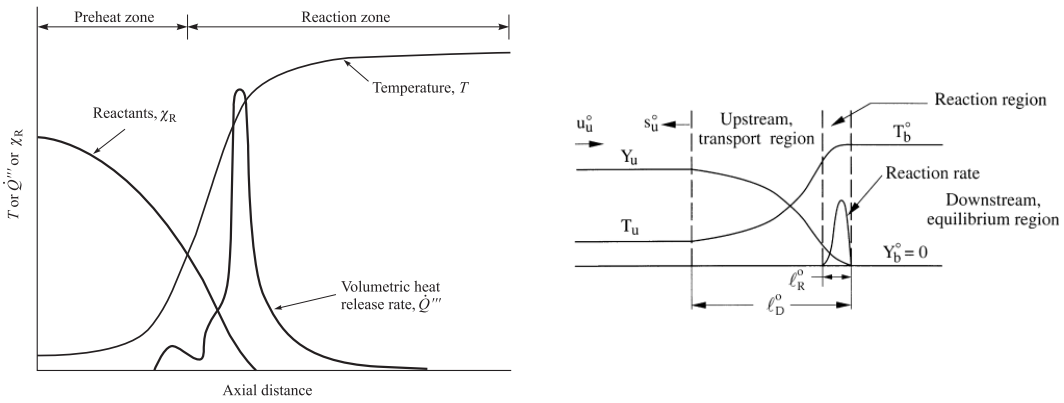

(a) (b)

Fig. 2.6 – Premixed flat flame structure by (a) Turns [32], *(b) Law et al.* [39].

Considering a flame sheet rather than a cone-shaped flame by flatting the reaction region (luminous zone), Turns [32] divides stabilised premixed flat flame into preheat zone and reaction zone based on the study conducted by Friedman [47], as shown in Fig. 2.6 (a). The preheat zone is the region where the combustible gases are heated with

small amounts of heat release. While in the reaction zone, where the major of the reactions happens, most of the chemical energy is released. The reaction zone contains two sub-level regions, the rapid and slow chemistry regions. Law et al. [39] show a slightly different classification of the region, as shown in Fig. 2.6 (b). They divide the flame into the transport region, reaction region and equilibrium region. Note that $l_R^O \ll l_D^O$, since the thickness of the reaction region can be quite thin. However, it needs to be noted that the diffusion and leakage of the species, including intermediate products, fuel and oxidiser, still exist within this region, making the reaction happen in a region rather than a sheet. But the reaction region of a premixed flame is significantly thinner than a diffusion flame. The reason for these two different classifications is that Law et al. [39] define the downstream boundary of the reaction zone based on the concentration of the fresh mixture, while Turns [32] takes the final burnout of radical species as the indicator of the end of the reaction region. Therefore, the rapid reaction region is basically the same as the whole reaction region defined by Law et al [39]. Tran et al. [48] experimentally investigate the flame structure based on the mole fraction of testing gases and intermediates. The results were in good agreement with both theoretical models given by Turns and Law et al [32,39].

The T_{ad} of premixed flame is highly depending on the Φ of premixed gases, as shown in Fig. 2.7 [39]. An increase-then-decrease trend of T_{ad} and Φ can be obtained. It can also be found that the maximum T_{ad} is achieved when the Φ slightly greater than the stoichiometric condition ($\Phi = 1$). Both the reasons for this trend and the shifting of maximum T_{ad} are discussed in Section 2.1.5.

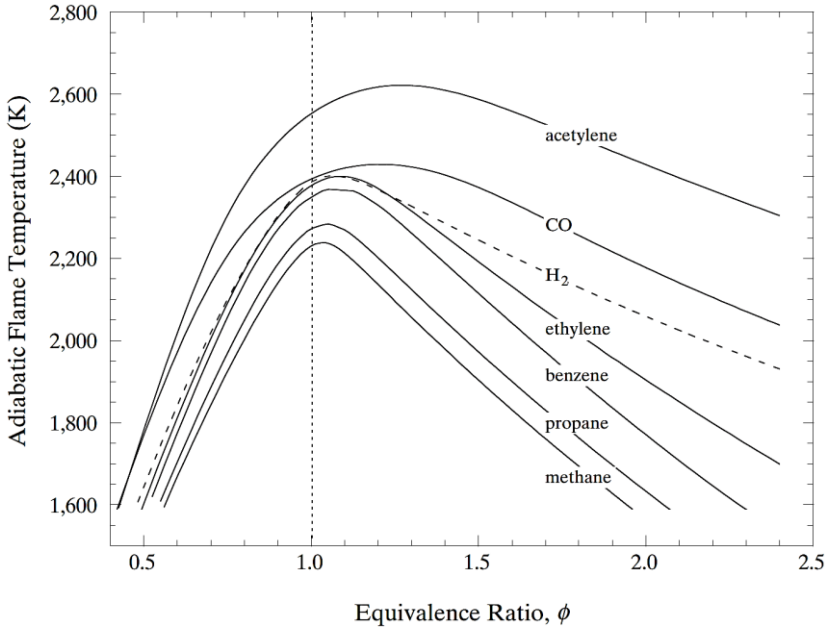

Fig. 2.7. The relationship between the T_{ad} and Φ for different premixed fuel-air mixture at standard temperature and pressure (STP) [39].

2.1.5 Fundamentals of Hydrocarbon

Hydrocarbon is one of the most common fuels in combustion applications, such as natural gas (Methane) and diesel (a combination of higher alkanes). Hydrocarbon is a series of organic chemicals consisting of only hydrogen and carbon elements. Therefore, the hydrocarbon mixture could be expressed in the general form C_xH_y based on the ratio of carbon and hydrogen mole fraction. The net chemical reaction of hydrocarbon with air can be expressed in the form shown below:

$$\mathrm{C_xH_y} + a(\mathrm{O_2} + 3.76\mathrm{N_2}) \rightarrow \mathrm{xCO_2} + \frac{\mathrm{y}}{2}\mathrm{H_2O} + 3.76\mathrm{aN_2} \qquad \textbf{2.8}$$

where a represents $x + \frac{y}{2}$. Based on the ratio in this equation, the equivalence ratio for hydrocarbon can be expressed in a simpler form, which is:

$$\Phi = \frac{a_{stoic}}{a} \qquad \textbf{2.9}$$

The hydrocarbon can be characterised as saturated, unsaturated and aromatic hydrocarbon. This thesis is mainly focusing on the burning of saturated hydrocarbon.

The saturated hydrocarbon only contains single bond, and each carbon molecule is bonded to 4 neighbour molecules, as the maximum number of bonds a carbon molecule can have. Thus, the carbon molecule is 'saturated'. Normally, the saturated hydrocarbon with 1 to 3 carbon atoms is in the form of gas at room temperature and pressure. Liquid hydrocarbons usually have 4 to 19 carbon atoms, whereas solid hydrocarbons have more than 20 carbon atoms. The general form for saturated hydrocarbon can be expressed as: C_nH_{2n+2}. A series of examples of saturated hydrocarbon is given in Table 2.1.

Table 2.1. Series of Saturated hydrocarbon

Name	Number of Carbon atoms per molecule	Chemical Formula
Methane	1	CH_4
Ethane	2	C_2C_6
Propane	3	C_3C_8

Glassman categorises the higher alkanes oxidation process into eight sequential processes [37]:

1) Break of the C-C bond in fuel molecule.

2) Break of the newly formed hydrocarbon radicals, and the formation of alkenes with the creation of hydrogen atoms.

3) Formation of the radicals from the newly created hydrogen atoms.

4) Newly created fuel molecules react with the hydrogen, oxygen and OH atoms.

5) Similar to step 2, the creation of alkenes and hydrogen atoms

6) Establishment of HCO and H_2CO during the oxidation process of alkenes which is initiated by Oxygen atoms.

7) Oxidation process of CH_3, H_2CO, and CH_2 and formation of carbon monoxide.

8) Oxidation of moist carbon monoxide.

From steps 1 to 2, the hydrogen is firstly oxidised to water when oxygen is available. While the hydrogen gas is mainly produced in step 4, as the product of the oxidisation of unsaturated alkenes. Therefore, the formation of hydrogen gas is prior to the carbon monoxide (in step 7), which results in the position of the peak mole fraction of hydrogen in a diffusion flame being prior to the carbon monoxide, as shown in Fig. 2.5. In step 8, the reaction $CO + OH \rightarrow CO_2 + H$ releases almost all of the heat of the whole hydrocarbon combustion process [37].

Section 2.1.4.2 demonstrates that, for all premixed fuel-air mixtures, there is an observed increasing-then-decreasing trend of T_{ad} when Φ increases. The lower T_{ad} under the off-stoichiometric condition is due to the fact that a portion of released heat is utilised to heat the excess reactants [39]. Besides, the existence of unconsumed carbon monoxide and hydrogen under the fuel-rich condition of hydrocarbon combustion can increase the mean specific heat of the product, which result in lower T_{ad} [39].

Meanwhile, the maximum T_{ad} of premixed flame is achieved at $\Phi > 1$ rather than at $\Phi = 1$ for all hydrocarbons-air mixtures, shown in Fig. 2.7. This is caused by the reduced amount of heat release due to the product dissociation during the process of hydrocarbon combustion. More dissociations exist in the fuel-lean condition, resulting in the shifting of T_{ad} to the fuel-rich side [49].

In the combustion process of hydrocarbons, certain elementary reactions can generate excited radicals that emit photons when their electrons transition to lower energy states. The emitted photons result in the glowing of the flame and the bluish colour of the flame. This phenomenon is called flame chemiluminescence. The flame colour of hydrocarbons in the visible range is mainly attributed to CH^* and $C_2{}^*$ [50]. Besides, another excited radical OH^* is also a major spontaneous emission in flames [51].

Therefore, the emission intensity of these excited radicals and the intensity ratio between them are utilised to indicate the flame structural properties, strain rate and heat release rate [51–56]. For the premixed flame, CH^* and OH^* are more preferred for the flame analysis [51,57]. Thus, the chemiluminescence of CH^* and OH^* are usually utilised to indicate the unsteady heat release and analyse the heat release fluctuations of hydrocarbon flame.

2.1.6 Combustion instabilities

Combustion instabilities during a combustion process can appear under different conditions and present different characteristics. In combustion systems, they are usually manifested as undesirable pressure oscillations or perturbations within the system. Although the oscillating combustions can be utilised in some pulsating combustion systems to increase the burning rate, in most cases of normal engines, they usually result in severe degradations of engine performance or even structural damages [58]. The mechanisms of combustion instabilities can be very complex and strongly depend on the system properties because they usually arise from the complex nonlinear interactions between multiple physical phenomena. Some of the instabilities can occur regardless of the existence of a confined chamber. This section introduces some common instabilities during the combustion processes, including intrinsic flame instabilities, chamber and system instabilities, and thermoacoustic instabilities. The discussions of thermoacoustic instabilities are given in Section 2.2.

2.1.6.1 Intrinsic flame instabilities

The intrinsic flame instabilities are caused by the instabilities related to the basic flame speed and flame front, including the effects of thermo-diffusivity and chemical reactions, and hydrodynamic instabilities. They are usually directly associated with the properties of reactants and flow.

- Thermal and chemical related instabilities

The dominant type of instabilities may be different for liquid fuel and gaseous fuel [58]. In combustion systems which utilise liquid fuel, the intense unsteady heat transfer due to the phase change of fuel droplets (evaporation) can be the dominant instability, such

as the unsteady evaporation caused by the presence of bubble ejections and strong deformations of the droplet [59]. For gas-fuelled combustion systems, the properties related to convective flow and the hydrodynamic strain play more important roles in resulting in the instabilities in systems. The thermo-diffusive instabilities can arise from the property changes of fluid due to the temperature changes and can be associated with the relationship between thermal (α_t) and molecular diffusivity ($\mathfrak{D}$) [58,60]. The stability of the flame front under these types of instabilities is able to be indicated by a dimensionless number, Lewis number (Le), which is utilised to describe the ratio between these diffusivities, defined as below:

$$Le = \frac{\alpha_t}{\mathfrak{D}} = \frac{\kappa}{\rho \mathfrak{d} c_p} \qquad \textbf{2.10}$$

where κ denote the thermal conductivity, ρ is the density, and $\mathfrak{d}$ is the diffusion coefficient, and c_p is the constant pressure heat capacity. A stable flame front can be formed when $Le > 1$, whereas thermo-diffusive instabilities can be established if $Le < 1$, leading to an unstable flame front.

In addition, the chemical effects can also be related to the intrinsic instabilities as the combustion reaction consists of multiple elementary reactions. The chemical-kinetic instability of the combustion can be caused by the changes in chemical reaction speed and transport due to the reaction condition or equilibriums of species, leading to intrinsic heat release rate fluctuation [61]. It has been reported that mutual interaction between the chemical reaction and the acoustic wave. The amplification of acoustic wave can result from the chemical reaction, and the acoustic wave is able to affect the chemical induction time notably as well [62].

- Hydrodynamic related instabilities

The hydrodynamic instabilities usually involve vorticity fluctuations in the flow field. A vortex can be generated by the shear flows within the flow field, which can be found in various conditions, such as high Reynolds number flows, flows with great velocity or density difference, and the flow passing by the bluff bodies. The presence of vortices in flow can lead to turbulent motions of the flow. Therefore, the hydrodynamic instabilities in the flame region during the combustion processes may bring turbulence

to both non-reacting and reacting flows [58]. A turbulence flow can be indicated by the Reynolds number, which is a dimensionless number to quantify the ratio of inertial force and viscous force, defined as:

$$Re = \frac{u\mathcal{L}}{\nu} = \frac{\rho u\mathcal{L}}{\mu} \qquad \textbf{2.11}$$

where u is the flow velocity, $\mathcal{L}$ is the characteristic linear dimension, ν denotes the fluid kinematic viscosity (m^2/s), μ denotes the fluid dynamic viscosity (Ns/m^2). $\mathcal{L}$ is usually calculated as the ratio of volume of a system to its surface area. For instance, $\mathcal{L}$ of a tube or duct when fluid flow through it is its hydraulic diameter. A turbulent flow usually has a *Re* greater than 4000 when the fluid flow through a pipe [63], which means the effects of inertial force within the flow are far larger than the viscous force outside the boundary layer. Under this circumstance, the flows away from the boundary layer are effectively inviscid, which can originate the vorticity in the flow [64]. The flow instabilities in a turbulent flow can arise from the emergence of free shear layers that are generated at the locations where the boundary layer separates. Large-scale instabilities can be further resulted by the stretching and amplifying effect of base flow on the originated vorticity [64]. The coherent structures can be eventually formed by this process. These flow instabilities accompanying with the chemical reaction in the reacting flow may lead to unsteady heat release and fluctuations of the flame speed, thereby initiating the combustion instabilities [2,58,64]. The combustion instabilities arising from these interactions between vortex and flame play dominant roles in fuel-lean combustors [65]. Furthermore, the shedding of vortices and the coherent structures formed by this process can resonate with the acoustic field and the acoustic wave generated by the thermoacoustic instabilities, thereby leading to combustion instabilities [58].

The Darrieus-Landau flame instability describes the instability that results from the significant density variations across a flat flame front [58]. This instability states that the flame front is unstable when it is subjected to the perturbation of any wavelength since the thermal expansion may result in a lower density of the gaseous combustion products rather than the unburnt gaseous reactants. This type of instability may result

in a wrinkled flame front, and the growth rate of small bulges and troughs resulting from the small wavelength perturbations can be greater than the larger ones.

Besides, the vorticity can also originate at the interface between two fluids with different densities (Rayleigh-Taylor instability), which is contributed by the body force. It is caused by the destabilisation of the high-density fluid due to gravity when a low-density fluid is located below [64]. This type of instabilities is often found in combustion systems which involve rapid flame front propagation, such as deflagrations, detonations and explosions [66,67], and can also be found in ducted flame with separated fuel and oxidant supplies [68].

In addition, the velocity gradient at the interface between two fluids can also produce vorticity at their interface due to the destabilisations of shear layers, as known as Kelvin-Helmholtz instabilities. As discussed above, the free shear layers exist within a turbulent flow. The presence of Kelvin-Helmholtz instabilities can lead to these free shear layers losing their stability [69]. The Von Karman vortex street is possibly formed through the creation of a sequence of vortices, which is caused by the roll-up of shear layers [70]. This type of instability involves vortex shedding can possibly modulate the flame surface area, thereby leading to unstable combustion processes.

2.1.6.2 Chamber and system instabilities

Chamber instabilities refer to the instabilities initiated when combustion occurs in a combustion chamber and are caused by the interactions between combustion and the chamber properties, including the acoustic and fluid-dynamic instabilities. The acoustic instability results from the amplification of acoustic waves due to the acoustical coupling of pressure fluctuation with the natural acoustic mode of the chamber [6,38]. Fluid-dynamic instabilities are related to the changes in flow conditions due to the presence of enclosure chambers. For instance, the energy dissipation at the wall resulting from the oscillatory boundary layers and the flow boundary layers near the chamber wall can lead to changes in flow conditions inside the chamber [38].

Besides the effects directly from the combustion chamber, the system instabilities are caused by the interactions of the feed-system and exhaust-system. Since the system instability is usually characterised by the pressure fluctuation throughout the chamber

[6]. It was found that the pressure can modulate the flow rate of a supplied premixed gas when the self-sustained oscillation was initiated [71]. In a combustion system with a partially premixed configuration, these instabilities can result in fluctuations in fuel supply due to the existence of pressure drop in the vicinity of fuel injects. This will be discussed in Section 2.2.3.

2.1.6.3 Thermoacoustic instabilities

Thermoacoustic instabilities are mainly attributed to the interactions between fluctuations of heat release and pressure [2]. When the fluctuations are coupled with the acoustics of a combustor chamber, a strong oscillation with great amplitude at certain frequencies can be excited. The initiation mechanism of the thermoacoustic instabilities follows Rayleigh criterion [9]. The discussions of thermoacoustic instabilities are in Section 2.2.

2.2 Thermoacoustics

2.2.1 Background knowledge of acoustics

2.2.1.1 Sound pressure Level

Acoustic pressure is the magnitude of the local pressure variation to the ambient pressure caused by the acoustic wave [72]. It can be expressed in the mathematical equation as:

$$p_{sound} = P_{Total} - P_{static} \quad \textbf{2.12}$$

where P_{Total} is the pressure after being disturbed by an acoustic wave, and P_{static} is the static ambient pressure. The range of audible acoustic pressure is extremely wide, which approximately between 10^{-12} and $10\ \mathrm{W/m^2}$ for the audible intensities [72]. Therefore, the logarithmic scales are used to describe the acoustic pressure and intensities. The sound pressure level in decibel (dB) is defined as:

$$SPL = 20log_{10}\frac{p_e}{p_{ref}} \quad \textbf{2.13}$$

where p_e is the effective acoustic pressure amplitude and p_{ref} is the value of the sound pressure corresponding to the auditory threshold at 1 kHz, which is $2 \times 10^{-5}\ Pa$ in the air [72]. Thus, the sound pressure level of the acoustic wave for the effective sound pressure of $2 \times 10^{-5}\ Pa$ is 0 dB.

2.2.1.2 Analysis of the frequency of the standing wave

A standing wave is a kind of wave that does not propagate, and thus no energy and momentum transfer occurs [72]. The wave can be formed by the interference of two identical sinusoidal waves propagating in opposite directions. For a standing wave, the medium particles execute harmonic oscillation, and the oscillations of involved particles are in the same frequency but with different amplitudes. However, the standing wave cannot carry or transfer the energy since it is not propagating. A typical standing wave can be formed by the vibration of a string with both ends fixed. Besides, for the gaseous medium, the standing wave can be formed by the superposition of a travelling wave and its reflected wave when it is incident to a rigid boundary.

For the standing wave on a string, the standing wave is stationary in the horizontal direction, and the string length determines its wavelength depending on the harmonic modes. Several specific frequencies can be excited under symmetrical or unsymmetrical boundary conditions. The boundary condition for the vibration of a string is the fixed-fixed condition since both ends of the string are fixed. The system can be considered to be one-dimensional. The wave equation of the 1-D can be expressed as [73]:

$$\frac{\partial^2 s}{\partial {x_l}^2} = \frac{1}{c^2}\frac{\partial^2 s}{\partial t^2} = -\omega^2 \qquad \textbf{2.14}$$

where s denotes displacement of the particle away from neutral position, x_l denotes longitudinal position, t represents time, c denotes wave speed (acoustic speed for the acoustic wave), and ω denotes angular frequency ($\omega = 2\pi f$ where f is the frequency in Hz). Assume that the displacement s is dependent on x and t separately, the general solution for the equation would be:

$$s(x_l, t) = X(x_l)T(t) \quad \textbf{2.15}$$

Substitute 2.15 to 2.14, the wave equation would be in the following form:

$$\frac{c^2}{X(x_l)}\frac{\partial^2 X}{\partial {x_l}^2} = \frac{1}{T(t)}\frac{\partial^2 T}{\partial t^2} = -\omega^2 \quad \textbf{2.16}$$

where $\frac{\partial^2 s}{\partial {x_l}^2} = \frac{\partial^2 X}{\partial {x_l}^2}T(t), \frac{\partial^2 s}{\partial t^2} = \frac{\partial^2 T}{\partial t^2}X(x_l)$. c was moved to the left-hand side (LHS) of the equation to be with X to find the relationship between sound speed and frequency.

Since the standing wave is the linear superposition of two simple harmonic waves, the solution can be expressed in the following form:

$$X(x_l) = Asin\frac{\omega}{c}x_l + Bcos\frac{\omega}{c}x_l, \quad \textbf{2.17}$$

$$T(t) = Csin\omega t + Dcos\omega t, \quad \textbf{2.18}$$

And

$$s(x_l, t) = X(x_l)T(t) = \left(Asin\frac{\omega}{c}x_l + Bcos\frac{\omega}{c}x_l\right)\sqrt{(C^2 + D^2)}\,cos(\omega t - \varphi) = \left(Msin\frac{\omega}{c}x_l + Ncos\frac{\omega}{c}x_l\right)cos(\omega t - \varphi), \quad \textbf{2.19}$$

where A, B, C, D, M and N are constants and $M = A\sqrt{(\mathrm{C}^2 + \mathrm{D}^2)}, N = B\sqrt{(\mathrm{C}^2 + \mathrm{D}^2)}$

For the fixed-fixed boundary condition, $s(0, t) = s(L, t) = 0$. It is obvious that N=0 at $s(0, t) = 0$, and $Msin\frac{\omega}{c}x_l = 0$ at $s(L, t) = 0$, where L denotes the medium length. The fixed-end acts as the node. The value of M cannot be 0 unless the string is not oscillating. Therefore, to satisfy this condition,

$$sin\frac{\omega}{c}x_l = 0, \quad \textbf{2.20}$$

And then,

$$\frac{\omega}{c} x_l = n\pi, \tag{2.21}$$

where n is the mode number, and $n = 1,2,3 \cdots k$, $k \in \mathbb{N}^*$. Note that $\omega = 2\pi f$, 2.21 can be written in the form of frequency, as:

$$f = \frac{nc}{2L}, \tag{2.22}$$

Based on the value of n, it gives a series of sine waves with different frequencies. These are harmonic modes of oscillation. The frequency of the first mode ($n = 1$) is called the fundamental frequency, which has a wavelength (λ) of twice the string length, as $\lambda = 2L$. And $n = 2$ for the second harmonic mode, of which the frequency is twice the fundamental frequency, and the wavelength is equal to the string length. Likewise, $n = 3$ for the third harmonic mode, as shown in Fig. 2.8. It can be concluded that for the symmetrical boundary conditions, the relationship between the wavelength and string length can be expressed as:

$$\lambda = \frac{2L}{N}, \tag{2.23}$$

For the free-free boundary condition, the relationship between λ and L remains the same. The free-end acts as the antinode of the wave rather than the node for the fixed-end, as shown in Fig. 2.8. It is obvious that the relationship among the frequency, length of the medium, and sound speed is valid for the Free-Free Boundary conditions.

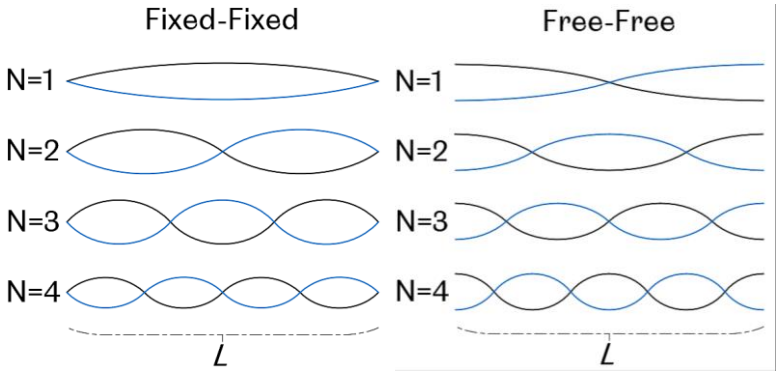

Fig. 2.8 - Different harmonic modes of the standing wave for the Fixed-Fixed and Free-Free boundary condition.

However, the unsymmetrical boundary conditions define different modes and relationships between the λ and L, since the fixed and the free end bring the node and antinode, respectively, as shown in Fig. 2.9. Under this condition, the wavelength of the fundamental mode is quadruple of the medium length, and double for the second harmonic mode. Meanwhile, the oscillation frequency under this condition is doubled than the case at symmetrical boundary conditions. Therefore, the frequency and wavelength can be summarised as follows:

$$f = \frac{nc}{l}, \quad \textbf{2.24}$$

$$\lambda = \frac{4L}{n}, \quad \textbf{2.25}$$

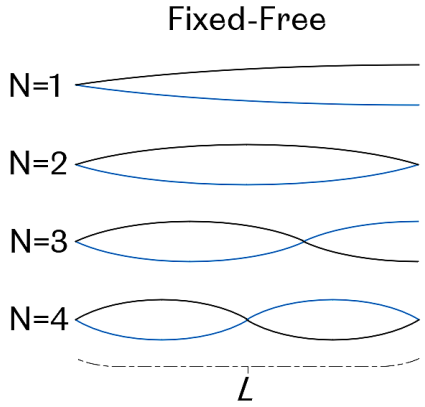

Fig. 2.9 - Unsymmetrical Fixed-Free condition

2.2.1.3 Standing wave in tube

The standing wave in a tube can be considered to be similar to the standing wave of a string. Therefore, the standing wave in a tube can be analysed by applying the standing wave model on a string under different boundary conditions. For the closed-open-ended tube, the standing wave inside would be in a similar form as the fixed-free boundary, whereas the free boundary for the open-end tube. In detail, in terms of the particle velocity, the close end and open end can be considered as fixed boundary (node) and free boundary (antinode), respectively, as shown in Fig. 2.10. Meanwhile, the tube length can be considered to be the string length, because the medium is air and the tube length can be considered to be the medium length. Novotny [74] has pointed out that there is a 90° of the phase difference between the particle velocity and the pressure, which means the velocity node (where the particle velocity is 0) would be the pressure

antinode. Thus, the open end would be the node of the pressure, while the closed end would be the antinode.

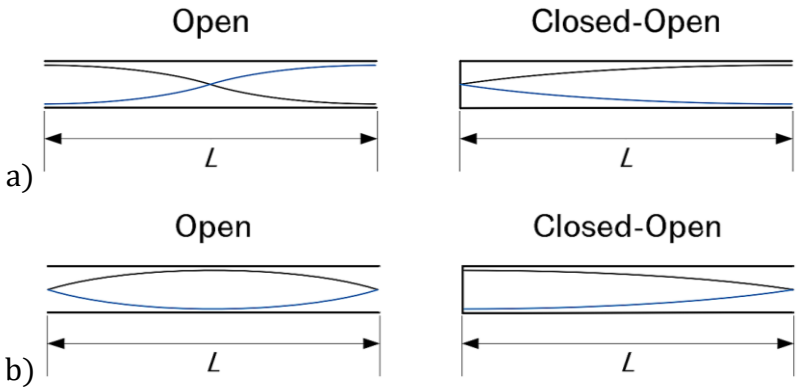

Fig. 2.10 - a) Particle Velocity, b) Pressure amplitude in the Open-open and Closed-Open Tube

However, the oscillation frequency in an organ tube is found to be slightly lower than the result from the calculation by 2.22 or 2.25 [75]. The difference between the actual and calculated frequency result from the reflection boundary of the tube end. Consider a set of particles at the open tube end, they periodically move inward to the tube and then outward. As the particles move outward, they will not be reflected at the tube end since the open tube end is not the rigid reflection boundary. The particles will keep moving outward until all the particles reach the point where the antinode is obtained. Whereas for the close-end boundary condition, all particles are reflected at the end since the end acts as a rigid reflection boundary. Therefore, an end correction of the length needs to be applied to the open end of the tube. According to Rayleigh [75], It is found that the end correction is a function of the resonance chamber hydraulic diameter (d) and can be varied depending on the experimental conditions. While in practical conditions, the following equation (2.26) is usually used for the calculation of end correction for a single open end ($\triangle e$):

$$\triangle e = 0.3d, \tag{2.26}$$

2.2.2 Introduction of thermoacoustic instability

Thermoacoustic instability caused by combustion instability is the self-sustained pressure and velocity oscillations with noticeable amplitude, which appear in reaction flows [2].

The source for providing the considerable temperature gradient is vital to the excitation of thermoacoustic oscillations. It can be in various forms depending on the type of thermoacoustic systems. Heat sources or heating-cooling effects are mainly utilised to trigger thermoacoustic instability. Rijke tube [7] and Sondhauss tube [76] are typical examples of thermoacoustic systems with a heat source. In these systems, the heat source is usually located at the lower part of a tube (or upstream region of the flow direction) [6]. In thermoacoustic systems driven by the heating-cooling effects, they usually consist of a set of hot and cold heat exchangers and are utilised as the power output of thermoacoustic engines [77,78]. Merkli and Thomann [79] successfully predicted and observed the existence of sound for this system. This thesis primarily focuses on the system with a heat source.

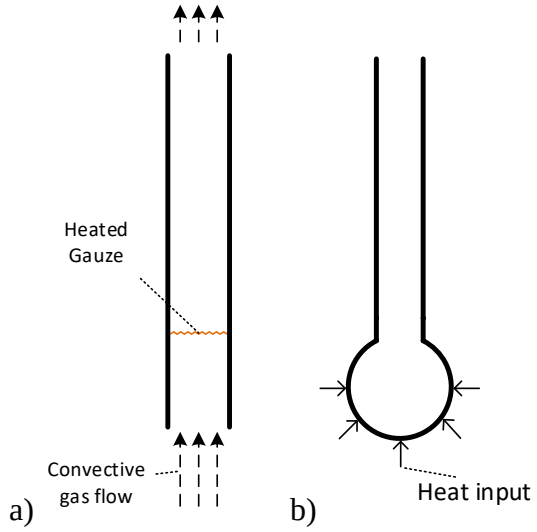

Fig. 2.11. a) Classic Rijke tube and b) Sondhauss tube.

Higgins [80] first observed the heat-excited sounding phenomenon by putting the hydrogen diffusion flame at the lower part of a vertical open-ended glass tube in 1777. It was found that the sound only occurs when the flame is placed at a certain position. Sondhauss [76] then replaced the flame with a closed bulb at the lower end but kept the upper end open. It was found that acoustic oscillations can also be excited when the bulb is heated. Rijke [7] developed the experiment conducted by Higgins [80] by changing the flame to a metal gauze (as a flat heat source) and placing it at the lower part of the tube. It was observed that the heat-excited acoustic oscillation with considerable amplitude could be generated when removes the flame after heating the metal gauze. It was also found that the most intense oscillation was triggered at the

gauze position of a quarter of the tube length from the tube lower end. Due to its relatively simple structure but apparent and intense thermoacoustic oscillations, Rijke tube was widely utilised for studying thermoacoustic instabilities. The schematic figures for both Rijke tube and Sondhauss tube are presented in Fig. 2.11. Feldman et al. [81] developed the Sondhauss tube by adding the cooling parts, by which the heat-to-acoustic conversion was enhanced. They stated that the driving process was like a heat engine, and the way that the oscillator operated was on the thermodynamic cycle.

2.2.3 Mechanism of Thermoacoustic instabilities

Thermoacoustic instabilities are attributed to the nonlinear interaction between the fluctuations of heat release and pressure perturbations if they respond to each other. Lieuwen [64] pointed out that the oscillation of the gaseous medium can be caused by unsteady heat release. The detailed process can describe as follows: the unsteady heat release from a heat source causes the thermal expansion of the gaseous medium, leading to the oscillations of the system. The example given by Raun [6] describes the process of initiating the oscillation of the gaseous medium: the heat is first conducted into the layer of gas, which is adjacent to the suddenly heated wall, causing the expansion of the layer. The layer then forces back to the wall or surroundings. Under this circumstance, the oscillation would be enhanced, and the amplitude would increase if the oscillation of pressure is in phase with layer expansion since the pressure pulse arrives when the gas layer is expanding. The difference in the source of providing temperature gradient can lead to the different ways in the heat transfer between medium and source, which means the different mechanisms for the excitation of oscillation [6]. Regardless of the system, a necessary condition for initiating the oscillation is the mutual encouragement between the heat and pressure fluctuations. A feedback loop can be formed when the heat and pressure fluctuations are in a favourable phase. Rayleigh [9] described the necessary conditions which should be satisfied for the triggering and developing the heat-driven thermoacoustic oscillation.

2.2.3.1 Rayleigh Criterion

Lord Rayleigh [9] proposed a criterion to determine whether the thermoacoustic oscillation can be triggered. The criterion states that the relationship between heat

release and pressure fluctuation is vital for triggering oscillations: the vibration would be encouraged if the heat is added to the medium when the medium reaches the greatest condensation, or removed when the medium reaches the greatest rarefaction. Otherwise, the vibration would be weakened [9]. It can be explained in terms of the phase difference between the heat release and the pressure fluctuation that the oscillation is encouraged when the heat and pressure fluctuations are in phase. As a qualitative conceptual explanation, the original form of Rayleigh criterion cannot quantify the change in the degree of coupling between heat and pressure fluctuations caused by the change in phase difference between them. In order to quantitatively and concisely express the idea of Rayleigh criterion, Putnam [10] further developed Rayleigh criterion to a mathematical form, as shown below:

$$\int \dot{p}(t)\dot{q}(t)dt > 0, \textit{ driving}$$

$$\int \dot{p}(t)\dot{q}(t)dt < 0, \textit{ damping} \qquad \textbf{2.27}$$

where $\dot{p}(t)$ and $\dot{q}(t)$ denote the oscillating components of pressure and heat release rate, respectively, and both of them are in the time-domain. The LHS term quantifies the coupling of heat release fluctuation and pressure fluctuation. This inequation indicates that the oscillation can only be triggered when the heat release fluctuation is in phase with the pressure fluctuation. In detail, the oscillation would be driven and amplified if the phase difference ($\theta_{Heat-Pressure}$) satisfies $|\theta_{Heat-Pressure}| < 90^{\circ}$. Otherwise, the LHS term would be less than 0 when $|\theta_{Heat-Pressure}| > 90^{\circ}$, implying the damping to the oscillation. For the condition of $|\theta_{Heat-Pressure}| = 90^{\circ}$, either driving or damping effect to the oscillation occurs. The thermoacoustic oscillation excited under this situation can have notable nonlinearity [17]. In this nonlinear system, the driving effect cannot cause the unlimited growth of oscillation amplitude. The oscillation will be in a relatively stable state with fewer amplitude changes once the oscillation is fully developed. Since $\theta_{Heat-Pressure}$ can be time-variant, the Rayleigh index (RI) for each cycle is further developed by introducing the period of oscillation to 2.27:

$$RI = \frac{1}{T}\int_0^T \dot{p}(\chi,t)\dot{q}(\chi,t)dt, \qquad \textbf{2.28}$$

where T denotes the period of one oscillation cycle and χ denotes the position. Thus, the coupling of heat and pressure fluctuations can be quantified in the time-domain.

2.2.3.2 Convection-driven thermoacoustic oscillation

The classic Rijke tube with heated gauze can trigger convection-driven thermoacoustic oscillation. The fundamental understanding of Rijke tube was stated by Rayleigh [9], that sound excitation is due to variation of density or pressure of the upward convective gas flow due to the natural convection inside a tube. The main reason for the convection phenomenon is the temperature gradient generated by the heated gauze.

As discussed in Section 2.2.1.3, for a classic open-ended Rijke tube, the tube ends would be the node for pressure and the antinode for the particle velocity. Considering the fundamental mode is excited in a Rijke tube, there is an antinode of pressure and a node of velocity located at the centre of the tube. The particle velocities at both the lower and upper parts of the tube are inwards at the time before the pressure reaches the first peak (first quarter of the oscillation cycle). During this process, the particle velocity can constructively combine with the mean flow velocity in the tube due to the presence of upward convective flow. This combination results in enhanced heat transfer at the heated gauze. The presence of time lag in the heat transfer process at the gauze causes the heat release and pressure fluctuations to be in a favourable phase, leading to the driving effect on the oscillation. However, the heat release and pressure fluctuations are not in phase if the heated mesh is placed at the upper half of the tube. The particle velocity is opposite to the flow velocity during the quarter of one pressure fluctuation cycle before the pressure reaches its maximum value, resulting in heat transfer detraction at the mesh. Under these circumstances, the oscillation is damped. This mechanism also explains that the oscillation can also be excited by a cooled gauze located at the upper half of the tube with a forced hot flow [7].

According to this mechanism, the most intense oscillation for the fundamental mode is excited when the heated gauze is placed at the lower quarter of a tube, because the

maximum product of velocity and pressure can be obtained at this position. For the higher harmonic modes, the position of the gauze for the most driving effect corresponds to the mode number.

2.2.3.3 Combustion-driven oscillation

- Direct and indirect combustion noise

In a combustion system, the combustion noise can be categorised into direct and indirect combustion noise according to the generating mechanism. The direct noise sources usually associate with the fluctuation of heat release rate which is caused by the combustion instabilities. The self-excited thermoacoustic oscillation resulting from the fluctuation of combustion heat release is one of the representative combustion noises caused by the direct noise source. It can be initiated when the fluctuation of pressure has comparable frequencies with the natural oscillation mode of the chamber, and the fluctuation of heat release and pressure are coherent and at a fixed frequency. Thus, the oscillation usually consists of several frequency components, which are the harmonic and the subharmonic modes of the system. It will be discussed in the following part of this section.

The indirect noise sources are mainly attributed to the flow field. Dowling and Mahmoudi [82] stated that indirect noise can be generated if the entropy and vorticity perturbations accelerate at the turbine. The indirect combustion noise will not be discussed in detail in this thesis, because the aeroacousic noise caused by flow and vorticity perturbation is not dominant in the present study due to the low general flow speed. The possible combustion noise source in a real gas turbine engine is shown in Fig. 2.12. Therefore, the combustion noise consists of both direct and indirect noise in a real gas turbine engine.

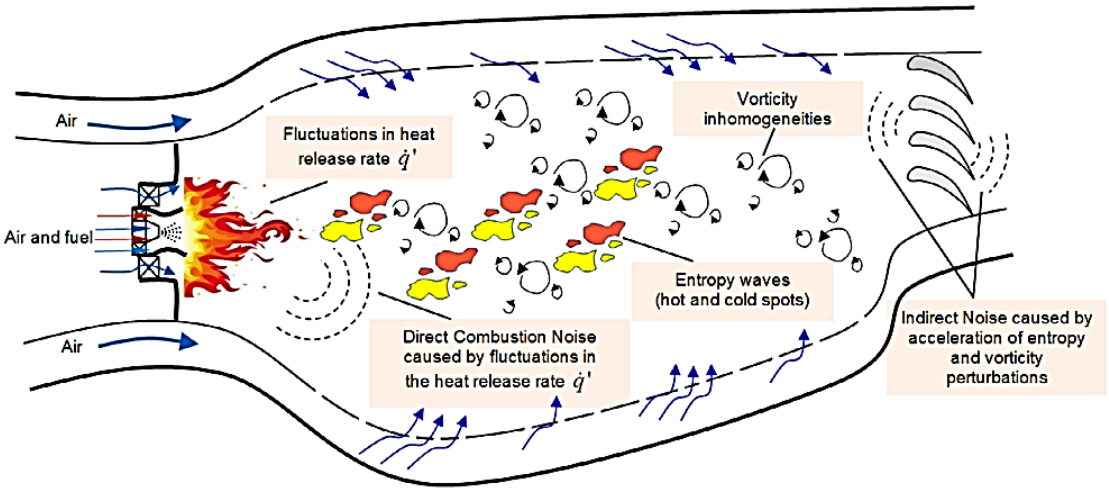

Fig. 2.12 - The possible combustion noise source in the combustion chamber of the gas turbine [82].

- Trigging mechanisms of combustion-driven oscillation

Flame is another common form of heat source in a thermoacoustic system. However, the combustion-driven oscillation is slightly different from the convection-driven due to the different types of convection and initial conditions. Richardson has noticed that Rayleigh criterion is not fulfilled in the system with combustion-induced oscillation [83]. It could not explain or predict all the oscillations because some of the oscillations were out of the range of prediction. The combustion-driven thermoacoustic oscillation is mainly attributed to combustion instabilities. The combustion instabilities can result in fluctuations of flame heat release, which can initiate thermoacoustic oscillations. The pressure fluctuation can further enhance the unsteady combustion and may cause other combustion instabilities that were not involved previously involved [2].

Putnam [84] mentioned that the oscillation could be triggered by the period energy release in the combustion system, including unsteady fuel and oxidiser flow, fluctuation of the flame front area, pulsating flame instability due to the periodic heat transfer or losses between the flame and flame stabiliser. Putnam [2] concluded five important mechanisms of flame-driven-acoustic-oscillation, including pulsations of feed supply, turbulence, pressure coupling, laminar flame speed pulsating and flame area variations. Sujith also summarised the similar mechanisms that can result in and contribute to the positive feedback between the fluctuations of heat and pressure, which includes the

modulation of flame surface area, fluctuations of local and global Φ, coherent structural properties in the flow field, entropy waves and the dynamical properties of droplets. The introduction of mechanisms related to flame and Φ will be more focused.

The mechanism which is primarily responsible for driving oscillations induced by a laminar premixed flame is the modulation of the flame surface area resulting from interactions between the flame and pressure fluctuations [2,6,85]. In Section 2.1.4.2, the flame front of a premixed laminar flame is determined by the equilibrium between S_L and flow velocity of the unburned gas that is normal to the flame front. The equilibrium can be disrupted when the pressure fluctuations disturb the flame. The disturbances caused by the pressure fluctuation first affect the root of the flame. Due to the presence of the flow component in the tangential direction along the flame, the disturbances would be convected upwards in the direction of the flame front, resulting in the wrinkling of the flame front [2,85,86]. Considering the pressure fluctuation is periodic, the flame front is modulated to wrinkle with the pressure fluctuations, leading to the periodic fluctuating flame surface area. An example of wrinkled flame modulated by the external acoustic excitation is shown in Fig. 2.13. The changes in the surface area of a premixed flame imply the variation in heat release, owing to the proportional relationship between them. Then, the thermoacoustic oscillation is triggered when the heat release fluctuation is coupled with the acoustic field within the chamber. In addition, thermoacoustic systems with a flame holder stabilised premixed flame are also subjected to the same mechanisms described above.

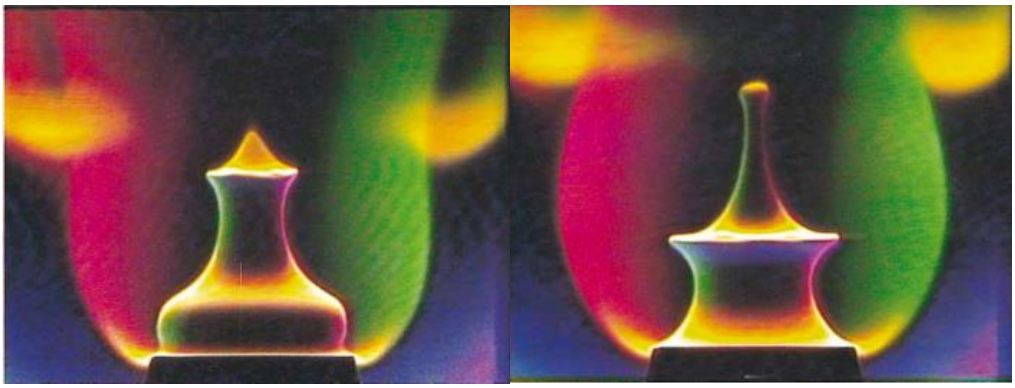

Fig. 2.13. Schlieren images of flame modulated by the external acoustic excitation at 75 Hz [86].

The Φ fluctuations can also contribute to and sustain the feedback loop between heat release and pressure fluctuations in the combustion systems with a partially premixed configuration [40,87,88]. In this type of combustion system, the fuel and air are separately supplied from different sources, and they are mixed in the gas supply pipeline at a short distance before the burner nozzle. Once the thermoacoustic oscillations are initiated, acoustic waves can propagate through the burner nozzle and then perturb the pressure and gas flow velocity in the gas supply pipeline. Under this circumstance, the pressure and velocity fluctuations in the gas supply pipeline near the fuel injector can modulate the fuel supply [87]. Consequently, the periodic oscillation of Φ and the inhomogeneous distribution of local Φ may arise, as shown in Fig. 2.14. The fluctuation of Φ further leads to fluctuated heat release rate of the flame, thereby contributing to the thermoacoustic oscillations. However, a certain phase difference between the pressure fluctuation at the flame and the fluctuation of Φ at the flame root exists, of which the value is determined based on the mean flow velocity in the gas supply pipeline and the distance between the fuel injector and burner nozzle. Meanwhile, a phase lag exists between Φ fluctuation and total heat release fluctuation [87]. Therefore, the Φ fluctuation only contributes to the thermoacoustic instability in this combustion system when the Rayleigh criterion is satisfied.

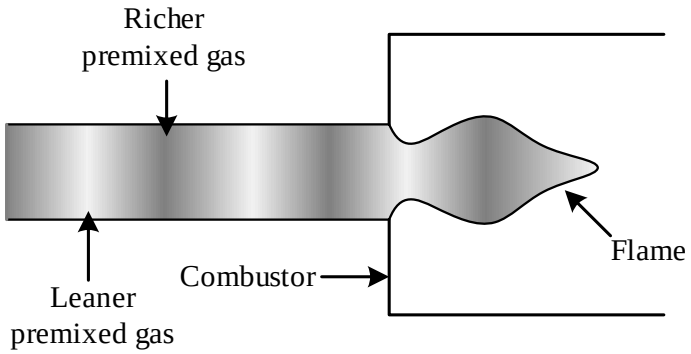

Fig. 2.14. Schematic figure of inhomogeneous distribution of Φ along the gas supply pipeline.

Flow instabilities accompanied by the presence of turbulence can be formed in the region with great velocity gradients or near bluff bodies. As the flow passes through such regions, periodic vortex shedding can be generated, resulting in the perturbation of flame, thereby leading to periodic fluctuations of heat release [65,89]. The mutual interactions between vortex shedding and heat release can be established then. Such

flow instabilities mainly contribute to the thermoacoustic instabilities in the swirl combustor and the bluff-body combustor.

For the combustion system with unevenly premixed or diffusion combustion, such as liquid and solid rockets, the entropy waves are potentially generated because the inhomogeneous combustion heat release caused by unevenly mixed fuel can lead to the non-uniform temperature distribution within the reacting flow. As the entropy wave convects downstream to the exit of the combustor, the acoustic wave can be generated by the acceleration of the entropy waves when they pass through the nozzles, leading to the acoustic driving to the thermoacoustic instabilities [2,82,90].

The droplet instabilities are mainly attributed to the vaporisation process of a droplet. In a liquid fuel combustion system, the liquid fuel undergoes a phase change from liquid to gas. The fluctuated heat transfer may result from the oscillatory and unsteady vaporisation of a droplet in the combustion system due to the velocity and pressure perturbation. Thus, thermoacoustic oscillations can be driven at specific frequencies [91].

The interaction between heat and pressure fluctuation can be summarised from the mechanism discussed above, that the unsteady heat release can result from the pressure perturbation in a combustion system, and the feedbacks from the self-excited oscillation further modulate the combustion and result in the fluctuated heat release. As a result, it eventually leads to the generation of large amplitude pressure fluctuation. However, such interaction cannot lead to the infinite growth of the oscillation amplitude. Therefore, the system may be highly nonlinear and have significant nonlinear characteristics.

2.2.4 Nonlinear dynamical properties of thermoacoustic system

The system under a stable state can become linearly unstable once the disturbances are applied to the system. If the system is a normal system, whose eigenvectors are orthogonal, the system response monotonically decays as the system eigenvectors decay [18]. Conversely, for a non-normal system, such as a thermoacoustic system, the system response does not decay as the eigenvectors decay.

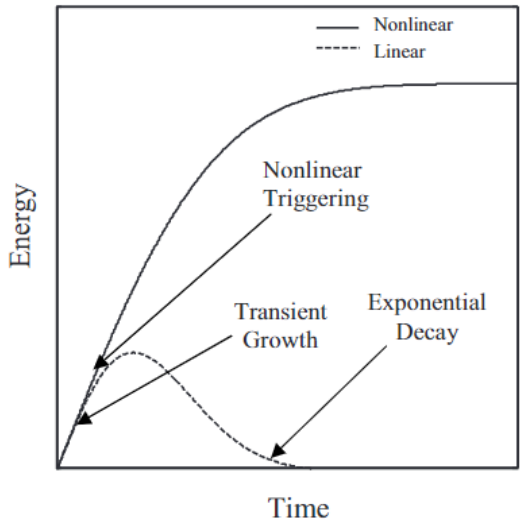

Fig. 2.15. Time-evolution of acoustic energy for the linear and nonlinear process [18].

In a non-normal system, a transient growth process of small disturbances can result from its non-normalities, and the system can spontaneously start to oscillate with a positive growth rate of amplitude which is dominated by the linear effects [92]. This process is initiated by the linear combination of system eigenvectors. However, the positive growth rates cannot result in the infinite growth of the oscillation amplitude if no further disturbance is added. Under the circumstance that the linear effect keeps dominating the system, the oscillation will start to decay exponentially once the oscillation reaches the maximum amplitude if the transient growth process lasts for a sufficiently long time, as shown in Fig. 2.15 by the dashed line [18]. As the response of a linear system is directly proportional to the input signal, small inputs can produce only small responses, which may decay over time. On the contrary, the oscillation can be further amplified if the nonlinear effects come into play. The nonlinear effects can result in situations that the short-term transient growth processes lead to self-sustained oscillations. In a thermoacoustic system, the feedback loop between the heat and acoustics is established during this process. Similarly, the oscillation amplitude cannot infinitely increase since the nonlinearities in the system limit the growth of oscillation amplitude, as shown by the solid line in Fig. 2.15. The system will eventually oscillate at a certain amplitude and frequency (-ies), which is called limit-cycle oscillations, after passing the first bifurcation point to the limit-cycle oscillations [2].

In conclusion, thermoacoustic systems are generally nonlinear and non-normal, and the nonlinearities can be attributed to the interaction between the flame and acoustic wave [2]. The nonlinearities of a thermoacoustic system can also be affected by the nonlinearities of the flow field within the combustion chamber. Thus, similar to the schematic shown in Fig. 2.15, the developing process of self-excited thermoacoustic oscillation consists of two stages, the onset process contributed by linear effects, and the limit-cycle oscillation, which is dominated by the nonlinear effects, as shown in Fig. 2.16.

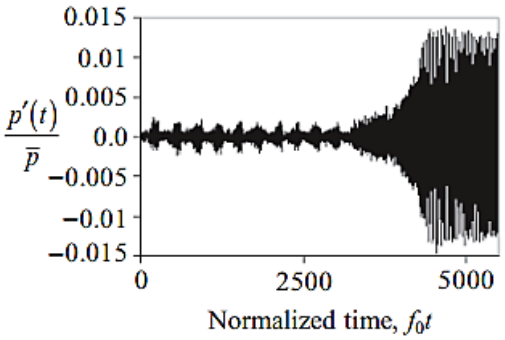

Fig. 2.16. Growing process of the oscillation amplitude [64].

As a nonlinear system, the thermoacoustic system can have several nonlinear characteristics of the system state, including system state bifurcation, intermittency, quasiperiodic and limit-cycle oscillation, depending on the initial conditions [2]. Besides, the system can possibly undergo the transition to chaos, which is an irregular state with unpredictable system behaviours [2].

2.2.4.1 System bifurcation and limit-cycle

The bifurcation of a system describes a qualitative transition of the system from a stable state to an unstable state caused by the changes in control parameters [2,93]. The system can present different properties before and after the bifurcation points. Hopf bifurcation is commonly observed in the thermoacoustic systems since the thermoacoustic systems are usually the higher dimensional dynamical systems [2]. A transition from the stable system to the unstable system with limit-cycle oscillations can be observed during Hopf bifurcation.

- Hopf bifurcation

The Hopf bifurcation describes the system state transition from a steady state to a periodic oscillation. Thus, Hopf bifurcation can result in the formation of periodic limit-cycle oscillation in a thermoacoustic system. For the system with the control parameters before the Hopf bifurcation, any system perturbation due to the disturbance will be damped, and the system will return to stable states. In the phase space, the trajectory of the system moves spirally towards a fixed point, and the trajectory is called a stable spiral, as shown in Fig. 2.17 (a). Conversely, if the control parameters are after the bifurcation point, this fixed point with stability becomes unstable, and its trajectory can reach the closed loop orbit, which results from a limit-cycle attractor [2]. Under these circumstances, the trajectory will eventually return to this orbit even if the trajectory of the system is perturbated by the disturbance. This is a limit cycle of a system, as shown in Fig. 2.17 (b).

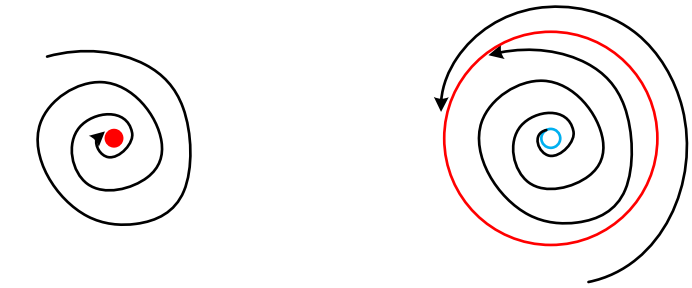

(a) Before bifurcation point

(b) After bifurcation point

Fig. 2.17. Schematic of the trajectory (a) before and (b) after the bifurcation point. The black lines denote the trajectory in phase space, red elements denote the attractor.

There are two types of Hopf bifurcation: supercritical Hopf bifurcation and subcritical Hopf bifurcation [93]. Fig. 2.18 shows the schematic figure in phase space of these two types of bifurcations. μ represents the control parameter, the green solid and red dashed line represent stable and unstable limit cycle attractor, respectively. During the supercritical Hopf bifurcation, the system generally becomes unstable, and a stable limit cycle with low amplitude is formed as the control parameter changes. Thus, the stable limit cycle attractor with limited amplitude attracts the trajectory toward it. For the system nearly after the bifurcation point, the oscillation amplitude gradually increases as the system moves away from the bifurcation point, as shown by green solid line in

Fig. 2.18 (a). In contrast, during the subcritical Hopf bifurcation, an unstable limit cycle is created when the system becomes unstable as the control parameter changes. The oscillations with considerable large amplitude suddenly emerge once the system passes through the bifurcation point, indicating that an unstable limit cycle attractor repels the trajectory away from it, as shown by the red dashed line in Fig. 2.18 (b).

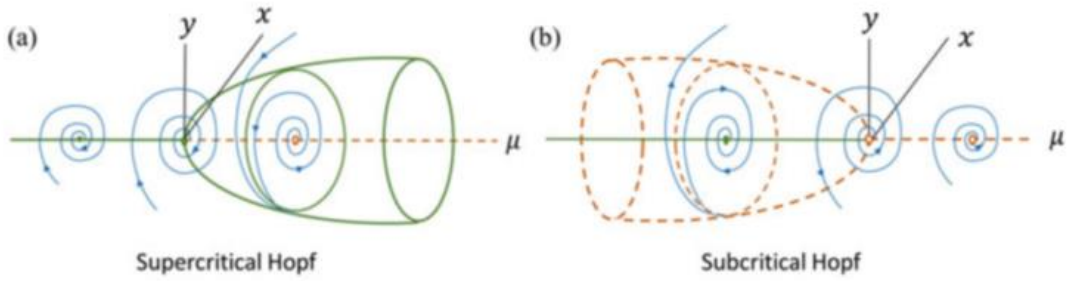

Fig. 2.18. Comparison of supercritical and subcritical Hopf bifurcation. The solid line represents the stable branch, while the dashed line for the unstable branch [2].

- Limit-cycle oscillation

In thermoacoustic systems, the self-excited oscillation caused by the nonlinear interaction between the heat and pressure fluctuations is typical limit-cycle oscillation. It can occur after the bifurcation point. Generally, a limit-cycle oscillation is usually periodic, self-sustained, with a relatively stable amplitude and discrete frequencies, and only exists in nonlinear systems [2]. The isolated and closed curves of a limit-cycle attractor can be obtained when projecting the trajectory of the system to a higher-dimensional phase space. The trajectories of the system with limit-cycle oscillation will return to the same position in the phase space after a certain time, indicating the recurrence of the system state. Therefore, the system with limit-cycle oscillation can have strong deterministic natures.

The limit-cycle oscillations can be categorised into three different types according to the stability of the limit cycle: stable limit cycle, unstable limit cycle and semi-stable limit cycle [93]. They present different responses when the system is disturbed by the disturbance. In systems with a stable limit cycle, the attractor can attract the trajectory back at an exponential rate once the trajectory is perturbed [2,94]. The unstable limit cycle is different from the stable limit cycle, the trajectory of the system in phase space

diverges from the attractor exponentially once the system receives the disturbance. A semi-stable limit cycle is defined as the system having some trajectories on one side of the attractor diverging from it while the rest of the trajectories on the other side converge to it, which means the attractor is attracting at one side but repelling at the other side [94].

2.2.4.2 Period-n and quasi-periodic oscillations

In thermoacoustic systems, the self-excited oscillations can consist of multiple frequencies due to the nonlinear interactions within a system [95–99]. A period-n oscillation refers to a type of oscillation which is characterised by the presence of multiple discrete frequencies with commensurate relationships between them [2], such as integer relationships. In phase space, the trajectory of a period-n oscillation will return to the same position after n periods. An example of a system that exhibits period-n oscillation is the thermoacoustic system with harmonic limit-cycle oscillations. In this case, the oscillation is considered to be period-2 if the fundamental and the second harmonic modes are excited, where the frequency of the second harmonic mode (f_{2nd}) is doubled than the fundamental mode (f_{1st}), as $2f_{1st} = f_{2nd}$. Besides, the period-2 oscillation can also result from the harmonic and its corresponding subharmonic mode, where the subharmonic mode has half the frequency of the corresponding harmonic mode. It is possible to excite the subharmonic responses in the thermoacoustic system driven by the premixed and diffusion flame with the presence of external acoustic excitations [55,100], in which the diffusion flame can generate more complex frequency responses.

Quasi-periodic oscillations are in contrast to period-n oscillations, since quasi-periodic oscillations can consist of multiple incommensurate frequencies [93]. Under these circumstances, the trajectories in the phase space will not repeat themselves after a certain time period, meaning that the oscillation is quasi-periodic. Meanwhile, the phase space might present a two-torus structure. The beating oscillation in the thermoacoustic system usually has the characteristics of quasi-periodicity, which results from two incommensurate frequencies with similar values [17,22].

2.2.4.3 Chaotic oscillation and intermittency

Chaotic oscillations are defined as oscillation that is aperiodic with a broad and continuous frequency spectrum in which no noticeable dominant frequency or harmonics can be observed [93,101]. In such systems, the system states never repeat but with limited deterministic nature [2], which is different from an unpredictable system with a random process. The chaotic states are usually highly sensitive to the initial conditions, meaning that significant changes in system states with exponential divergences from the original state can result from the finite changes in the initial conditions [102]. Intermittency describes the random fluctuations of the system states between chaotic and periodic states [103]. Both chaotic oscillations and intermittency can also be triggered in the thermoacoustic systems and usually occur around the bifurcation points of system states [19,22,104–106].

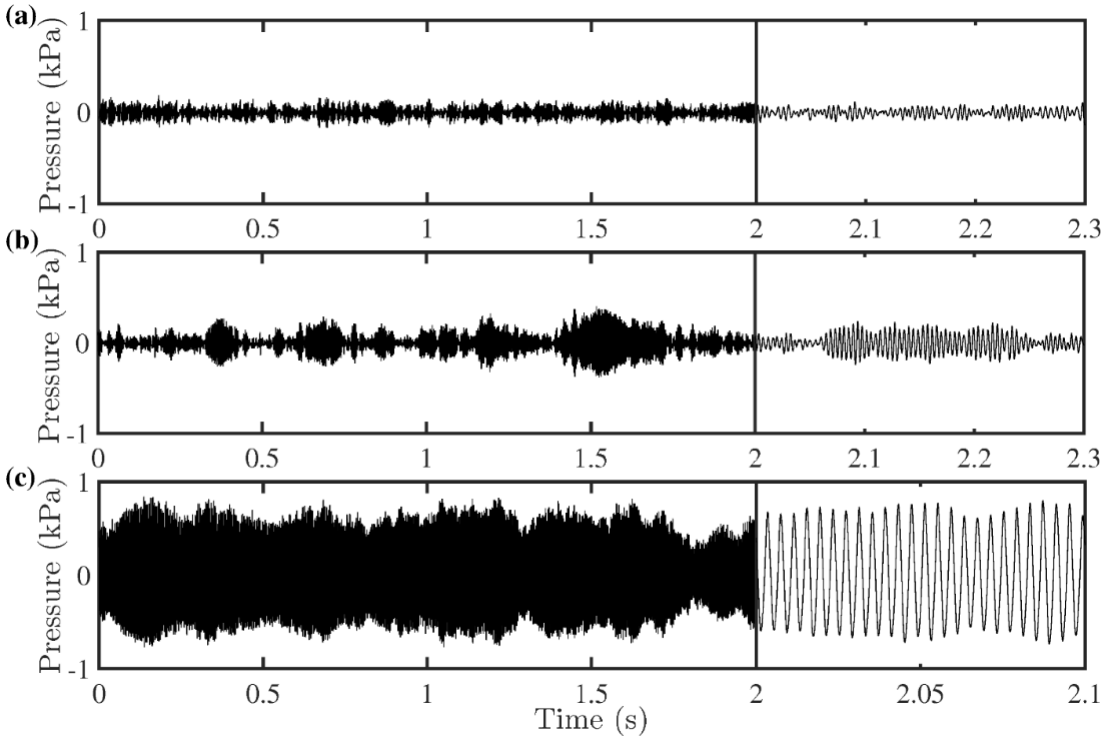

Fig. 2.19. Thermoacoustic oscillation with (a) Chaotic oscillation (Combustion noise), (b) Intermittency, and (c) Limit-cycle oscillation [17].

2.3 Time-domain analysis method for nonlinear system

As discussed in Section 2.2.4, thermoacoustic systems can be highly nonlinear in system dynamics, which means the system dynamical properties can be temporally

dependent. For these systems, the linear time series analysis method might not be sufficient to investigate the system behaviours and reveal the nonlinear characteristics of a system. Therefore, the nonlinear data analysis method should be utilised to investigate the system dynamical properties of thermoacoustic oscillation.

2.3.1 Construction of the phase space

The phase space of a system refers to a multi-dimensional space which is constructed from the independent system variables, of which the coordinates are determined by these variables [2,93]. The single point in phase space represents a state of the system, called the 'state point'. The trajectory in the phase space is formed by the evolution of state points, showing the time-evolution of the system. Furthermore, the system dynamics and behaviours can be indicated by such trajectories.

However, it is difficult to define and obtain the solutions for a real system because the variables involved can be very complex. Therefore, it is nearly impossible to construct the phase space based on all system variables and thus characterise the system. For the analysis of a real nonlinear dynamic system, obtaining the properties of attractors is usually sufficient to characterise the system rather than obtaining the complete original phase space. It is found that the dynamics of the system, which is governed by an attractor, can be reconstructed from the time series of a single dynamic variable. Sufficient information about the other system variables can be provided by this single variable [107–109]. This method for reconstructing phase space based on a time series of a single variable is proposed by Takens and is known as Takens' embedding theorem (Takens' theorem) [109]. Takens' utilises the time delays (τ) to obtain the space vectors from a single signal measured and thus reconstruct the phase space for the system. The dimension of the phase space is determined by the embedding dimension (D).

For instance, define a time series of pressure fluctuation ($p(t)$) measured from the system at a sampling rate of Fs, with a total data length of N_p:

$$p(t) = \left[p(1), p\left(1+\frac{1}{Fs}\right), p\left(1+\frac{2}{Fs}\right), \dots\dots, p\left(1+\frac{(N_p-1)}{Fs}\right)\right], \quad \textbf{2.29}$$

According to Takens' theorem, delay $p(t)$ by a predefined τ to obtain a series of delayed time series $p_{t+\tau}$, $p_{t+2\tau}$,…, $p_{t+(D-1)\tau}$, where $p_{t+\tau} = \left[p(1+\tau), p\left(1+\frac{1}{Fs}+\tau\right), p\left(1+\frac{2}{Fs}+\tau\right), \ldots\right]$. The number of delayed time series is determined by the optimum embedding dimension (D). Then, the space vector can be obtained from the delayed time series:

$$\mathbf{P}_{\mathrm{t}}(\mathrm{D}) = [p_t, p_{t+\tau}, p_{t+2\tau}, \cdots, p_{t+(D-1)\tau}] \quad \textbf{2.30}$$

Note that the delayed time series can also be obtained backwards, as $p_{t-\tau}$, $p_{t-2\tau}$,…, $p_{t-(D-1)\tau}$, and the corresponding space vectors can be obtained accordingly. Note that the equation and parameters are in the time-domain.

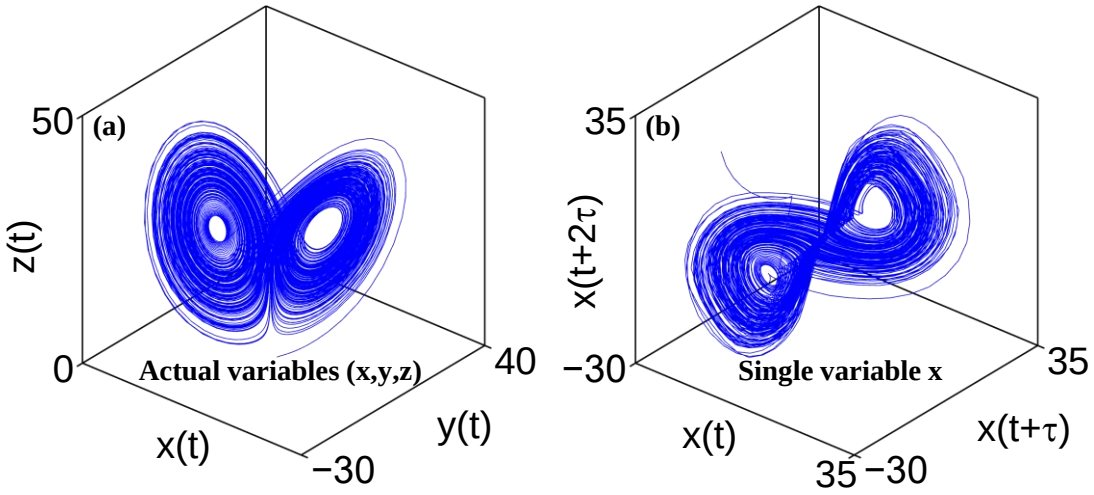

Fig. 2.20. The phase space for the Lorenz attractor constructed from (a) the actual system variables (x,y,z), and reconstructed from (b) space vector which is obtained based on Takens theorem with $D = 3$ and $\tau = 5$.

The 3-dimensional phase space of Lorenz attractor constructed from the space vector based on Takens' theorem is shown in Fig. 2.20 (b). It can be found that the trajectory reconstructed from single variable (as shown in Fig. 2.20 (b)) is not exactly the same as that in the original phase space (Fig. 2.20 (a)). While the phase space constructed based on Takens' theorem clearly exhibits the two-lobes attractor, which is one of the

most important properties of Lorenz attractor and can be found in the original phase space.

During the reconstruction of phase space, τ is of great significance in obtaining the appropriate space vector and reconstructing an appropriate phase space that accurately reflects the properties of the original system. Selecting either an improperly small or large τ can result in the incorrect properties of reconstructed phase space, leading to a failure to characterise the system adequately. In detail, the over-correlated space vectors can result from an excessively small τ, leading to a trajectory which consists of points that are not sufficiently separated in phase space. Conversely, an excessively large τ can result in under-correlated space vectors, which may lead to the erroneous generation of random attractors [2]. In practice, the first zero-crossing point of the autocorrelation function and average mutual information methods are commonly utilised depending on the system properties [110].

The autocorrelation function can determine the degree of correlation between a time series and a delayed version of it over a time delay τ_c ($\tau_c \geq 0$). In this case, the autocorrelation for time series $p(t)$ ($\mathrm{R_{pp}}$) can be calculated by the following equation:

$$\mathrm{R_{pp}}(\tau_c) = \frac{\sum_{k=1}^{N_p-\tau_c}[p(t_k+\tau_c)-\bar{p}(t)][p(t_k)-\bar{p}(t)]}{\sum_{k=1}^{N_p}[p(t_k)-\bar{p}(t)]} \quad \textbf{2.31}$$

where $\bar{p}(t)$ is the time-averaged value of $p(t)$. Thus, a series of τ_c and the corresponding $\mathrm{R_{pp}}$ can be obtained. The maximum value is obtained at the $\tau_c = 0$, indicating its original position. The optimum τ can be determined by the first zero-crossing point of $\mathrm{R_{pp}}(\tau_c)$. The first zero-crossing point of the autocorrelation function method is usually utilised in a system with relatively high periodicity and smooth phase space. If the correlation within the time series is not obvious, the average mutual information method is preferred for determining an optimum τ. In this case, the degree of mutual correction $I(\tau_c)$ based on average mutual information method can be determined as:

$$I(\tau_c) = \sum_{p(t_k),p(t_k+\tau_c),k=1}^{N_p-\tau_c} P[p(t_k), p(t_k+\tau_c)]\, log_2 \left[\frac{P[p(t_k), p(t_k+\tau_c)]}{P[p(t_k)]P[p(t_k+\tau_c)]}\right] \quad \textbf{2.32}$$

where $P[p(t_k)]$ is the induvial probability density of $p(t_k)$, and $P[p(t_k), p(t_k+\tau_c)]$ is the joint probability density of $[p(t_k), p(t_k+\tau_c)]$. The optimum τ can be determined for most of the nonlinear dynamic systems by the criterion of $\frac{I(\tau_c)}{I(0)} = \frac{1}{5}$ [110].

Another important parameter for reconstructing phase space is the optimum minimum embedding dimension. Similarly, the inappropriate embedding dimension can also lead to inadequate correlations in phase space. An insufficient *D* results in the over-correlation around a specific state point, while excessive *D* for the under-correlation. The over-correlated points of a certain state point are called false neighbours, which are usually formed when projecting an attractor with high-dimensional properties to a low-dimensional phase space [110]. Removing the false neighbours for the appropriate phase space reconstruction is vital. The false nearest neighbour (FNN) method is usually utilised to find the minimum *D* to remove the false neighbours around a certain state point [111]. The distance ($S_k(D)$) in the phase space with a dimension of D between $\mathbf{P}_{t_k}(\mathrm{D})$ and its nearest neighbours, $\widehat{\mathbf{P}}_{t_k}(\mathrm{D})$ can be obtained based on the Euclidean distance:

$$S_k(D) = \sqrt{\sum_{i=1}^{\mathrm{D}} [\widehat{\mathbf{P}}_{t_k}(\mathrm{D}) - \mathbf{P}_{t_k}(\mathrm{D})]^2} \quad \textbf{2.33}$$

By increasing the attractor dimension from D to $D+1$, the $S_k(D+1)$ can be obtained according to 2.33. The $\widehat{\mathbf{P}}_{t_k}(\mathrm{D})$ can be considered to be a false neighbour if $S_k(D+1) > S_k(D)$. Note that both $\mathbf{P}_{t_k}(\mathrm{D})$ and $\widehat{\mathbf{P}}_{t_k}(\mathrm{D})$ are in the phase space. In the practice, a commonly used criterion based on the standard deviation of $p(t)$ (σ_a) to indicate the attractor size is usually utilised for identifying whether the neighbour is a false nearest neighbour [111]:

$$\frac{S_k(D+1)}{\sigma_a} \geq 2 \tag{2.34}$$

$$\sigma_a = \sqrt{\frac{1}{N_p}\sum_{i=1}^{N_p} p(i) - \bar{p}(t)} \tag{2.35}$$

The minimum D can be determined by iteratively increasing its value until a significant reduction in false neighbours is achieved.

2.3.2 Wayland translation error

In the reconstructed phase space based on Takens' theorem, the continuity of the phase space is one of the important properties to indicate the system behaviour. Wayland et al. propose a method to measure the determinism of a time series quantitatively [112]. The quantitative measure is obtained from the continuity of dynamical evolution, which is implemented by calculating the translation error of the neighbours around a certain state point in the reconstructed phase space [113]. For instance, if the system is fully deterministic, the points located near each other in the phase space will be mapped to the corresponding points, which also are closed together [112]. Wayland method has been utilised to reveal the deterministic natures of many types of system, including the thermoacoustic system, wind noise, and even the system with high levels of uncorrelated noise [112–114].

For a time series $p(t)$, Wayland translation error can be calculated as follows. The space vector for reconstructing the phase space can be obtained from 2.30, where τ is determined by the method discussed in Section 2.3.1. For a certain state point $\mathbf{P}_0$, its k nearest neighbours ($\mathbf{P}_1, \dots, \mathbf{P}_i, i = 1, \dots, k$) can be determined based on the Euclidean distance between them as shown in 2.33. Here, the nearest neighbours cannot be temporally correlated with each other. To achieve this, the temporal difference between $\mathbf{P}_i$ and $\mathbf{P}_0$ should be greater than τ. Then, the images of $\mathbf{P}_0$ ($\mathbb{P}_0$) and its neighbours ($\mathbb{P}_1, \dots, \mathbb{P}_i, i = 1, \dots, k$) can be obtained by determining a certain time interval m for

images. The translation vector between the images and original point can be obtained from:

$$\mathbf{v}_{\text{trans}}(i) = \mathbb{P}_i - \mathbf{P}_i, \tag{2.36}$$

For a system with high deterministic nature, the $\mathbf{v}_{\text{trans}}(i)$ should be approximately equal for each point. The average $\mathbf{v}_{\text{trans}}(i)$ over k nearest neighbours is calculated as:

$$\bar{\mathbf{v}}_{\text{trans}}(i) = \frac{1}{k+1}\sum_{i=0}^{k} \mathbf{v}_{\text{trans}}(i), \tag{2.37}$$

where $k+1$ means that $\mathbf{v}_{\text{trans}}$ for $\mathbf{P}_0$ is also taken into consideration. Based on $\bar{\mathbf{v}}_{\text{trans}}(i)$, then translation error can be determined by:

$$e_{trans} = \frac{1}{k+1}\sum_{i=0}^{k} \frac{\|\mathbf{v}_{\text{trans}}(i) - \bar{\mathbf{v}}_{\text{trans}}(i)\|^2}{\|\bar{\mathbf{v}}_{\text{trans}}(i)\|^2}, \tag{2.38}$$

where $\|.\|$ denotes the Euclidean length. In practical situations, e_{trans} is usually calculated multiple times by selecting different $\mathbf{P}_0$ to eliminate the unexpected deviation and obtain a reliable result.

Based on 2.38, it can be concluded that, for a system with high deterministic nature, the e_{trans} should be nearly 0, because $\mathbf{v}_{\text{trans}}(i) = \bar{\mathbf{v}}_{\text{trans}}(i)$ under this circumstance. Conversely, if a system consists of random processes, such as white gaussian noise, the e_{trans} will be nearly 1 [112].

2.3.3 Recurrence analysis

2.3.3.1 Recurrence plot

Poincaré proposed a famous statement during the discussion of the restricted three-body problem: 'the system recurs infinitely many times as close as one wished to its initial

state' [115]. Therefore, the recurrence of the system state for any dynamic system can be one of the most important characteristics. Eckmann et al. first propose a method to visualise and investigate the recurrence behaviour of a dynamical system through its phase space, which is called recurrence plot (RP) [116]. In the phase space, if the trajectory of the system can return to a similar position where it previously visited, this situation means the system state recurs, namely recurrence. The recurrence plot refers to the plot for visualising the recurrence of the system state, which consists of these recurrence points. The system dynamical properties can be indicated by the different structural properties in the plot [2,115,116].

In a real system, it is nearly impossible for the trajectory of system to revisit the exact same position as before. Therefore, a threshold (ε) of Euclidean distance between two trajectory points in the phase space is necessary to be defined to determine whether the system can be considered to recur, as shown in Fig. 2.21.

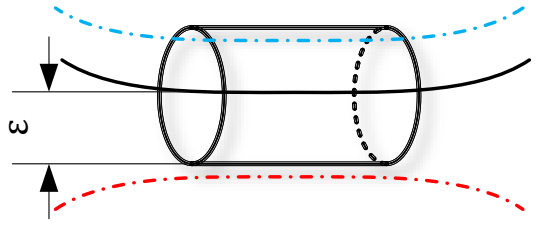

Fig. 2.21. Schematic for showing the determination of recurrence of system state. The black solid line in the centre of the threshold tube with a radius of $\boldsymbol{\varepsilon}$ *is the reference trajectory in the phase space, the blue dashed line is the trajectory that is considered to recur, and the red dashed line is not recurred.*

The recurrence matrix ($\mathbf{R}_{i,j}$) for a time series with the consideration of ε can be constructed by:

$$\boldsymbol{R}_{i,j} = \Theta\left(\varepsilon - \left\|\boldsymbol{x}_i - \boldsymbol{x}_j\right\|\right) \quad i,j = 1,2,3,\cdots,N, N \in \mathbb{R}^* , \tag{2.39}$$

where $\mathbf{x}_i$ and $\mathbf{x}_j$ is the space vector constructed by 2.30 based on Takens' theorem. Θ is the Heaviside function defined as:

$$\Theta(x) = \begin{cases} 0, & x < 0 \\ 1, & x \geq 0 \end{cases} \quad \textbf{2.40}$$

Thus a 2-dimensional matrix which only consists of 0 and 1 can be constructed, at where the element of 1 denotes the recurrence of the state and 0 for the no recurrence. One of the crucial parameters for correctly indicating the recurrence properties of the system is ε. It is usually to select the relatively small ε but still contains sufficient recurrence points for a certain system state [2]. In practical situations, ε is usually determined based on the attractor size, as 10% of the mean or maximum diameter of the attractor [117]. Another critical parameter is the embedding dimension of the space vector. The selection of optimum minimum D is the same as the selection for phase space reconstruction, which utilises the FNN method, as discussed in Section 2.3.1.

Depending on the system dynamical properties, the different structures formed by the recurrence points can be obtained in the plot. A solid main diagonal line from the left bottom corner to the right top corner can be formed by $\boldsymbol{x}_i = \boldsymbol{x}_j, i = j$, expressing the same point on the trajectory. This line is called the line of identity (LOI). For a periodic system, its plot mainly consists of diagonal structures parallel to the LOI. The continuities of diagonal structures can indicate the periodicity of the system. A summary of usually formed structures and the dynamical properties indicated are listed in Table 2.2 [115]:

Table 2.2. Structures in the recurrence plot and the properties they indicate.

Structures	**Properties of the system state**
Diagonal line parallel to LOI	System is in a periodic state with considerable periodicity and deterministic natures, and the system behaviours repeat over time.
Diagonal line orthogonal to LOI	The evolution of system state is similar in the reversed direction of time.

Homogeneously distributed points	System is in a chaotic state, system behaviours are not periodic and predictable.
Isolated points	System state is fluctuating, system behaviours may be random and uncorrelated.
Vertical and horizontal line	System state is not changed over time, system is in laminar states.
Bowed structures	System states evolve similarly but at different velocity, the dynamical properties of system is changing.
Periodic occurred structure	System has cyclic behaviours, and the distance between the periodic structures indicates the period of the cyclic behaviours
Interrupted structures	Current system state transits to another different state.
Fading structures	The instincts trends might be contained in the system variables.

2.3.3.2 Recurrence quantification analysis (RQA)

As discussed in the previous section, the structural properties can be highly related to the system dynamical properties, while the recurrence plot can only provide a qualitative analysis of the system, which may lead to the ignorance of small structures in the plot [115]. Therefore, it is necessary to measure the degrees of complexity of the system by quantifying the structural properties in the plot through statistical measures. By which the recurrence of the trajectory of the system in the reconstructed phase space can also be revealed. This method for quantitively characterising the structural properties in a plot is known as recurrence quantification analysis (RQA), and is mainly contributed by Zbilut, Webber and Marwan et al. [118–120]. The statistical measures can be categorised into three major types according to the type of structures they are based on, including the density of the points, diagonal and vertical structures. The LOI is usually excluded in the calculations of all RQA measures [115]. It has been verified that the system state transition between the periodic and chaotic states and the bifurcation points can be clearly identified through the measures for quantifying the

diagonal lines [120,121]. The measures that quantify vertical structures can indicate the chaos-chaos transition [120]. The commonly used RQA measures are introduced and discussed below.

1. Measure for density of points

- Recurrence rate (RR)

Recurrence rate is the most straightforward measure among all RQA measures, which presents the percentage of recurrences in a plot. It calculates the ratio of the recurrence point to all state points in the phase space utilised in the recurrence plot. For a system without any recurrence, the RR is 0, whereas it equals to 1 for the system that is completely recurred. It is usually in the form of percentage.

$$RR(\varepsilon) = \frac{1}{N^2}\sum_{i,j=1}^{N} \boldsymbol{R}_{i,j}(\varepsilon)\,, i \neq j, \tag{2.41}$$

where N represents the total length of recurrence data.

2. Measures for diagonal structures

- Determinism (DET)

Determinism quantifies the ratio of recurrence points which form the diagonal lines to all recurrence points in RP. For a correlated system with considerable periodicity, it forms long continuous diagonal lines and less isolated recurrence points. Under this circumstance, the DET of this system is approaching 1, indicating a deterministic system. Conversely, an uncorrelated system with chaotic states results in the lack of diagonal structures and massive isolated recurrence points, leading to a DET of nearly 0, which implies the low determinism characteristics of the system.

$$DET = \frac{\sum_{l=l_{min}}^{N} lP(l)}{\sum_{l=1}^{N} lP(l)}, \tag{2.42}$$

where $P(l)$ is the histogram of the diagonal lines with a length of l. l_{min} is the minimum diagonal line length, which determines the minimum number of continuous points in the diagonal direction which are considered to be a diagonal line.

- RATIO

RATIO calculates the ratio of DET to RR. Although DET and RR have a similar tendency in most systems, the DET can have independent variations from RR in some cases. For instance, the system has constant DET but decreasing RR when a qualitative transition occurs [119].

$$RATIO = \frac{DET}{RR}, \tag{2.43}$$

- Longest diagonal line (L_{max}) and divergence (DIV)

The longest diagonal line is the length of the longest diagonal line in the RP. Based on L_{max}, the DIV can also be determined as the inverse of L_{max}, indicating the degree of trajectory diverging in the phase space. For a periodic system, a very high value of L_{max} can be obtained, indicating a lower degree of the divergence of system (small DIV), while a low L_{max} and high DIV for a chaotic system or the system with significant state changes.

$$L_{max} = \max\left(\{l_i\}_{i=1}^{N_l}\right), \tag{2.44}$$

$$DIV = \frac{1}{L_{max}}, \tag{2.45}$$

where N_l denotes the total number of diagonal lines in the RP.

- Average diagonal line length (ADL)

Average diagonal line length calculates the average length of all diagonal lines in RP. It can quantify the degree of parallelism and the average predictability time by indicating the average time that two segments on the trajectory in the phase space gathered. For a periodic system, the ADL can be high, indicating the system has great parallelism in the phase space, and the system state is less likely to be interrupted. Conversely, for a chaotic system and the system with periodically changed state, a small ADL is obtained.

$$ADL = \frac{\sum_{l=l_{min}}^{N} lP(l)}{\sum_{l=l_{min}}^{N} P(l)}, \quad \textbf{2.46}$$

- Shannon Entropy (ENT)

Shannon entropy of the signal quantifies the complexity of RP from the aspect of diagonal lines. It is calculated based on the probability distribution of the diagonal line with an exact length of l, which is defined as $p(l) = P(l)$. For the signal of a system with high complexity, such as a chaotic system, the ENT can be significantly high, while very low ENT for a periodic signal.

$$ENT = -\sum_{l=l_{min}}^{N} p(l) ln p(l), \quad \textbf{2.47}$$

Note that the ENT has the unit of nat if it is calculated based on natural logarithm ln. It can also be calculated based on log_2, with the unit of bit.

3. Measures for vertical structure

- Laminarity (LAM)

Laminarity calculates the ratio of the recurrence point that forms the vertical structures to all recurrence points in the RP. It quantifies the occurrence of laminar states in the signal, where the laminar state is a state with significantly small oscillation amplitudes,

and the system seems trapped in a state. It is usually utilised to indicate the laminar phase of a system with intermittency [2].

$$LAM = \frac{\sum_{v=v_{min}}^{N} vP(v)}{\sum_{v=1}^{N} vP(v)}, \quad \textbf{2.48}$$

where $P(v)$ denotes the histogram of vertical lines with the length of v. v_{min} denotes the minimum vertical line length, which determines the minimum number of continuous points in the vertical direction that can be considered to be a vertical line. For a periodic system, the LAM is nearly 0 since the barely vertical structure can be found in the RP.

- Trapping time (TT)

Trapping time calculates the average vertical line length, which can quantify the mean time of the system in the laminar phase. It indicates how long the system remains in a specific state and how long the state is trapped.

$$TT = \frac{\sum_{v=v_{min}}^{N} vP(v)}{\sum_{v=v_{min}}^{N} P(v)}, \quad \textbf{2.49}$$

Among these three main types of measure, the RR, which is based on the recurrence density, can be applied to investigate both chaotic and periodic systems. The measures calculated based on the diagonal structures are mainly utilised to quantify the periodicity and the complexity of the system, and to indicate the transition between the periodic and chaotic states, or two periodic states. They can be utilised to efficiently indicate the system deterministic natures and distinguish two periodic states. However, they cannot indicate the characteristics of a chaotic state, thereby distinguishing two chaotic states. The measures calculated based on the vertical structure can be utilised to find and indicate the transition between two chaotic states, which cannot be implied from the diagonal structures. They can be utilised to investigate intermittency and characteristics of chaotic states, but they are not capable of analysing a periodic system due to the absence of vertical structures.

2.4 Summary

This chapter serves as an essential introduction and literature review for the present study. It covers the basic combustion theory, including some combustion definitions, flame characteristics and combustion instabilities. Meanwhile, this chapter reviews the background related to thermoacoustics research, including the phenomenon, mechanisms, nonlinearities, along with basic nonlinear system knowledge. Furthermore, the chapter introduces various analysis methods that are instrumental in investigating the dynamics of nonlinear systems. The comprehensive background knowledge presented in this chapter provides valuable guidance for the research conducted in this study.

Chapter 3 General methodology

The aim of this thesis is to investigate the characteristics of thermoacoustic oscillations in a combustion-based Rijke tube. To characterise such phenomenon, the parameters, including temperature, oscillation frequnency, amplitude, flow conditions at tube end and so on, play important roles in this project. In order to provide a clear presentation of the methodology for this study, the general experimental setup and the data acquisition system utilised will be introduced. The descriptions of the experimental setup for each study are given in the corresponding chapter.

3.1 General setup for the Rijke tube test rig

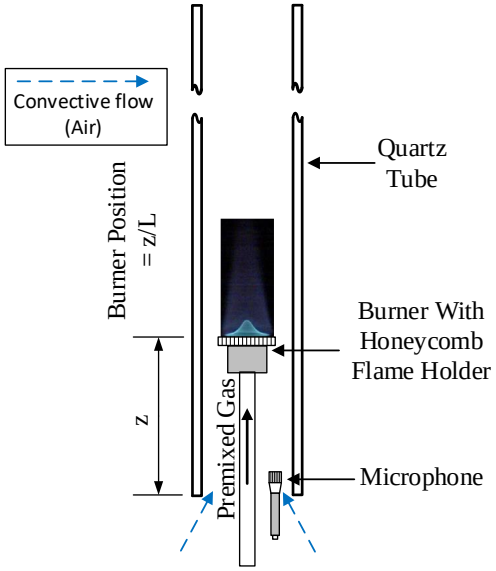

Fig. 3.1. Schematic of the general setup of Rijke tube

The general setup for the combustion-based Rijke tube is shown in Fig. 3.1. And a photo for test rig is shown in Fig. 3.2. In order to trigger the thermoacoustic oscillation, a relatively high length-to-diameter ratio of the tube was utilised to meet the requirement of the sufficient temperature gradient between the upstream region and downstream region in the tube to the flame. Meanwhile, to meet the requirement of flame capturing, the transparent quartz tubes were selected as the main part of the Rijke tube. Two quartz tubes with the same length of 1.0 m and the same thickness of 2 mm,

but with different inner diameters of 40 and 50 mm were utilised as the resonance chamber of the Rijke tube. In order to ensure the tube is placed vertically, a tube-fixing base, which is connected to 3-D servomotor-driven stand, is used to fix the tube. The dimension of the tube and the tube-fixing base are shown in Appendix.

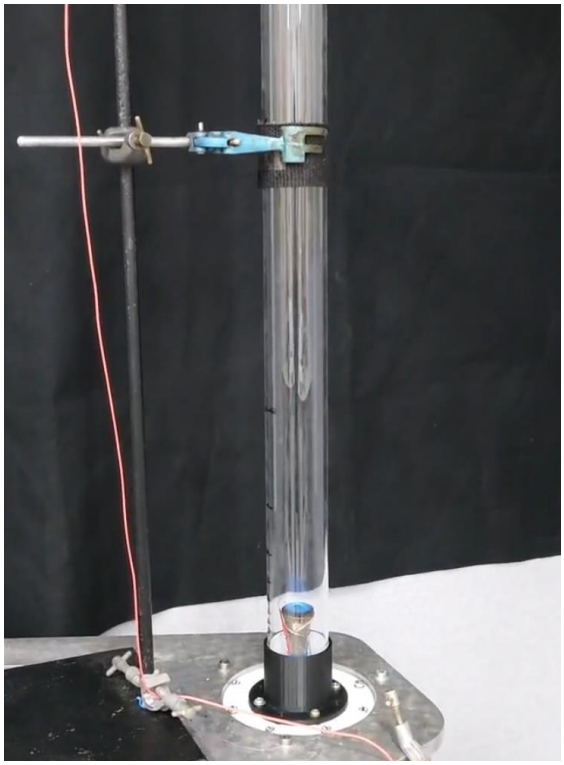

Fig. 3.2 – Fixing part of the tube.

The flame images and the schlieren images in this study were captured by Photron FASTCAM SA4. The CMOS image sensor of the camera has a resolution of 1024×1024. Under this resolution, the maximum FPS (frames per second) can reach 3,600 fps. The recording colour depth under colour mode would be 12-bit for each RGB channel (by using Bayer colour filter), and 12-bit for the image under monochrome mode. The camera is controlled by using the software PFV4 4.0.6.2. By using this software, both FPS and shutter speed can be controlled.

Two digital flow controllers were used to control methane and air flow rates separately. The flowmeter is manufactured by Aalborg Instruments & Controls, Inc. The flow ranges of methane and air flow controller are 0-6 L/min and 0-10 L/min, respectively. Both were well factory-calibrated before the experiment, with accuracy of ± 0.05 % for methane and ± 0.1 % for air.

Both acoustic and temperature were acquired by using a National Instrument data acquisition system. NI 9205 Voltage input module is used to acquire the voltage signal from the microphone. This signal is conditioned by the PCB 482C05 conditioner. The temperature signal was recorded by the NI 9217 thermocouple module, and the temperature was measured by using Type N thermocouples. NI 9205 and NI 9217 modules were connected to the NI cDAQ-9178 chassis, and the chassis was connected to a desktop computer. Besides, two flowmeters were connected to and controlled by NI 9264 Voltage output module. The Labview 2019 program was used to control this data acquisition system and control the flow controllers. The schematic of the data acquisition system is shown in Fig. 3.3. The specification for the system can be found in Appendix of this thesis.

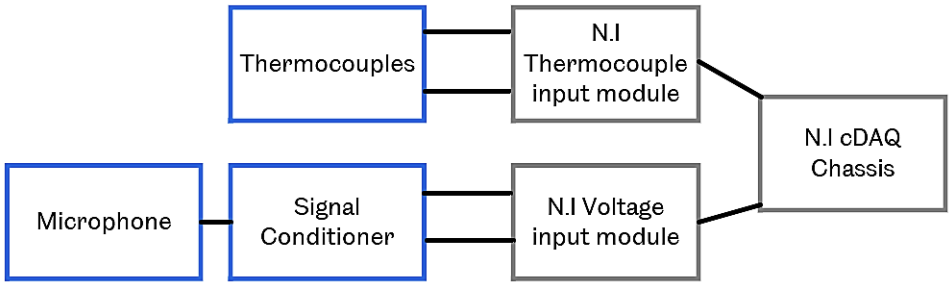

Fig. 3.3. Schematic of the temperature and acoustic signal acquisition system.

3.2 Measurement of parameters

3.2.1 Temperature measurement

In this project, Type N thermocouples are used to measure the temperature at top and bottom end of the tube, as shown in Fig. 3.4. The probe material is Inconel Alloy 600, which is consisted of Nickel, Chromium and Iron, and can provide a temperature range up to 1250 °C. By considering the temperature boundary layer near the tube wall, both the thermocouples are placed at the centre line of the tube.

Fig. 3.4. RS PRO Type N thermocouple

3.2.2 Microphone

A PCB prepolarised 377C10 condenser microphone with an ICP 426B03 preamplifier is used to obtain the acoustic signal. The maximum sound pressure level it can record is 173 dB, and its frequency range is 5 Hz – 70 kHz. The frequency response characteristic for the microphone is pressure field based. Fig. 3.5 shows the frequency response under the different frequencies of the microphone, a large version for this image is shown in Appendix. According to the result of the preliminary experiments, major of the self-excited oscillation is in the range from 10 Hz to 2000 Hz, which is in the linear frequency response range of the microphone (Highlighted by red lines). The maximum sound pressure level is around 125 dB, which is also in the measurable range of this microphone. Therefore, the microphone could be used to measure the dynamic pressure after the calibration based on a reference signal. The specifications of the microphone are also shown in Appendix.

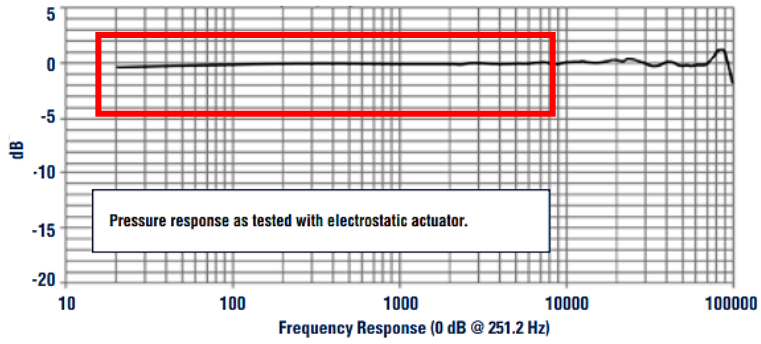

Fig. 3.5. Frequency response for 377C10 microphone.

- Microphone Calibration

According to the definition of sound pressure level, the sound pressure level can be calculated for a certain acoustic pressure. For 1 Pa and 10 Pa of acoustic pressure, the corresponding sound pressure level in the unit of dB would be:

$$20log_{10}\frac{1}{2\times10^{-5}} \approx 94 \text{ dB}, \quad \textbf{3.1}$$

$$20log_{10}\frac{10}{2\times10^{-5}} \approx 114 \text{ dB}, \quad \textbf{3.2}$$

In this study, the microphone was calibrated against a sine signal of 114dB at 1000 Hz. Fig. 3.6 shows the calibration signal. In this diagram, the y-axis represents the signal value in voltage, and the x-axis represents the time. The upper (E_{upper}) and the lower (E_{lower}) envelop of the 10 Pa calibration signal were obtained. The average of the summed absolute values was calculated afterwards, of which the value represents the acoustic wave with an amplitude of 10 Pa:

$$V_{10\,Pa} = \frac{|E_{upper}|+|E_{lower}|}{2}, \quad \textbf{3.3}$$

where $V_{10\,\text{Pa}}$ denotes the voltage reading that represents 10 Pa in acoustic pressure. Then the pressure fluctuations time series can be converted from voltage to pressure by:

$$p(t) = 10 * \frac{V_{p(t)}}{V_{10\,\text{Pa}}}, \quad \textbf{3.4}$$

where $V_{p(t)}$ denotes the raw data of pressure fluctuations time series in volt.

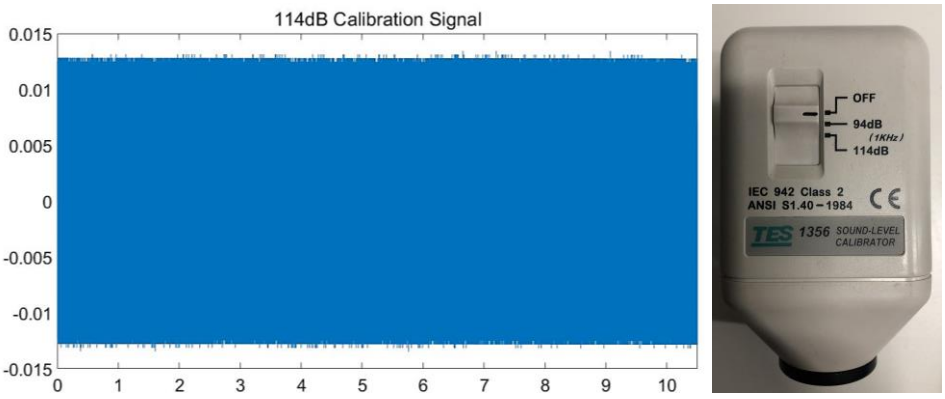

Fig. 3.6. 114dB, at 1kHz calibration signal (Left), TES 1356 Sound-level Calibrator. (Right).

3.2.3 System synchronising

In Chapter 6, the thermal imaging system was synchronised with the microphone to analyse the temporal relationship between mesh temperature and pressure fluctuations.

Besides, the high-speed imaging system was also synchronised with the microphone to investigate the corresponding heat and flow conditions in a different way. Both systems utilised the Transistor-Transistor logic (TTL) signal for synchronisation. TTL signal can be used to define the digital signal '0', and '1' by the following criteria [122]:

$$Digital\ signal\ value = \begin{cases} 0, & 0 \leq voltage \leq 0.7 \\ 1, & 1.5 \leq voltage \leq 5' \end{cases} \quad \textbf{3.5}$$

A typical TTL circuit is shown in Fig. 3.7. According to the figure, it can be seen that the change of the voltage is implemented based on the hardware level, which gives a very low delay compared to software-level implementation. Based on the different models of TTL components, the delay ranges from 1 nsec to 10 nsec.

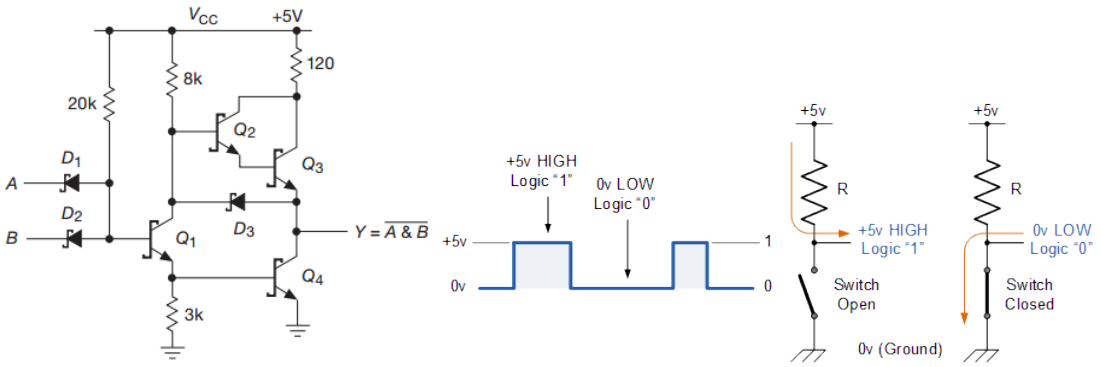

Fig. 3.7. TTL gate (Left) and schematic for TTL.

For the high-speed schlieren system, the high-speed camera, FASTCAM SA4 was utilised as the master unit for the experimental data acquisition system. According to the specification of the FASTCAM SA4, the high-speed imaging system is able to produce a 5V TTL output signal with a delay of 45 nsec once it starts to record as the master control. For the thermal imaging system, the NI myDAQ module was utilised to generate a digital 5V TTL output signal based on its built-in TTL circuit. NI 9178 chassis provides two PFI trigger ports that can detect analogue and digital trigger signals. For analogue signals, it uses the level and slope of the analogue signal to initiate the data acquisition, but its delay is significant. While for the digital signals, both the rising and falling edges of the TTL signal can be used to determine whether to initiate the acquisition process, of which the delay is acceptable. Therefore, the digital trigger

with the rising edge detection is used for synchronising. Simplified schematic diagrams for each system are shown in Fig. 3.8 and Fig. 3.9.

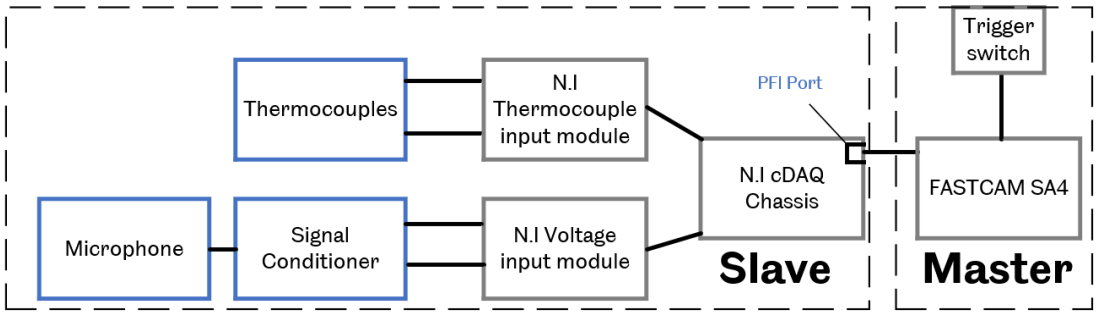

Fig. 3.8. Schematic of the synchronising system for High-speed schlieren imaging system.

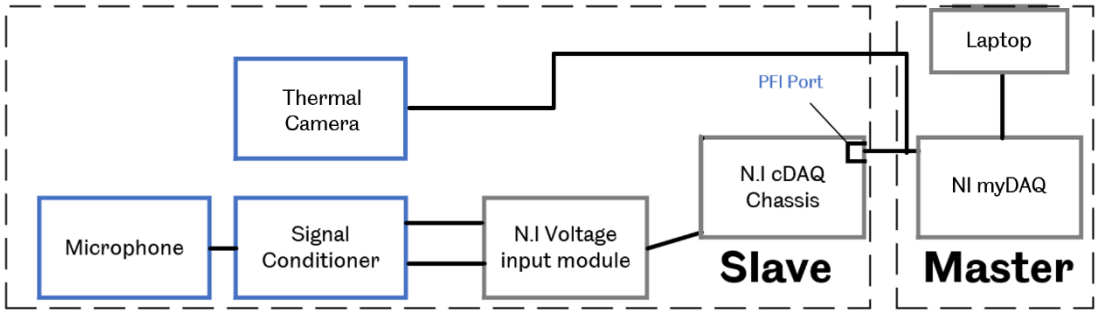

Fig. 3.9. Schematic of the synchronising system for the thermal imaging system.

3.3 Parameters setting for the acoustic, temperature and Imaging signal

3.3.1 Imaging system

The light intensity received by CMOS image sensor is based on three important parameters, which are the aperture of the lens, exposure time and ISO setting of the image sensor. Meanwhile, the exposure status is mainly determined by the sensor-received light intensity. The underexposure represents the insufficient light received by the sensor, which usually leads to the loss of the signal detail due to a lack of light intensity. Overexposure is another incorrect condition of the exposure status. Oppositely, it indicates excessive amounts of light the sensor receives and results in a too-bright image. The loss of signal detail can also be resulted in, while the principle is

opposite to the underexposure condition, that the light is intense enough to cover the details. In some extreme cases, the pixel value of the underexposure image could be 0 since no data can be captured or 1 for the overexposure image with overloaded signals, respectively. Under these situations, the image data cannot be used even after the post-processing, eventually leading to the loss of the signal details. A series of images under different exposure conditions is shown in Fig. 3.10. It can be seen that both underexposure and overexposure lose significantly amount of details compared to the photo at right exposure level.

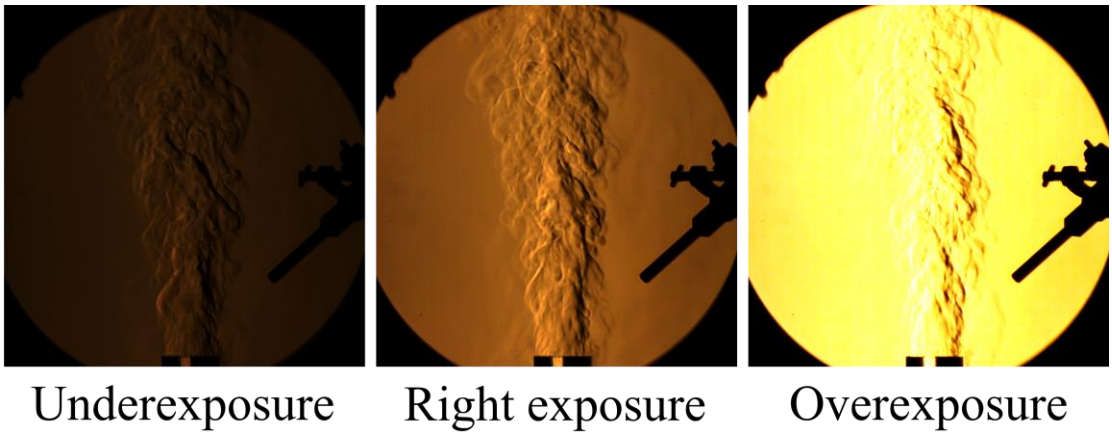

Fig. 3.10 – Images under different exposure condition.

In this study, the ISO for the FASTCAM is set to be constant at 4000. Therefore, in order to obtain image data with acceptable quality, it is important to adjust the aperture and exposure to the proper value.

Based on the preliminary experimental result, the maximum frequency of the pressure fluctuation was found to be lower than 1500 Hz. Nyquist-Shannon sampling theorem stated that the signal would be reconstructed perfectly when the sampling rate was at least twice the highest frequency components. Thus, the maximum frequency (f_{max}) that can be analysed is half of the sampling rate, which can be expressed as: $f_{max} = {f_{Sampling\ rate}}/{2}$. By assuming the flow perturbation at the top end of the tube is at a similar frequency of pressure fluctuation, the minimum value of 3000 for the FPS is required according to Nyquist–Shannon sampling theorem. A lens with 200 mm of focal length and f/3.5 of the aperture was mounted to the high-speed camera.

Considering the conditions including strong convection and time-varying flow condition at the top end of the tube, the shutter speed was set to $^{1}/_{12000}$ to achieve the balance between capturing instantaneous flow patterns and maintaining proper exposure.

3.4 Experiment design

Investigating system responses to different system parameters is prior task for the experiments in this study since the nonlinear thermoacoustic oscillation can be very sensitive to the external environment. Hence, the experiment design in this study has been optimised to minimise the unexpected influence caused by other parameters and produce intense thermoacoustic oscillations.

3.4.1 Material, dimensions and the type of the tube

According to the literature, the previous studies were mainly carried out in round tubes, such as Soundhauss and Rijke tubes. Meanwhile, the round-shaped combustion chamber is mostly utilised in the combustion system. Therefore, the experiments in this study were focused on the round tube, aiming to offer good validations with the previous studies. Transparent quartz was selected as the material of the tube for the ease of flame image capturing and the measurement of mesh temperature. Meanwhile, quartz can resist high temperatures when a combustion process happens inside it. The length of tube was 1.0 m to ensure the frequency response of the fundamental and the second modes are in the linear response region of the microphone. In order to determine the effects caused by inner diameter, the tubes with inner diameters of 40 and 50 mm were tested.

3.4.2 Burners

- Burner Selection

Two burners with nozzle diameters of 4 mm and 8 mm were tested at the beginning. However, it was found that the flame could not sustain since the blow-off of the flame was observed when the burner entered the quartz tube. As discussed in section 2.1.4,

the stable flame front is determined when the equilibrium between the S_L and flow speed is achieved. The relationship between these two parameters is related to both the flashback and the lift-off phenomena [32]. Thus, the reason for the blow-off flame might result from the excessive velocity of the gas supply and the relatively high local flow velocity at the end of the nozzle. Based on this, the burner was placed inside the tube before the ignition, and the flame was ignited by using an electric spark igniter. Besides, the burner with an exit diameter of 15 mm was utilised to decrease the velocity of the gas supply.

- Flame Stabiliser

Although the diameter of the burner and flow rate was optimised, the flame was not as stable as expected. The erratically fluctuating and vibrating of the flame was observed. In order to stabilise and localise the premixed laminar flame, a steel honeycomb was attached to the top of the burner nozzle. The results after applying the stabiliser were improved, that a high-amplitude periodic oscillation and a relatively stable flame could be achieved in most cases.

3.5 Data processing and analysis

3.5.1 Acoustic (dynamic pressure) data

The intense acoustic oscillation could be obtained when the thermoacoustic oscillations are excited. According to the SPL value of the sound measured by using an SPL meter, the maximum SPL was around 130 dB. Although the microphone used in this study can stand for a maximum SPL of 173 dB, it is still possible to obtain the overloaded signal if it uses the improper settings of the current source level. An overloaded signal is a signal that exceeds the maximum measuring range of the sensor. As shown in Fig. 3.11, the signal value would be 1 for any overloaded sampling point, which can lead to the distortion of the signal. The overloaded signal can result in the loss of information and accuracy. Therefore, the current source provided by the signal conditioner was set to 4 mA, which was tested to be able to avoid any possible overloaded signal, even under the condition of high dynamic pressure variation.

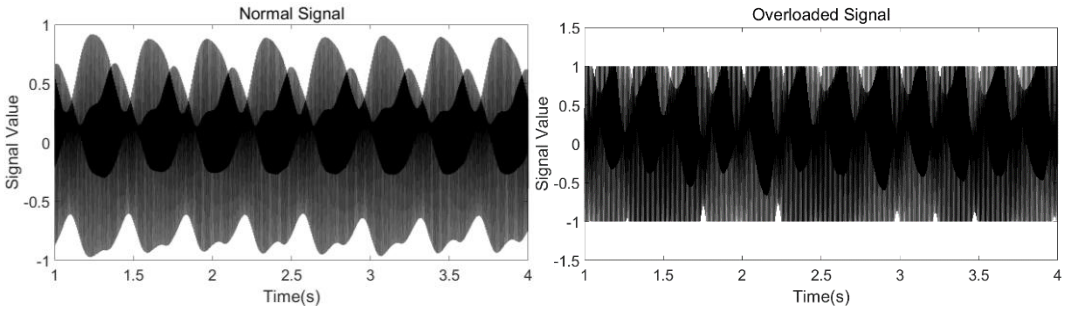

Fig. 3.11 - Comparison of Overloaded Signal and Normal Signal.

It was found that the signal would offset away from the balanced position due to the electrical noise and the polarised error. From the sample captured by the microphone, the signal is generally offset with a constant value. Therefore, the acquired signal underwent a detrending process based on a constant value to eliminate the signal shift. The comparison before and after the detrending process is shown in Fig. 3.12.

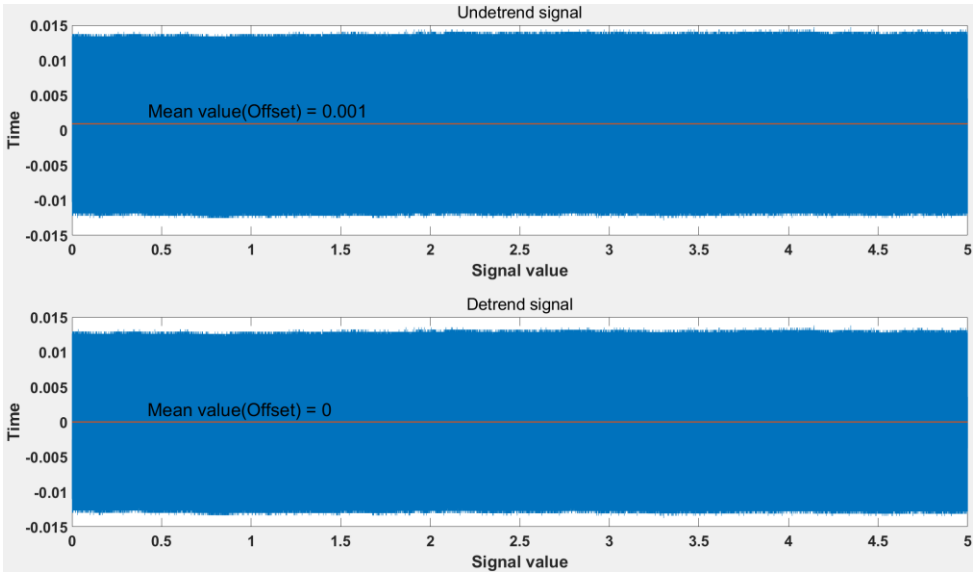

Fig. 3.12 – Comparison between un-detrended and detrended signal.

3.5.2 Phase space reconstruction and Recurrence analysis

The recurrence analysis was utilised in this study to investigate the system nonlinear dynamics by analysing the state recurrence of the system. As discussed in Section 2.2.4, the recurrence of system states for a dynamic system is usually considered to be a crucial characteristic for describing the system behaviours, especially for the systems with both noticeable periodicity and complexity, such as the thermoacoustic systems

driven by combustion instabilities. Therefore, recurrence analysis has been utilised by many studies to explore the thermoacoustic system response to the control parameter changes [19,25,26,104,123–126]. By visualising the recurrence and identifying the different states for a dynamical system from phase space, this approach can uncover the recursive nature of the system state and identify the state transitions which may be ignored when the traditional time-domain analysis is applied.

As discussed in Section 2.3, the recurrence analysis is an analysis method based on the phase space of the dynamic system. In this study, the pressure fluctuations time series is measured by a single pressure-field microphone, which means that a single system variable was obtained for representing the system dynamical properties. Therefore, the Takens embedding method was utilised to construct the higher dimensional space vectors based on the pressure fluctuations time series ($p(t)$) for the phase space reconstruction [109]. The method for constructing the space vector is shown in the corresponding chapters since the different space vectors (including the original value and normalised value) were constructed according to the requirements of analysis. In this section, a general form of space vector ($\mathbf{P_t}(\mathrm{D})$) will be used in the following parts. As mentioned in Section 2.3.1, the key parameter time-delay τ for constructing the phase space can determined by autocorrelation function or average mutual information method [114]. In practical situations, the autocorrelation function is usually utilised when the system is relatively stable, and the noise does not significantly pollute the signal. The average mutual information method is utilised when the system presents strong chaotic characteristics, or the signal has strong noise levels. For the studies carried out in this thesis, the thermoacoustic oscillations were generally periodic with relatively low complexities, and neither intermittency nor chaos states were found. Meanwhile, the noise level of the measured signal was relatively low. Therefore, the optimum τ was determined according to first zero-crossing point of autocorrelation function. An example of the τ determination is given in Fig. 3.13.

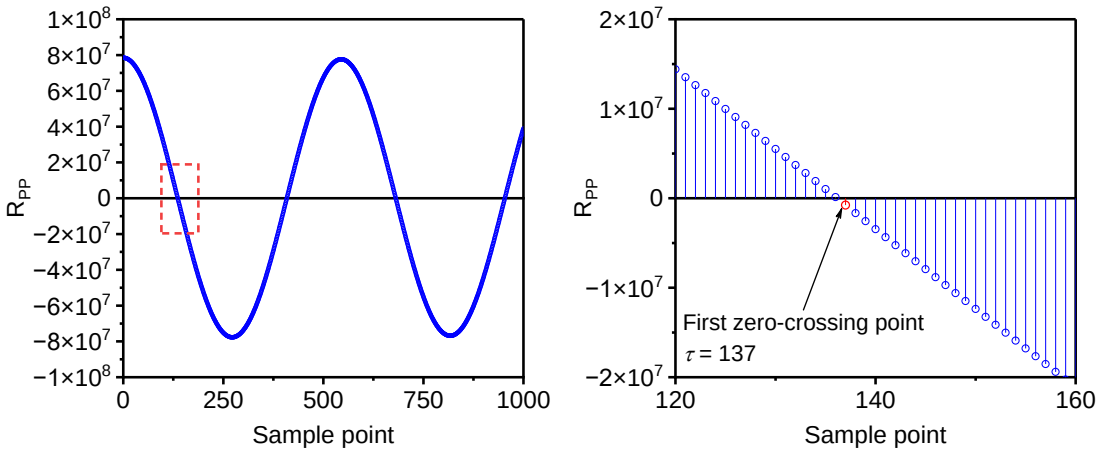

Fig. 3.13. Example of determination of τ by using the first zero-crossing point of autocorrelation function.

It is also critical to determine the optimum embedding dimension D for the recurrence analysis. An excessively high D can result in spurious correlations in the phase space. In contrast to this, the orthogonal diagonal structures to the LOI in RP can be formed by the inappropriately low D. From the discussion in Section 2.3.1, D was determined based on the FNN method. The example results of FNN for some cases are shown in Fig. 3.14.

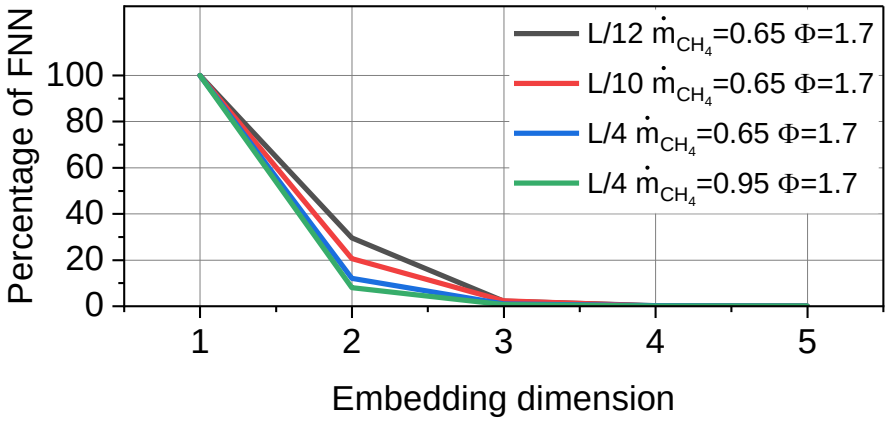

Fig. 3.14. Example results of FNN.

It can be seen that the percentage of FNN decreases to approximately 0 when D is greater than 3. Therefore, D was set to 3 in this study unless specifically mentioned.

Based on the constructed space vector, the binary recurrence matrix ($\boldsymbol{R_{i,j}}$) can be constructed based on 2.39. In the case of $\mathbf{P'_t}(\mathrm{D})$, $\boldsymbol{R_{i,j}}$ is in the following form:

$$\boldsymbol{R}_{i,j} = \Theta\left(\varepsilon - \left\|\boldsymbol{P'}_{\boldsymbol{i}}(D) - \boldsymbol{P'}_{\boldsymbol{j}}(D)\right\|\right) \quad i,j = 1,2,3,\cdots,N, \qquad \textbf{3.6}$$

According to Eq. 3.6, $\boldsymbol{R}_{i,j}$ will be 0 if the $\left\|\boldsymbol{P'}_{\boldsymbol{i}}(D) - \boldsymbol{P'}_{\boldsymbol{j}}(D)\right\|$ exceeds ε, or 1 for those smaller than ε. In this study, the black points in the RP denote $\boldsymbol{R}_{\boldsymbol{i,j}} = 1$, whereas $\boldsymbol{R}_{\boldsymbol{i,j}} = 0$ is represented by the white colour. The selection of ε is critical in recurrence analysis since the improper ε may lead to an unfaithful result, as discussed previously [117]. A criterion that ε should not exceed 10% of the mean phase space diameter has been proposed by Schinkel et al. and Marwan et al. [115,117]. Meanwhile, it is also suggested that the standard deviation can be taken into account for the captured noisy discrete signal or the signal measured from a real system [115]. Therefore, the threshold in this study was set as 15% of the standard deviation (σ) of the pressure fluctuation time series signal, which was suggested by Zan et al. [123]. This value also satisfied the criterion of mean phase space diameter. For a periodic system with a smooth phase space, a high sampling rate can result in spurious quantifications and large amounts of exclusively diagonal line structures in RP. Based on the definition of DET mentioned in Section 2.3.3, a very high DET can be resulted, of which the value can be over 99%. The excessively high DET can lead to the situation that the characteristics of periodic systems cannot be clearly and sufficiently indicated [23,127]. It has been suggested that 8 to 10 sampling points should be included within each period [105]. In this study, a down-sampling process was conducted to meet the requirements of 10 sampling points per period by selecting 10 space vectors with a constant time interval for each period. Therefore, the high accuracy of results and clear indications of state changes can be achieved.

Once the binary recurrence matrix had been achieved, the RQA was carried on for further quantifying the structural properties in the corresponding RP. RQA measures utilised for the analysis of each study are presented in the corresponding chapters.

3.5.3 Uncertainties

The microphone utilised in this study has a sensitivity of 1.0mV/Pa according to its specifications provided by the manufacturer. However, the sensitivity of the microphone can be slightly different from the value provided by the manufacturer depending on the testing conditions. According to the testing results of the microphone,

its sensitivity remained relatively stable once it was connected and powered on (up to ±2% for 10 Pa signal). And a noticeable change in sensitivity only happened when the microphone was disconnected and powered off and then reconnected (up to ±10% for 10 Pa signal). Therefore, a calibration process was conducted before each set of the experiment to obtain its actual sensitivity.

Apart from the sensitivity changes, the microphone underwent a settling process once it was powered on. During this process, the neutral output voltage of microphone would fall from 10 V to around 0 V, which took around 5 mins. Therefore, a settling time of 10 mins for the microphone was also applied once the microphone was powered on to ensure the stable output of the microphone. In addition, the background noise of the microphone was found to have a stable peak-to-peak voltage level of around 5μV (equivalent 0.005 Pa), which is significantly weaker than the acoustic pressure of excited sound and can be neglected. Meanwhile, the level of surround noise was at an average level around 35dB (equivalent 0.001 Pa), which is significant weaker than the self-excited thermoacoustic oscillation. Furthermore, in order to eliminate the reflection of sound (echo), the anti-reflection panel was equipped in the lab, especially around the experimental setup.

Besides the error caused by the microphone, the SPL calibrator utilised in this study was at Class 2 Level and has an accuracy of sound pressure level of 0.5 dB (equivalent 0.00002 Pa). The battery for the calibrator was changed every 2 weeks to ensure the calibrator works at the proper voltage. In addition, the SPL calibrator was also calibrated before this study started to ensure the accuracy of its output signal intensity.

Therefore, taking both the error caused by the microphone and the calibrator, the maximum error can be around ±2%, which would not affect the trends observed in this study, because the difference in oscillation amplitude between two tests with different parameter was much greater than ±2%.

Regarding the frequency analysis, the Fast Fourier Transform (FFT) can provide a resolution of 0.1 Hz since a signal with 10s of total length was utilised to conducted FFT. The 0.1 Hz resolution is sufficient for distinguishing the difference in frequency between two tests in this study.

Chapter 4 Investigation of the self-excited oscillation response to the equivalence ratio

The study in this chapter has been published in the Journal of Sound and Vibration:

'X. Liu, H. Zhou, Y. Lai and Y. Zhang, Equivalence ratio independence and dependence ranges of system responses for a nonlinear thermoacoustic oscillation in a Rijke tube, *Journal of Sound and Vibration*, 2023.'

According to Elsevier's Policy of Copyright, I, the author, can use this work (in full or in part) in this thesis.

4.1 Introduction

Thermoacoustic instability has been one of the most challenging yet unignorable problems during the development of gas turbines for decades. The self-excited oscillation caused by the instability is highly possibly triggered in an acoustic resonator which involves combustion or heat exchanges [2,64,128]. Rayleigh [9] revealed the mechanism of triggering thermoacoustic oscillation, that is the coupling effect between unsteady heat release rate and pressure fluctuations when they are in-phase, which is known as the Rayleigh Criterion. However, as a qualitative description, Rayleigh Criterion is hard to obtain information about the stability of the system and quantify the system behaviour.

Although successful theoretical models have been built for revealing the excitation mechanism of thermoacoustic instabilities [10,17,128–131], the insightful information for identifying the system dynamics in a combustion system remains insufficient. Aiming at investigating the nonlinear thermoacoustic oscillation, the Rijke tube has been widely used to conduct experimental studies in a laboratory scale [3,8,18,52,132–

134]. It has been found that the combustion-induced thermoacoustic instabilities in a Rijke tube are mainly attributed to complex nonlinear interaction among acoustic, flame properties and hydrodynamics [135]. The nonlinear relationships between the interactions and system responses have been extensively focused on [2,3,8,27,104,135,136]. For instance, the oscillation amplitude and system frequency response can be affected by airflow around the flame and nozzle position to different extents [134]. Zhang et al. [137] noted the importance of fuel supply flow and swirl number on the oscillation in lean combustion with a swirl burner. Heckl and Howe [27] studied the effects of the hydrodynamic region on the self-excited oscillation in a Rijke tube with a flame holder. A nonlinear mathematic model was proposed to explain the influence of hydrodynamic range on both system frequency response and oscillation amplitude. Zhao and Chow [8] further developed the hydrodynamic region theory by introducing the drag effect of ambient fluid after the experimental investigations in a Rijke tube. Many experimental studies have been conducted to indicate the crucial role of equivalence ratios in thermoacoustic instabilities, such as the critical condition for triggering a self-excited sounding [138], possible equivalence ratio ranges for triggering beating oscillations [52], and trends of eigenfrequencies and oscillation amplitude with varied equivalence ratios [26]. Besides, many numerical studies have been carried out to explain and predict thermoacoustic oscillation in various combustion systems. It has been proved in various combustors that the LES can successfully predict both the system eigenfrequency and the oscillation amplitude [44,139,140]. Based on the unsteady compressible Navier Stokes equation, good agreement between the numerical and experimental results of the mode frequency, mode shapes and oscillation amplitude were obtained in both the classic Rijke tube and Rijke-Zhao (Y-shape) tube [132,141]. It has also been found that numerical methods can be efficient for investigating quasi-periodic oscillation. Both the beating frequency and heat release fluctuation can be obtained from the numerical investigations [52,97].

The nonlinear thermoacoustic oscillation in a combustion system is caused by the complex interactions among several physical properties, which leads to the significantly time-varied system states. Therefore, the time domain statistical analysis and measurements can provide insightful and meaningful information to characterise the thermoacoustic system. Some studies applied two-microphone and multi-microphone techniques to investigate the acoustic-related properties (e.g. acoustic

impedance, wave velocity and frequency composition) in a tube chamber with either self-excited oscillation or external acoustic source [142–145]. The phase space constructed based on the time-delay embedding method is extensively utilised to determine system intermittency and chaos-order transition in various combustion systems [104,105,135,146]. The recurrence analysis for the investigation of the thermoacoustic system was introduced, and great efforts were made by Sujith and Gotoda [19,23,105,147–150]. It has been found that the Recurrence plot (RP) can effectively describe and analyse combustion and thermoacoustic instabilities in various combustion systems [19,23,25,26,104,105,123–125,147–150]. The periodicity, chaoticity, state transition and intermittency can be indicated through the specific internal structure, pattern equality and density of recurrence points [26,104,105,124]. By applying the recurrence quantification analysis (RQA), the RP also can be used to identify system dynamics quantitatively [115]. As an effective analysis method, RP can efficiently identify the nonlinear relationship between system dynamics and system parameters.

Although many studies have investigated both the frequency response and oscillation amplitude under different system parameters, the studies for investigating the nonlinear trend of system eigenfrequency to equivalence ratio remain insufficient. Meanwhile, it has been reported that the existence of internal nonlinear interaction between different harmonic modes in thermoacoustic oscillations [20]. Thus, the relative 'phase difference' between different modes can be important for indicating the characteristics of changes in time-evolution of pressure fluctuations. The thermoacoustic instabilities under fuel-rich conditions are also less studied, while fuel-rich combustion is more preferred in the field that requires higher combustion stability [151,152]. For example, the primary zone of Rich-burn, Quick-mix, Lean-burn (RQL) combustor dominates and initiates the combustion process. The equivalence ratio in the primary zone can be up to 2.5 [152]. Therefore, this work aims to intensively investigate the influence of the equivalence ratio on system nonlinearities in a Rijke tube. In this work, the eigenfrequency of self-excited oscillation, the phase difference between harmonic modes, and system dynamics have been focused on. The pressure time series data of self-excited thermoacoustic oscillations under different conditions have been obtained in a Rijke tube with a laminar premixed flame. The time-domain analysis has been conducted to investigate the effect of the equivalence ratio on the phase difference and

system dynamics properties through the phase differences and recurrence analysis. The phase difference between the harmonic modes was achieved by decomposing the pressure signal based on the FIR (Finite impulse response) phase-linear filter. The system dynamics were investigated and quantified by the recurrence plots (RP) and recurrence quantification analysis (RQA).

4.2 Experiment setup and data analysis method

4.2.1 Experimental setup

A vertically anchored Rijke tube was utilised to investigate the self-excited oscillations, with a heat source in the form of a laminar premixed methane flame. Fig. 4.1 shows the schematic figure of the experiment setup. The quartz tube of 1 m in total length was utilised in the present work. A honeycomb flame holder of 28 mm in diameter was attached at the top of the nozzle for generating a stable conical shape premixed flame. The blockage ratio of the flame holder was about 22%. Since it has been reported that the effect of the flame holder on the thermoacoustic oscillations frequency can be neglected when the blockage ratio is smaller than 25% if the inlet Mach number is below 0.15 [128]. The flame was ignited by a single spark generated by a piezo spark igniter.

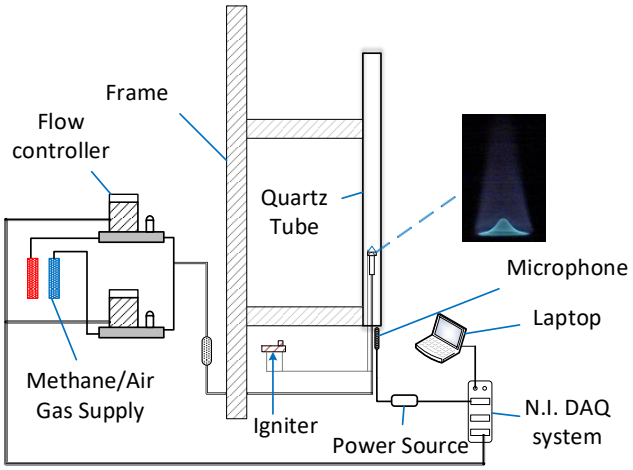

Fig. 4.1. Schematic figure of the flame-driven Rijke tube system.

Aalborg GFC17 mass flow controllers were applied to control both air and methane flowrates with an accuracy of 0.05% for methane and 0.1% for air. The methane

flowrates ($\dot{m}_{CH_4}$) were set as 0.65 L/min, 0.8 L/min and 0.95 L/min. Under a specific $\dot{m}_{CH_4}$, the equivalence ratio (Φ) ranged from 0.8 to 5.0, which is obtained by changing the air flowrate. It should be noted that those cases with too small equivalence ratios to trigger the oscillations were ignored in the present work since this study mainly focuses on fuel-rich conditions ($\Phi > 1$). The different steps of Φ were applied to ensure more precise analysis results due to the different sensitivity of system properties to Φ in different ranges, as shown in Table 4.1. For instance, a finer step of 0.05 was selected for $1.1 < \Phi < 1.7$ since the most complex trend between system response and Φ was observed in this range. The burner position was set as L/4, L/6, L/10 and L/12 from the bottom of the tube. The pressure fluctuations time series signal was measured by a pressure transducer microphone (PCB 377C10 and preamplifier PCB 426B03). The pressure-field microphone was placed at the bottom end and in the axial direction of the tube to ensure the pressure wave can incident in the perpendicular direction to the diaphragm and the temperature is not exceeding the upper limit of microphone operating temperature. The microphone unit utilised in the present work has a linear response range from 10 Hz to 5000 Hz, which means the typical self-excited oscillation frequency in the present work (around 180 Hz) is in the linear response range. The microphone was calibrated against a signal of 10 Pa at 1000 Hz before each experiment to ensure the accuracy of the result. The pressure signal with a length of at least 10 seconds was collected at a sampling rate of 100,000 Hz to provide a clear view of the recurrence plot and the accuracy of frequency analysis. NI-9205 Voltage input module with the Chassis cDAQ-9178 was utilised to collect the microphone signal. A stabilisation process of 3 minutes before recording was operated to ensure the stableness of the system and the system exit from the transition process.

Table 4.1. The step in different equivalence ratio ranges.

Equivalence ratio range	**0.8 ~ 1.1**	**1.1 ~ 1.7**	**1.7 ~ 2.0**	**2.0 ~ 3.0**	**3.0 ~ 4.0**	**4.0 ~ 5.0**
Step	0.1	0.05	0.1	0.2	0.25	0.5

4.2.2 Data processing and analysis

4.2.2.1 *Phase difference*

In order to analyse the relative positions between the components of different harmonic modes in the time domain, a FIR (Finite impulse response) filter was utilised to decompose the original time series signal to get the components of different harmonic modes. The 100,000 sample points (1 s) at the start and end of the filtered signal were cut to eliminate the unstable ranges. In the present work, the fundamental harmonic mode was taken as the reference with no phase shift, shown as:

$$y_f = A\ sin(t), \quad \textbf{4.1}$$

$$y_{n-th} = B\ sin\big(n\ (t - \varphi)\big), \quad \textbf{4.2}$$

where y denotes the sinusoidal signal. The subscript f, n indicates the fundamental and n-th harmonic mode. φ is the phase difference to identify the relative position between two different harmonic modes in the oscillations. In the present work, the phase difference calculation focused on the fundamental (y_f) and second (y_{2nd}) harmonic modes. The higher harmonic modes were ignored due to their neglectable intensity. If there is no phase difference between y_f and y_{2nd} ($\varphi = 0$), the relative 0 phase point of them will be the same. However, it is difficult to locate the relatively 0 phase point for the discrete time series. Therefore, the local maximum point (M) was used to determine the local phase difference for each period in the present work.

A reference phase (φ_{ref}) is defined for the calculation of the local phase difference of each period, since the local maximum points of y_f and y_{2nd} are at different positions due to the difference in frequency. The φ_{ref} is the time difference between the local maximum points of y_f and y_{2nd} when $\varphi = 0$. In the present work, the fundamental and the second harmonic modes were mainly focused on, which means an integer relationship of 2 between their frequency exists. An example of the determination of φ_{ref}^{α} is given as follows. Considering a periodic signal y that contains two different frequencies with an integer relationship of 2 between them, and there is no phase difference between them:

$$y = sin(x) + sin\ (2x), \quad \textbf{4.3}$$

where $y_1 = sin(x)$ and $y_2 = sin(2x)$. We take the y_1 as the reference of the relative phase (the value of x). The maximum point of the y_1 is located at the point where the relative phase ($\varphi_{max}^{y_1}$) is $\varphi_{max}^{y_1} = \frac{\pi}{2}$, while the maximum point of y_2 is located at $\varphi_{max}^{y_2} = \frac{\pi}{4}$. Therefore, the reference phase (φ_{ref}) between y_1 and y_2 will be $\frac{\pi}{2} - \frac{\pi}{4} = \frac{\pi}{4}$, as shown in Fig. 4.2. Meanwhile, the maximum point of a sine wave is located at the quarter of its period. Therefore, the φ_{ref} can be calculated based on the difference between the period of y_1 (2π) and y_2 (π), as shown below:

$$\varphi_{max}^{y_1} = \frac{1}{4} * 2\pi = \frac{\pi}{2}; \quad \varphi_{max}^{y_2} = \frac{1}{4} * \pi = \frac{\pi}{4}, \tag{4.4}$$

$$\varphi_{ref} = \varphi_{max}^{y_1} - \varphi_{max}^{y_2} = \frac{\pi}{4}, \tag{4.5}$$

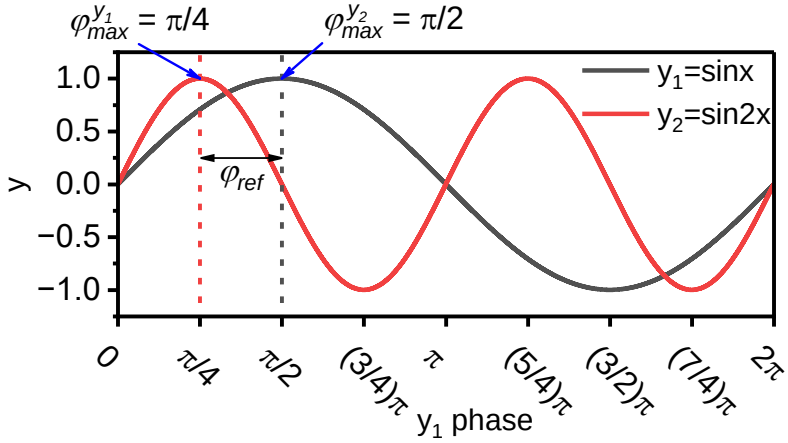

Fig. 4.2. Example of $\varphi_{max}^{y_1}$, $\varphi_{max}^{y_2}$ and φ_{ref}.

Note that the local maximum point of a sine wave is at the quarter of the period, the φ_{ref} can be then calculated based on the period of the y_f and y_{2nd}. In the present work, the phase difference between the fundamental and second harmonic modes varied with time. Meanwhile, the captured time series data of pressure fluctuations and the filtered signals were in discrete form. Thus, the local phase difference for each cycle of the oscillation in the filtered signal. The period for i-th oscillation can be obtained by the time difference between local maximum point at i and i + 1, as $period_n^{i-th} = M_n^{i+1} - M_n^i$. Therefore, the local reference phase at α-th period of the fundamental mode ($\varphi_{\mathrm{ref}}^{\alpha}$) is:

$$\varphi_{ref}^{\alpha} = \frac{(M_f^{\alpha+1} - M_f^{\alpha}) - (M_2^{\beta+1} - M_2^{\beta})}{4}, \quad \textbf{4.6}$$

where α, β denotes the α/β -th period of the fundamental/second harmonic mode. Note that the β-th period of the second harmonic mode is at the same time as the α-th period of the fundamental harmonic mode. The φ_{ref}^{α} calculated by Eq. 4.6 is in the unit of the sample point.

Based on φ_{ref}^{α}, the local phase difference at α-th period of the fundamental mode ($\varphi_{f,2}^{\alpha}$) can be calculated as:

$$\varphi_{f,2}^{\alpha} = \frac{2\pi}{(M_2^{\beta+1} - M_2^{\beta})}(\varphi_{ref}^{\alpha} - (M_f^{\alpha} - M_2^{\beta})), \quad \textbf{4.7}$$

The mean phase difference ($\overline{\varphi_{f,2}}$) and the standard deviation (σ) are:

$$\overline{\varphi_{f,2}} = \frac{1}{k}\sum_{\alpha=1}^{k} \varphi_{f,2}^{\alpha}, \quad \textbf{4.8}$$

$$\sigma = \sqrt{\frac{1}{k}\sum_{\alpha=1}^{k}\left(\varphi_{f,2}^{\alpha} - \overline{\varphi_{f,2}}\right)^2}, \quad \textbf{4.9}$$

where k represents the k-th period of the fundamental mode. The σ was used to quantify the amount of variation for the local phase difference. The phase would be realigned if the $\varphi_{f,2}^{local}$ is greater than 2π, since the period of the second harmonic mode has the double value of the fundamental modes. Note that all variables present in the equations above are in time-domain.

A sample for the calculation of $\varphi_{f,2}^{local}$ is provided as follows, as shown in Fig. 4.3. In this case, the local maximum points of α-th and α+1-th periods of fundamental harmonic mode are at 26391 and 26926, respectively. And 26393, 26660 for the local maximum points of β-th and β+1-th periods of second harmonic mode. Therefore, for α-th oscillation, the φ_{ref}^{α} can be calculated by Eq. 4.6 as:

$$\varphi_{ref}^{\alpha} = \frac{(26926 - 26391) - (26660 - 26393)}{4} = 67\ points, \quad \textbf{4.10}$$

According to Eq. 4.7, the $\varphi_{f,2}^{\alpha}$ is:

$$\Phi_{f,2}^{\alpha} = \frac{2\pi}{(26660-26393)}\big(67-(26391-26393)\big) = 1.624\,rad, \qquad \textbf{4.11}$$

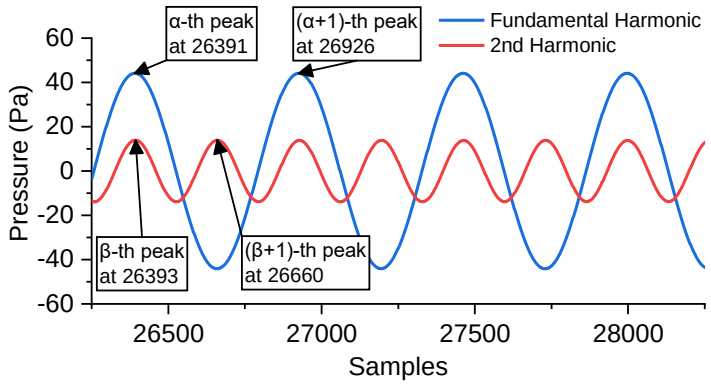

Fig. 4.3. Example of calculation for the local phase difference $\varphi_{f,2}^{local}$.

4.2.2.2 *Recurrence plot (RP) and Recurrence Quantification Analysis (RQA)*

The recurrence of the system state is an important characteristic for describing the system behaviour. Therefore, the recurrence analysis can effectively reveal the system dynamics properties of the nonlinear self-excited thermoacoustic oscillation. The RP enable the visualisation of recurrences and the identification of different states for a dynamical system from the phase space [105,115]. It has been utilised for analysing both external and self-excited thermoacoustic oscillation [25,26,104,123,124]. In the present work, the space vector in the phase space was obtained based on Takens' time-delay embedding method [153]. For a discrete pressure fluctuation time series $p(t) \in \mathbb{R}$, the space vector $\mathbf{x}_t$ with an embedding dimension of D can be constructed from:

$$\boldsymbol{P_t}(D) = \big(p(t), p(t-\tau), p(t-2\tau), \cdots, p(t-(D-1)\tau)\big), \qquad \textbf{4.12}$$

where t denotes the time. τ is the time delay. In the present work, τ was determined based on the first zero-crossing point of the autocorrelation functions and D was set to 3 for all cases according to the results of the false nearest neighbour (FNN) method, as discussed in Section 3.5.2. Based on the $x_t(D)$, the binary recurrences matrix $\mathbf{R_{i,j}}$ can be expressed in the following form:

$$\boldsymbol{R_{i,j}} = \Theta\big(\varepsilon - \|\boldsymbol{x_i} - \boldsymbol{x_j}\|\big) \quad i,j = 1,2,3,\cdots,N, \qquad \textbf{4.13}$$

where ε denotes the threshold for recurrence plot computation, $\mathbf{x}_i$ and $\mathbf{x}_j$ are the space vectors and the subscripts i and j are the sequence number of space vectors obtained by Eq 4.12. $\|\boldsymbol{x}_i - \boldsymbol{x}_j\|$ is the norm of the difference between $\boldsymbol{x}_i$ and $\boldsymbol{x}_j$; Θ is the Heaviside function which has the definition as: $\Theta(x) = 0, if\ x < 0;\ \Theta(x) = 1, if\ x > 0$; N is the number of points for recurrence analysis. The ε was set to 15% of standard deviation (σ) of pressure fluctuation time series signal. A down-sampling process was also carried out to avoid the excessively high DET, as discussed in Section 3.5.2.

In order to quantify the system dynamics from the RP, Recurrence Rate (RR), Determinism (DET), Shannon Entropy (ENT) and average diagonal line length (ADL) were obtained in the present work. The corresponding equations are expressed below:

$$RR(\varepsilon) = \frac{1}{N^2}\sum_{i,j=1}^{N} R_{i,j}(\varepsilon), \quad \textbf{4.14}$$

$$DET = \frac{\sum_{l=l_{min}}^{N} lP(l)}{\sum_{l=1}^{N} lP(l)}, \quad \textbf{4.15}$$

$$ADL = \frac{\sum_{l=l_{min}}^{N} lP(l)}{\sum_{l=min}^{N} P(l)}, \quad \textbf{4.16}$$

$$ENT = -\sum_{l=l_{min}}^{N} p(l) ln p(l), \quad \textbf{4.17}$$

where N represents the total length of the recurrence data, $P(l)$ is the histogram of the diagonal line with the length of l, and l_{min} is the predefined minimum length of the diagonal line. In the present work, l_{min} is set to 2. $P(l)$ is the probability of the occurrence of the diagonal line with a length of l, which is calculated from $p(l) = P(l)/N_l$. N_l is the number of diagonal lines. The unit of ENT in the present work is nat. For the RR, it can be used to measure the density of recurrence points based on the recurrence matrix $\mathbf{R}_{i,j}$. Based on the diagonal structure in the plot, DET is defined as the ratio of the recurrence points that forms the diagonal lines to all recurrence points in **R**. Thus, DET is able to show the occurrence probability of similar states in the system. The ADL was used to indicate the degree of parallelism and the average time of two segments in the trajectory being close to each other [115]. Shannon information entropy was used to quantify the complexity of the system by obtaining the appearance probability of the diagonal lines with the length of exactly l in the plots.

4.3 Results and Discussion

In the present work, the self-excited thermoacoustic oscillation driven by a premixed methane-air laminar flame in a Rijke tube was investigated. The frequency response and oscillation amplitude (denoted by root mean square value of pressure) of the system were obtained at different methane flowrates, equivalence ratios and burner positions. An Φ-independence range and an Φ-dependence range were discovered under a given methane flowrate from the results. In detail, the system eigenfrequency trended to be independent with changing Φ. The time-domain analysis of phase difference, RP and RQA were processed for a further understanding of the characteristics of changes in time-evolution of pressure fluctuations ($p(t)$) and the system dynamics in Φ-independence. As a developed calculation method in the present work, the phase difference was calculated to obtain the relative time difference between the fundamental and second harmonic modes. The phase difference and recurrence analysis results validate the existence of Φ-independence and Φ-dependence range. By comparing the systems with different Φ in the Φ-independence range at the same methane flowrate, similar characteristics from characteristics of changes in $p(t)$ and system dynamics between the systems can be discovered.

4.3.1 Determinations of Φ-dependence range and Φ-independence ranges

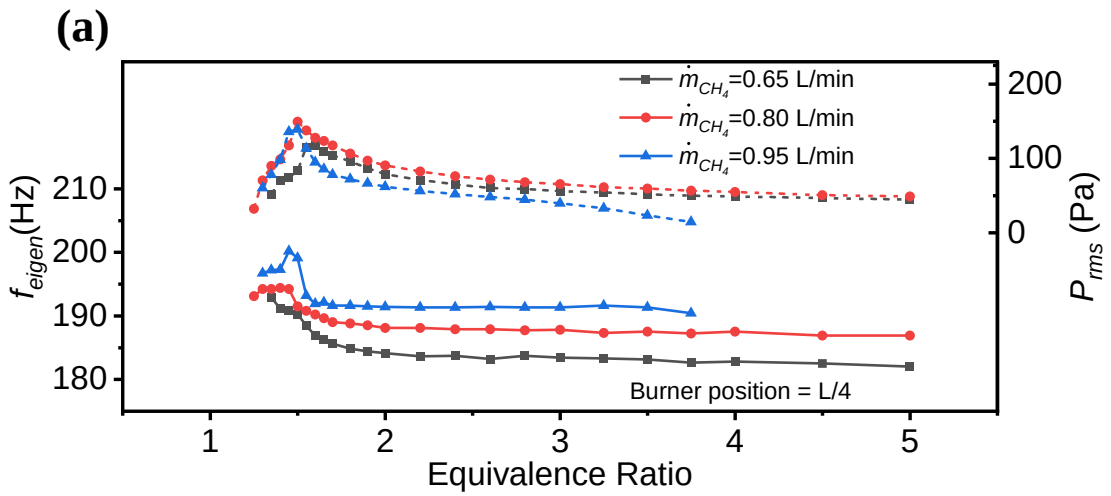

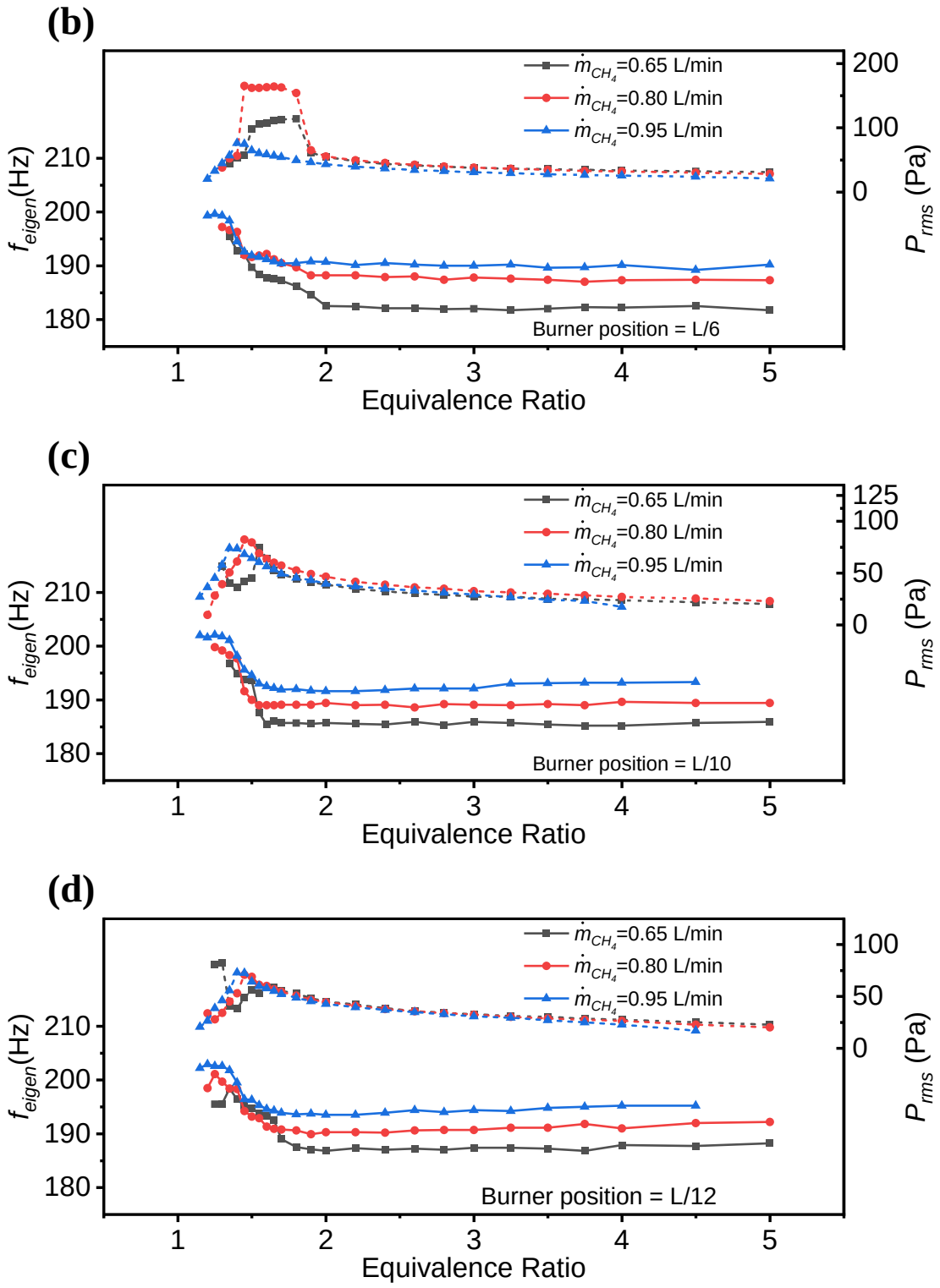

Fig. 4.4. f_{eigen} *and* P_{rms} *to Φ diagram for the cases under different burner positions(a) L/4, b) L/6, c) L/12 and d) L/12) and* $\dot{m}_{CH_4}$.

The eigenfrequency (f_{eigen}) and the root mean square value of pressure (P_{rms}) for the cases under different parameters are shown in Fig. 4.4. Considering the effects of system parameters on the system response, experiments at different burner positions

and $\dot{m}_{CH_4}$ are conducted to verify the changing trends of f_{eigen}. The similar nonlinear trends between f_{eigen} and Φ can be observed in all cases regardless of system parameter changes. The f_{eigen} presents high sensitivity to the change of Φ in the range of approximately 1.1 to 2.2, and most cases show a decreasing trend, as shown in Fig. 4.4 (a). However, as the Φ keeps increasing, the f_{eigen} trended to be stable and insensitive to the change of Φ. It can be also found that the f_{eigen} generally has a greater value in the Φ-dependence than in the Φ-independence range. According to the sensitivity of f_{eigen} to Φ, the range that the f_{eigen} presents high independence on Φ is defined as the Φ-independence range. Similarly, the Φ-dependence range is for the range that f_{eigen} is highly dependent on Φ. A criterion for determining the range can be raised based on the difference between corresponding f_{eigen} and the reference frequency in Φ-independence range ($\overline{f_{IR}}$). The $\overline{f_{IR}}$ is calculated from the mean f_{eigen} of all the cases with $\Phi \geq 3$, since it has been found that $\Phi = 3$ would be beyond the critical Φ ($\Phi_{critical}$) between the Φ-dependence and Φ-independence range. From the experimental results, it is found that the value of 0.5% in frequency difference between the f_{eigen} and $\overline{f_{IR}}$ is a proper criterion value for the critical Φ. It can be expressed as:

$$\frac{(f_{eigen}-\overline{f_{IR}})}{\overline{f_{IR}}} = \begin{cases} > 0.5\% & \Phi - dependence\ range \\ \leq 0.5\% & \Phi - independence\ range \end{cases} \quad \textbf{Eq. 4.18}$$

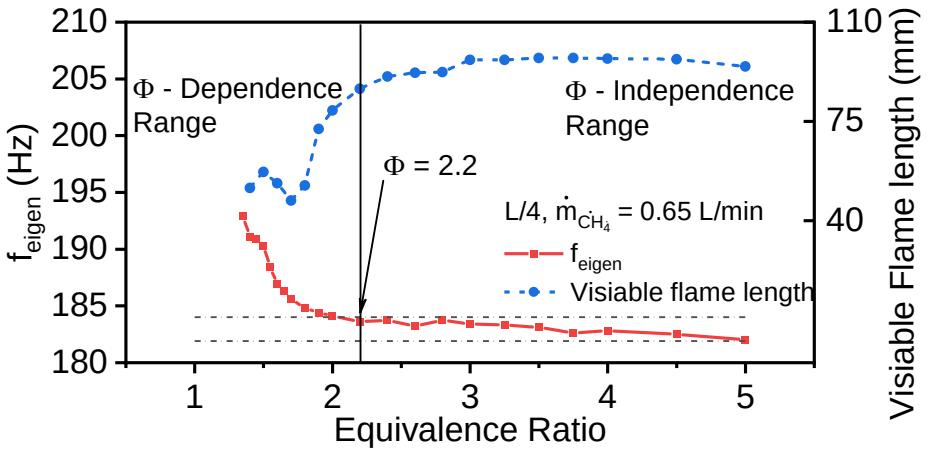

Fig. 4.5. Example of determination of the Φ-dependence and Φ-independence range for the case at L/4 of burner position and $\dot{m}_{CH_4} =$ 0.65 L/min. The red solid line represents the f_{eigen} and blue dashed line for the visible flame length. The critical Φ is at $\Phi = 2.2$. The upper and the lower critical frequency for the range determination is 183.7 Hz and 181.9 Hz, respectively, shown in dashed-dot lines.

For instance, Fig. 4.5 shows the determination of the Φ-dependence and Φ-independence ranges for the cases at a burner position of L/4 and $\dot{m}_{CH_4} = 0.65$ L/min. From the typical flame photos shown in Fig. 4.6, it can be found that the flame length increases with the increasing Φ before the Φ_{critical}, while becomes less varied with Φ once the Φ exceeds the Φ_{critical}. Thus, the trend of flame length is also in good agreement with the Φ-dependence and Φ-independence range.

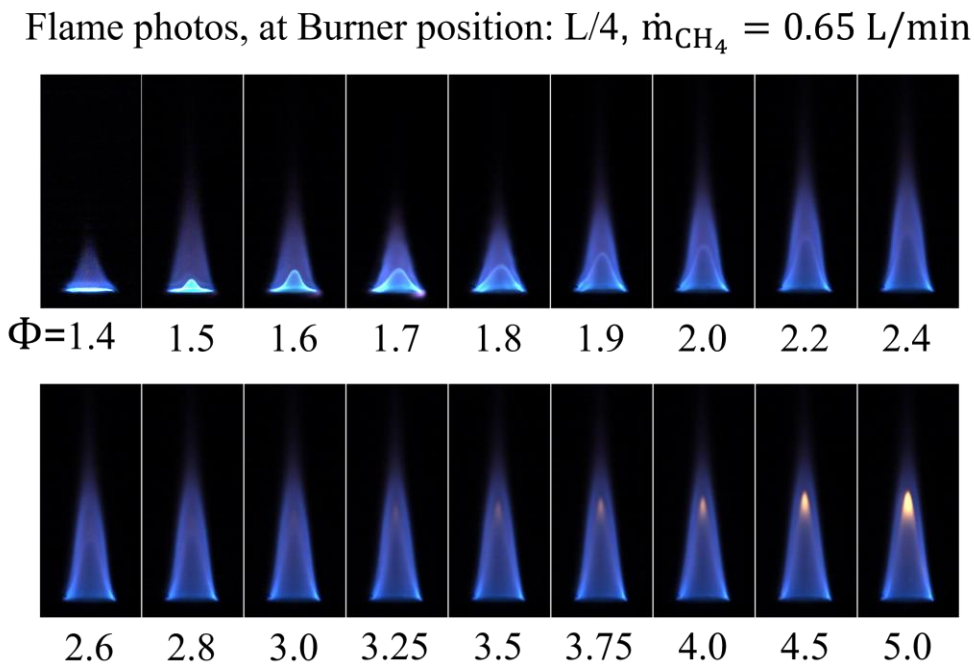

Fig. 4.6. Flame photos under different Φ for the case at burner position of L/4 and $\dot{m}_{CH_4}$=0.65 L/min.

The Φ_{critical} and the relevant results of cases under different system parameters are shown in Table 4.2. The percentage difference between the f_{max} and $\overline{f_{IR}}$ validates the obvious eigenfrequency change as the Φ changes. Besides, the results of P_{rms} are presented in Fig. 4.4. A trend that the P_{rms} rapid increases in Φ-dependence range and then smoothly decreases in Φ-independence can be observed in the different cases regardless of changing system parameters. It is also found that the turning point of P_{rms} is located in Φ-dependence range. Thus, the oscillation amplitude of the system also conforms to the Φ-dependence and Φ-independence range determined based on the f_{eigen}.

Table 4.2. The relevant results of $\overline{f_{IR}}$, percentage difference between f_{max} and $\overline{f_{IR}}$ and the $\Phi_{critical}$ under different conditions.

Burner position	**L/4**			**L/6**			**L/10**			**L/12**		
$\dot{m}_{CH_4}$ (L/min)	**0.65**	**0.8**	**0.95**	**0.65**	**0.8**	**0.95**	**0.65**	**0.8**	**0.95**	**0.65**	**0.8**	**0.95**
$\overline{f_{IR}}$ (Hz)	182.8	187.2	191.2	182.1	188.3	190.8	185.6	189.2	192.6	187.5	191.1	194.7
$\frac{f_{max}-\overline{f_{IR}}}{\overline{f_{IR}}}$ (%)	5.55	4.27	4.71	7.32	5.23	4.97	6.03	5.60	4.88	5.81	5.23	4.21
$\Phi_{critical}$	2.2	2.0	1.7	2.0	1.9	1.65	1.6	1.5	1.5	1.8	1.6	1.6

4.3.2 Characterisation of Φ-dependence and Φ-independence ranges

The results of both f_{eigen} and P_{rms} show that the system presents a more sensitive response to the change of Φ in the Φ-dependence range than the Φ-independence range. From the time-evolution of the oscillation, it can be found that the amplitude of oscillation tends to be more fluctuated when the system is in the Φ-dependence range, as shown in Fig. 4.7. Besides, the case that the amplitude presents less time-variant characteristics tends to have simpler and 'cleaner' frequency spectrum compared to the cases that the amplitude is strongly varied with time, as shown in Fig. 4.7 (c).

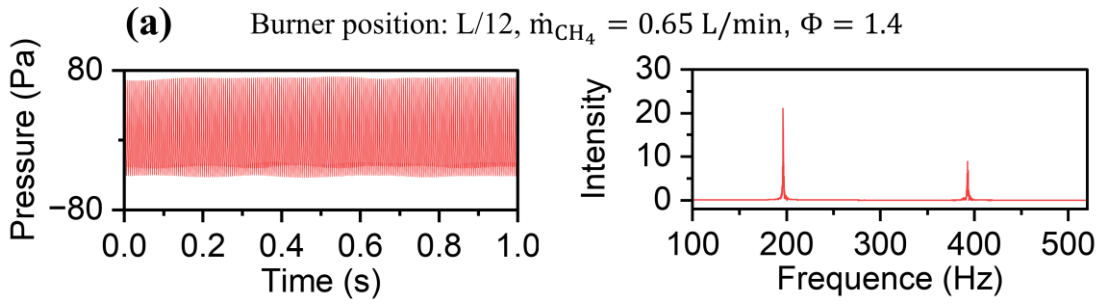

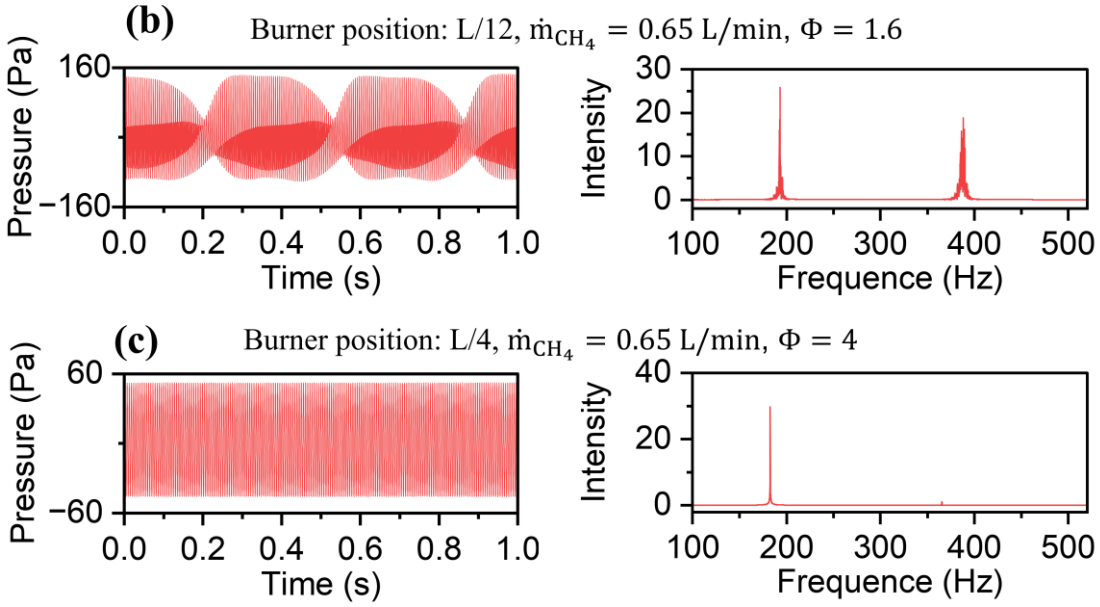

Fig. 4.7. The time-evolution of the pressure fluctuations (left) and the frequency spectrum (right) for the representative cases, (a) typical case in Φ-dependence range, (b) quasi-periodic oscillation (beating), (c) typical case in Φ-independence range. The experimental conditions are shown in the corresponding figures.

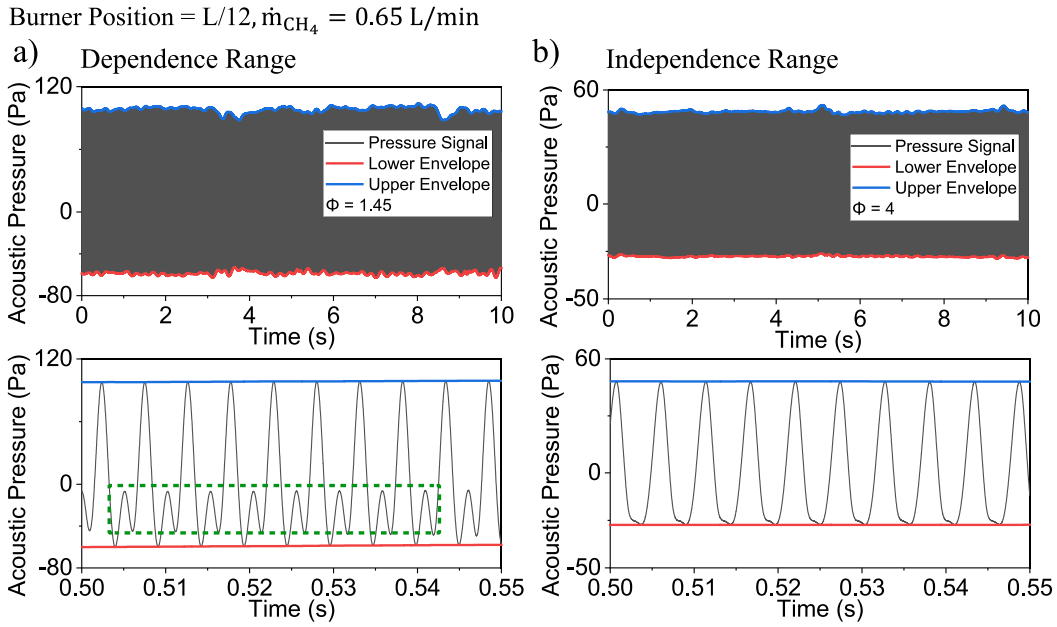

Fig. 4.8. Time-evolution of the pressure fluctuations for the cases of the burner at L/12, $\dot{m}_{CH_4}$ = 0.65 L/min, a) Φ = 1.45 and b) Φ = 4. The diagram below them is their detailed zoom in time-evolution waveform. The green dash line highlights the difference in waveform between a) period-2 oscillation to b) period-1 oscillation. The blue and red lines represent the upper and lower envelope of the waveform, respectively.

An example case of L/12 in burner position and $\dot{m}_{CH_4} = 0.65$ L/min is presented in Fig. 4.8 (a) and (b). The standard deviation of the upper (σ_u) and lower (σ_l) envelop for the waveform in Φ-dependence range (Fig. 4.8 (a), $\Phi = 1.45$) are $\sigma_u = 3.053$ and $\sigma_l = 1.857$. Relatively, the corresponding values in Φ-independence range (Fig. 4.8 (b), $\Phi = 4$) are $\sigma_u = 0.8044$ and $\sigma_l = 0.4161$, which is much smaller than the case of $\Phi = 1.45$. The difference in σ_u and σ_l indicate a larger variation of oscillation waveform envelope in Φ-dependence range than Φ-independence range. Besides, a clear shape in the waveform which indicates the period-2 oscillation can be observed in Fig. 4.8 (a) and highlighted by the green dashed line, while does not exist in Fig. 4.8 (b). The shape in Fig. 4.8 (a) indicates the notable intensity of the second harmonic mode. It needs to be noticed that the 2nd harmonic mode in the case of $\Phi = 4$ still have an intensity that cannot be neglected, although it is less intense than the fundamental mode. By analysing the superposition of two sinusoidal signals with different frequencies, it is found that the relative position ('phase difference') between them in the time domain plays an important role in affecting the characteristics of changes in $p(t)$. The phase difference and its variation with time can result in the variation of instantaneous oscillation amplitude and the shape of the time-series waveform. Therefore, the phase difference analysis is conducted to quantify the characteristics of changes in $p(t)$ oscillation characteristics in both ranges.

4.3.3 Case analysis under different system parameters

Although the variations of f_{eigen} and time-evolution of pressure fluctuation show the existence of the Φ-dependence and Φ-independence range, it is necessary to further investigate the system behaviour in both ranges in terms of characteristics of changes in $p(t)$ and system dynamics. Therefore, the phase difference analysis based on the FIR filter for the characteristics of changes in $p(t)$ and both RP and RQA analysis for the system nonlinear dynamics are applied for further investigation in the present work.

4.3.3.1 *Phase difference analysis (characteristics of changes in $p(t)$)*

The results of the mean phase difference ($\overline{\varphi_{f,2}}$) and corresponding standard deviation σ with the changing Φ under different parameters are shown in Fig. 4.9. It can be found that the trend of both $\overline{\varphi_{f,2}}$ and σ conform to the determined Φ-dependence and Φ-

independence range based on f_{eigen}. For the cases of L/12 in burner position and $\dot{m}_{CH_4}$= 0.65 L/min, it is found that the $\overline{\varphi_{f,2}}$ trended to be stable and insensitive to the change of Φ when the Φ exceeds 1.8 while showing greater sensitivity before this Φ. Meanwhile, σ of $\varphi_{f,2}^{local}$ trends to be approximately 0 once the Φ becomes greater than 1.8, which indicates a very stable $\varphi_{f,2}^{local}$ during the oscillation. Under such circumstances, the system can be considered that has a lower complexity and approaches more stable limit-cycle oscillation in the Φ-independence range. By comparing the case with different $\dot{m}_{CH_4}$, from 0.65 to 0.95 L/min, it can be found that the trends of $\overline{\varphi_{f,2}}$ to Φ is similar, but the $\overline{\varphi_{f,2}}$ of the case at $\dot{m}_{CH_4}$= 0.95 L/min is less varied with Φ when case is in Φ-independence range. By comparing the case at a higher burner position, from L/12 to L/10, no significant difference can be observed from the trends of $\overline{\varphi_{f,2}}$, but a larger difference in σ can be found as the burner moves downwards. Combining the results of the case at L/4 of the burner position, it is found that the trend of $\overline{\varphi_{f,2}}$ for all cases are similar, that both the $\overline{\varphi_{f,2}}$ and σ significantly changes if the system is in the Φ-dependence range and then gradually approaches constant value once it passes the $\Phi_{critical}$. Meanwhile, the changing rate of $\overline{\varphi_{f,2}}$ with increasing Φ becomes smaller once the Φ exceeds $\Phi_{critical}$, which indicates that the trend of $\overline{\varphi_{f,2}}$ is strong related to the Φ-dependence and Φ-independence range. The σ in Φ-dependence range are generally greater than those in the Φ-independence range, which further evidences a more stable and less complex system in the Φ-independence range. Besides, it is found that the value of σ is decreased along with the raising burner position and increasing $\dot{m}_{CH_4}$. Note that such results may indicate a more unstable oscillation at lower burner positions and lower $\dot{m}_{CH_4}$.

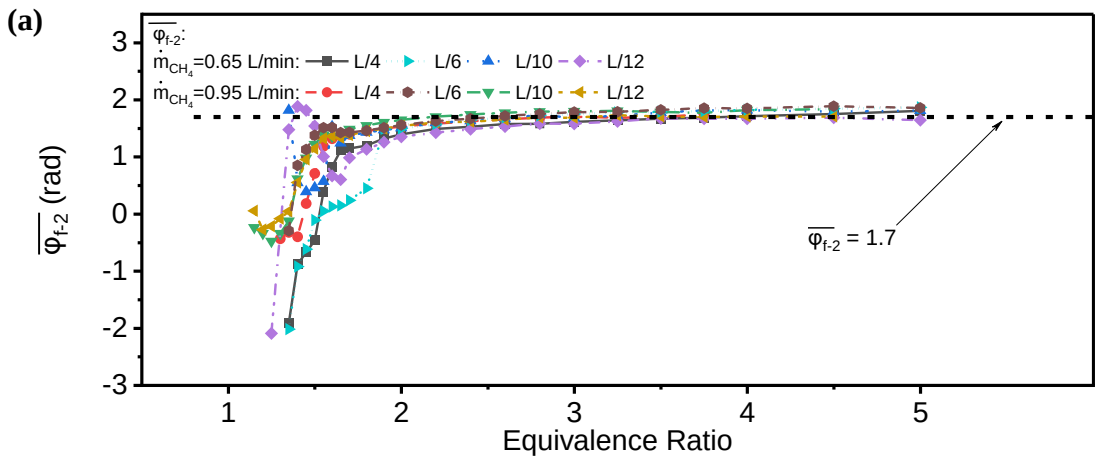

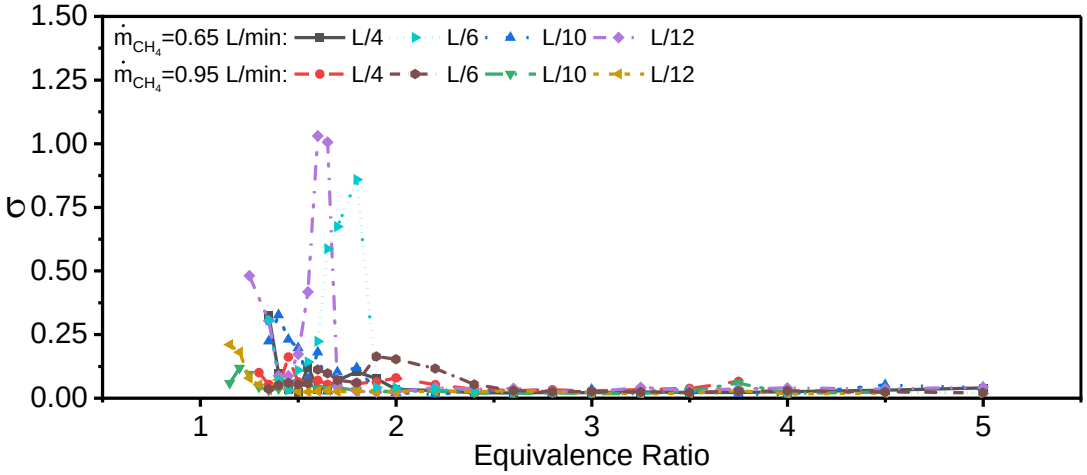

Fig. 4.9. Variation of a) $\overline{\varphi_{f,2}}$, b) σ to Φ. The colours represent the different case as shown in the legend.

Then focusing on the case with the largest σ (purple line in Fig. 4.9 (b), conditions as L/12, $\dot{m_{CH4}} = 0.65$ L/min and $\Phi = 1.6$), the corresponding frequency decomposing diagram and variation of $\varphi_{f,2}^{local}$ are shown in Fig. 4.10. From the original signal, it can be found that the beating oscillation is triggered in this case, and the system presents a quasi-periodic characteristic, as shown in Fig. 4.10 (a). Meanwhile, it is found that the second harmonic mode dominates the beating oscillation rather than the fundamental mode, although the fundamental mode has a higher mean intensity, as shown in Fig. 4.7 (b). From the diagram of the variation of $\varphi_{f,2}^{local}$, shown in Fig. 4.10 (b), the presence of $\varphi_{f,2}^{local}$ frequently sudden phase shifting indicates an unstable system with a relatively high σ (about 1.03) and quasi-periodic characteristics. The results indicate the existence of frequency fluctuations during the self-excited oscillation when the beating oscillation is triggered.

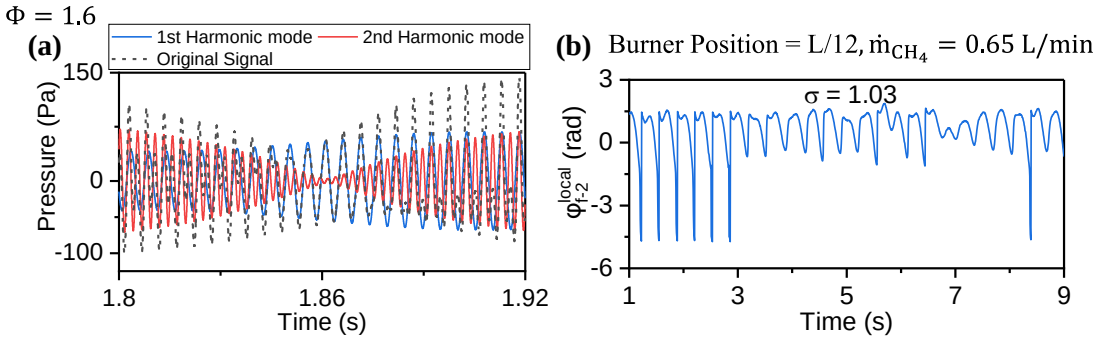

Fig. 4.10. a) Frequency decomposing, and b) $\varphi_{f,2}^{local}$ diagram for the case L/12, $\dot{m}_{CH_4} = 0.65$ L/min and $\Phi = 1.6$. The case of the beating oscillation being triggered.

Comparatively, the same diagrams for the case in the Φ-independence range at the same burner position and $\dot{m}_{CH_4}$ but a larger Φ of 3 is shown in Fig. 4.11. From both diagrams of frequency decomposing and $\varphi_{f,2}^{local}$, it can be observed that the $\varphi_{f,2}^{local}$ of the case in the Φ-independence range is more stable than the cases of $\Phi = 1.6$ which is in the Φ-dependence range. Since only slight variations of $\varphi_{f,2}^{local}$ with time ($\sigma = 0.023$) can be obtained, as shown in Fig. 4.11 (b).

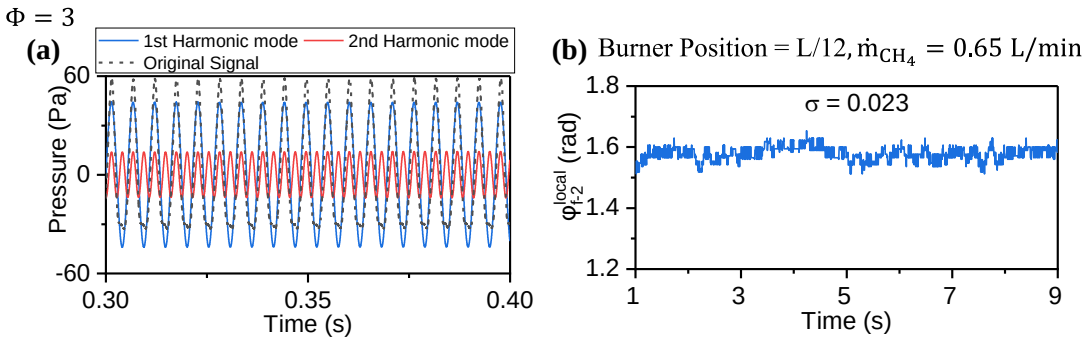

Fig. 4.11. a) Frequency decomposing, and b) $\varphi_{f,2}^{local}$ diagram for the case L/12, $\dot{m}_{CH_4} = 0.65$ L/min and $\Phi = 3.0$. The case in Φ-independence range.

As an example of the oscillation without beating oscillation in the Φ-dependence range, Fig. 4.12 (a) shows the time-evolution of the pressure fluctuations and the corresponding fundamental and second harmonic modes for the case of L/4 , $\dot{m_{CH4}} = 0.65$ L/min, $\Phi = 1.35$. It can be found that the intensity of the second harmonic mode is lower than the fundamental mode. Due to the low intensity of the second harmonic mode, a similar waveform and phase between the fundamental mode and the original signal can be seen in Fig. 4.12 (a). Although the frequency decomposing diagram shows a similar pattern to Fig. 4.11 (a), the $\varphi_{f,2}^{local}$ in Fig. 4.12 (b) presents a time-varied trend that is clearly decreasing trend with time. The unstable $\varphi_{f,2}^{local}$ and a greater σ of 0.326 indicate the oscillation is more complex and time-variant compared to the case L/12, $\dot{m}_{CH4} = 0.65$ L/min and $\Phi = 3.0$.

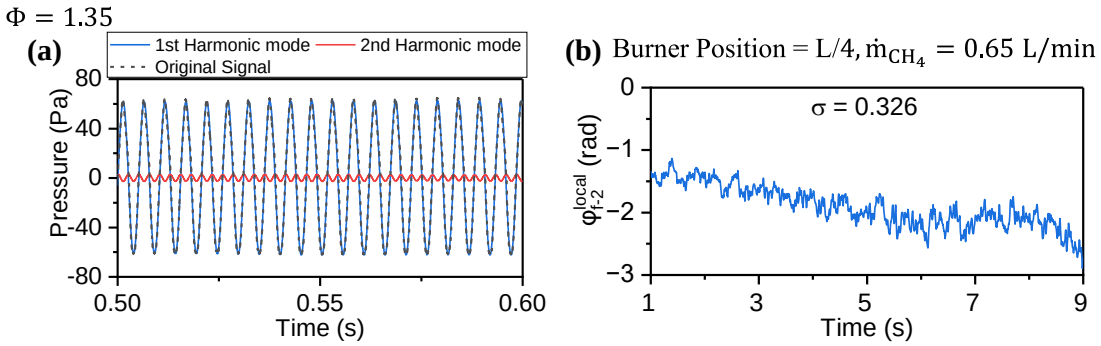

Fig. 4.12. a) Frequency decomposing and b) $\varphi_{f,2}^{local}$ diagram for case L/4,$\dot{m}_{CH_4}$ = 0.65 L/min and Φ = 1.35. The case in Φ-dependence range.

In summary, it is found that both the trends of $\overline{\varphi_{f,2}}$ and the corresponding σ of $\varphi_{f,2}^{local}$ are strongly related to the characterisation of Φ-dependence and Φ-independence range. The similar value of Φ_{critical} for the trends of phase difference analysis and f_{eigen} can be found. Therefore, the Φ-dependence range and Φ-independence range can be also applicable for determining the dependency of characteristics of changes in p(t) on Φ. In detail, the $\overline{\varphi_{f,2}}$ is sensitive to the change of Φ in the Φ-dependence range but becomes less sensitive once the system enters the Φ-independence range. The σ in the Φ-dependence range is greater and presents greater variations than those in the Φ-independence range, indicating a more complex system in the Φ-dependence range. In addition, due to the greater sensitivity of phase difference to Φ, it can assist in the determination of both ranges. Besides, the $\overline{\varphi_{f,2}}$ in Φ-independence range shows less sensitivity to the change of burner position and $\dot{m}_{CH_4}$. It can be found that the values of $\overline{\varphi_{f,2}}$ under different burner positions and $\dot{m}_{CH_4}$ are similar in the Φ-independence range with approximate values ranging from 1.6~1.8 rad as the Φ increases. Considering the slight influence of $\dot{m}_{CH_4}$ on the phase difference as $\dot{m}_{CH_4}$ increases, the characteristics of changes in $p(t)$ in the Φ-independence range might be strongly influenced by the acoustic properties of the resonance chamber.

Therefore, the trend of phase difference to varied Φ validates the existence of the Φ-dependence range and Φ-independence range. Since no significant phase difference changes in the Φ-independence range as the Φ changes can be observed. It can be considered that the characteristics of changes in $p(t)$ conform to the range defined

based on f_{eigen} and the system presents similar characteristics of changes in $p(t)$ in the Φ-independence range under the same system parameters.

4.3.3.2 Recurrence plot and RQA

Recurrence analysis is applied to investigate system nonlinear dynamics in the present work. Fig. 4.13 shows the RPs of the cases at a burner position of L/12 and $\dot{m}_{CH_4} =$ 0.65 L/min. It can be found that most cases present uniformly distributed periodical patterns with clear continuous diagonal lines except the case at $\Phi = 1.6$ where the beating oscillation is triggered. The RP of the case at $\Phi = 1.25$ shows a great amount of scatter points rather than continuous diagonal lines, indicating the strong time-variant nature of the system. For the cases with relatively stable oscillation without significant change of the time-evolution of pressure fluctuations, a 'periodic' pattern without complex sub-structure can be observed, such as $\Phi = 1.35$, 2, 2.4 and 3, as shown in Fig. 4.13 (b) (d) (e) and (f). The clear continuous diagonal lines indicate that the system is highly periodic and quasi-stable [25,26,105,125]. For the case with more periodic natures ($\Phi = 1.35$, 2, 2.4 and 3), the diagonal lines tend to be more gathered, and fewer scatter points can be found compared to the case with higher complexity ($\Phi = 1.25$). Besides, although the density of diagonal lines seems to be higher for the case of $\Phi =$ 1.35, the diagonal lines are more frequently interrupted and more scatter points can be found in the plot compared to the case in the Φ-independence range ($\Phi =$2, 2.4 and 3). Therefore, it can be considered that the cases in the Φ-independence range have more periodic natures and is more stable than the cases in the Φ-dependence range without quasi-periodic characteristics.

For the case at $\Phi = 1.6$ with quasi-periodic characteristics, a frequently pattern change with 'high density' and 'low density' areas can be clearly observed (Fig. 4.13 (c)), indicating the unstable system with state changes. The 'high density' area indicates the relatively stable oscillation (Fig. 10 (c2)), whereas the 'low density' area (Fig. 10 (c1)) represents where the beating happens. From Fig. 4.13 (c), the bowed structure can be observed, which indicates the evolution of states has similarities but with different changing rates (the change of the frequency in this case), and the dynamic of the system is changing with time [115]. Meanwhile, no clear continuous diagonal lines can be observed apart from the LOI, which evidences the system state is strongly interrupted

and the state transition frequently happens. From Fig. 4.13 (c1), it can be found that the plot of 'low density' area (beating region) mainly consists of scatter points, and diagonal lines exist only next to the LOI. As the system exits the beating region, more recurrence points start to appear, and several diagonal lines start to be generated by the relatively stable oscillation, as shown in Fig. 4.13 (c2) ('high density' area). The presence of the pattern 'density' change also evidences the existence of multiple states in a quasi-periodic system.

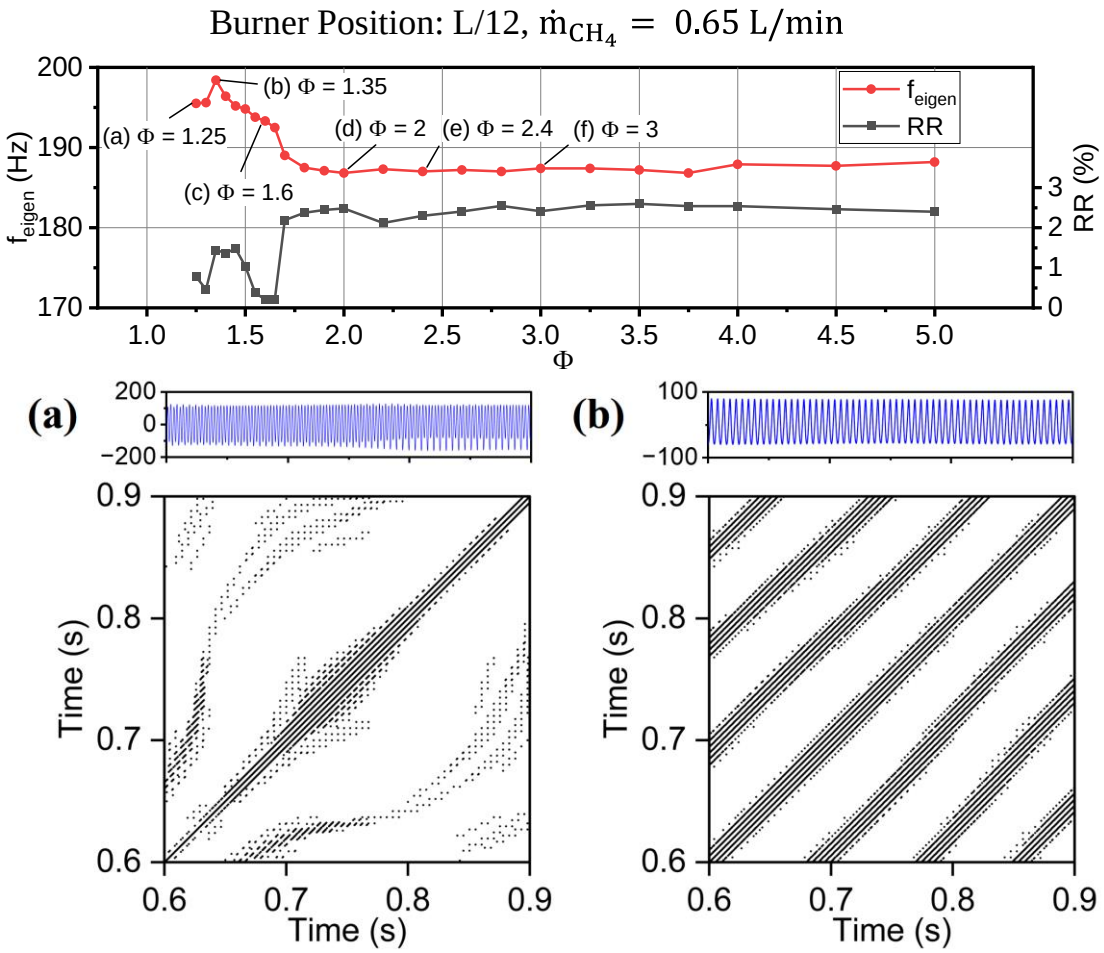

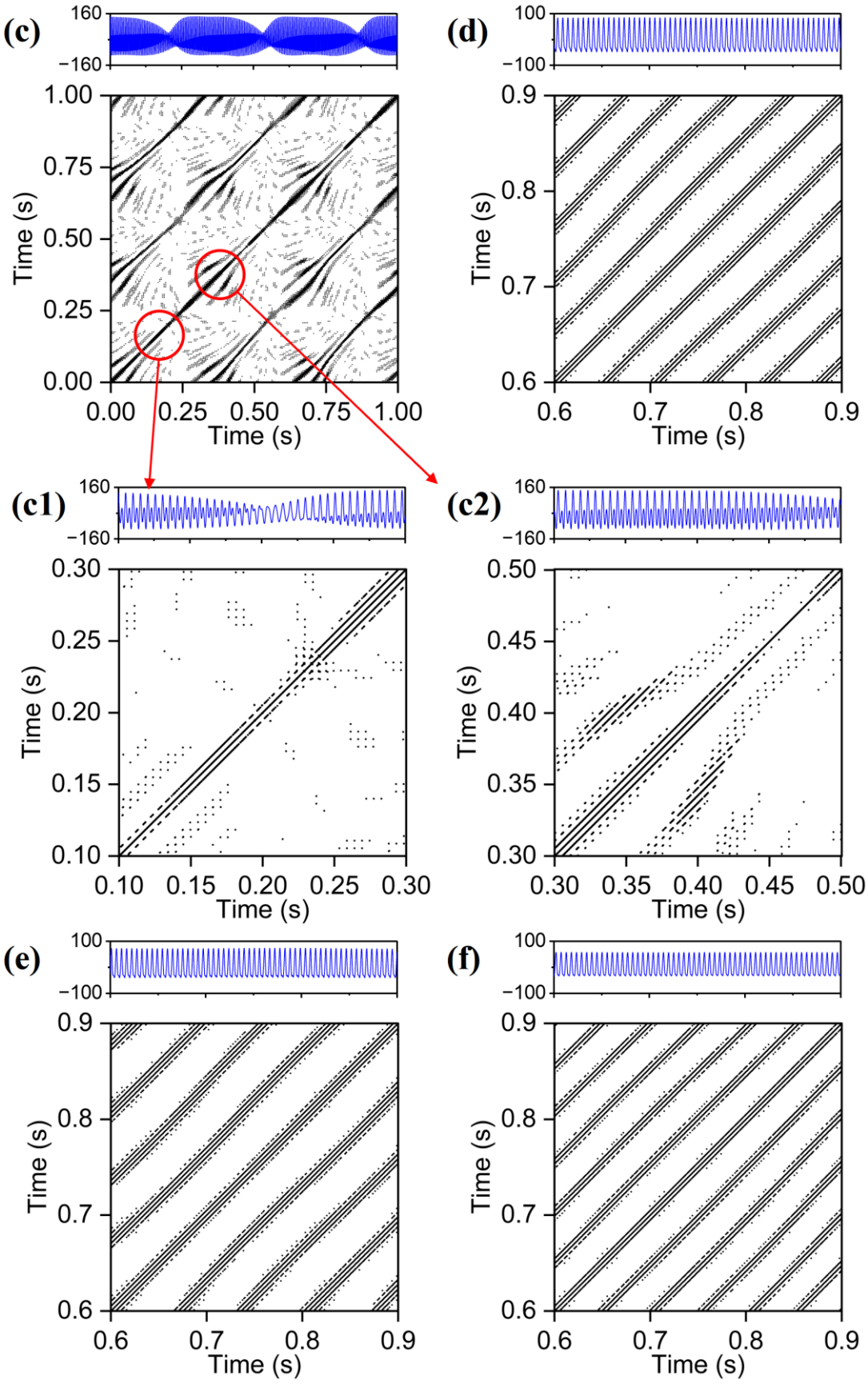

Fig. 4.13. Recurrence plots at (a) $\Phi = 1.25$*, (b)* $\Phi = 1.35$*, (c)* $\Phi = 1.6$*, (d)* $\Phi = 2$*, (e)* $\Phi = 2.4$ *and (f)* $\Phi = 3$ *and the* f_{eigen} *and RR to* Φ *diagram for case L/12,* $\dot{m}_{CH_4} = 0.65$ *L/min. (c1):*

Zoomed RP of (c) at the low density area (beating range). (c2): Zoomed RP of (c) at the high density area. D = 3, τ is determined by first zero-crossing point of the corresponding autocorrelation function.

By comparing the curve of f_{eigen} and RR, it can be found that the range of RR and f_{eigen} presenting great sensitivities to the change of Φ is coincident with each other. A higher RR results from more recurrence points in the plot, indicating that the system dynamics can be also in agreement with the Φ-dependence and Φ-independence range.

To further quantify the system nonlinear dynamical properties, RR, DET, ENT and ADL are calculated based on the structural characteristics in the corresponding RP. The RR and DET are used to indicate the system recursiveness and occurrence of similar states for the thermoacoustic oscillation, respectively. The ENT can provide a quantitative measure of the system chaoticity. The ADL can indicate the divergence of the two segments in the phase space trajectory [115,124]. The results of these measures are shown in Fig. 4.14.

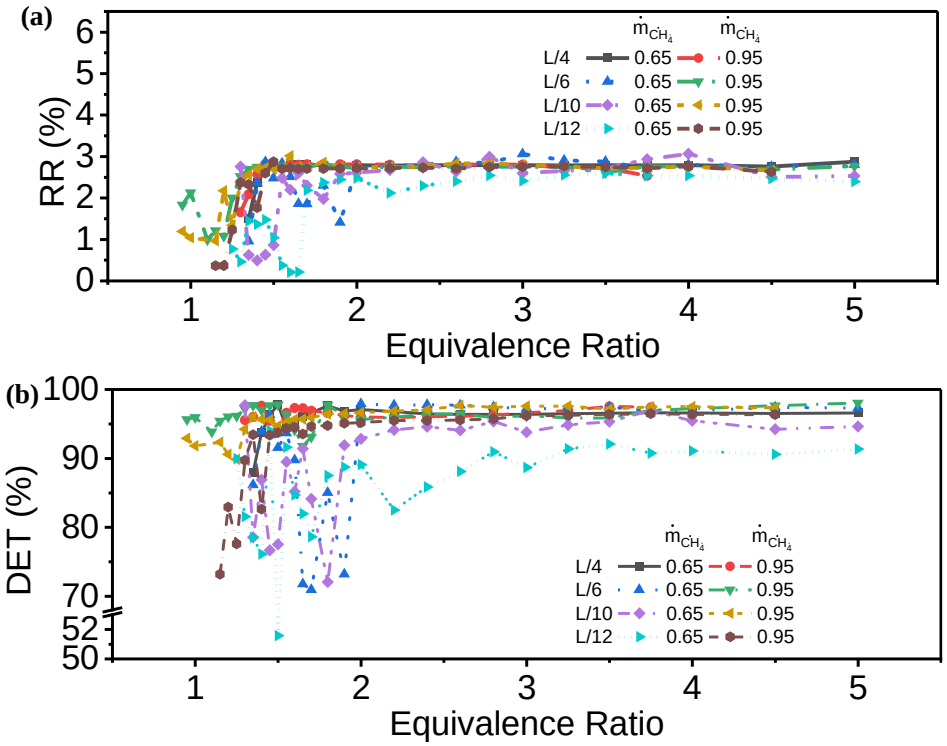

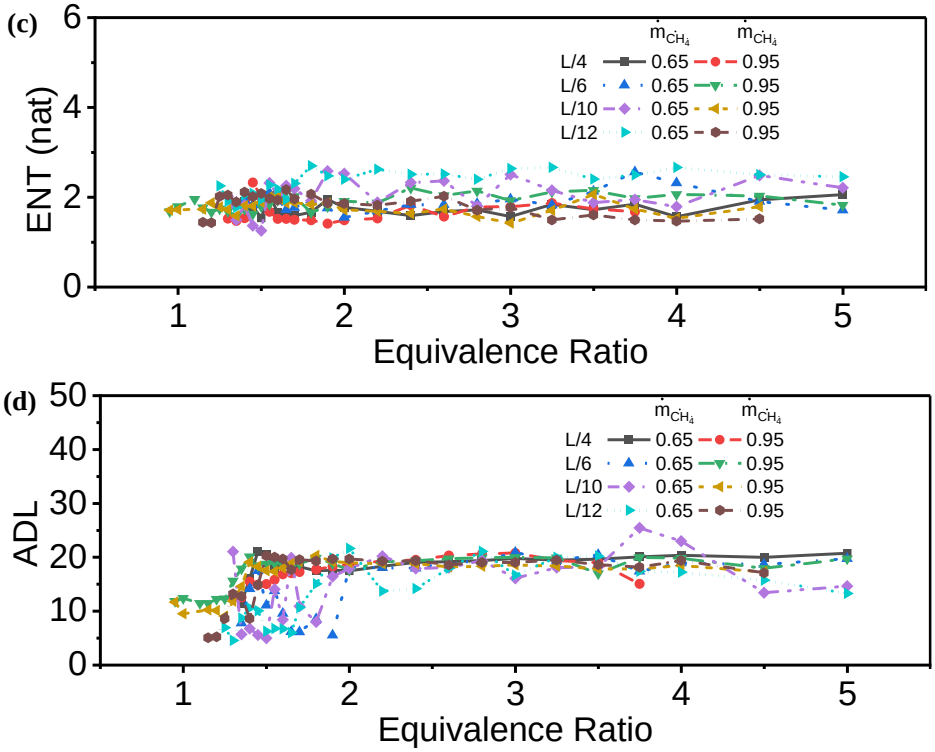

Fig. 4.14. Variation of four measures of RQA as the equivalence ratio changes. These four figures represent the: a) recurrence rate, b) determinism, c) Shannon entropy, and d) average diagonal length. The different curves with different colours represent the case with different burner positions or methane flowrate.

The RQA results are generally in agreement with the findings from the analysis of RP. Focusing on the same cases at a burner position of L/12 and $\dot{m}_{CH_4} = 0.65$ L/min, it is observed from Fig. 4.13 that the cases in the Φ-independence range (Φ =2, 2.4 and 3) have greater densities of recurrence points than the case in the Φ-dependence range (Φ =1.25, 1.35 and 1.6). The higher density of recurrence points results in a greater RR for the cases in the Φ-independence range. Meanwhile, the systems in the Φ-independence range have similar patterns of parallel and continuous diagonal lines, but the distinguishable difference in pattern for the systems in the Φ-dependence range. Therefore, the values of RR for the system in the Φ-independence range are similar and insensitive to the change of Φ, but strongly vary with Φ if the system is in the Φ-dependence range, as shown in Fig. 4.14 (a).

From the structural properties of the pattern, the longer diagonal lines with fewer interruptions can be observed from the RP of the system in the Φ-independence range, and the RP is mainly composed of diagonal lines as the less amount of scatter points

exists, as shown in Fig. 4.13 (d) ~ (f). In contrast, the RP of the system in the Φ-dependence range has short and less diagonal structures and the RP mainly consists of scatter points and very short diagonal line fragments, as shown in Fig. 4.13 (a) ~ (c). The difference in the amount of diagonal lines results in the lower DET and ADL for the system in the Φ-dependence range. It can be found that the value of DET for most systems in the Φ-independence range is generally greater than 90%. However, for the systems in the Φ-dependence range, a clear lower DET that mostly ranges from 51% to 90% can be obtained, as shown in Fig. 4.14 (b). Furthermore, the DET and ADL show a high dependence on Φ in the Φ-dependence range due to the considerable pattern change but low dependence in the Φ-independence range caused by similar patterns.

Different from the RR, DET and ADL, the ENT presents a low sensitivity to the change of Φ in both the Φ-dependence and Φ-independence range, and the values of ENT are relatively small, even for the system with quasi-periodic characteristics (Φ =1.6). The low sensitivity and the small value of ENT are caused by the considerable periodicity of the system and the neglectable chaoticity, since neither intermittency nor the chaotic state is found in the present work.

By comparing the systems at different burner positions and $\dot{m}_{CH_4}$, the same findings can be drawn that the RR, DET and ADL present great sensitivities to the change of Φ in the Φ-dependence range but insensitivity in the Φ-independence range, as shown in Fig. 4.14. Meanwhile, the ENT shows less dependence on Φ in both ranges. It can be found that the higher RR and DET in the Φ-independence range can be obtained for all the cases, indicating a more stable system with less time-variant characteristics and a higher occurrence probability of similar states in the Φ-independence range, as shown in Fig. 4.14 (a) (b). The lower ADL in the Φ-dependence range indicates that the two segments in the phase space trajectory tend to diverge faster and have lower degrees of parallelism in the phase space [124]. The result of ADL further evidences the more time-variant characteristics for the system in the Φ-dependence range. Besides, the results of ENT indicate that the systems in the present work are generally periodic without noticeable chaoticity.

In summary, the RR, DET and ADL present different sensitivity as the Φ changes, which proves that the change of the system dynamics is also in agreement with the Φ-dependence and Φ-independence range. Thus, the existence of both ranges can be highlighted from the system dynamics. Meanwhile, the independence of ENT on Φ shows that the chaoticity of the system is less influenced by the Φ if the self-excited limit-cycle or quasi-periodic oscillation is triggered.

4.4 Chapter Summary

In this chapter, the present study explored the impact of equivalence ratio (Φ) on self-excited thermoacoustic oscillations in a Rijke tube. Experiments were conducted with varying Φ, burner positions, and methane flowrate. Time-domain data analysis methods were also used to assess system nonlinearity. The result discovered a nonlinear trend in the system's frequency response to Φ, while eigenfrequency (f_{eigen}) showed sensitivity to Φ within a Φ-dependence range and insensitivity within a Φ-independence range. Results from phase difference and recurrence analysis confirmed these findings and indicated more stable oscillations within the Φ-independence range. The study highlights Φ as a critical factor influencing self-excited thermoacoustic oscillations. The methods employed offer valuable insights into oscillation characteristics and system dynamics, making them applicable to various combustion systems with nonlinearities. In summary, this study emphasises the significance of Φ in influencing thermoacoustic oscillations and introduces effective analysis techniques for understanding system behaviour.

Chapter 5 Effects of system parameters on system behaviours

5.1 Introduction

Self-excited thermoacoustic oscillation can be triggered in various systems, including the thermoacoustic heat engine and several types of combustors [13,15,21,74,126]. As a challengeable yet important problem, it strongly enhances the combustion instability in the combustion systems [6,17,26,58,137,154,155]. For the combustion systems with enclosed combustion areas, such as gas turbine engines and rocket engines, the intense oscillation could be negative for the performance of combustors, resulting in a low efficient combustion process and even structural damage [58,156]. Therefore, predicting and controlling of thermoacoustic instabilities in the combustion systems could be critical.

Rayleigh revealed the trigger mechanism of thermoacoustic oscillation, which is about the interactions between unsteady heat release and pressure fluctuation when they are in-phase [9]. And it had been proved that this coupling effect was highly nonlinear [157]. The triggered self-excited oscillation presents a combination of linearity and nonlinearity during the developing process [18]. The self-excited thermoacoustic oscillation generally becomes nonlinear from oscillation properties [17] and system state bifurcation [155] when the oscillation is fully developed.

Combustion-induced thermoacoustic instabilities are attributed to the complex combustion-acoustic-flow interactions with the existence of combustion instabilities [6,158]. The potential control methods can be provided by exploring these complex interactions. In order to realise complex nonlinear thermoacoustic systems in lab-scale, the Rijke tube is one of the general setups for triggering the thermoacoustic oscillation [6]. A number of investigations have been conducted to study the characteristics of

nonlinear oscillations in the Rijke tube [8,18,27,52,133,159,160]. Also, both the nonlinearity and the non-normality of the system have been discovered in Rijke tubes [18,159], that the system states can be strongly affected by the initial conditions. For instance, the rapid growth or decay of oscillation can be initiated by either flow or acoustic disturbances even if such disturbances have limited intensity. The flame dynamics in these systems have been studied by the G-equation method, and the flame response to acoustic perturbation has been obtained [24,161]. Some studies have pointed out the importance of the hydrodynamic region around the flame holder in a Rijke tube [8,27]. The nonlinear theoretical model about the hydrodynamic region indicates that the system eigenfrequencies and amplitudes can be nonlinearly proportional to system conditions. The hydrodynamic theory indicates the influences of hydrodynamic region position, temperature distribution in tube and geometry properties of the system on generating the self-excited oscillations [8].

The critical roles of several parameters in generating the thermoacoustic oscillations, including system parameters (e.g. equivalence ratio, fuel flowrate, swirl number) [25,26,114,137,155] and flame dynamics [17,155,162] have been extensively investigated within various combustion systems. It has been found that the equivalence ratio is able to influence many oscillation behaviours, such as frequency response and triggering conditions of beating oscillations [26,52]. The fluctuation of the equivalence ratio has been theoretically proved to be critical for driving the instabilities in a low nitrogen oxide (NOx) gas turbine under lean combustion conditions [40]. The significant effects of fuel flowrate on both amplitude and eigenfrequency of self-excited oscillation in a low swirl burner have been verified [26]. It has been found that both spatial distributions of local equivalence ratio and heat release within the flame area are critical for corresponding thermoacoustic oscillations, also the flame shape is able to influence the relevant oscillation properties [162,163]. Besides, it has been studied that many combustor properties, including fuel injector location, fuel line length, flame location and burner geometry, are effective in characterising stability region, growth factors and states bifurcation in various combustion systems [18,40,104].

Due to the characteristic of nonlinear systems, the system states can be strongly varied with time. Therefore, nonlinear time series analysis methods have been utilised to provide insightful information about system dynamics. Based on trajectory and

Poincaré maps constructed from time series measurements in thermoacoustic system, the phase space analysis has been utilised to determine system dynamics, including chaoticity, periodicity and intermittency route to chaos [104,114,126,146]. The recurrence plot (RP) is able to provide a direct view of the dynamical properties and the recursiveness of the system [25,26,104,105,124]. Based on the RP, the recurrence quantification analysis (RQA) enables the quantitative descriptions of the system dynamics by obtaining numbers of statistical measures [115]. Therefore, the similarities of systematic dynamics among the different nonlinear systems can be identified, then the system behaviour can be compared among several systems.

Many studies have extensively investigated the effects of different system parameters on the system responses under fuel-lean combustion conditions. However, the fuel-rich combustion condition is preferred for applications which require higher reliability and stableness of combustion, such as Rich-burn, Quick-mix, Lean-burn (RQL) engine. As a reliable system in stationary applications, the rich combustion initiates combustion process in a RQL engine [152]. Meanwhile, the study of nonlinear trends of system responses and the systematic analysis of the different system parameters in a Rijke tube still remains insufficient. Therefore, this study aims to intensively characterise system behaviour and response in a Rijke tube with varied system parameters, including equivalence ratio, fuel flowrate, burner position and tube inner diameter. The pressure fluctuation time series signal has been obtained to analyse system characteristics. The characteristics of the system under different system parameters have been revealed by using multiple time-domain analysis methods. The phase space which is constructed based on the time-delayed embedding method has been applied to qualitatively indicate system nonlinearities. The calculation of Wayland translation error for the trajectory in phase space has been conducted to quantify the system deterministic nature. Both system nonlinear dynamics and recurrence have been investigated by utilising RPs and quantified by the statistical measures from RQA.

5.2 Methodology

5.2.1 Experiment setup

The Rijke tube usually consists of a vertically anchored both-open-ended tube and heating elements placed at the lower half of tube [6]. In the present work, the experiments were conducted in a Rijke tube with a honeycomb flame holder. The heat source was in the form of a premixed methane-air flame. The schematic figure of the experiment setup is shown in Fig. 5.1. The quartz tubes (40 and 50 mm in diameters) with a total length of 1 m were utilised as the chamber of the Rijke tube. A honeycomb flame holder with a 22% blockage ratio was applied for stabilising the flame, since the influence of flame holder with this blockage ratio on the thermoacoustic oscillations under the low Mach number conditions can be neglected [128]. During the tests, the burner position was measured from the top of flame holder top to the lower end of tube (z). The Aalborg GFC17 Mass flow controllers were utilised to control flow rates of methane and air, with the accuracy of 0.05% for the methane and 0.1% for the air. The methane flow rate ($\dot{m}_{CH_4}$) was ranged from 0.6 to 1.0 L/min with a step of 0.05 L/min. The equivalence ratios (Φ) at a specific $\dot{m}_{CH_4}$ then could be obtained by the step-changing air flow rates.

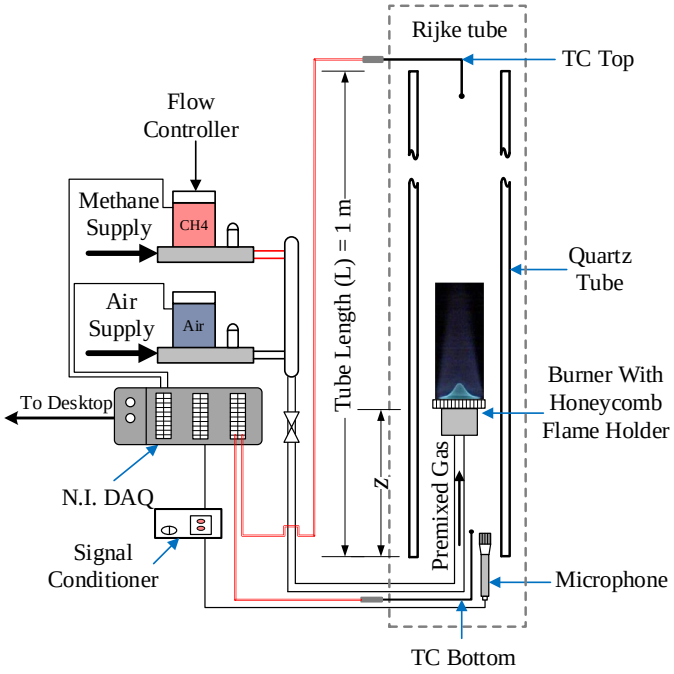

Fig. 5.1 Schematic figure of the flame-driven Rijke tube.

The same pressure-field microphone units as used in the study presents in Chapter 4 were utilised to capture the pressure signal at the same sampling rate. Besides, the same calibration process was conducted. Two RS type-N thermocouples (TC) were used to measure the temperature at both upper and lower ends of tube. The accuracy of thermocouples was ± 1.5 K. The measured temperature data was acquired by the NI-9211 Temperature Input Module at a sampling rate of 10 samples per second. Also, the same length of stabilisation time was applied before acquiring data.

5.2.2 Data processing method

5.2.2.1 Phase space analysis

In the present work, the 3-dimensional phase space was constructed to investigate the oscillation properties in the time-domain. The trajectory in the phase space was obtained based on the time series data of the pressure fluctuations. Based on the Takens' time-delay embedding theorem [109], the vector in the phase space, which was formed by the pressure time series data, can be expressed in the following form:

$$\boldsymbol{P}^*{}_t(D) = \left(p^*(t), p^*(t-\tau), p^*(t-2\tau), \cdots, p^*(t-(D-1)\tau)\right), \qquad \textbf{5.1}$$

where the $\boldsymbol{P}^*{}_t(D)$ represents the vector in phase space with an embedding dimension of D, $p^*(t)$ denotes the normalised time series pressure fluctuations data at time t, τ denotes the time delay. In order to compare the trajectories with different oscillation amplitude, the pressure time series $(p(t))$ was normalised $(p^*(t))$ based on its maximum absolute value, as $p^*(t) = p(t)/(\max(|p(t)|))$. The time delay is critical for forming phase space trajectory by the time-delay method. The inappropriate time delay values could lead to the incorrect correlation between the points and the trajectory, making it unable to indicate the correct characteristics of oscillations [114]. The autocorrelation function and average mutual information are suggested to determine the value of time delay [114,126]. In the present work, the time delay was determined by the first zero-crossing point of the autocorrelation functions since the self-excited oscillation was periodic with low complexity and chaoticity, neither no intermittency nor chaos states were found. The Wayland translation error (e_{trans}) was utilised to further recognise the system stability by quantifying system deterministic nature. The

algorithm is proposed by Wayland et al. [112], and it is applicable to the time delay vector from the time series data [113,114]. For the space vector obtained from time-delayed embedding method, the translation vectors ($\mathbf{v}_{\mathrm{trans}}$) will be in the following form:

$$\boldsymbol{v}_{trans}(t_k) = \mathbb{P}^*{}_{t_k+m} - \boldsymbol{P}^*{}_{t_k}, \quad \boldsymbol{P}^*{}_{t_k} \in \{\boldsymbol{V}\}^K, \tag{5.2}$$

where subscript m denotes the specific time interval for the determination of translation vectors, of which the value is suggested to be the same value as τ [113]. $\{\boldsymbol{V}\}^K$ is the series of neighbour vectors with the amount of K to the randomly selected $\boldsymbol{P}'_{t_0}$. The subscript k represents the k-th nearest neighbour vectors to $\boldsymbol{P}^*{}_{t_0}$. In the present work, K was set to 100 to provide the reliable result on $\overline{\boldsymbol{v}}(t)$. The vectors in $\{\boldsymbol{V}\}$ are in the nearest order, which is determined based on the Euclidean metric between the $\boldsymbol{P}^*{}_{t_k}$ and $\boldsymbol{P}^*{}_{t_0}$. The nearest neighbour should satisfy $|t_k - t_0| > \tau$ to avoid the temporal correlation [112,113]. The average translation vectors $\overline{\boldsymbol{v}}(t_k)$ then can be defined as below:

$$\overline{\boldsymbol{v}}(t) = \frac{1}{K+1}\sum_{k=0}^{K} \boldsymbol{v}_{trans}(t_k), \tag{5.3}$$

Then, e_{trans} can be calculated based on the following equation:

$$e_{trans} = \frac{1}{K+1}\sum_{k=0}^{K} \frac{\|\boldsymbol{v}_{trans}(t_k) - \overline{\boldsymbol{v}}(t)\|^2}{\|\overline{\boldsymbol{v}}(t)\|^2}, \tag{5.4}$$

In the present work, in order to provide a better statistical result, the median e_{trans} was obtained by randomly selecting 10 different $\{\boldsymbol{V}\}$ and calculating the corresponding e_{trans}. K was set as 100 to provide reliable results of $\overline{\boldsymbol{v}}(t)$ and e_{trans}. The value of e_{trans} could provide quantitative measures of system deterministic nature. Generally, smaller e_{trans} indicates more deterministic system, while higher e_{trans} for more chaotic and complex system. For a system with an ideally random nature, the value of e_{trans} would be 1, while the criterion value of e_{trans} for a deterministic system would be 0.01 [114].

5.2.2.2 Recurrence analysis

The states recursiveness in a dynamical system is usually considered as a key characteristic to describe the system behaviour in a system with high complexity, such as the combustion instability in a combustion system [19,26,125]. Therefore, the recurrence analysis could effectively determine the system dynamics of self-excited thermoacoustic oscillations in a Rijke tube [26,126]. Recurrence Plot enables the visualisation of states recurrence by obtaining recurrence matrix **R**. **R** is a binary matrix as below:

$$\boldsymbol{R}_{i,j} = \Theta\left(\varepsilon - \left\|\boldsymbol{x}^*{}_i - \boldsymbol{x}^*{}_j\right\|\right) \quad i,j = 1,2,3,\cdots,N, \tag{5.5}$$

where $\boldsymbol{x}^*$ denotes the normalised space vector obtained from the discrete time series data $p^*(t)$ according to the time-delayed embedding method, as shown in Eq. 5.1. Subscripts i and j are sequence of space vector and coordinates. $\left\|\boldsymbol{x}^*{}_i - \boldsymbol{x}^*{}_j\right\|$ denotes the norm of difference between $\boldsymbol{x}^*{}_i$ and $\boldsymbol{x}^*{}_j$. Θ is the Heaviside function. ε is the recurrence threshold to determine whether two target points can be considered as recurrent. The selection of ε is critical in recurrence analysis since the improper ε may lead to an unfaithful result [117]. The threshold in the present work was also set as 15% of standard deviation (σ) of pressure fluctuation time series signal. In the present work, embedding dimension for recurrence analysis D was set to 3 according to the FNN method. The time delay for recurrence analysis (τ) was also determined based on first zero-crossing point of autocorrelation functions. A down-sampling process was carried out to avoid the excessively high DET, as discussed in Section 3.5.2.

Based on the structural properties of the RP, the Recurrence Quantification Analysis (RQA) can further quantify system dynamics. In the present work, four measures, including recurrence rates (RR), determinism (DET), Shannon Entropy (ENT) and average diagonal line length (ADL), were used to indicate various system nonlinear dynamics, including both periodicity and complexity [115,124,125]. These measures can be expressed in the following forms:

$$RR(\varepsilon) = \frac{1}{N^2}\sum_{i,j=1}^{N} \boldsymbol{R}_{i,j}(\varepsilon), \tag{5.6}$$

$$DET = \frac{\sum_{l=l_{min}}^{N} lP(l)}{\sum_{l=1}^{N} lP(l)}, \tag{5.7}$$

$$ADL = \frac{\sum_{l=l_{min}}^{N} lP(l)}{\sum_{l=min}^{N} P(l)}, \quad \textbf{5.8}$$

$$ENT = -\sum_{l=l_{min}}^{N} p(l) ln p(l), \quad \textbf{5.9}$$

where N denotes data length for recurrence analysis which is obtained from time series signal based on embedding dimensions. The density of recurrence points in the RP can be determined by RR. DET is defined as the ratio of recurrence points which forming the line structure in the diagonal direction to all recurrence points. $P(l)$ represents histogram of the diagonal lines with a length of l. l_{min} denotes the least length of diagonal, and the value in the present work was set to 2. The occurrence of similar states can then be determined by DET. The average diagonal line length (ADL) is able to obtain the average time that two segments in the trajectory are close to each other, and the degree of parallelism. The ENT is able to determine Shannon Entropy based on the entropy of $p(l)$. $p(l)$ represents the probability of appearance for the diagonal line with a length of exactly l. $p(l)$ is obtained by $p(l) = P(l)/N_l$, where N_l denotes the number of diagonal lines. The system complexity and chaoticity can then be indicated by ENT. The Shannon Entropy in the present work was calculated based on the natural logarithm with the unit of nat.

5.3 Results and Discussion

Thermoacoustic oscillations are usually involved with the interactions between heat release and pressure fluctuation. Therefore, the system parameters, including fuel flowrate ($\dot{m}_{CH_4}$), equivalence ratio (Φ), burner position (z) and tube inner diameter (ID), are able to strongly influence oscillation behaviours. In the present work, the effects of these system parameters on both system frequency response and systematic characteristics are focused on. Based on experimental results, multiple system analyses, including frequency analysis, phase space and corresponding translation error, and recurrence analysis, are conducted to reveal the frequency response, deterministic natures and nonlinear dynamics of thermoacoustic systems under different system parameters.

5.3.1 System frequency response and oscillation amplitude

The results of eigenfrequency (f_{eigen}) and root mean square acoustic pressure (P_{rms}) for the case at L/4 and L/12 of burner positions with varied methane flowrates are shown in Fig. 5.2. It is found that the eigenfrequencies of these cases are the fundamental harmonic mode due to its greater intensity than higher harmonic modes. For 40 mm cases, by comparing the results at the same burner position, it can be found that the eigenfrequency presents similar nonlinear trends along various equivalence ratios under the same $\dot{m}_{CH_4}$, as shown in Fig. 5.2 (a) and (b). In detail, a certain Φ-sensitive range ($1.3 \leq \Phi \leq 2$) and an Φ-insensitive range ($\Phi > 2$) of f_{eigen} can be obtained from the Fig. 5.2. In Φ-sensitive range, it is found that f_{eigen} is sensitive to the change of Φ, and a decreasing trend of f_{eigen} with increasing Φ can be observed in most cases. Be different from the Φ-sensitive range, the f_{eigen} becomes insensitive to Φ changes and the f_{eigen} becomes nearly constant once Φ becomes greater than 2. The nonlinear trends between f_{eigen} and Φ might be caused by the changing rate of net heat release to Φ in the range of $\Phi > 2$. It has been reported that the net heat release of premixed methane flame in fuel-rich range is inversely proportional to increasing Φ when the methane flowrate keeps constant, and the decreasing rate of net heat release decreases with increasing Φ, especially when Φ is greater than 2. Although as a finding, the phenomenon of critical Φ is not the main object in the present work.

Besides, an increasing-then-decreasing trend of P_{rms} is found among all cases, that the turning point is mostly around 1.4 to 1.7 of Φ. The key factor behind such phenomenon might be found as the spatial distribution of local heat release along flame. It has been found that both deformation and oscillation of flame (including flame suppression and stretch) due to acoustic wave could result in the inhomogeneity of local Φ and the local heat release rate in flame [40]. Considering the flame is relatively shorter in the range $1.4 < \Phi < 1.7$, the greater gradient of local Φ within the flame can be achieved. Due to the influences from local heat release rate and Φ, the heat release rate fluctuations can be strongly affected and driven by the self-excited pressure oscillation. Thus, the heat release rate fluctuations may become more in-phase with pressure fluctuations, which implies the increasing Rayleigh index [9,58]. As a result, the effect of excitation becomes more intense and leads to a greater oscillation amplitude. It is also found that

the turning point of P_{rms} is slightly prior to the turning point of Φ, that P_{rms} is earlier became less sensitive to Φ than f_{eigen}. It implies the critical roles of Φ in characterising self-excited thermoacoustic oscillations that the system response could be nonlinearly related to Φ. It may also indicate the system response delay between amplitude and frequency.

By comparing the curves of f_{eigen} at different $\dot{m}_{CH_4}$, the importance of fuel flowrate in characterising oscillations can be highlighted. It can be seen that the systems with a higher $\dot{m}_{CH_4}$ generate higher f_{eigen} regardless of burner position change, especially in the Φ-insensitive range. In order to further analyse the system frequency response with varied $\dot{m}_{CH_4}$ in the Φ-insensitive range, the mean stable eigenfrequency ($\bar{f}_{stable}$) is obtained by calculating the mean value of f_{eigen} in the Φ-insensitive range ($\Phi > 2$). The curves of $\bar{f}_{stable}$ to $\dot{m}_{CH_4}$ are plotted in Fig. 5.2 (d). It can be found that $\bar{f}_{stable}$ presents an approximately linear relationship with increasing $\dot{m}_{CH_4}$. Similar gradients of $\bar{f}_{stable}$ trending lines with varied $\dot{m}_{CH_4}$ can be observed from the cases at different burner positions or ID. Overall, considering the situation of larger fuel flowrate, the eigenfrequency increase might be caused by higher total heat release and higher mean temperatures [26]. However, the P_{rms} presents a very small difference with varied fuel flowrates after the turning points. From the cases of 50 mm ID, the nonlinear trends between f_{eigen} and Φ can be also obtained, also the influence of $\dot{m}_{CH_4}$ on both f_{eigen} and P_{rms} are illustrated (e.g. Fig. 5.2 (c)). Besides, the linear relationship between $\dot{m}_{CH_4}$ and $\bar{f}_{stable}$ at different burner positions are obtained (e.g. Fig. 5. 2(d)).

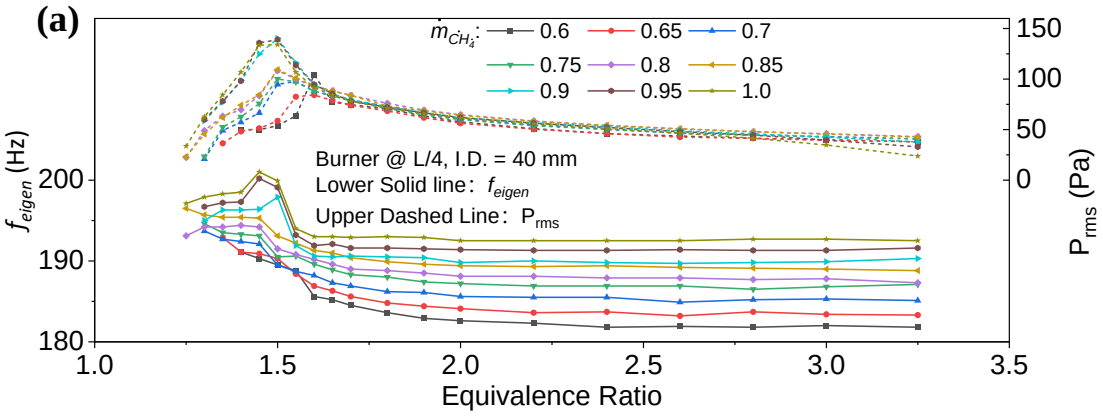

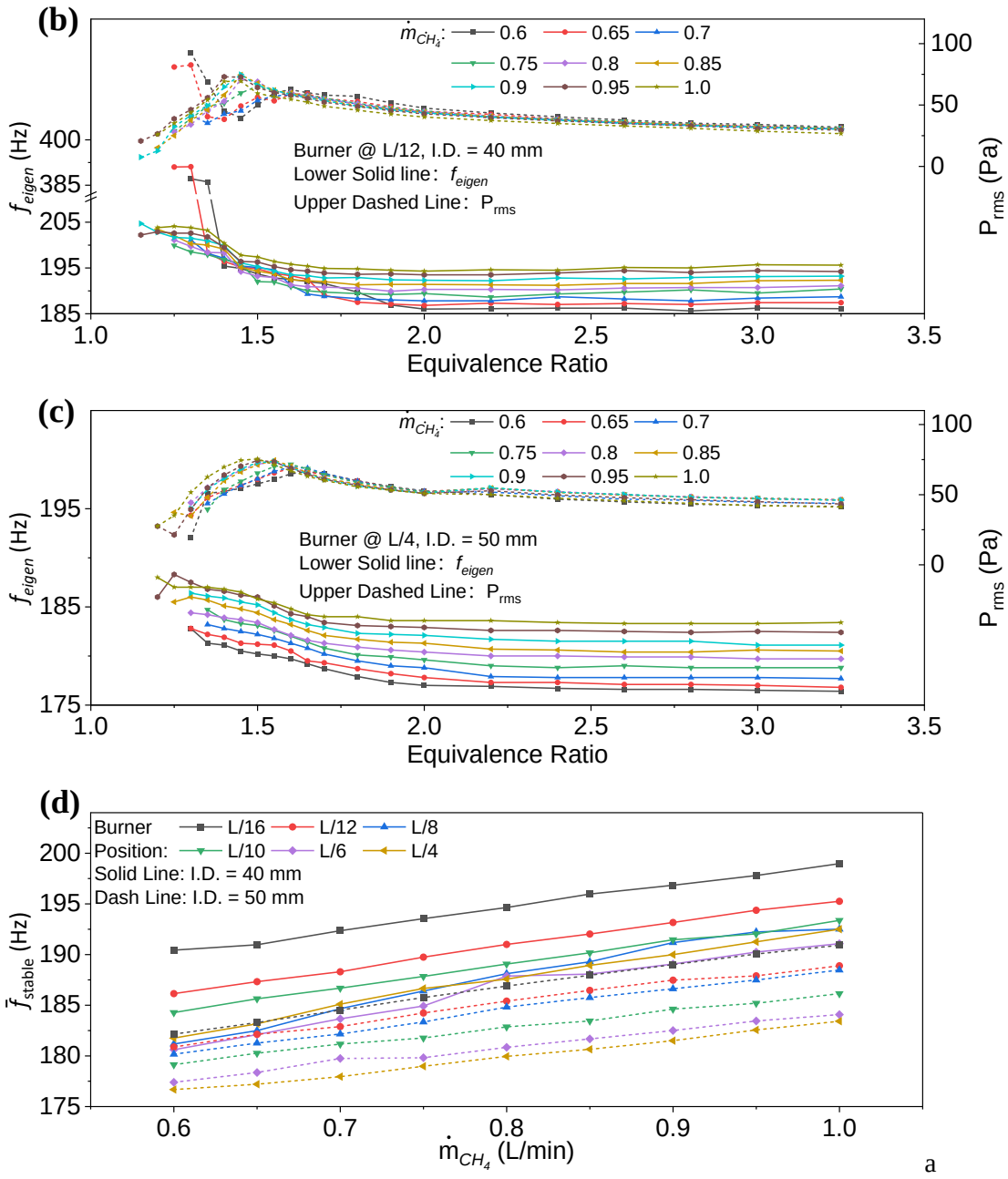

a

Fig. 5.2. f_{eigen} and P_{rms} with various equivalence ratios ($\dot{m}_{CH_4}$ ranged from 0.6 to 1.0 L/min) under the conditions: (a): ID = 40 mm, burner position of L/4; (b): ID = 40 mm, burner position of L/12; (c): ID = 50 mm, burner position of L/4. The corresponding f_{eigen} and P_{rms} are represented by solid lines and dashed lines respectively in figure (a) to (c). Figure (d) represents the $\bar{f}_{stable}$ changes to the $\dot{m}_{CH_4}$ at various burner positions, where the solid and dashed lines denote the 40 mm and 50 mm, respectively.

Fig. 5.3 presents the corresponding system eigenfrequency under various equivalence ratios at different burner positions, demonstrating that f_{eigen} is noticeably affected by burner position across the entire Φ range. Approximate 10 Hz of $\bar{f}_{stable}$ change under

the same $\dot{m}_{CH_4}$ and ID can be obtained when moving burner from L/4 to L/16. Focusing on the changes of $\bar{f}_{stable}$ to burner position, the cases of 40 mm present non-monotonical trends of $\bar{f}_{stable}$ with increasing burner position can be obtained, as shown in Fig. 5.3 (d). Such non-monotonical trends are likely caused by the hydrodynamic region around the flame holder, since similar trends have been theoretically and experimentally discovered by Heckl and Zhao in the Rijke tube [8,27]. However, it is found that the trends are monotonically decreasing in the cases of 50 mm ID. The reason for the monotonical trends in the 50 mm tube might be the less influence from the hydrodynamics region due to the larger ID. It is also found that the burner position could be vital to the changes of dominant mode, as the harmonic modes shifting of eigenfrequencies can be found in some cases, as highlighted in Fig. 5.2 (b), Fig. 5.3 (a) and (c). The second harmonic mode can be the dominant mode (the intensity of the fundamental mode is neglectable) when Φ is closer to 1 and the burner is at lower positions such as L/16 and L/12. Considering the longer region after flame when the burner is moved downward, both effective length and acoustic reflection boundary are changed, which may further lead to the change of instability trait of flame [25]. Meanwhile, higher heat power also leads to the change in oscillation modes [160]. Thus, the shift of dominant harmonic mode can be triggered under such circumstances. For the oscillation amplitude, the important role of burner position also can be discovered from the high dependency of P_{rms} on burner position at a low $\dot{m}_{CH_4}$, as shown in Fig. 5.3 (a) and (c). From the Fig. 5.3 (d), it is found that the increasing rates of $\bar{f}_{stable}$ to $\dot{m}_{CH_4}$ at different burner positions are similar, which means those trends are regardless of burner position change. Meanwhile, similar gradients of $\bar{f}_{stable}$ change with increasing $\dot{m}_{CH_4}$ are found from both 40 and 50 mm cases. Therefore, it can be concluded that the linear relationships between $\dot{m}_{CH_4}$ and $\bar{f}_{stable}$ are independent with both burner position and tube ID.

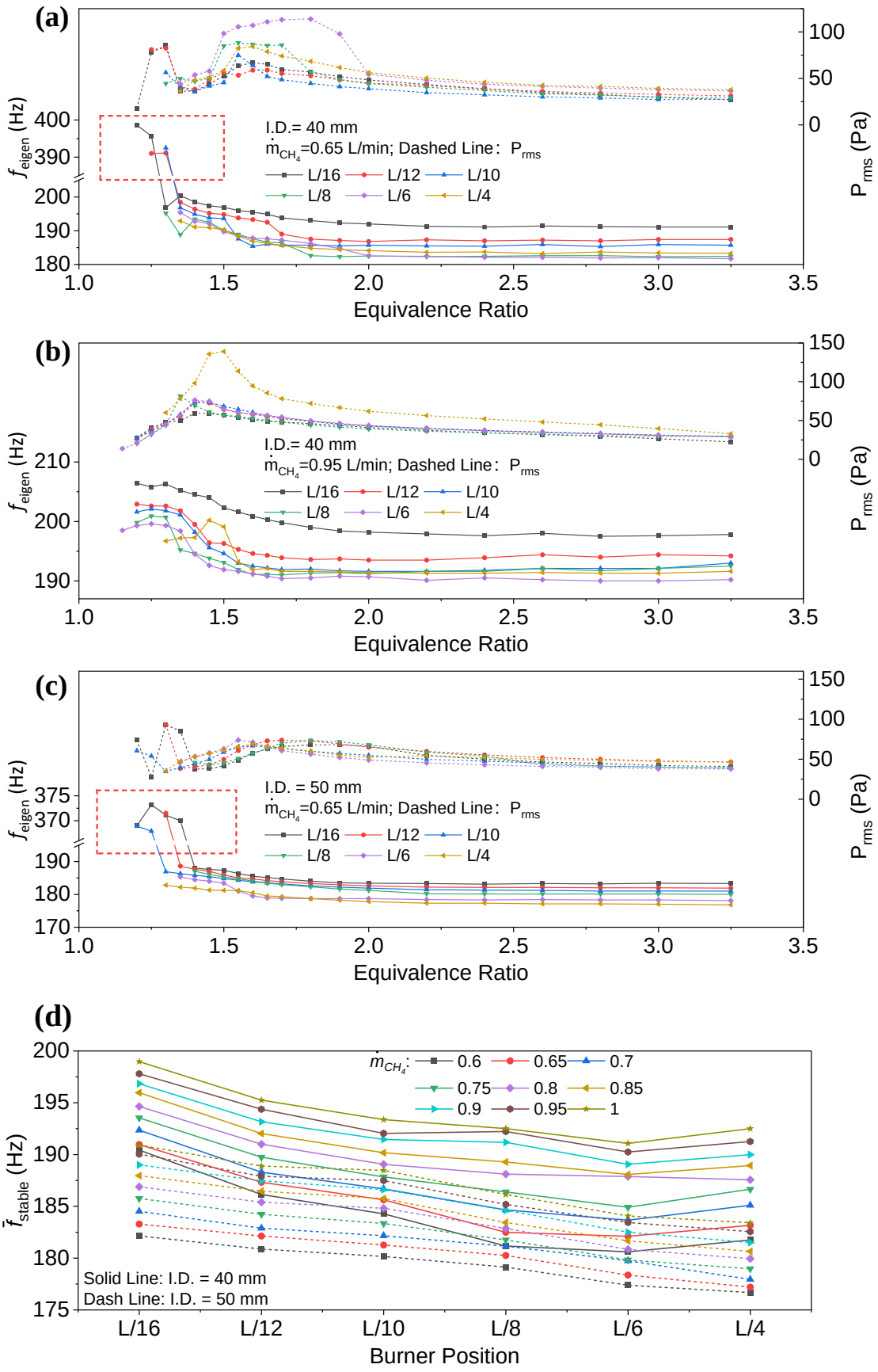

Fig. 5.3 f_{eigen} and P_{rms} to varied equivalence ratios at burner positions from L/4 to L/16 in the system under the condition: (a): ID = 40 mm, $\dot{m}_{CH_4}$ = 0.65 L/min; (b): ID = 40 mm, $\dot{m}_{CH_4}$ = 0.95

L/min; (c): ID = 50 mm, $\dot{m}_{CH_4}$ = 0.65 L/min. The corresponding f_{eigen} and P_{rms} are represented by solid lines and dashed lines respectively in figure (a) to (c). Figure (d) represents the $\bar{f}_{stable}$ changes to the burner positions at various methane flowrates, where the solid and dashed line denote the 40 mm and 50 mm, respectively.

Besides, it can be found that increasing ID can lead to decreasing eigenfrequency, as shown in Fig. 5.2 and Fig. 5.3. For such decreasing trend, it could be caused by the decreased mean sound speed in tube due to lower mean temperature at downstream region in 50 mm tube. Since the input heat remains constant (the heating source remains the same), the mean temperature of the downstream flow is heated into a lower value due to the larger corresponding volume caused by a larger ID. In order to validate such point, a simplified model is developed in the present work. The tube can be generally divided into two regions based on the temperature. The region after flame (downstream, represented by subscript u) is the high temperature region, while the region before flame is low temperature region (upstream, represented by subscript d). Compared to the total length of tube, the flame length is relatively short. Thus, it can be assumed that the effects of acoustic characteristics inside the flame are neglected since the less influence by sound speed changes inside the flame. Note that it is assumed that gases at both upstream and downstream region are homogenous. Considering the sound speed difference due to temperature difference at both regions, the average sound speed, c_{avg}, along the tube can be expressed as:

$$c_{avg} = \frac{L}{t_a} = \frac{L}{\frac{l_u}{c_u}+\frac{l_d}{c_d}}, \quad \textbf{5.10}$$

where L is the length of the organ pipe and $t_a$is the travelling time of acoustic wave. Respectively, l_u and l_d represent the length of the upstream and downstream region. Considering that the heating effect of the flame is mainly in axial direction of fuel jet rather than the radial direction, the temperature near the flame in the radial direction would be relatively lower compared to the temperature in the axial direction after the flame. Due to the lower temperature in radial direction of flame, the flame region is considered as the low temperature region. Then, η can be determined by the ratio of the sum of burner position and flame length to the tube length. Based on η, l_u and l_d can be expressed as:

$$l_u = \eta L, \quad l_d = (1-\eta)L, \tag{5.11}$$

Assuming the gas in tube is ideal, and substituting the l_u, l_d into Eq. 5.10, the expression for c_{avg} based on ideal gas law then can be given as:

$$c_{avg} = \frac{\sqrt{\gamma_u T_u \gamma_d T_d R}}{(1-\eta)\sqrt{\gamma_u T_u} + \eta\sqrt{\gamma_d T_d}}, \tag{5.12}$$

where γ is the adiabatic index, the value is determined based on measured temperature T. R denotes the gas constant. The frequency of standing wave in organ pipe with the consideration of end corrections (e) can be calculated by the following equation:

$$f = \frac{nc}{2(L+\Delta e)}, \tag{5.13}$$

where n represents the mode number. In this analysis, $n = 1$ for fundamental mode. The end correction in the present work is determined by $\Delta e = 0.6 * ID$ for both-end-open tube. Therefore, substituting Eq. 5.12 into Eq. 5.13, the ratio between the frequency in the tube with ID of 40 mm (f_{40}) to 50 mm (f_{50}) can be expressed as:

$$r_{40/50} = \frac{f_{40}}{f_{50}} = \frac{\left(\frac{\sqrt{\gamma_u T_u \gamma_d T_d}}{(1-\eta)\sqrt{\gamma_u T_u} + \eta\sqrt{\gamma_d T_d}}\right)_{40\ mm}}{\left(\frac{\sqrt{\gamma_u T_u \gamma_d T_d}}{(1-\eta)\sqrt{\gamma_u T_u} + \eta\sqrt{\gamma_d T_d}}\right)_{50\ mm}} \times \frac{(L+\Delta e_{50})}{(L+\Delta e_{40})}, \tag{5.14}$$

Based on measured T_u and T_d, the results of $r_{40/50}$ are shown in Fig. 5.4. It can be seen that the results from modelling prediction are in good agreement with the experimental results. The analysis results prove the important roles of average sound speed and mean temperature inside tube in characterising the frequency response of the Rijke tube.

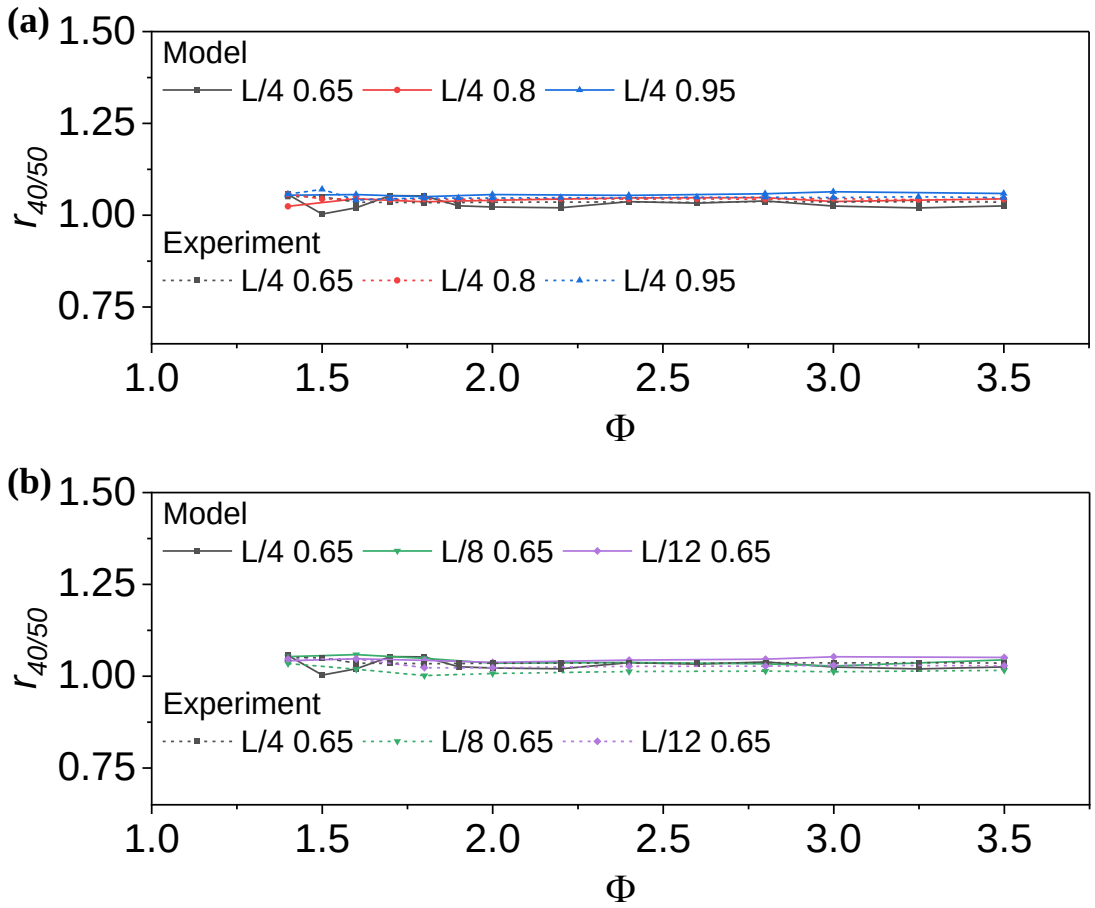

Fig. 5.4 Ratios of eigenfrequencies in ID 40 mm to 50 mm tube with the varied equivalence ratios under (a): $\dot{m}_{CH_4}$, and (b): burner positions. The legend is in the form of: {Burner position, $\dot{m}_{CH_4}$}. The solid lines represent the experimental data of the eigenfrequency ratio, and the dashed lines represent the modelling prediction result based on measured temperatures at both ends of the tube.

The results of system response in both eigenfrequencies and oscillation amplitudes have shown that the system could be generally divided into two ranges based on the sensitivity to Φ. The system appears to be similar in such ranges among all cases. Therefore, for ease of comparison, $\Phi = 1.4$ and 3.0 are specially selected for further analysis and comparisons in most cases.

5.3.2 System properties from Phase space

The 3-dimensional phase space of pressure fluctuations is constructed based on the time-delayed embedding phase space vector [109], $\boldsymbol{P'}_t(3) = \left(p^*(t), p^*(t-\tau), p^*(t-\right.$

$2\tau)\big)$. The time series data of pressure fluctuations $p'(t)$ are normalised based on the maximum value of corresponding time series, thus the trajectories of the oscillations with different amplitudes become comparable. The results of 3-dimensional phase space are shown in Fig. 5.5. It can be seen that the trajectories of periodic oscillation are clearly formed in all cases, and the differences in the 'width' of trajectory can be clearly observed as well. For the trajectory with a 'thinner' width, the system would be more periodic and stable. At the burner positions of L/4, a single-loop trajectory can be observed in all cases, which implies the period-1 oscillation under such conditions. Meanwhile, it also indicates that the oscillation is characterised by a single frequency [22]. The trajectories for the cases at $\Phi = 1.4$ present the 'widest' trajectory regardless of the changes of $\dot{m}_{CH_4}$ when the burner is at L/4. At the same $\dot{m}_{CH_4}$, the 'thinner' trajectories at increased Φ indicate the oscillations with more limit-cycle characteristics. The trajectory 'width' change indicates the more stable and less complex oscillation as the combustion condition become richer when the burner is placed at higher burner positions. For the system in the Φ-insensitive range (Φ =3.0), the changes of $\dot{m}_{CH_4}$ show less influence on the properties of oscillations since the trajectories present barely noticeable change with increasing $\dot{m}_{CH_4}$. While the stableness of the system slightly varies with the increasing $\dot{m}_{CH_4}$ when $\Phi = 1.4$ at the same burner position. However, as the burner is moved lower to L/16, the trajectory become more complex and 'wider' as Φ increases, as shown in Fig. 5.5 (d) and (h). The beating oscillation is triggered for the cases at Φ =3.0 and L/16 of burner position. It can be found that the trajectories of $\Phi = 3.0$ are obviously wider and more complex than $\Phi = 1.4$ cases. Both the trajectories of are 2-tori in the phase space, which implies that oscillations have two incommensurate frequencies [22]. Such properties indicate the quasi-periodic oscillations at $\Phi = 3.0$ and L/16 of burner position. Besides, the oscillations in fuel-rich combustion conditions show lower complexity and stability at a higher burner position (L/4) compared to the cases at a lower burner position (L/16).

$\dot{m}_{CH_4}$=0.65 L/min

I.D. = 40 mm, L/4

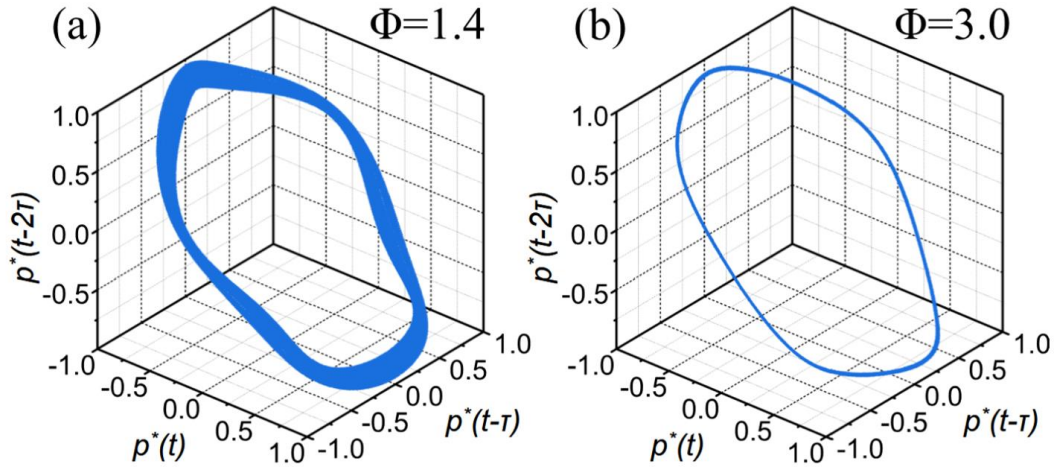

I.D. = 40 mm, L/16

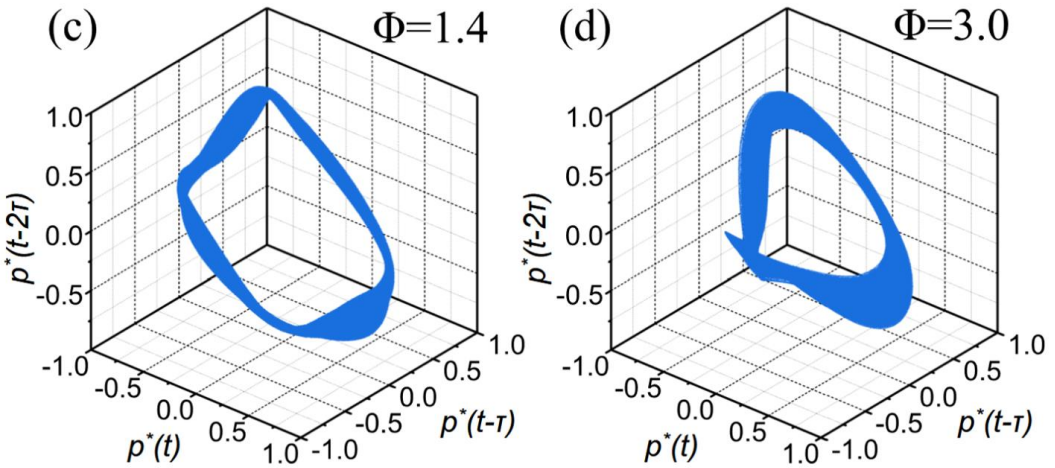

I.D. = 50 mm, L/4

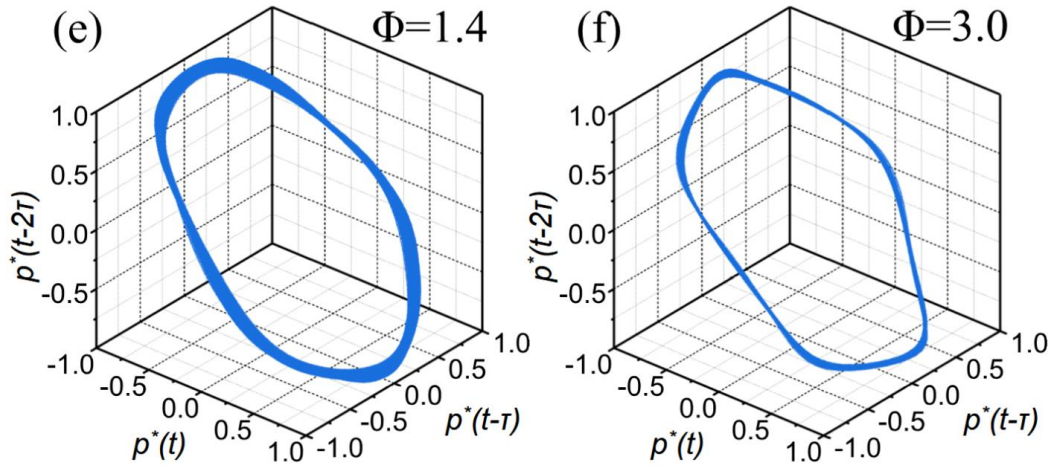

I.D. = 50 mm, L/16

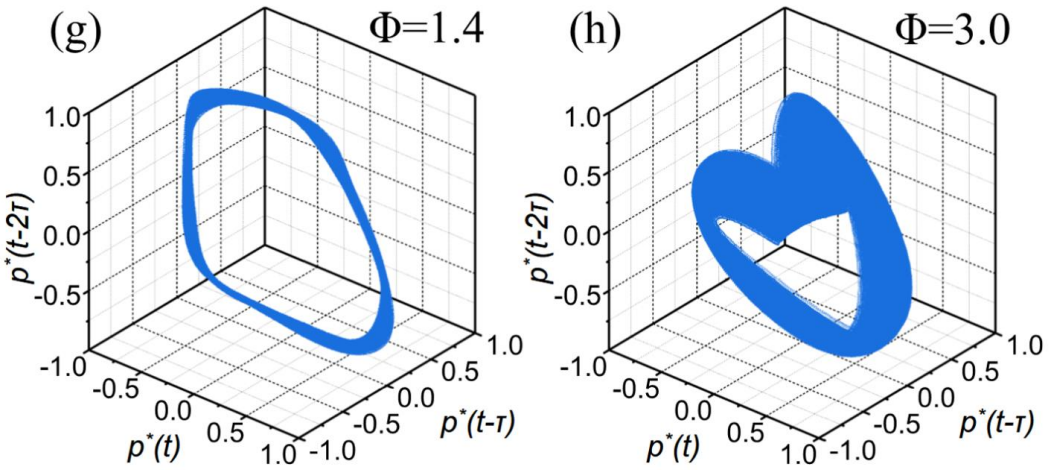

$\dot{m}_{CH_4}$=0.8 L/min

I.D. = 40 mm, L/4

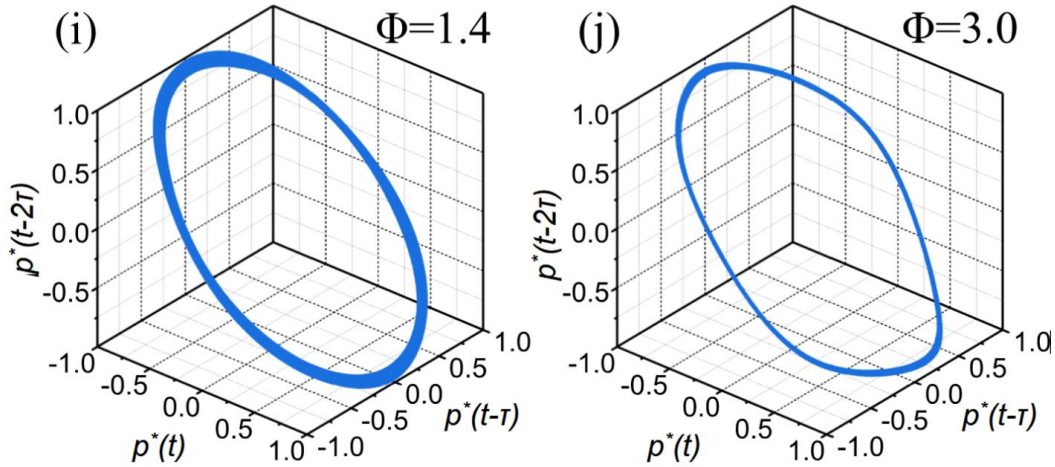

$\dot{m}_{CH_4}$=0.95 L/min

I.D. = 40 mm, L/4

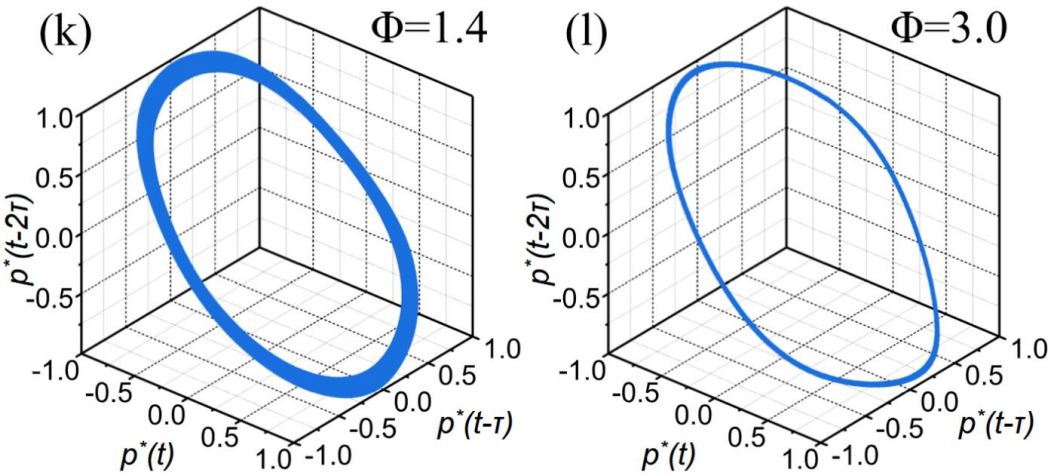

Fig. 5.5 The trajectories the normalised time series data which are reconstructed from the normalised space vectors $(p^*(t), p^*(t-\tau), p^*(t-2\tau))$ in the 3-dimensional phase space under different conditions. ((a)~(h): the $\dot{m}_{CH_4} = 0.65$ L/min; (i), (j): $\dot{m}_{CH_4} = 0.80$ L/min; (k), (l): $\dot{m}_{CH_4} = 0.95$ L/min. The corresponding Φ is shown at the top-right corner of each figure, and the burner positions and ID of the tube are shown on the top of the set of figures.)

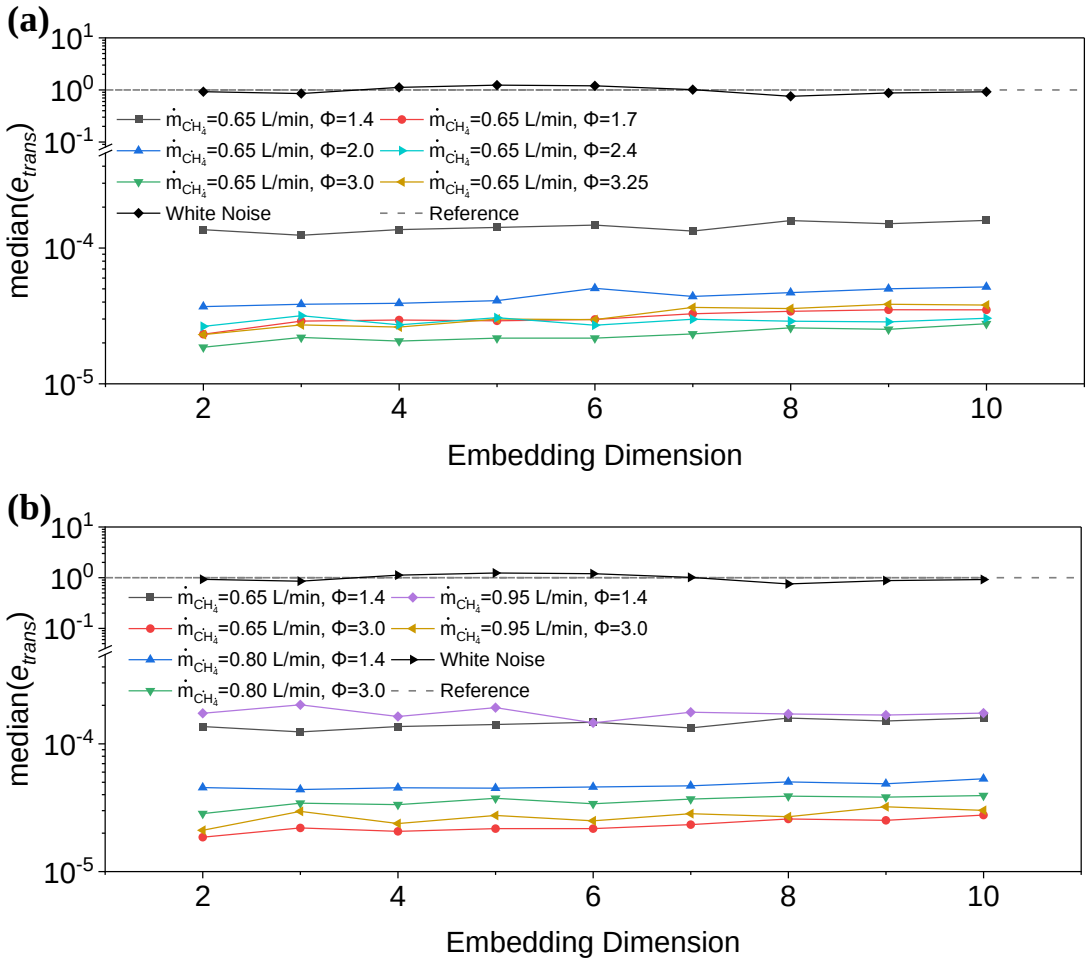

Fig. 5.6 $median(e_{trans})$ and Gaussian white noise to embedding dimension for the time series data of pressure fluctuation at (a) different Φ and (b) $\dot{m}_{CH_4}$, with the K = 100. The dashed line at e_{trans}=1 represents the ideally random process.

In order to further determine the characteristics of system from the results of phase space analysis, the Wayland method is conducted to obtain the e_{trans} of trajectory, as shown in Fig. 5.6 and Fig. 5.7. The e_{trans} slightly increases with the increasing embedding dimensions when the embedding dimension is greater than 3 in most cases. It indicates more parallelism of neighbouring trajectories at lower embedding dimensions in this system [114]. The values of the median e_{trans} of self-excited oscillations are smaller than the gaussian white noise (about 1) and the criterion value

for the deterministic system (0.01), as the order of magnitude is about 10^{-5} to 10^{-2}. This implies that the triggered oscillations can be considered as periodic oscillations and the systems have sufficient deterministic natures. In the cases at ID of 40 mm, it is found that the e_{trans} can be affected by the combustion related parameters since its values range from 10^{-5} to 10^{-4}, as shown in Fig. 5.6. By comparing the cases with the same $\dot{m}_{CH_4}$ as shown in Fig. 5.6 (a), it can be observed that the e_{trans} tends to decrease with the increasing Φ, which indicates the more periodic and less complex oscillation at a higher Φ. While slight changes can be still observed from some cases with increased Φ even in the Φ-insensitive range. The effective role of Φ in system deterministic nature can be highlighted, since the fluctuation of e_{trans} shows that the system states are still slightly varying with Φ, as shown in Fig. 5.6. Meanwhile, it also shows that the Wayland method is more effective to reveal the properties of system, as the frequency response is relatively stable in the Φ-insensitive range, as shown in Fig. 5.2. Considering the special properties of the cases at $\Phi = 1.4$ and 3.0 as discussed above, they are selected to represent the system deterministic natures. Compared to the cases of $\Phi = 3.0$, it can be found that the $\dot{m}_{CH_4}$ is more efficiently influencing the e_{trans} when $\Phi = 1.4$. The e_{trans} of the cases at $\Phi = 1.4$ strongly vary with the increasing $\dot{m}_{CH_4}$ as shown in Fig. 5.6 (b). In contrast, the e_{trans} for the cases of $\Phi = 3.0$ have the similar values with each other without great difference, and the value are smaller than the cases of $\Phi = 1.4$. Therefore, the deterministic nature of system can be more likely affected by $\dot{m}_{CH_4}$ if the system is in the Φ-sensitive range (conditions as lower Φ).

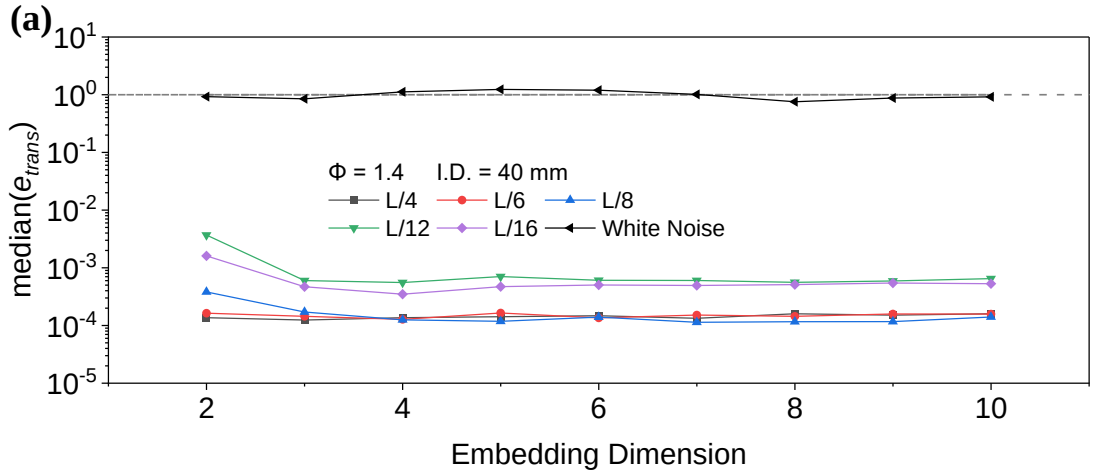

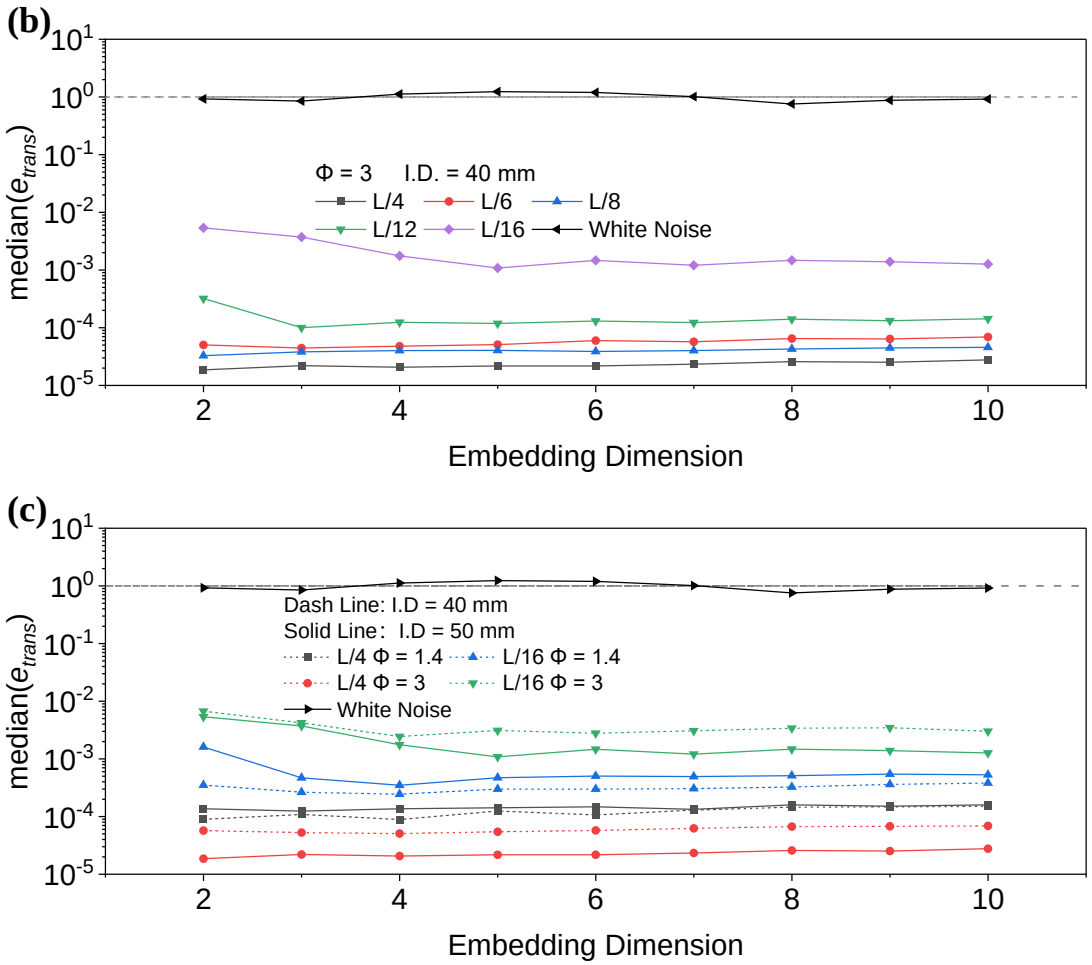

Fig. 5.7 The $median(e_{trans})$ to embedding dimension under different burner positions for the cases with different Φ of (a) Φ = 1.4 and (b) Φ = 3 but the same $\dot{m}_{CH_4}$ of 0.65 L/min. (c) Comparisons between the system with different IDs. K = 100. The dashed line at e_{trans}=1 represents the ideally random process.

From Fig. 5.7, it can be seen that the e_{trans} appears to be more variant with burner position changes, as its values are in larger ranges of 10^{-5} to 10^{-2}. Thus, the burner position can be more effective in influencing system stability and deterministic nature compared to Φ and $\dot{m}_{CH_4}$. Meanwhile, the e_{trans} tends to be more affected by the burner position changes as the burner moves to a lower position. The e_{trans} is found to be higher at a lower burner position (L/12 and L/16) in conditions of $\Phi = 1.4$ and 3.0. The higher value of e_{trans} implies that the system becomes less deterministic and more complex when the burner approaches the lower tube end. It is possibly caused by more complex flow conditions around the flame at the position closer to tube end. The nonlinear oscillation can be more easily affected by external disturbance under this condition, as the effect of flow around the flame has been found to be vital to the

oscillation stability [160]. Under such circumstances, it seems that a lower overall supply flowrate and amount of heat release might increase the sensitivity of the system to flow disturbance around the flame. The cases with higher Φ but the same $\dot{m}_{CH_4}$ can be the examples of the case with lower overall flowrate and heat release. Because the net heat release of the premixed methane flame has been found to be inversely proportional decreasing with the increasing Φ under the same $\dot{m}_{CH_4}$, if Φ is in the investigated range of this study [52,164]. From the experimental results, it can be found that the variation of e_{trans} to the burner position become more apparent when $\Phi = 3.0$ for both cases of ID 40 and 50 mm (in the Φ-insensitive range). By comparing the results between cases of ID 40 and 50 mm, the change of tube ID shows less influence on e_{trans} than burner positions. It can be found that e_{trans} for the cases of 50 mm are greater than cases of 40 mm when $\Phi = 3.0$, while the similar value of e_{trans} are obtained in the cases of $\Phi = 1.4$. Therefore, both the influences of burner position and ID on the system deterministic nature at $\Phi = 3.0$ validate that the decreases in heat release and overall flow rate might enhance the sensitivity of system to the flow conditions around flame. In summary, the quantitative analysis of e_{trans} validate the findings obtained from phase space diagram while providing more insightful information about the system deterministic nature.

5.3.3 Recurrence analysis

The results of phase space analysis show the system with remarkable deterministic natures, high periodicity and the absence of noticeable state transition in most cases. For such stable systems, the pattern of RP can be similar, and the result of RP might not be informative enough for the detailed analysis, as shown in Fig. 5.8 (a), (b) and (c) and (e). Several clear continuous diagonal lines can be observed, which evidences the system with high periodicity and probability of occurrence of similar states. Slight differences between them still can be noticed, that the pattern for high periodic oscillation (Fig. 5.8 (a) and (b)) have less scattered points, and the diagonal lines tend to be more gathered than lower periodic oscillation (Fig. 5.8 (c) and (e)). However, the cases with quasi-periodic oscillation show noticeably different patterns, as shown in Fig. 5.8 (d) and (f). It can be found that the RPs of quasi-periodic oscillation present frequent pattern changes with different densities, which indicates the frequent shift of system state. During the state shifting progress, the discontinuous diagonal lines can be

observed as they are interrupted by the pattern changes due to the state changes. The existence of bowed structures in RP can be found as well, which implies the changing of system dynamics [115].

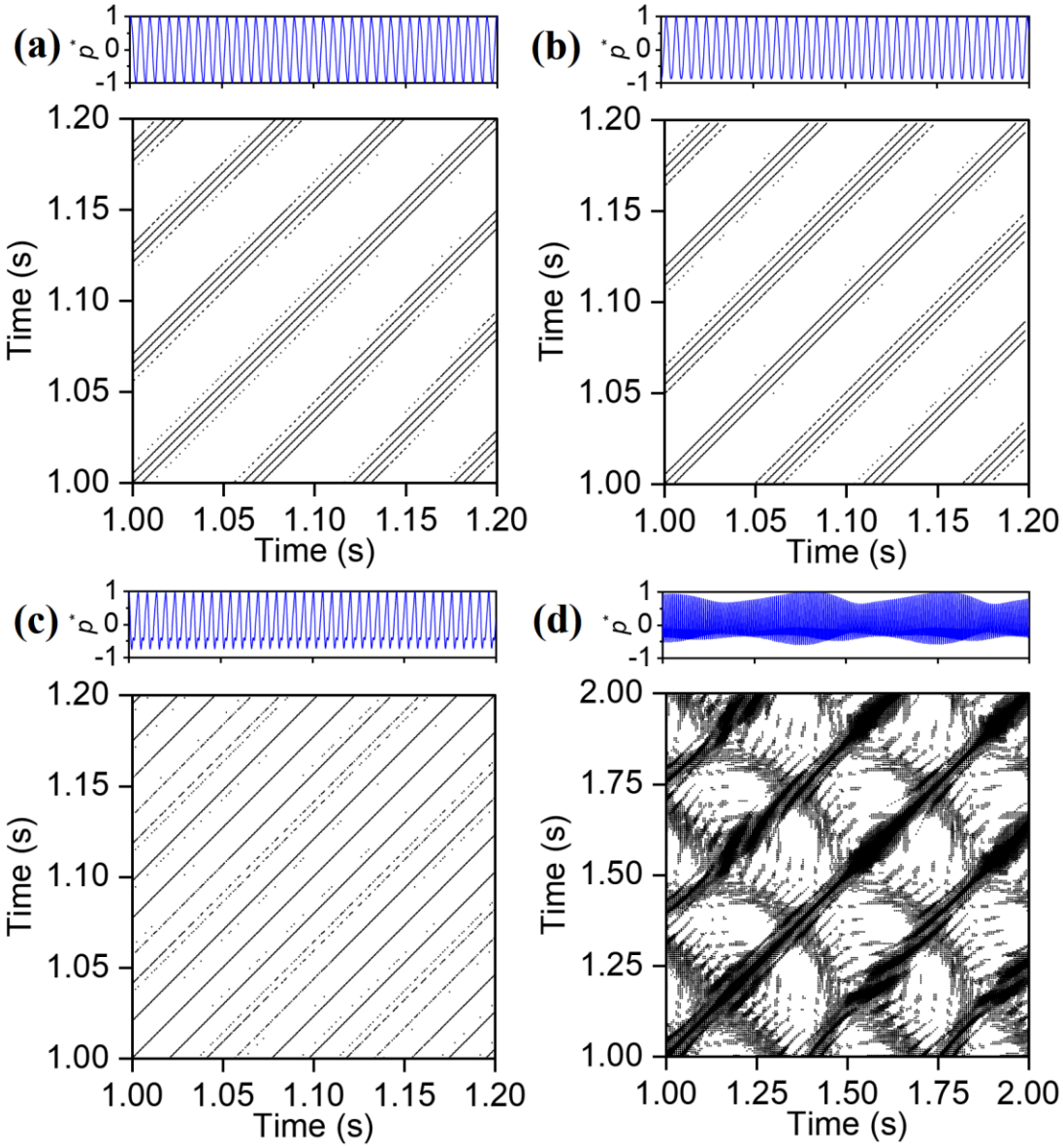

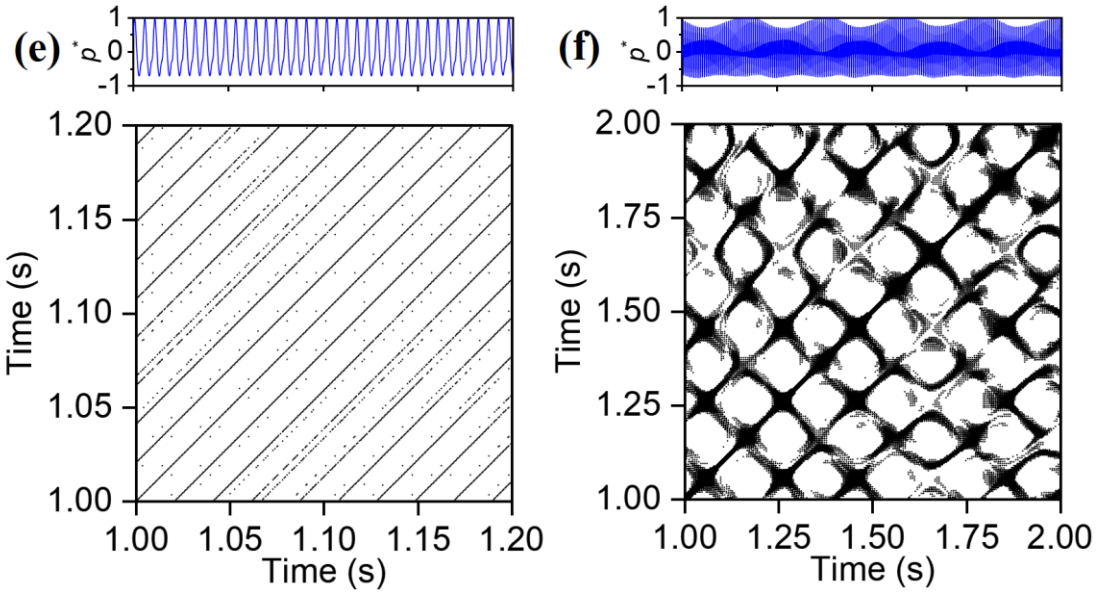

Fig. 5.8 RPs for the cases: (a) ID = 40 mm, L/4, $\dot{m}_{CH_4}$ = 0.65 L/min Φ=1.4; (b) ID = 40 mm, L/4, $\dot{m}_{CH_4}$ = 0.65 L/min, Φ=3.0; (c) ID = 40 mm, L/16, $\dot{m}_{CH_4}$ = 0.65 L/min, Φ=1.4; (d) ID = 40 mm, L/16, $\dot{m}_{CH_4}$ = 0.65 L/min, Φ=3; (e) ID = 50 mm, L/16, $\dot{m}_{CH_4}$ = 0.65 L/min, Φ=1.4; (f) ID = 50 mm, L/16, $\dot{m}_{CH_4}$ = 0.65 L/min, Φ=3; The D = 3 is for all cases, τ is determined based on the first zero-crossing point method, ε = 0.15σ. The time-evolution of pressure fluctuations figures with normalised pressure oscillation amplitude (p) are shown above each RP.*

In order to further discover the recurrence properties of system, RQA is applied to the results of RP to characterise the system nonlinear dynamics quantitatively, as shown in Fig. 5.9.

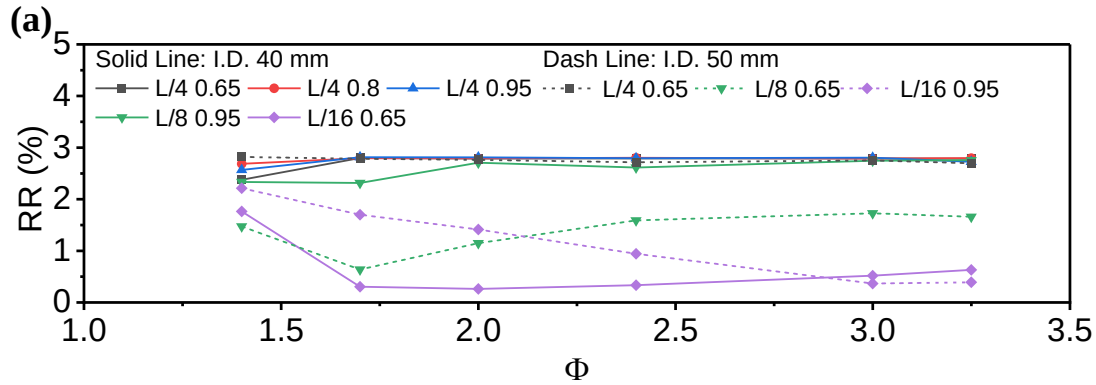

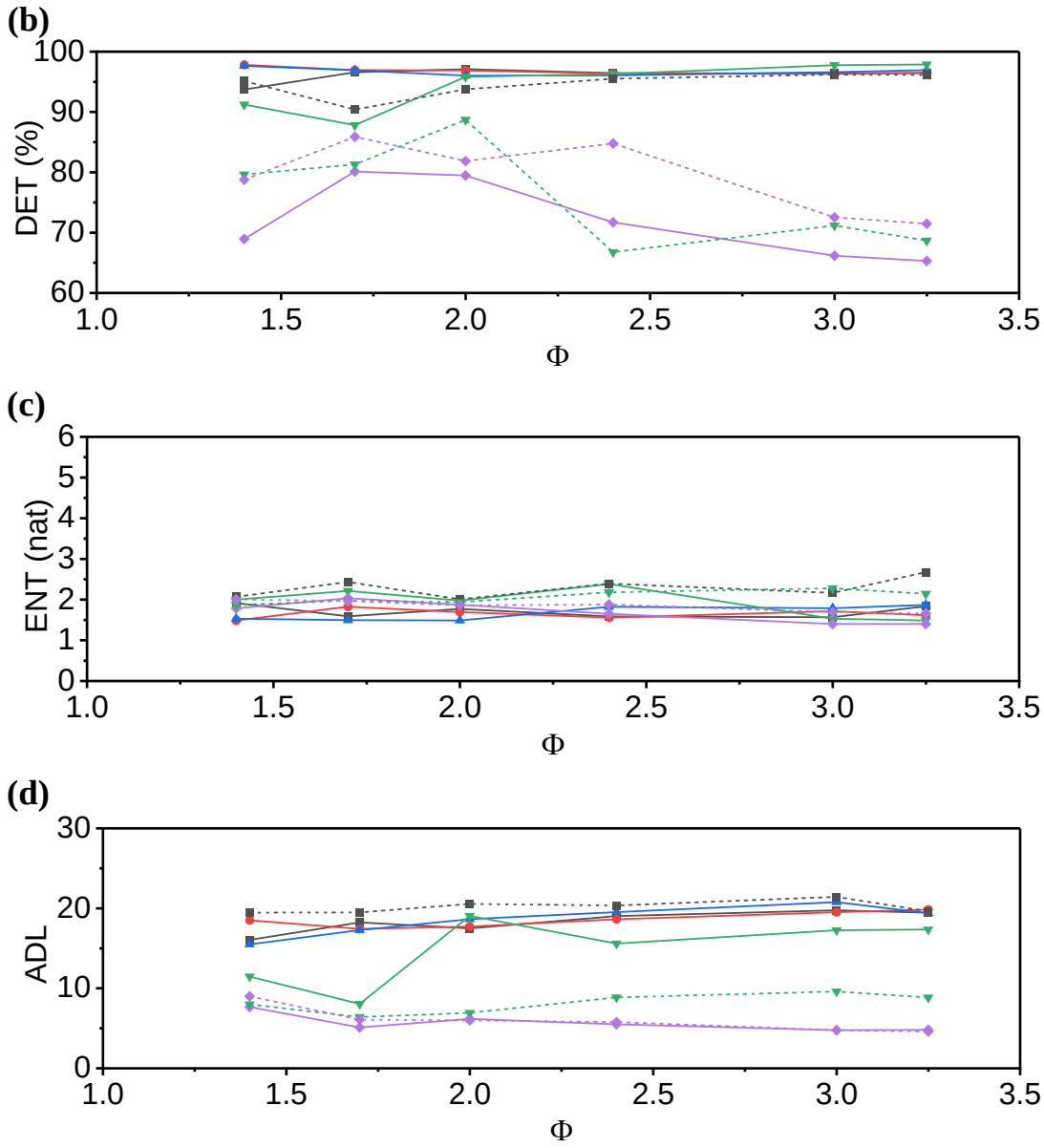

Fig. 5.9 The result of RQA at various Φ, burner positions, $\dot{m}_{CH_4}$, and tube ID The four figures represent (a) Recurrence Rate, (b) Determinism, (c) Shannon Entropy and (d) Average diagonal line length.

For the cases at L/4 of burner position and 40 mm of ID, slight differences of both RR and DET can be obtained when Φ and $\dot{m}_{CH_4}$ are changed. The values of DET for the cases at L/4 and ID 40 mm are found to be greater than 90%, indicating the considerable amount of diagonal structures in RPs [127]. The high value of DET (shown in Fig. 5.9 (b)) validates the finding from phase space analysis, that the system is more deterministic and less complex if the burner is at a higher position. Also, it is found that the values of ENT for the same cases are relatively small, which indicates the neglected chaoticity of system. From Fig. 5.9 (d), it can be seen that the ADL slightly increases

with the increasing Φ, which shows the greater degrees of parallelism of the trajectory in phase space [124]. This trend indicates that the system state at higher Φ tends to be more sustainable with fewer interruptions. The more stable systems at higher Φ might be caused by the weakening flow instabilities due to lower overall flowrates at higher Φ but the same $\dot{m}_{CH_4}$. Thus, the oscillation can be less disturbed by the flow around flame. Under this circumstance, the probability of the system states being interrupted would be less, and the states would be more likely sustained.

The RQA results also validate the results of phase space analysis, that the system dynamics could be more easily affected by burner positions. It can be seen that all these measures become more sensitive to Φ changes when the burner is moved downwards (L/8, L/16) in the ID 40 mm system. The decreases in both RR and DET can be found when the burner is moved from L/4 to L/16. Meanwhile, both RR and DET of the cases at L/16 are significantly lower than those at L/4 and L/8, which indicates a more unstable and complex system at this position, as shown in Fig. 5.9 (a) (b). The results of DET generally conform to the results of e_{trans}, that the systems present considerable periodicity and deterministic nature if the burner is placed above L/8, while the system becomes more complex when the burner is at L/16. The low DET value of approximately 65% at L/16 of burner position implies fewer diagonal structures in RP and less occurrence of similar states. Meanwhile, the state can change more frequently in the system with low DET, such as the quasi-periodic oscillations (beating oscillations in this case). The ADL results show that the segments in trajectory tend to diverge faster at lower burner position. The system state under this condition is more likely interrupted and less sustainable. However, the results of ENT show inapparent differences as the burner moved to a lower position. It implies that significant amounts of diagonal structures still exist in RP, although the system state is interrupted. Thus, the system becomes more complex when the burner is moved to a lower position, but the oscillation is still periodic with neglected chaoticity. The larger RR, DET and ADL at a higher burner position likely result from less disturbance in the region far from the lower tube end. Thus, the state of the nonlinear oscillations is more likely sustaining and has fewer state variations. In addition, RR, DET and ADL show greater sensitivities to the Φ changes at a lower burner position, which also indicates the significant state change due to the complex flow conditions around the lower tube end.

For the RQA results of 50 mm cases, similar findings can be concluded that a lower burner position might result into a system with higher complexity. Besides, by comparing the cases of both 40 and 50 mm ID, it is found that the inner diameter of tube also is able to influence the system dynamics. The system becomes more complex when the tube ID is increased to 50 mm, which is evidenced by a generally higher ENT of the 50 mm cases. In addition, for the cases at lower burner positions (L/8, L/16), the corresponding values of RR and DET also show apparent differences when the ID is changed. It further indicates that the flow condition around flame can be vital for characterising the dynamical properties of thermoacoustic oscillations since the flow condition can be more stable at the deeper position of tube. The influence of ID on the degrees of parallelism is found to be limited, which is implied by the minor changes in ADL values as the ID increases. By comparing the result between 40 and 50 mm ID cases, the results indicate that a more complex system can be generated if the chamber of the Rijke tube has a greater diameter. The experiments with more inner diameters will be conducted to verify such findings. In conclusion, it is proved that the system parameters investigated in the present work are effective for changing the system nonlinear dynamics to varying extents, and the burner position presents a more decisive role in influencing the system.

5.4 Chapter Summary

In this chapter, the present study focused on the impact of various system parameters on self-excited thermoacoustic oscillations in a Rijke tube. Analysis of oscillation amplitude, system frequency response, and the system dynamical properties revealed significant influences of these parameters. The study validated both Φ-independence and Φ-dependence ranges as discussed in Chapter 4. A quasi-linear relationship between fuel flowrate and mean stable eigenfrequency was observed in the Φ-insensitive range, regardless of parameter changes. Eigenfrequencies were inversely proportional to burner positions and tube inner diameter, with the changes in temperature and mean acoustic speed being the main reason for changes in eigenfrequency when tube diameter changes. Increasing equivalence ratio led to a more deterministic system with reduced complexity, except when quasi-periodic oscillations were triggered. Burner position significantly impacted system dynamics, resulting in

more complexity and instability at lower positions, with increased sensitivity to equivalence ratio changes. The study emphasised the critical roles of these parameters in influencing thermoacoustic oscillations and highlighted the effectiveness of analysis methods in understanding system behaviour.

Chapter 6 Experimental investigation on the effects of the mesh at the downstream region

6.1 Introduction

Thermoacoustic instabilities initiated by unstable combustion constitute a major concern in various combustion systems due to their negative influences to the combustion system. It has been found that the thermoacoustic could be triggered in both fuel lean and rich conditions with different types of fuel [8,26,52,114,165]. The presence of thermoacoustic oscillation in the combustion system could potentially result in low combustion efficiency and structural damage. Therefore, the understanding of thermoacoustic instabilities could be vital for the development of various combustion systems.

Rayleigh has revealed the trigger mechanism of the thermoacoustic oscillation: the oscillation would be triggered when the heat release fluctuations are in phase with pressure fluctuations in the time-domain [9]. The oscillation generated by the coupling effect could have both linear and nonlinear characteristics depending on the development of the system [18,157]. The fully developed system would have the nonlinear characteristics of limit-cycle oscillation [17,166], quasi-periodicity and intermittency [155]. Thus, the study related to the self-sustain thermoacoustic oscillation mainly focuses on the release and transfer of heat in the system, and the acoustic properties of the resonance chamber. In a combustion system, the unsteady heat release is mainly generated by the perturbations of the flame area and is considered as the primary source to trigger acoustic radiation [86,167]. Several studies have investigated the effects of the parameters related to the combustion and flame dynamics on characterising the self-sustain oscillation. The equivalence ratio and the flow

conditions have been discovered to be able to affect the eigenfrequency, oscillation mode and stability of the system [26,52,95,145,158,167]. It has been found that the system could transit from the periodic mode to the quasi-periodic mode under specific equivalence ratios and overall heat power [52,98]. Some studies have investigated the effect of inhomogeneous spatial distribution of local equivalence ratio and its fluctuation in a thermoacoustic system [40,88]. It has been found that the local equivalence ratio could be affected by the flame responding to acoustic waves and the fuel flowrate. The fluctuations and inhomogeneity could hence lead to the variation of heat release and changes in the flame dynamics [168]. Meanwhile, the vital role of the air split ratio and the flow around the flame has been highlighted in characterising both system response and oscillation amplitude [160,169]. For a Rijke tube system with a flame holder, some studies focused on the effect of hydrodynamic region, which is around the flame holder, on the system response [8,27]. The effect of flame position, the upstream and downstream temperature and tube diameter on the oscillation behaviour have been theoretically and experimentally verified through the hydrodynamic region theory.

Currently, the majority of the controlling methods for thermoacoustic instabilities are passive control with the consideration of reliability and cost [167]. The passive control method is mainly achieved by modifying the system parameters that could influence the heat release or acoustic properties. Perforated plate structures have been found to be effective in mitigating thermoacoustic instabilities by attenuating the acoustic wave when the plate was placed at upstream in the combustion chambers [167,170–172]. The mitigating effect is contributed by the generating of vortices at the orifices edge of the perforated plate, because of the acoustic impedance provided by vortices and the dissipation of the acoustic energy [173,174]. The decrease of the eigenfrequencies was observed when the plate was equipped. The changes in Rayleigh conductivity of the perforated plate can be achieved by changing the perforated hole diameter and the distance between each hole. It has been found that the change in Rayleigh conductivity is related to the attenuation effect on both the oscillation amplitude and frequency response. It has also been reported that the acoustic damping effect of the plate with compact holes would become stronger for mitigating high-pressure oscillation [171]. Besides, the perforated liner placed at the downstream region of the system can effectively control and suppress thermoacoustic oscillation [175–178]. The bias flow

can significantly increase the absorption coefficient of perforated liner and acoustic resistance, which further leads to a greater suppression effect [176,178].

The characteristics of self-excited nonlinear thermoacoustic oscillation can be varied with time and present different system behaviours, such as the shift of dominant mode, quasi-periodic oscillation, route to chaos and the bifurcations [17,18,22,106,145,179]. The analysis of the nonlinear system dynamics can be adequate for providing the understanding of the system behaviour. Recurrence analysis for the system state is a direct and efficient way to study the nonlinear dynamics of unstable combustion [26,105,145]. The dynamical properties of the system, such as system state variation and periodicity, can be intuitively indicated by identifying the structural properties in the recurrence plot (RP) [115]. The recurrence quantification analysis (RQA) can further quantify the system dynamics through statistical measures of the structural properties in the RP.

Many studies have extensively investigated the effect of perforated structure on attenuating thermoacoustic oscillation in the combustion system. While the attenuation effect on the eigenfrequency, oscillation amplitude and system dynamical properties by placing the perforated plate at the downstream region of the flame remains insufficient. It has been found that the downstream heat and flow condition could affect the system behaviour [8,176]. Besides, the perforate-like structures at the downstream region of the gas turbine combustor can be found in most gas turbine engines, such structures include the diffuser and nozzle guide vane prior to the turbine. Meanwhile, as another type of common perforated structure to provide flow conditioning, the woven mesh has not been utilised to control the thermoacoustic instabilities and its effect on acoustic attenuation is less focused on in the combustion system. It has been found that the woven mesh could result in acoustic pressure losses [180]. Therefore, this study aims to investigate the effect of woven mesh on suppressing and characterising the thermoacoustic oscillation in a Rijke tube. The effects of woven mesh with different mesh numbers and positions were investigated. A synchronised system consisting of a short wavelength infrared (SWIR) camera and pressure field microphones was utilised to obtain the synchronised data of the mesh temperature and the pressure fluctuation. A long wavelength infrared (LWIR) camera was applied to obtain the temperature

distribution of the tube surface. And a high-speed schlieren imaging system was utilised to investigate the heat and flow conditions above the mesh.

6.2 Experimental and data processing method

6.2.1 Experimental setup

In the present work, a vertically placed Rijke tube with an open-ends tube was utilised to trigger the thermoacoustic oscillation. The schematic figure for the experiment setup is shown in Fig. 6.1. The tube was made of quartz with a length of 1 m and an inner diameter of 40 mm. The heating element was in a form of premixed methane-air flame with different equivalence ratios (Φ) ranges from 1.4 to 2.2 with a step of 0.2. The burner with a honeycomb flame holder was placed at the lower quarter of the tube (L/4). The height of the burner was measured from the bottom end to the top of the flame holder. The honeycomb flame holder with a blockage ratio of 22% was fixed at the top of the nozzle. It has been found that the critical blockage ratio that can affect the thermoacoustic oscillation is 25% [128], which means the honeycomb flame holder applied in the present work has negligible effect on the oscillation. A piezo spark igniter was utilised to ignite the flame by generating a single spark. Once the flame was ignited, a stabilisation time of 3 minutes was applied to ensure the oscillation was fully developed. The different Φ were obtained by changing the air flow rate while keeping the methane flow rate ($\dot{m}_{CH_4}$) the same. The air and methane gases were controlled by Aalborg GFC17 flow controller with the accuracy of 0.05% for methane and 0.1% for air. The $\dot{m}_{CH_4}$ in the present work was 0.8 L/min and the corresponding air flow rate was determined based on the required Φ. The experiments also were conducted under the $\dot{m}_{CH_4}$ of 0.65 and 0.95 L/min to confirm the findings that were obtained from the present work.

Three different stainless steel (304L) meshes with different mesh numbers of 10, 20 and 30 (Mesh 10, Mesh 20 and Mesh 30) were investigated in the present work. The specifications of meshes utilised in the present work are shown in Table 6.1. The mesh position was determined from the tube top end to the position of mesh. The mesh was

placed at L/4, L/6, L/8, L/12 and at the top end of tube, to determine the influence of mesh position on the system behaviours.

A pressure-field microphone unit (model PCB 377C10 with a preamplifier PCB 426B03) was utilised to measure the pressure fluctuation time series at a sampling rate of 100,000 Hz. The unit was placed at the lower end of the tube to ensure that 1) the ambient temperature does not exceed the maximum operating temperature, and 2) the diaphragm of the microphone is perpendicular to the direction of pressure oscillation. Before every experiment, the microphone was calibrated against a signal of 10 Pa in amplitude at 1000 Hz. The microphone was connected to NI-9205 Voltage input module, which was connected to the Chassis cDAQ-9178.

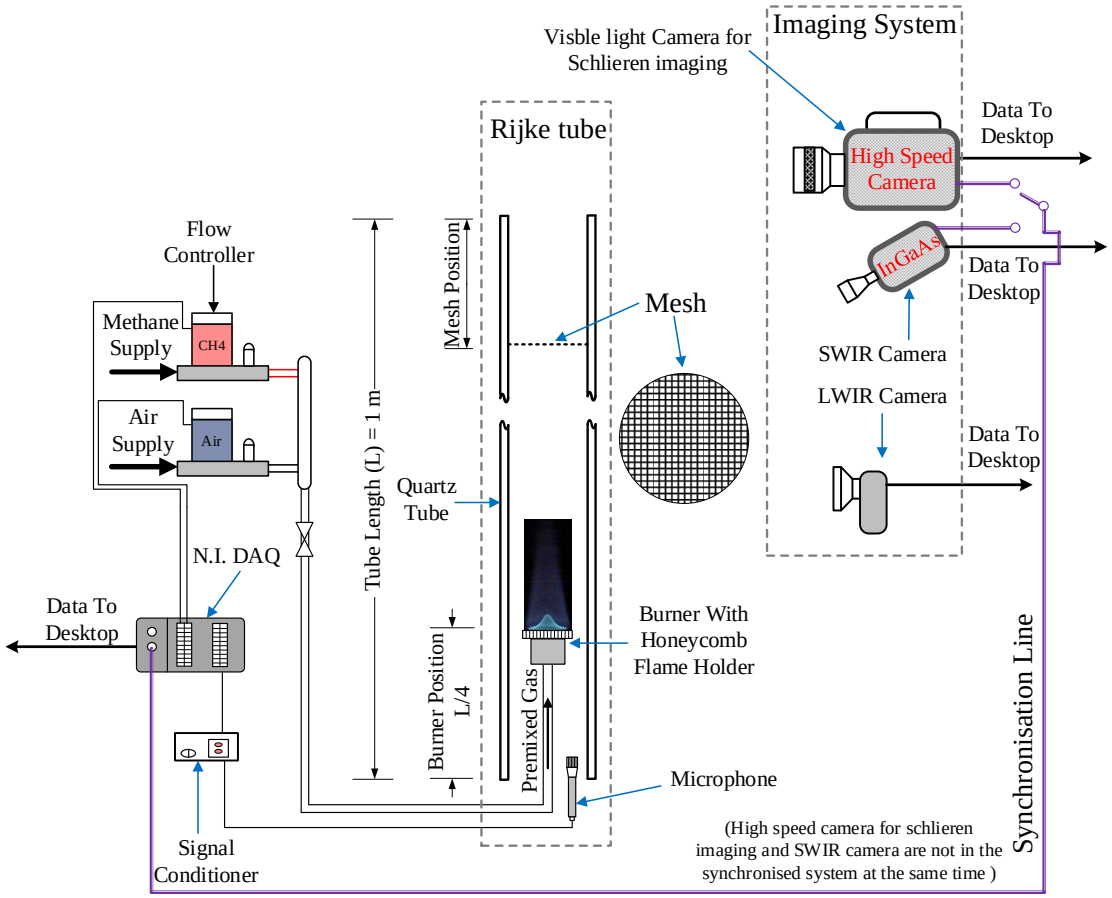

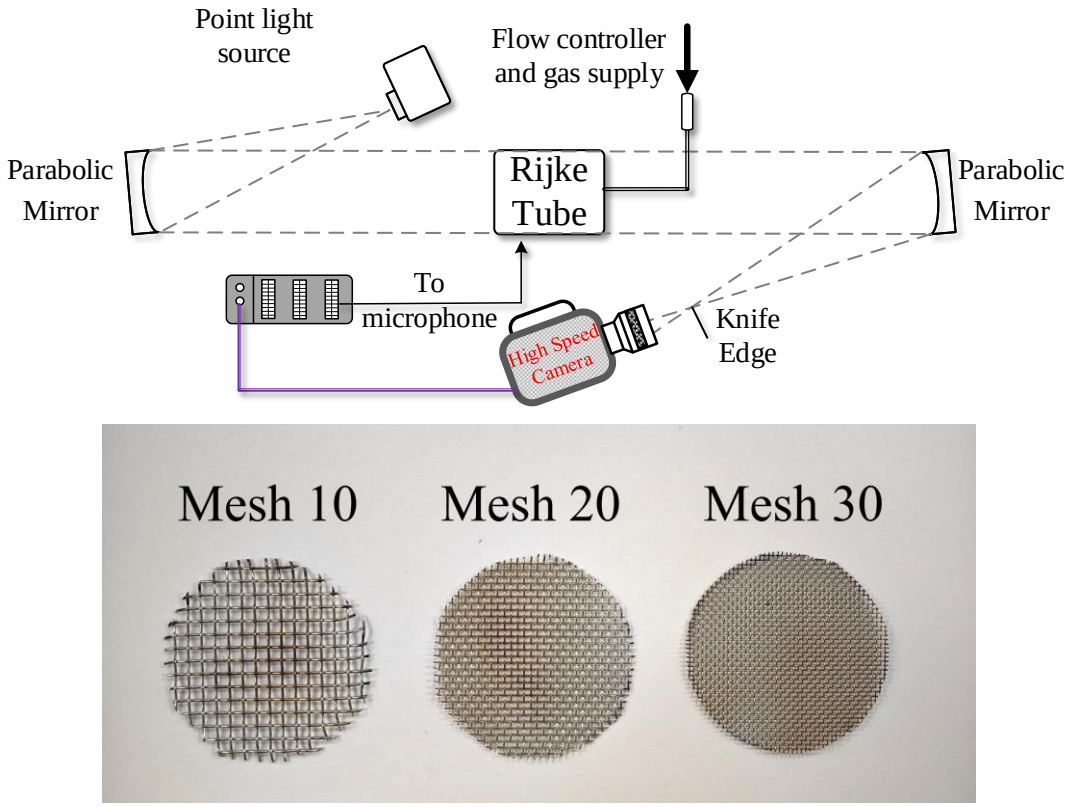

Fig. 6.1. Schematic figure of the experiment setup, data acquisition system and photo of mesh.

Table 6.1. Specifications of the meshes utilised in the present work.

Mesh Number	10	20	30
Nominal Aperture (mm)	1.98	0.915	0.567
Wire Diameter (mm)	0.56	0.355	0.28
Open Area	61%	52%	45%

The imaging systems in the present work consisted of a thermal imaging system and a schlieren imaging system. The thermal imaging system consisted of a Hamamatsu C12741-03 InGaAs SWIR camera, and a PyrOptik LWIR camera (model LW160). The SWIR camera was implemented to obtain the temperature of the mesh at a frame rate of 60 frames per second (FPS), whereas the FWIR camera was for obtaining the distribution of the tube wall temperature. The Photron FASTCAM SA-4 high speed camera was utilised in the schlieren imaging system to capture the schlieren image for investigating the heat and flow conditions at the top tube end under the self-excited thermoacoustic oscillation. The SWIR camera was synchronised with the microphone

and the thermocouples through the synchronising port on the Chassis cDAQ-9178. The schlieren imaging system was also synchronised with the microphone unit in the same way.

6.2.2 IR camera calibration and image processing

The InGaAs SWIR camera enables to capture 60 frames per second (fps) utilising the 2048 x 2048 pixels full sensor, which is ideal for monitoring the fluctuation of the mesh temperature temporally. A bandpass filter was utilised to restrict the spectral sensitivity in the range of 1490 nm – 1500 nm obtaining an accurate temperature reading from 300 ℃ to 700 ℃. A 100 mm prime lens with macro focusing was mounted with the camera, the optical aperture was fixed as f/4. The radiance calibration was based on Planck's Law, the procedure was similar to the work of Lai et al. [181,182]. 100 images were captured and averaged with a blackbody furnace (emissivity ~ 0.99) between 300 ℃ and 700 ℃, at increments of 50 ℃. The offset from zero digital-logic-levels, under unilluminated conditions, was determined by averaging 100 images with lens covered. The calibrated radiance temperature is shown in Fig. 6.2 (a) with the residuals. It is found the uncertainties were limited, which were under 1% in Kelvin. The mesh was made of polished stainless steel, type 304, and the reported emissivity can vary in the range of 0.2-0.35 [183]. Considering the high-temperature and air entrainment conditions inside the tube, we determined the emissivity of the mesh as the fixed value as 0.3. The transmission of the tube was measured at different temperatures, which was 92.91% on average. The transmission loss has been calculated as a correction of the measured temperature.

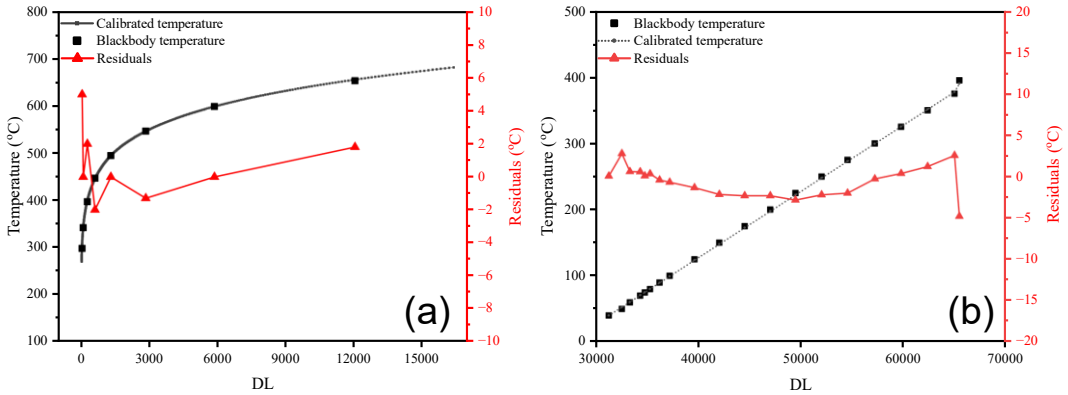

Fig. 6.2. Radiance calibration curve and uncertainty of measured temperature. (a): InGaAs SWIR camera and (b): Lepton LWIR camera.

The LWIR camera is sensitive to 8 μm – 14 μm allowing to the low-temperature objectives. The camera has a 640 x 512 pixels resolution, and the frame rate was fixed at 9 fps. 100 images were captured and averaged to obtain the camera signal (DL) using a blackbody furnace (emissivity ~ 0.99) in the range of 50 ℃ to 400 ℃. Fig. 6.2 (b) shows the calibration curve and measured uncertainty (red line). The fitted curve showed a good agreement with the blackbody temperature (R^2 = 0.9989). The maximum residual was found under 5 ℃ within this temperature range which provided adequate performance for the tube surface temperature monitoring. The tube was made of quartz glass, whose emissivity has been reported as 0.93 [184]. The digital level captured by the LWIR camera was corrected based on the emissivity before any calculation.

The raw image of the mesh was then processed to obtain the temperature of the mesh and eliminate the background signal at the position of the mesh holes at the same time. A series of imaging processing methods, including thresholding, rescaling for contrast enhancement, and binarisation based on the adaptive threshold were applied to extract the portions of mesh wires in the region of interest (ROI). An example is shown in Fig. 6.3.

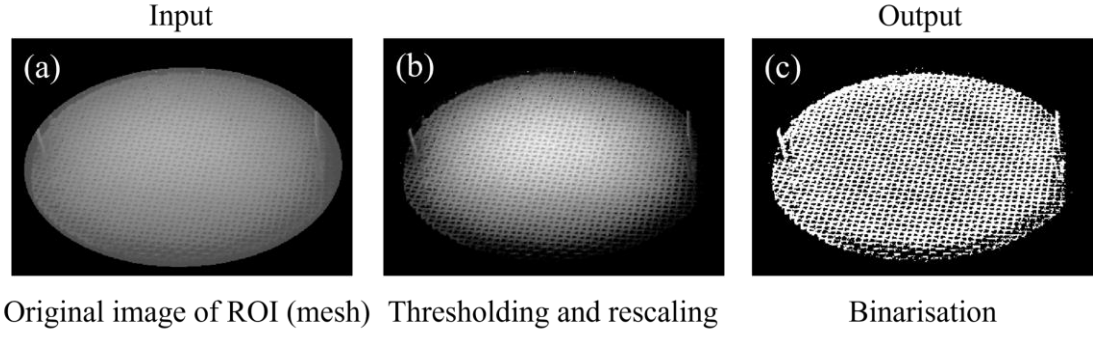

Fig. 6.3. An example of imaging processing for extracting the portions of mesh wires.

The mean mesh temperature (T_{mesh}^{mean}) was obtained from the ratio of local temperature to the area of the mesh wire in order to eliminate the nonuniformity of the temperature distribution, which can be expressed as below:

$$T_{mesh}^{mean} = \frac{\sum T_{local}}{N_{pixel}}, \quad \textbf{6.1}$$

where T_{local} denotes the local temperature of the mesh at the pixel, which is considered as the mesh wire, as shown in the white pixel in Fig. 6.3 (c). N_{pixel} is the total number of the corresponding pixels.

6.2.3 Recurrence analysis

The change and recursiveness of system states can be a crucial characteristic for describing the behaviour of a complex dynamical system since the system state can be varied with time. The Recurrence plot (RP) can intuitively indicate the state changes and dynamics properties from the phase space by the structural properties of the plot. And it is applicable for the investigation of the self-excited and external-forced thermoacoustic instabilities through the aspects of system dynamics [105,124,145,148]. In the present work, the space vector of the trajectory in the phase space was obtained based on Takens' theorem [109]. For the discrete time series of pressure fluctuations ($p(t)$), it can be expressed in the following form:

$$\mathbf{x}_{\mathrm{t}}(\mathrm{D}) = \big(p(t), p(t-\tau), p(t-2\tau), \cdots, p(t-(D-1)\tau)\big), \qquad \textbf{6.2}$$

where $\mathbf{x}_{\mathrm{t}}(\mathrm{D})$ is the space vector at time t with an embedding dimension of D, τ is the time-delay. In the present work, τ was determined based on the first zero-crossing point from the autocorrelation functions since the system generally presented relatively high periodicity and low complexity. Based on the $\mathbf{x}_{\mathrm{t}}(\mathrm{D})$, the lag-constructed RP can be generated by obtaining the recurrence matrix, **R**. **R** is a binary matrix which is defined as following form:

$$\boldsymbol{R}_{i,j} = \Theta\big(\varepsilon - \|\boldsymbol{x}_i - \boldsymbol{x}_j\|\big) \quad i,j = 1,2,3,\cdots,N, \qquad \textbf{6.3}$$

where $\boldsymbol{x}_i$ and $\boldsymbol{x}_j$ are the $\mathbf{x}_{\mathrm{t}}(\mathrm{D})$ that at $t = i, j$, respectively. $\|\boldsymbol{x}_i - \boldsymbol{x}_j\|$ is the norm of the difference between $\boldsymbol{x}_i$ and $\boldsymbol{x}_j$. Θ is the Heaviside function. ε is the predefined threshold to determine whether two points on the trajectory can be considered recurrent, and was set to 15% of the standard deviation of the pressure fluctuations time series [123]. A down-sampling process was performed to meet the suggested data points per period of 8 to 10 points for the distinguishable DET results [105]. D was set as 3 for all cases according to the results of the false nearest neighbours (FNN) method [115,145].

In order to quantify the system dynamics through the structural properties in the RP, the recurrence quantification analysis (RQA) was then conducted to obtain the statistical measurements of the RP. The statistical measures of diagonal structures can efficiently indicate the stability of the system state and its complexity. In the present work, the measurements based on the diagonal structures, including determinism (DET), Shannon Entropy (ENT), and the average diagonal line length (ADL), were applied to investigate the effects of the mesh on the system dynamics. DET is defined as the ratio of the recurrence points which forms the diagonal line to all the recurrence points. It can indicate the occurrence probability of similar system states for the system. The ADL provides the degree of parallelism for the system since it can show the diverging rate of the two segments in the trajectory. For the complexity of the RP in respect of diagonal structures, ENT enables the quantitative measurement of system complexity. DET, ENT and ADL can be calculated from:

$$DET = \frac{\sum_{l=l_{min}}^{N} lP(l)}{\sum_{l=1}^{N} lP(l)}, \quad \textbf{6.4}$$

$$ADL = \frac{\sum_{l=l_{min}}^{N} lP(l)}{\sum_{l=min}^{N} P(l)}, \quad \textbf{6.5}$$

$$ENT = -\sum_{l=l_{min}}^{N} p(l) ln p(l), \quad \textbf{6.6}$$

where N represents the number of points for recurrence analysis. l denotes the diagonal line with the length of l. l_{min} is the defined minimum diagonal line length, of which the value was set to 2 in the present work. $P(l)$ is the histogram of the diagonal line with the exact length of l. Based on $P(l)$, the probability of appearance for the diagonal line with a length of l, $p(l)$, can be defined as $p(l) = P(l)/N_l$, where N_l is the number of diagonal lines.

6.3 Results and discussion

6.3.1 System response

- Frequency and amplitude

In order to investigate the effect of mesh properties on the system response in respect of oscillation frequency and amplitude, the self-excited thermoacoustic oscillation was triggered under different mesh positions and mesh numbers. The system responses under different mesh positions and numbers are shown in Fig. 6.4. Both f_{eigen} and p_{rms} present similar trends to the increasing Φ can be observed for all cases. In detail, the f_{eigen} generally decreases with increasing Φ and tends to be less varied with Φ when Φ >1.8 for most cases, while the p_{rms} presents a trend of increase then decrease. The turning point of p_{rms} locates at Φ = 1.6 for most cases. The trends of f_{eigen} and p_{rms} show that the effect of Φ on system response is regardless of both mesh position and mesh number. It has been reported that heat release and mean temperature play important roles in the system eigenfrequency [26]. Meanwhile, the Rayleigh Index suggests that the oscillation amplitude is related to the relative phase between the heat release and the pressure fluctuation [131]. Thus, the results indicate that the existence of mesh has limited effects on influencing the relative heat release changes with respect to value and phase caused by the changes in Φ.

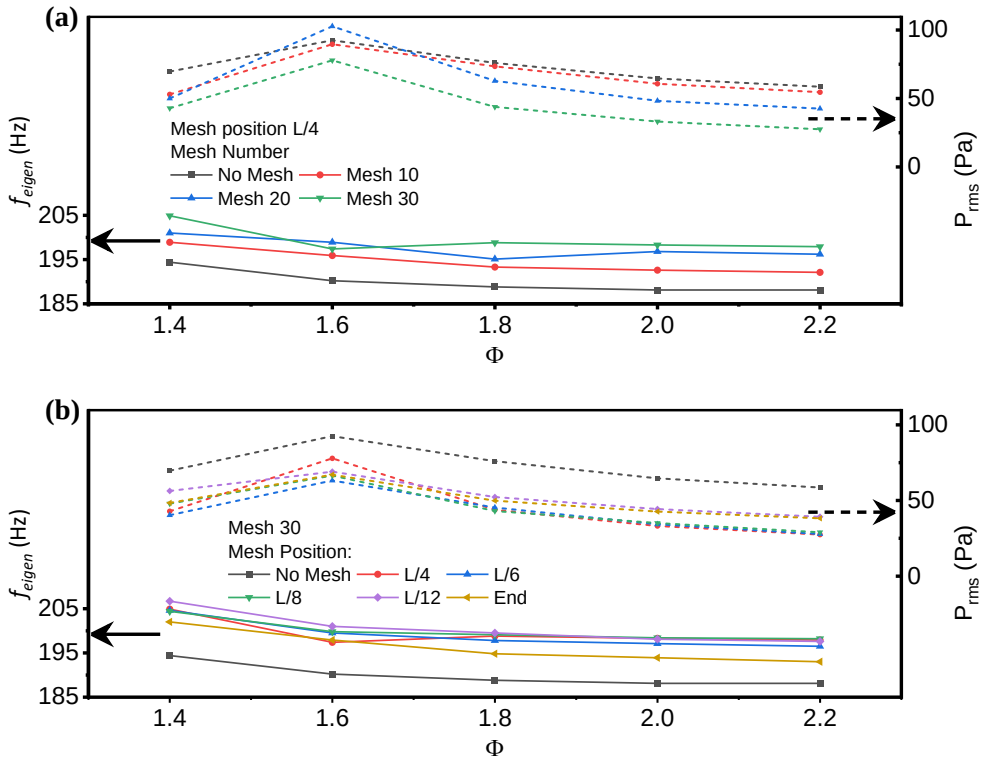

Fig. 6.4. Results of f_{eigen} and root mean square amplitude (p_{rms}) for the (a) different mesh number, (b) mesh position.

By comparing the cases with and without mesh, it can be found that the existence of the mesh has an observable influence on the value of f_{eigen}. The f_{eigen} of the cases without the mesh has the lowest value compared to the cases with the mesh, regardless of the mesh number and position. The difference of around 10 Hz in f_{eigen} can be found between the Mesh 30 and No Mesh, and approximately 5 Hz for the Mesh 10 and No Mesh. For the effect of mesh number, it can be seen that the f_{eigen} decreases as the mesh number increases and the maximum f_{eigen} under the same $\dot{m}_{CH_4}$ and Φ are usually obtained by the cases of Mesh 30, as shown in Fig. 6.4 (a). The f_{eigen} increases by approximately 6 Hz when changes the Mesh 10 to Mesh 30, and 4 Hz as the Mesh 10 changes to Mesh 20.

However, the f_{eigen} is not sensitive to the changes in mesh position compared to the cases with varied mesh numbers. From Fig. 6.4 (b), it can be found that the f_{eigen} present similar trends and values as the mesh moves from the L/4 to L/12, the difference in f_{eigen} is less than 1 Hz for most cases. While the f_{eigen} decreases by about 3 Hz when the mesh is placed at the upper end of the tube. Similarly, the f_{eigen} significantly decreases when the mesh is removed. Therefore, the f_{eigen} is more effectively influenced by the mesh number than the mesh position. However, it has been found that the addition of mesh at upstream region can lead to the increase of f_{eigen} [170], which is opposite to the results that the mesh is placed at the downstream region. The different effect of mesh at upstream and downstream region indicates the different mechanism for influencing the f_{eigen}. A possible reason for this could be the higher mean acoustic speed in the tube due to the higher downstream mean temperature. The presence of mesh at the downstream region could diffuse the upward convective flow and heat flow to minimise the temperature boundary layer, which results in a more uniform temperature profile post to the mesh. At the same time, the heated mesh could maintain the downstream temperature due to its high temperature. Therefore, a higher mean temperature at the downstream region could be resulted, leading to a greater mean acoustic speed in the tube. The temperature of the mesh will be further discussed in the following sections.

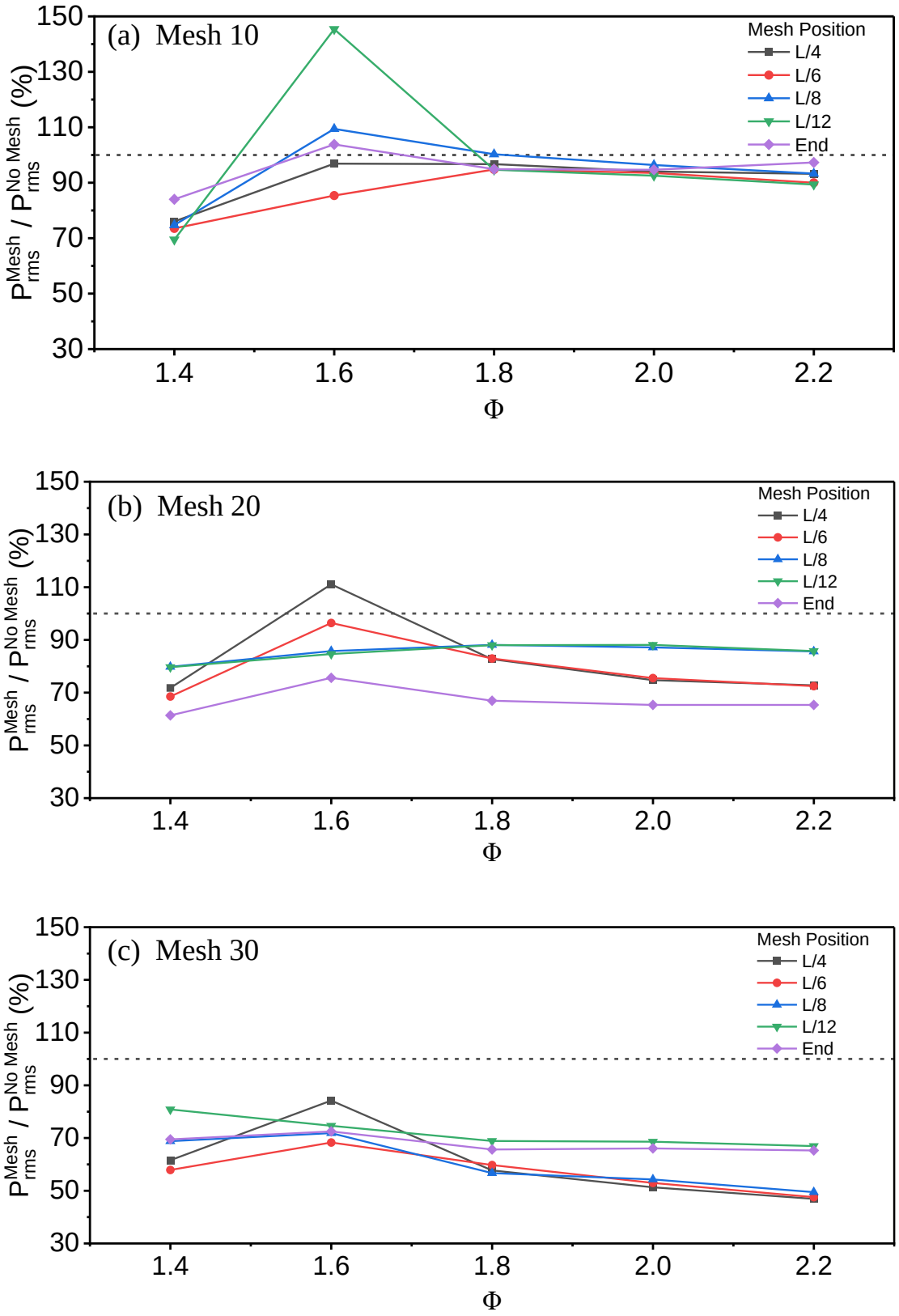

Fig. 6.5. Ratio of the cases with mesh to the corresponding cases without mesh under the same $\dot{m}_{CH_4}$. (a):Mesh 10; (b) Mesh 20; (c) Mesh 30.

For the oscillation amplitude, similar findings can be obtained, that the change in mesh number is more effectively influencing the f_{eigen} than the mesh position. From Fig. 6.4 (a), the oscillation amplitude is clearly suppressed when the mesh exists, as the p_{rms} of cases with mesh is generally lower than the cases without mesh. And the suppression effect of mesh increases with the increasing mesh number. It can be found that the values of p_{rms} for Mesh 30 are approximately half of the values for the cases without mesh, while the cases with Mesh 10 only show slight suppression effects. The ratio of p_{rms} for the cases with mesh (P_{rms}^{Mesh}) to the corresponding p_{rms} for No Mesh cases ($P_{rms}^{No\ Mesh}$) is obtained to represent the suppression effect of the mesh, as shown in Fig. 6.5. It can be seen that Mesh 10 barely has effects on suppressing the oscillation. While the Mesh 20 suppresses the amplitude of oscillation by approximately 10% to 35%. Mesh 30 has the strongest suppression effect, as the oscillation amplitude decreases by about 20% to 55%. Therefore, a higher mesh number tends to have a greater suppression effect regardless of the mesh positions. However, it needs to be noted that the addition of mesh can possibly trigger beating oscillation at Φ = 1.6. Under such circumstances, the oscillation can possibly become more intense for the cases with mesh than those without mesh. Apart from Φ = 1.6, the mesh presents relatively good suppression effects on the oscillation. The suppression effect of mesh on the oscillation is possibly caused by the changes in Rayleigh conductivity at the downstream region since the hole diameter is negatively related to the mesh number [171]. Meanwhile, the existence of mesh at the downstream region could disturb and dampen the upward convective and heat flow due to the changes in the open area at the downstream region and the creation of the vortices at the hole edges [174]. Besides, the additional heat disturbance and fluctuation at the upper half of the tube due to the mesh can provide the system with damping effects, which means changes in Rayleigh index [6,185]. The temperature distribution of mesh and the flow conditions after the mesh will be discussed in the following parts.

- Recurrence plot

The recurrence analysis is applied to investigate the effect of mesh on system dynamics. The RPs for showing the effects of mesh on the recurrence of system state are shown in Fig. 6.6. The diagonal structures, which consist of sets of gathered diagonal lines, can be observed from most of the cases in Fig. 6.6. The diagonal structures indicate a

periodic system without noticeable states variation and the system with neglectable chaoticity and relatively low complexity [115,127]. It can be seen that the diagonal structures are varied with the changing mesh numbers, as shown in Fig. 6.6 (a) to (d). For the cases without mesh, the diagonal structure presents sets of diagonal lines with clear continuity, and few scatter points can be observed near the diagonal structures. Similarly, the patterns of the RPs for Mesh 10, 20 and 30 are mainly formed by the diagonal lines, but the number of scatter points at the edge of each diagonal structure increases with the increasing mesh number. For the Mesh 30 case, the curved pattern can be observed, as highlighted in Fig. 6.6 (d), whereas the case of Mesh 10 and 20 presents straighter patterns of diagonal structure. The curved shape indicates the interrupted diagonal lines at the curved position, which implies the slight changes in the system state under Mesh 30 at the position of L/4. Meanwhile, the pressure time series shown on the top of the RP also presents fluctuations at the corresponding time point where the curved structured appears. Thus, the addition of mesh and the increase of mesh number can result in increased system complexity, and the system state is more likely interrupted.

Differ from the results of f_{eigen} and p_{rms}, the change in mesh position for the cases of Mesh 30 influences the system dynamics to a larger extent. When the mesh is placed at L/4, the system is generally periodic, although the interruptions of system states exist. However, as the mesh is moved to L/6, the system becomes quasi-periodic, that the beating oscillation is triggered. The RP for this case presents a different pattern from the other cases, that is the pattern with discontinuous diagonal structures and bowed shape, as shown in Fig. 6.6 (e). The pressure time series also presents strong time-variant properties that its amplitude fluctuates at where the RP pattern changes. The discontinuous diagonal structure represents the noticeable changes in the system state. The bowed shape indicates similar evolution of states but with different velocities, which means different frequencies for L/6 case [115]. The system of mesh position at L/8 becomes periodic with less complexity since the diagonal structures that consist of diagonal lines appear again, while the structures are still slightly curved, as shown in Fig. 6.6 (f). As the mesh keeps moving upwards to L/12, as shown in Fig. 6.6 (g), the diagonal structures become straighter without noticeably curved structure, indicating the system becomes more stable and periodic with inapparent system state changes. Its pressure time series also shows a very stable time-evolutions without noticeable

amplitude fluctuations. When the mesh moves to the top end of tube, the system becomes less stable with noticeable system state changes, as the clear curved shape can be found from the RP, as shown in Fig. 6.6 (h).

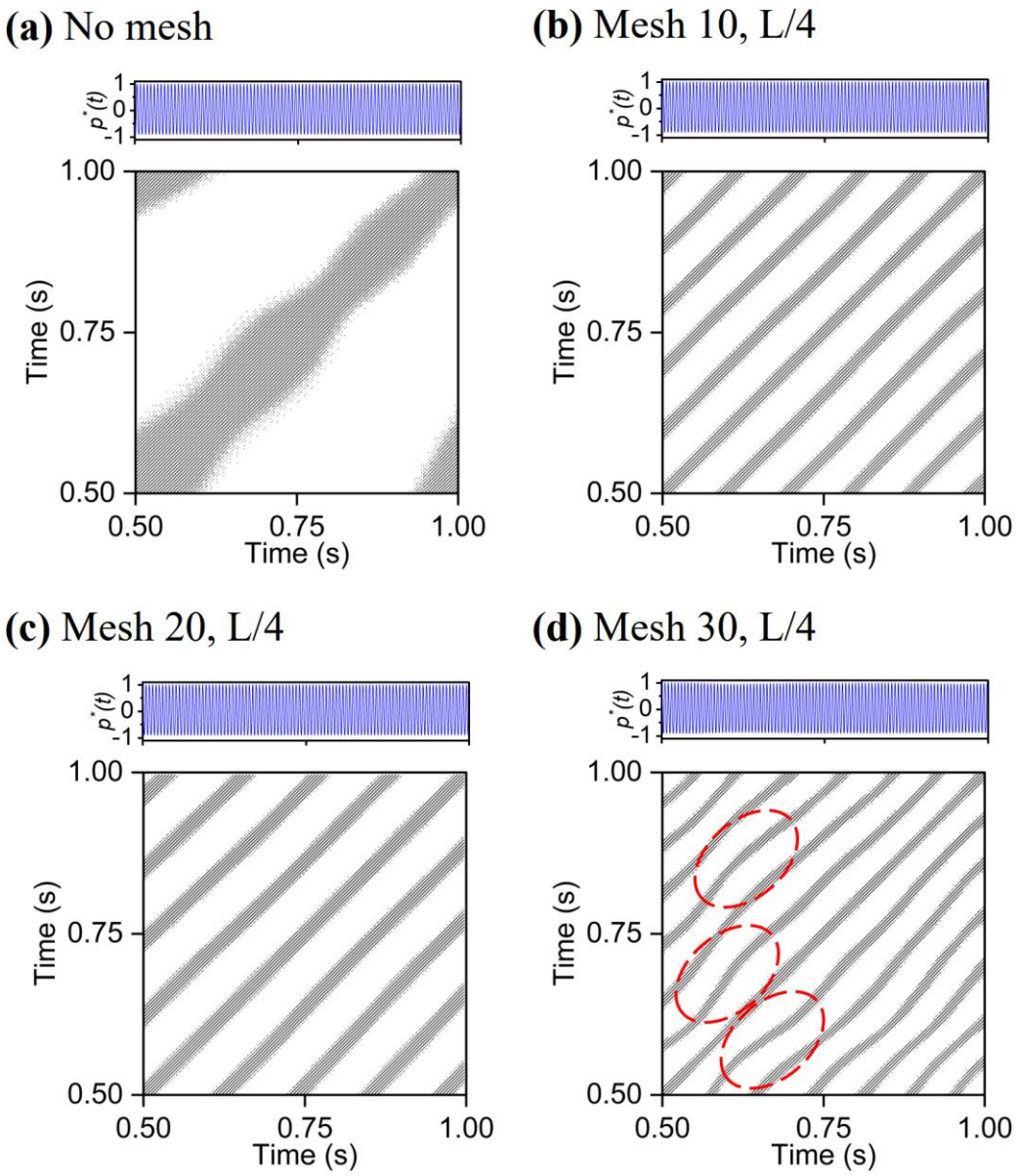

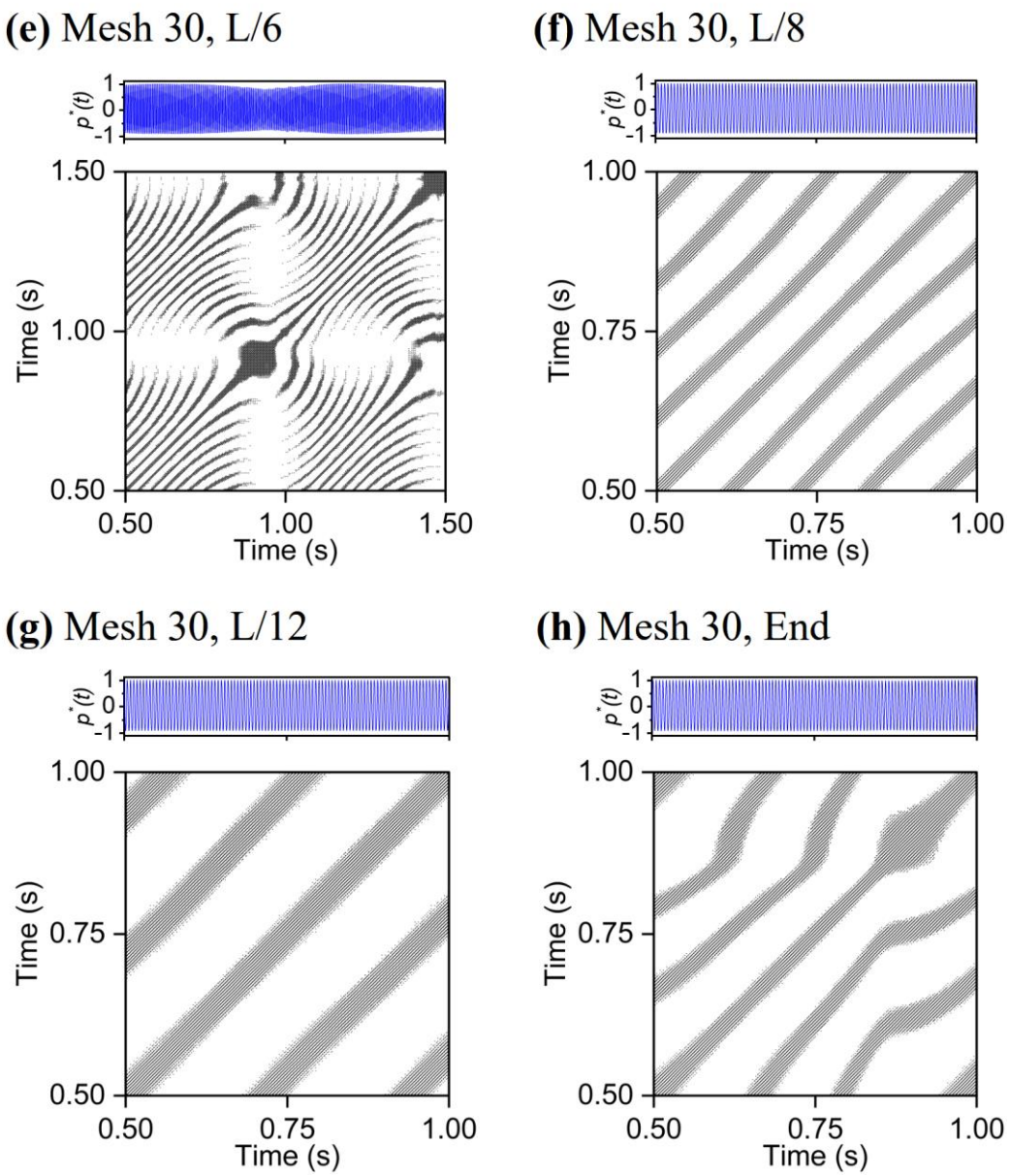

Fig. 6.6. The recurrence plot (RP) for the cases of L/4 at different mesh numbers of (a) No mesh, (b) Mesh 10, (c) Mesh 20 and (d) Mesh 30. And the case of Mesh 30 at different mesh positions of (e) L/6, (f) L/8, (g) L/12 and (h) top end. The D is set to 3 for all RPs, and the τ is determined by the first zero-crossing point of the autocorrelation function.

- Recurrence quantification analysis

Fig. 6.7 shows the RQA results for quantifying the system dynamics of the cases under different mesh numbers and two different mesh positions. It can be seen that the addition of mesh results in changes of all DET, ADL and ENT, indicating that the mesh can influence the system dynamical properties. From the Fig. 6.7 (a), the case without mesh has the greatest DET, and the DET is relatively stable when Φ changes. It shows

that the addition of mesh can increase the complexity of the system. By applying the mesh with different mesh numbers, it can be seen that the value of DET decreases as the mesh number increases for cases of L/4 and L/8. It represents a more complex system with less occurrence probability of similar system states at a higher mesh number. From the ADL, the system could have a lower degree of parallelism at a higher mesh number, and the case without mesh has the greatest degree of parallelism, as shown in Fig. 6.7 (b). The results show that the system state could be more frequently interrupted if the system is with a mesh or at a higher mesh number. Besides, although the ENT for all cases is relatively small, the ENT for the cases with mesh are generally greater than the case without mesh. The greater ENT for the cases with mesh also indicates that the addition of mesh could lead to a more random and complex system. It needs to be noted that the small ENT value shows the neglectable chaoticity of the system since no chaotic state is found.

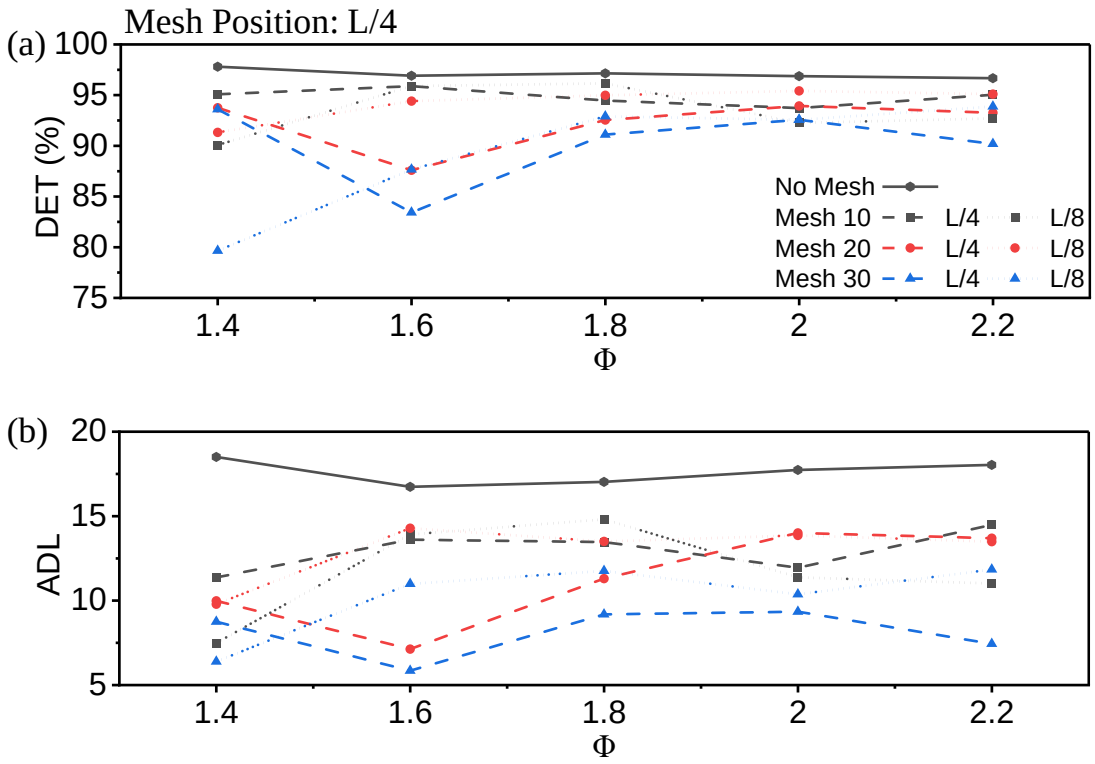

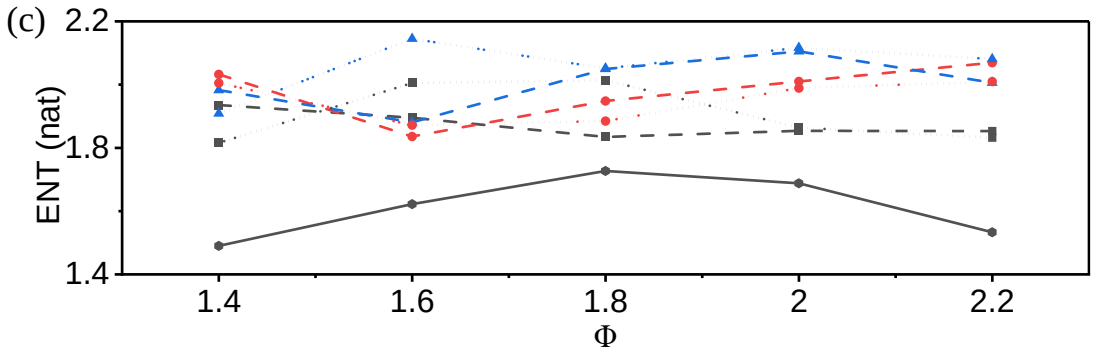

Fig. 6.7. RQA result for the cases with different mesh numbers.

The mesh position can also influence the system dynamical properties, as shown in Fig. 6.8. It can be seen that the DET and ADL show generally increasing trends. The values of DET and ADL are getting close to the cases without mesh as the mesh moves upwards, indicating the more effective role of mesh on the system oscillation at a lower position. It might be caused by the enhanced convective flow due to the greater mean temperature of mesh. Since the mesh at the lower position is closer to the flame, which means the stronger heating effect of radiation. The mean temperature of mesh will be discussed in the following section. However, for the ENT, the change in mesh position has limited effects apart from the case that mesh is at the top end, which means that the mesh number plays a more critical role in the system randomness. Therefore, it can be concluded that the system dynamics can be affected by the change in mesh number and position to different extents, which might indicate that the mesh can provide the system with additional disturbance and thus leads to the variation of the system state.

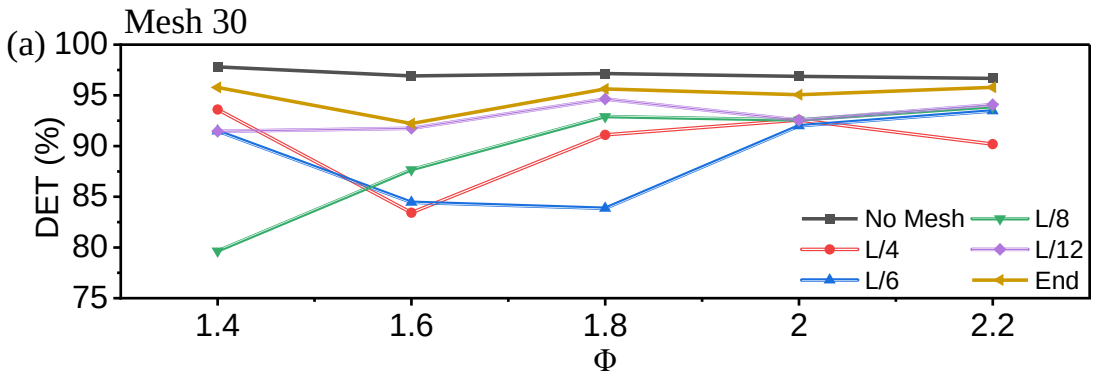

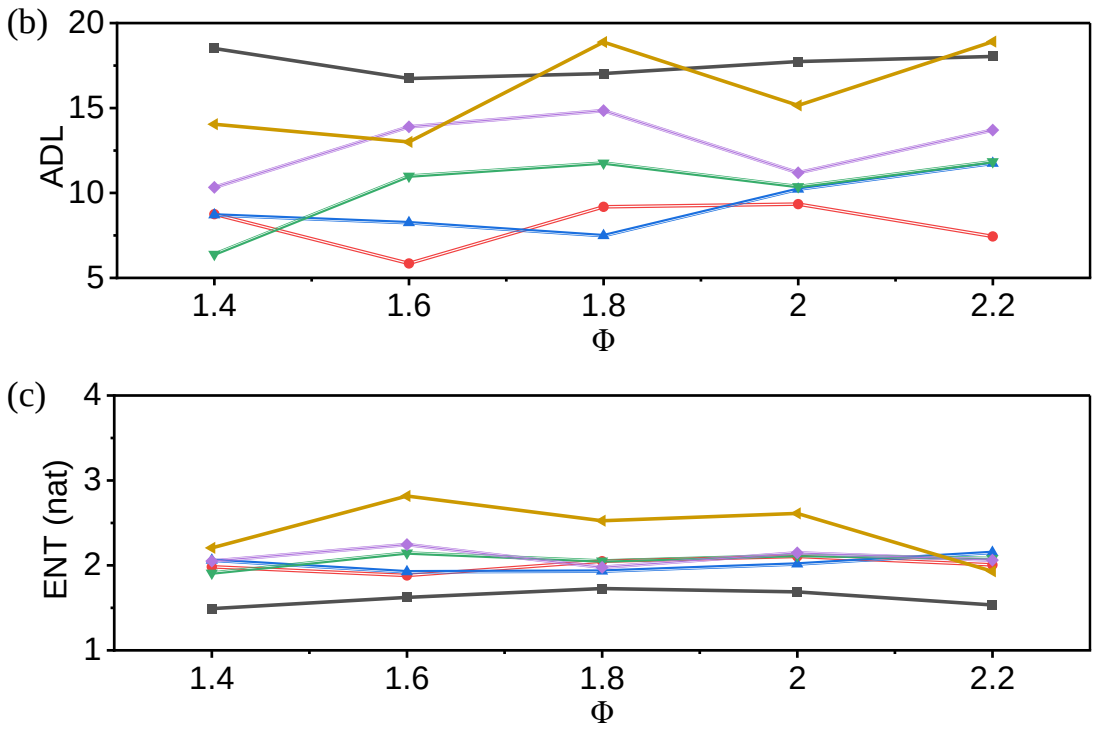

Fig. 6.8 RQA result for the comparison of different mesh positions.

6.3.2 Mechanism analysis

The results of system response in terms of f_{eigen}, p_{rms} and the system dynamics shows that the system can be significantly influenced by the mesh. As mentioned in the section 6.3.1, the mesh can act as an additional disturbance and fluctuation source of heat in the downstream region and can change the flow and heat conditions. Therefore, thermal imaging for the mesh and tube wall was conducted to discover the relationship between the mesh temperature and the system response. Meanwhile, the schlieren images of the region post to the mesh were captured to indicate the change of flow and heat conditions caused by the mesh.

6.3.2.1 Mesh temperature analysis

In the present work, a SWIR and a LWIR camera were utilised to obtain the mesh and tube wall temperature, respectively. The typical thermal images for the mesh with different mesh numbers are shown in Fig. 6.9. From the thermal images, it is found that the overall temperature of the mesh increases with the increasing mesh number since Mesh 30 has the largest area where the temperature is above 300 ℃, and the largest relative high-temperature area (above 515 ℃). It is caused by a narrower space between

the mesh wires at the higher mesh number. The narrower space results in enhanced heat transfer within the mesh, and the mesh can block more convective hot flow, which increases the mesh temperature. The corresponding time evolution of (T_{mesh}^{mean}) for the cases in Fig. 6.9 are shown in Fig. 6.10. The obtained T_{mesh}^{mean} conforms to the observation of the hot area from the thermal images in Fig. 6.9. Mesh 30 has the highest temperature among them, of which the temperature is approximately 25 ℃ higher than Mesh 20, and 50 ℃ higher than Mesh 10. Besides, it is found that the temperature of Mesh 30 presents more fluctuated temperature with time (e.g. from 10 to 20 s) than Mesh 20 and Mesh 10, indicating the more intense heat transfer at the mesh. Some quick temperature variations around 10 ℃ can be found from the curve of Mesh 30 (highlighted by solid line in Fig. 6.10), but not obvious for the curve of Mesh 20 and 10. The results conform to the result of system dynamics analysis, that the Mesh 30 tend to have a more complex system with more frequent variation of system state.

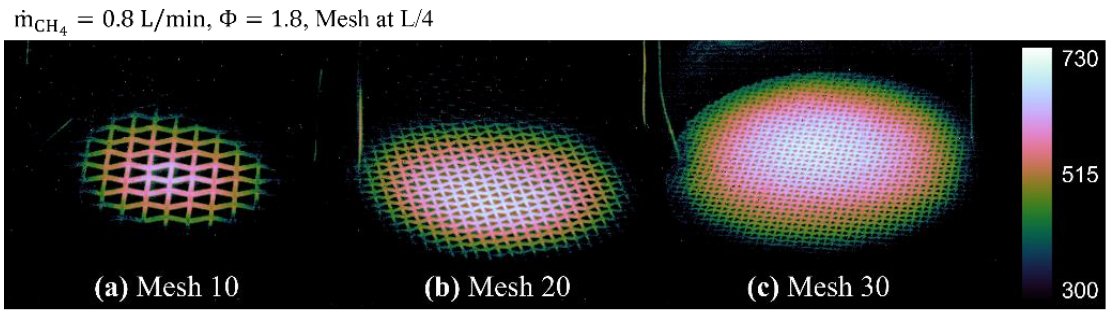

Fig. 6.9. Thermal images for the mesh with different mesh numbers under the condition of $\dot{m}_{CH_4}$ = 0.8 L/min, Φ=1.8, at the mesh position of L/4. The dark portion in the images represents the temperature which is lower than 300 ℃

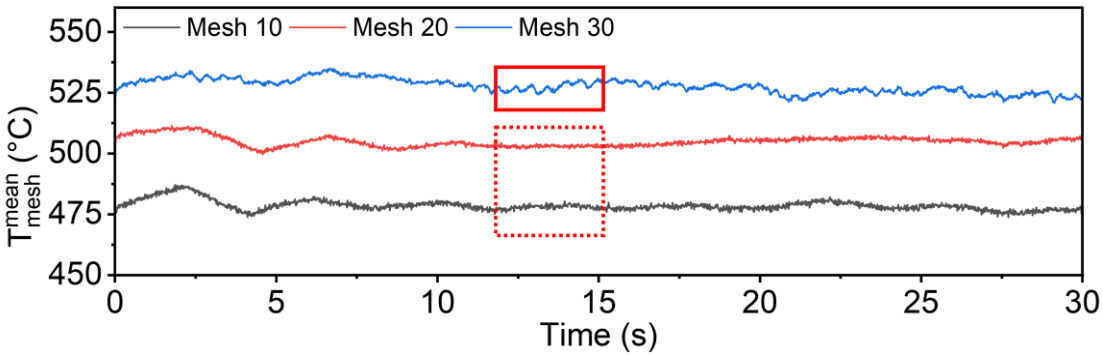

Fig. 6.10. Time evolution of T_{mesh}^{mean} for the cases conditions as $\dot{m}_{CH_4}$ = 0.8 L/min, Φ=1.8 at the mesh position of L/4.

Similarly, the time evolution of T_{mesh}^{mean} at different positions for Mesh 30 are shown in Fig. 6.11. It can be found that the case of L/4 has the highest T_{mesh}^{mean} since the mesh is closer to the flame than the other mesh positions, which means the stronger direct heating effect of radiation from the flame. As the mesh moves upwards, the T_{mesh}^{mean} becomes less varied with the changing mesh position until the mesh reaches the top end of the tube. Fig. 6.12 shows the time evolution of synchronised T_{mesh}^{mean} and the upper RMS envelope of the waveform for the pressure fluctuations (E_{RMS}^{upper}) for the case at L/4. The E_{RMS}^{upper} represents the fluctuations of the oscillation amplitude. From Fig. 6.12 (a), it is found that both T_{mesh}^{mean} and E_{RMS}^{upper} are relatively unstable and more time-variant. Although the changes in T_{mesh}^{mean} and E_{RMS}^{upper} are apparent, no periodic fluctuations for both T_{mesh}^{mean} and E_{RMS}^{upper} can be found from their time evolution. When the mesh is at L/6, the time evolution of the T_{mesh}^{mean} present the periodicity to a certain extent, and the temperature significantly decreases, as shown in Fig. 6.12 (b). It is caused by the intense amplitude fluctuations due to the beating oscillation triggered under this condition. It is found that the fluctuations of T_{mesh}^{mean} are in phase with the fluctuations of oscillation amplitude, indicating the existence of correlations between them. The presence of strong changes in the oscillation amplitude with time due to the beating oscillation can suppress the flame and result in the intense periodic disturbance of flow [52]. The intense disturbance could change the heat transfer at the mesh, resulting in periodic temperature fluctuations, and the suppression of the flame decreases the temperature.

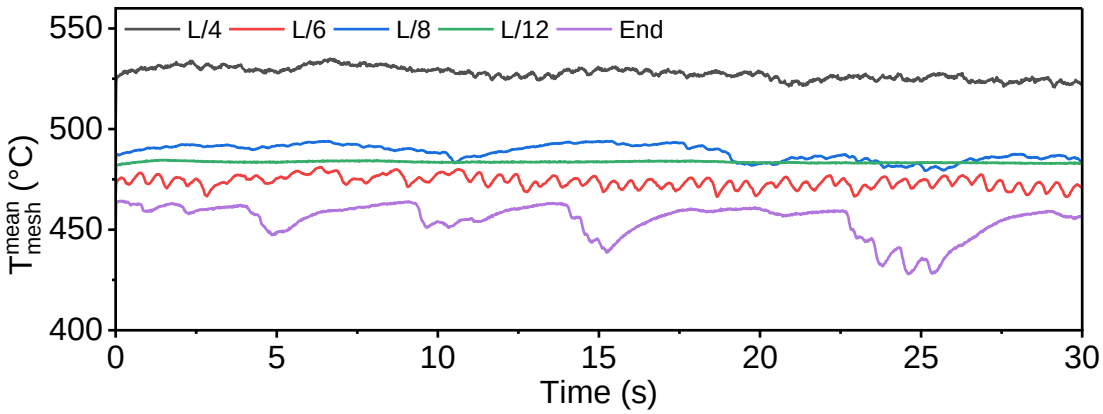

Fig. 6.11. Time evolution of T_{mesh}^{mean} for the cases of Mesh 30 at different mesh position, conditions as $\dot{m}_{CH_4}$ = 0.8 L/min and Φ =1.8.

As the mesh moves to the position of L/8 and L/12, the beating oscillation disappears for these two cases. The T_{mesh}^{mean} for L/8 still presents the apparent time-variant nature, but the periodic nature is absent due to the absence of beating oscillation. The case of L/12 has the stable time evolutions of T_{mesh}^{mean} and E_{RMS}^{upper} at the same time, as shown in Fig. 6.12 (c). Once the mesh reaches the top end of the tube, the T_{mesh}^{mean} becomes unstable, and significant changes with time can be observed, as shown in Fig. 6.11. It might be caused by the more intense convection and complex flow condition around the mesh. Since the mesh at the top end of the tube directly contacts the outer environment of low ambient temperature, resulting in a great temperature gradient and enhanced convective flow. By comparing these cases under different conditions, it is found that the time evolution of T_{mesh}^{mean} and the fluctuations of oscillation amplitude (via E_{RMS}^{upper}) present similar characteristics and temporal synchronicity, indicating the strong correlation between mesh temperature and oscillation behaviour.

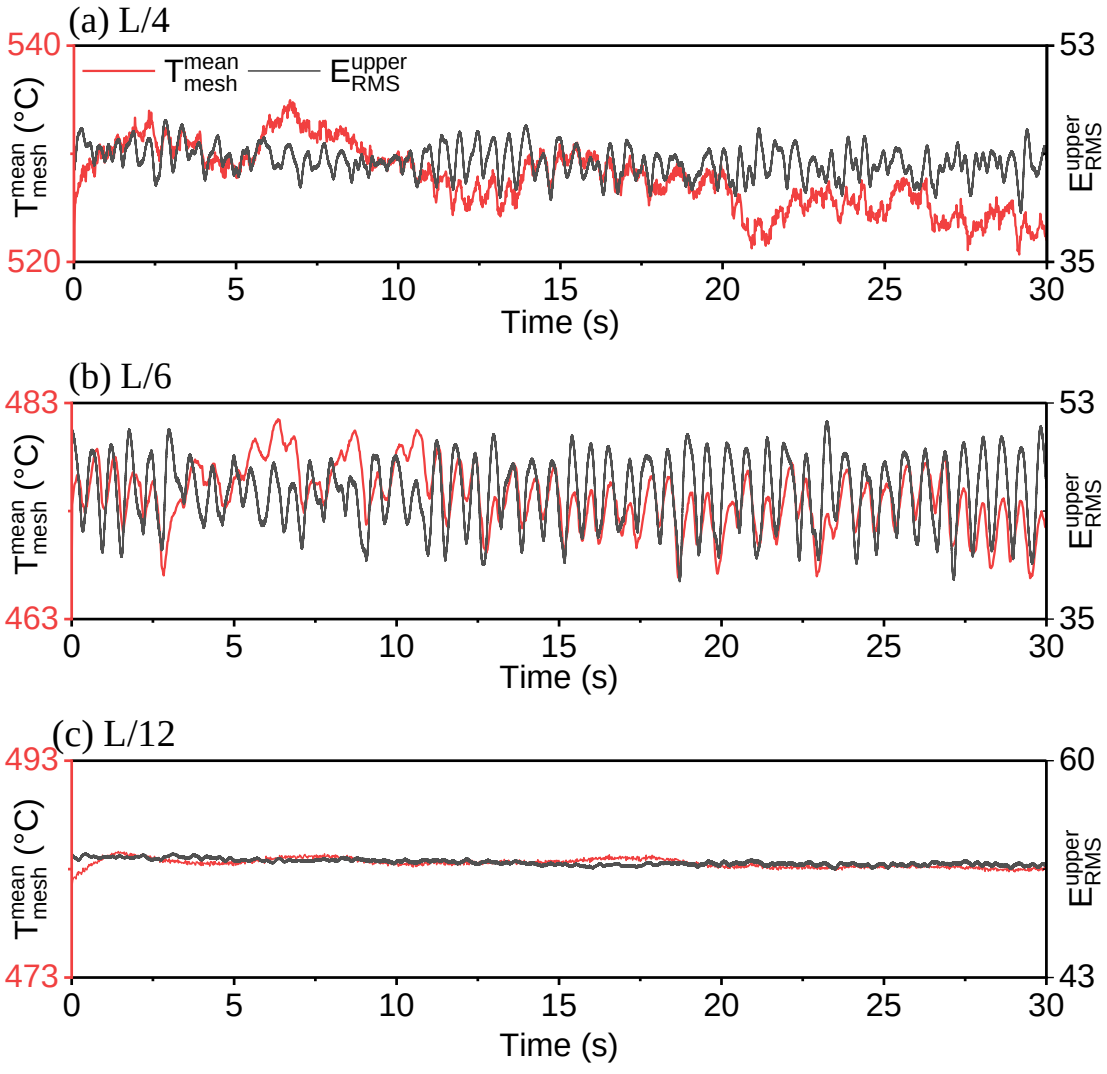

Fig. 6.12. Time evolution of synchronised T_{mesh}^{mean} and E_{RMS}^{upper} for the Mesh 30 cases under the condition of $\dot{m}_{CH_4}$ = 0.8 L/min, Φ =1.8, at different mesh position of (a) L/4, (b) L/6 and (c) L/12.

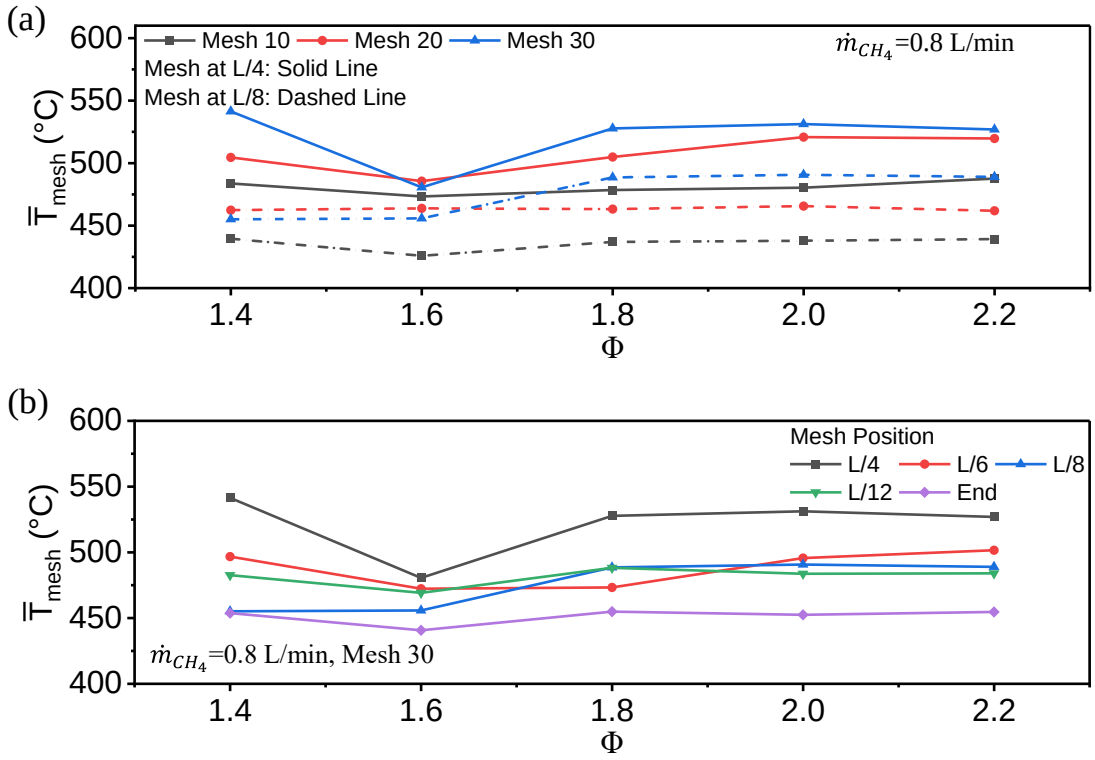

Fig. 6.13. Time-averaged temperature for the mesh under different: (a) Mesh number, and (b) Mesh position

The results of time-averaged T_{mesh}^{mean} ($\bar{T}_{mesh}$) for the mesh with different mesh numbers and at different positions are shown in Fig. 6.13. It is found that the cases of Mesh 30 have generally greater $\bar{T}_{mesh}$ than the cases of Mesh 10 and 20 for both L/4 and L/8. The $\bar{T}_{mesh}$ of different mesh numbers conforms to the findings from the single frame thermal images shown in Fig. 6.9, that the higher mesh number tends to have a greater $\bar{T}_{mesh}$. Meanwhile, it can also be seen that the mesh temperature is well heated under various Φ, since the similar value of $\bar{T}_{mesh}$ is obtained unless the quasi-periodic oscillation being triggered (Φ = 1.6, Mesh 30, L/4). Fig. 6.13 (b) also validates that the $\bar{T}_{mesh}$ tends to decrease as the mesh is moved to a higher position, especially for the cases in the range that system presents less time-varied properties (Φ > 1.8) [95].

In summary, the results show that good agreements in the time domain can be found between the time evolution of mesh temperature and the pressure oscillation. Meanwhile, a relatively high temperature can be obtained by the mesh regardless of

changes in mesh number and position. These validate that the mesh can act as an additional disturbance and fluctuation source of heat in the downstream region. Besides, comparing the RPs (as shown in Fig. 6.6) and the time evolution of T_{mesh}^{mean} (as shown in Fig. 6.10 and Fig. 6.11), it can be found that the degree of variation for the T_{mesh}^{mean} is in a good agreement with the results of RP. Compared to the cases of Mesh 10 and 20, the RP of Mesh 30 has curved shapes, which conforms to the more varied T_{mesh}^{mean} of Mesh 30 than Mesh 10 and 20. The cases with obvious pattern changes and curved shapes tend to have a greater variation of T_{mesh}^{mean} with time, such as the case of the mesh at L/6 and top end of the tube. In contrast, the case at L/12 has a slight variation of T_{mesh}^{mean}, of which the RP consists of straight diagonal structures with few interrupted diagonal lines and scatter points. The agreements between the time evolution of T_{mesh}^{mean} and the results of RP evidence the correlation between the mesh temperature and system dynamics.

6.3.2.2 Schlieren imaging

The mesh at the downstream region can affect the upward convective flow and the heat conditions at the downstream region. Since the perforated structure of the mesh can effectively obstruct and diffuse the flow. Besides, the heated mesh can act as an extra disturbance and fluctuation source of heat and influence the heat transfer in the downstream region. Therefore, a schlieren system is utilised to visualise the heat flow in the region post to the mesh. Note that schlieren images in this work only focused on the two experimental conditions, they are 1) No mesh and 2) mesh with different mesh numbers located at the tube end.

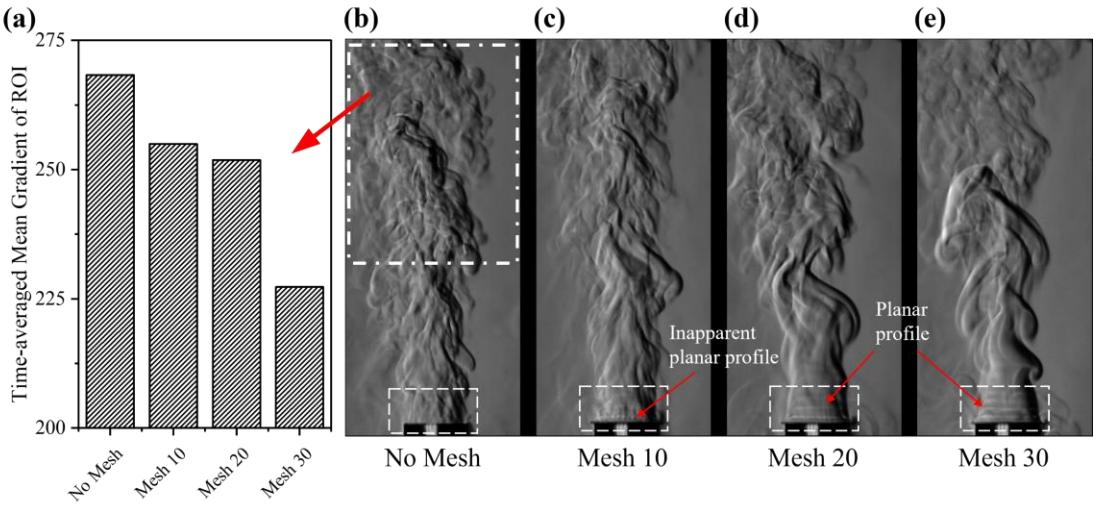

Fig. 6.14. (a) Time-averaged mean gradient of the region highlighted by dashed-dotted line. Schlieren images for the cases of b) No Mesh, (c) Mesh 10, (d) Mesh 20, (e) Mesh 30. as $\dot{m}_{CH_4} =$ 0.8 *L/min and* Φ *=1.8.*

The schlieren images for cases under different mesh numbers are shown in Fig. 6.14 (b)-(e). The existence of mesh can result in different patterns of the schlieren, indicating changes in heat and flow conditions. The white dashed-dotted line at the top of the figure highlights the region at a distance away from the tube end, where the hot flow is mainly driven by the convection outside the tube rather than the strong convection in the tube. It can be found that the flow pattern in the image of No Mesh is more complex than that of Mesh 30. The sharper edges of the pattern and stronger contrast can be observed from the image of No Mesh, as shown in the region highlighted in Fig. 6.14 (b), which indicates a more complicated temperature distribution [182]. To verify that No mesh has a more complex flow pattern, the time-averaged mean gradients based on Prewitt method for the region of interest (highlighted by dashed-dotted line) in each image are calculated to show the difference in the degree of inhomogeneities (via contrast level), as shown in Fig. 6.14 (a). It is found that the time-averaged mean gradient in this region tends to be less as the mesh number increases which indicates a smaller temperature gradient and more uniform temperature distribution in the corresponding region at a higher mesh number. This result evidences that the more complicated pattern is obtained by No Mesh case and implies a less turbulent flow condition at a higher mesh number. Besides, the difference in time-averaged mean gradient between Mesh 10 and 20 is relatively small, while a clearer difference between

Mesh 20 and Mesh 30 can be obtained. It might indicate that the heat and flow conditions are nonlinearly related to the open area of the mesh.

The white dashed line highlights the region that is immediately after the mesh. The planar shape pattern can be found in the cases of Mesh 20 and Mesh 30, while the pattern is not apparent in the case of Mesh 10 but still exists. For the case of No Mesh, no planar shape can be found. The sets of images to show the formation and the movement of the planar pattern are shown in Fig. 6.15. The 0 ms is defined as the hot flow starting to pass the mesh. From 0 ms to 2 ms, the hot gas flow inside the tube is 'pumped' out through the mesh, as highlighted by the solid arrow. It can be observed from the images at 1 ms that the hot flow is separated as the hot flow passes across the small hole of the mesh. Meanwhile, the pattern of the sub-flow presents a profile that is resulted by the boundary layer, indicating that the wire of the mesh around the mesh hole can effectively influence the flow conditions by providing the shear force. As the hot flow passes through the mesh, the pattern of each sub-flow starts to connect with each other and the boundaries between them disappear from 2 ms. A planar pattern of the hot flow is then formed after the integrating process of the sub-flow since 3 ms after the hot flow passes the mesh, indicating that a uniform flow with a uniform temperature profile is formed. Once such flow with the planar temperature profile is generated, the flow keeps moving upward stably with a speed of approximately 1.25 m/s, and the planar temperature profile sustains until the pattern disappears. Since approximately 5 ms from the flow starts to pass through the mesh, a new flow starts forming, as highlighted by the dashed arrow. The presence of planar patterns evidences the influence of the mesh on disturbing the flow and changing the heat transfer since such patterns represent the flow and temperature conditions. In addition, the planar profile might be one of the reasons for less complex heat and flow conditions. The lower time-averaged mean gradients at the region highlighted by the dashed-dotted line might also be caused by the planar profile.

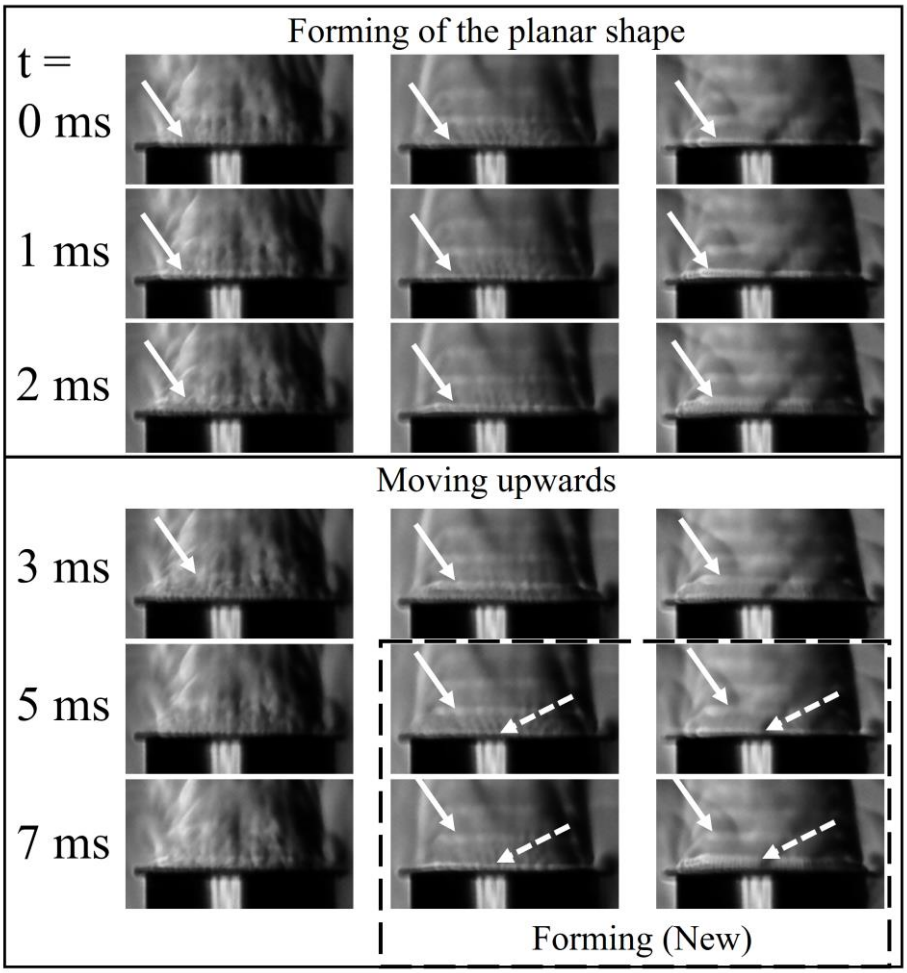

Fig. 6.15. Time evolution of the formation and the moving of the planar shaped pattern for the cases of Mesh 10, 20 and 30.

Therefore, the results of schlieren images evidence that the mesh can influence both the heat and flow conditions, since the diffusion of flow and the formation of planar patterns can be obtained when the mesh is placed. The results also show that the greater effectiveness of mesh in affecting the heat and flow conditions is obtained by a higher mesh number.

6.3.2.3 Discussion

According to the results of thermal and schlieren images, it can be summarised that the effects of mesh on the system response are mainly contributed by the changes of heat and flow conditions in the downstream region. It has been found that the downstream flow is critical to the oscillation frequency and amplitude, and the oscillation can be suppressed when downstream flow is disturbed [176]. In the present work, the

buoyancy effect of the convective flow can be relatively stronger due to the greater temperature at a higher mesh number. This leads to the more unsteady heat release of the mesh, which can be evidenced by the more frequently fluctuated temperature of Mesh 30, as shown in Fig. 6.10. Meanwhile, the smaller open area of Mesh 30 can diffuse and obstruct the flow more effectively, indicating by the schlieren images. The disturbance of the convective flow and the additional unsteady heat disturbance and fluctuation can lead to the unfavourable phase between the heat and pressure fluctuations, resulting in the suppression of the self-excited thermoacoustic oscillation. The mean temperature in the downstream region can become higher at a higher mesh number due to the obstruction of the upwards convective flow and greater temperature of mesh, as shown in Fig. 6.16 (a). The increasing mean temperature leads to the increase of mean acoustic speed in the tube, which results in a higher f_{eigen} of oscillation.

Although the change in mesh position also causes the change in $\bar{T}_{mesh}$, the f_{eigen} and p_{rms} are not sensitive to the change of mesh position. It indicates that the open area is also critical to the system response. Meanwhile, the region that is affected by the disturbance and heating effect from the mesh decreases as the mesh moves upwards, as shown in Fig. 6.16 (b). Therefore, the shorter region affected by the heating and disturbance effect of mesh indicates a smaller impact on the mean acoustic speed inside the tube and fewer effects of disturbance, leading to the less obvious changes in f_{eigen} and p_{rms}. Besides, the mesh would be an acoustic reflection boundary because the size of the mesh hole is smaller than the wavelength of the self-excited oscillation and the velocity potential would change when the pressure wave passes through the hole [75,186]. Thus, the changes in mesh position mean the changes in acoustic properties of the resonance chamber (tube) since the acoustic reflection boundary changes. The low sensitivity of f_{eigen} and p_{rms} response to mesh position changes implies that the changes in acoustic boundaries have only limited influences in changing the system response.

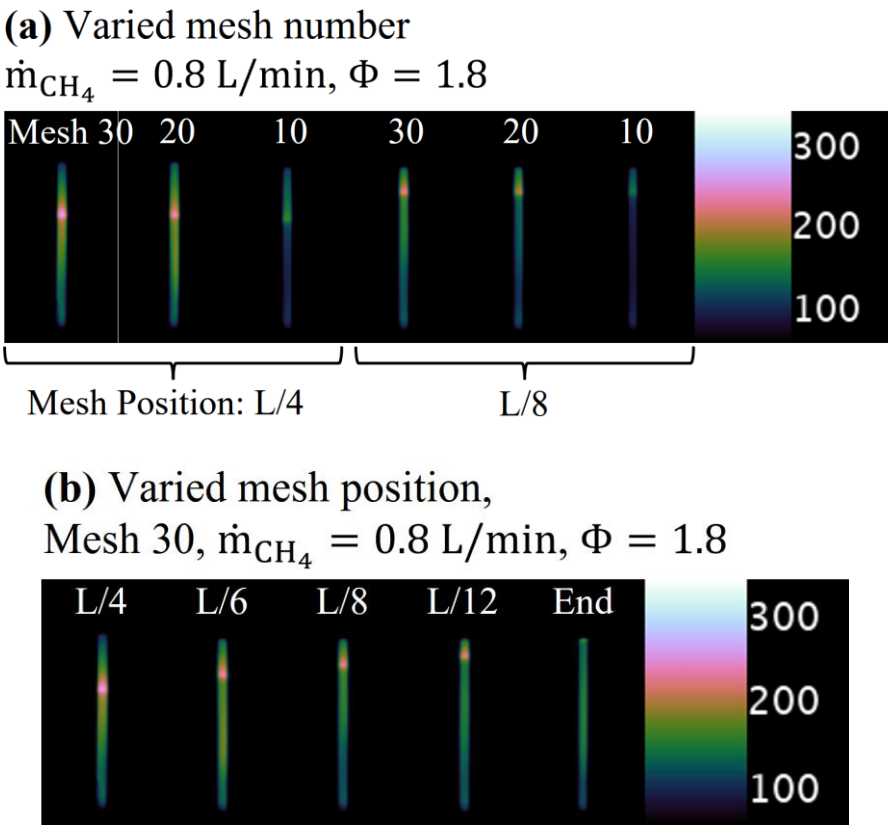

Fig. 6.16. Tube wall temperature measured by FWIR camera for the cases conditions as $\dot{m}_{CH_4}$ = 0.8 *L/min, Φ=1.8 for comparison of (a) Varied mesh number, (b) Varied mesh position. The tube wall temperature is measured after the stabilisation process, which means the temperature is stable and can be used to approximately indicate the temperature profile inside the tube.*

6.4 Chapter Summary

In this chapter, the present study investigated the effects of mesh placement in the downstream region of a Rijke tube on self-excited thermoacoustic oscillations. The system frequency and amplitude response were obtained based on the pressure fluctuation time series. The dynamic properties of the system were revealed by applying recurrence analysis. A thermal imaging system consisting of a short wavelength infrared (SWIR) camera and a long wavelength infrared (LWIR) camera was utilised to obtain the temperature distribution of the mesh and tube wall, respectively. A high-speed schlieren imaging system was utilised for the visualisation of the heat and flow conditions at the tube end with and without a mesh. The study demonstrated the effect of including a mesh in changing the oscillation eigenfrequency, suppressing the oscillation amplitude by up to 50 % and influencing the system dynamics. The greater

effectiveness of mesh was obtained by a greater mesh number. The results of thermal images with the mesh temperature analysis, and schlieren images for the flow conditions evidenced the influential role of the mesh on the downstream heat and flow conditions. The insights gained from this work provide a potential control method of self-excited, nonlinear thermoacoustic oscillations.

Chapter 7 Conclusions and future works

7.1 Conclusions

This thesis aims to study system behaviours of the self-excited thermoacoustic oscillations in a Rijke tube burner through the experimental investigation approach. In these works, the self-excited thermoacoustic oscillations were triggered under various system parameters and experimental conditions. Various methodologies for the system analysis were utilised in this study, including the Fast Fourier Transform (FFT), internal phase difference analysis, phase space reconstruction and its relevant analysis and recurrence analysis. More specifically, the FFT analysis was utilised to obtain the frequency response of the system. The analysis of the internal phase difference between the fundamental and second harmonic modes was developed and utilised to investigate the characteristics of changes in the time-evolution of pressure fluctuations. The phase space reconstruction and the relevant analysis characterised and quantified the system dynamical properties by analysing the trajectory of the state evolution in the phase space. The recurrences of system states, and thus the system nonlinear dynamics, including the complexity and periodicity, were qualitatively described and quantified through the recurrence analysis, including recurrence plot (RP) and recurrence quantification analysis (RQA). The effects of these parameters and conditions on influencing the oscillations were characterised qualitatively and quantitatively through these analysing methods.

Through the extensive investigations in this study, the main findings regarding the system behaviours of the self-excited thermoacoustic system in a Rijke tube burner under various parameters and the suggestions for future works are given in the following sections.

7.1.1 Investigation of equivalence ratio independence and dependence range of system response

In the study shown in Chapter 4, the self-excited thermoacoustic oscillation was triggered under various equivalence ratios. The investigations on how the system responds to changes in the equivalence ratio were carried out. In detail, the changes in frequency and amplitude were examined by carrying out FFT analysis and calculating the root mean square amplitude. To investigate the evolution and the nonlinearity of system, this study employed various time-domain data analysis methods, including the internal phase difference, RP and RQA. The novel calculation of phase difference analysis allowed for the assessment of characteristics of changes in time-evolution of pressure fluctuations (p(t)) by examining the relationship between the fundamental and second harmonic modes over time. The RP and RQA provided insight into the system nonlinear dynamics by identifying and quantifying the properties of corresponding RP. The main findings of this study are concluded below:

From the experimental results, it has been found that the self-excited thermoacoustic oscillation can be strongly affected by Φ under the fuel-rich condition. A nonlinear trend of system frequency response to Φ was discovered. Based on the dependence of oscillation eigenfrequency on Φ, a Φ-dependence range that the eigenfrequency (f_{eigen}) presented strong dependence on Φ, and a Φ-independence range that the f_{eigen} was insensitive to the change of Φ were obtained. The results of phase difference and recurrence analysis were in good agreement with the nonlinear trend of f_{eigen}. The good agreement indicated that the sensitivity of characteristics of changes in $p(t)$ and system dynamics to Φ also conformed to the Φ-dependence and Φ-independence range. Besides, the results of phase difference analysis showed that the local phase difference in the Φ-independence range had less time-variant characteristics with a lower value of standard deviation. It indicates a more stable oscillation in the Φ-independence range. Meanwhile, a more stable and less time-varied system was also evidenced by the results of the recurrence analysis. From the results of system dynamics via RP and RQA, it was found that the system in the Φ-independence range tended to have a higher periodicity and lower complexity. While the chaoticity can be neglected for the periodic and quasi-periodic systems in this study. The sensitivity of characteristics of changes

in $p(t)$ and system dynamics validated the existence of both ranges and highlighted the importance of Φ in influencing the self-excited thermoacoustic oscillations. As a meaningful yet interesting finding, the mechanism of similar mean phase difference in the Φ-independence range, regardless of system parameter changes, should be carried out in future work. Meanwhile, considering the effects of system parameters on both frequency response and system dynamics, further study is worthy of being continued.

This study shows the critical role of Φ on self-excited oscillation in a Rijke tube. In this study, a developed phase difference calculation was applied to observe the characteristics of thermoacoustic oscillation. It is found that the analysis of phase difference can effectively indicate characteristics of changes in $p(t)$ and detect the exact time point where the oscillation behaviour changes. The methods utilised in this study are applicable to different combustion systems with nonlinearities.

7.1.2 Investigation of system response to system parameters

The study shown in Chapter 5 experimentally examined the effects of system parameters, including the burner position, fuel flow rate and tube inner diameter, on the self-excited thermoacoustic oscillation. The oscillation frequency and amplitude were obtained based on the measured pressure fluctuations time series. Multiple time-domain analysis methods were employed to qualitatively describe and quantify the system nonlinear behaviour. Specifically, the phase spaces of the systems with different parameters were reconstructed based on the time-delayed embedding method, by which the system stability was revealed by identifying the attractors of the system under different conditions. The Wayland translation error allowed for the quantitative determination of the system deterministic nature. The recurrence analysis applied in this study also provided an efficient means of investigating the system dynamics of the thermoacoustic system.

It has been found that the system parameters investigated in this study significantly influence the eigenfrequency of thermoacoustic oscillations, the complexity and the periodicity of the system. The findings for the effect of system parameters which were investigated in this study can be summarised as followings:

- Both the Φ-insensitive range and Φ-sensitive range were found. The system frequency response presented different sensitivity to equivalence ratio changes at a constant fuel flowrate. The eigenfrequency in the Φ-sensitive range was greater than in the Φ-insensitive range.

- In Φ-insensitive range, the quasi-linear relationship between fuel flowrate and mean stable eigenfrequency can be highlighted. The quasi-linear trends had similar increasing rates, regardless of the system parameter change.

- The eigenfrequencies were inversely proportional to burner positions and tube inner diameter. A simplified model for validating the discussions about the lower eigenfrequency obtained in a larger diameter tube was developed. The change in average sound speed due to the mean temperature change was found as the main reason for eigenfrequency changes.

- It was found that the increasing equivalence ratio would increase the deterministic natures and decrease the complexity of system if the quasi-periodic oscillation was not triggered.

- Burner position could change the system dynamics to a larger extent. A more complex and unstable system with less deterministic natures was likely generated if the burner was at a lower position. The system states also were more easily affected by the changes of equivalence ratio at lower burner positions.

- The influence of tube inner diameter on characterising the system was obtained by the variation of system dynamics. However, the experiments at the tubes of more different inner diameters should be conducted in the future to quantify the effect of tube inner diameter on system nonlinear dynamics.

This study shows the critical roles of different system parameters on the self-excited thermoacoustic oscillation in the Rijke tube. It has been proved that the analysis methods utilised in this study are effective for quantifying the nonlinear characteristics of the thermoacoustic system in the time-domain, which are also applicable to various combustion system with nonlinear characteristics.

7.1.3 Effect of mesh on characterising the thermoacoustic oscillations

The study shown in Chapter 6 investigated the effects of mesh on self-excited thermoacoustic oscillations. It was revealed that the existence of mesh in the downstream region plays a critical role in influencing the thermoacoustic oscillation. To investigate the system dynamics qualitatively and quantitative, the study also employed recurrence analysis techniques. This study applied a thermal imaging system that consisted of a long-wavelength infrared (LWIR) camera and a short-wavelength infrared (SWIR) camera to investigate the temperature distributions of the mesh and tube wall. The time sequence images captured by the SWIR camera provided the time-evolution of mesh mean temperature (T_{mesh}^{mean}) and the time-averaged T_{mesh}^{mean} ($\bar{T}_{mesh}$). Besides, a high-speed Schlieren imaging system was also employed to visualise inhomogeneities at the tube end, which is post to the mesh. By which, the heat and flow conditions respond to the mesh can be revealed. The main findings of this study are summarised below:

- The addition of the mesh can affect the system response in terms of the oscillation frequency and amplitude, and the system dynamical properties. The changes of mesh number and positions can lead to changes in the mesh effectiveness in influencing the system to different extents.

- The suppression effect of the mesh on the oscillation amplitude was discovered. The oscillation was more suppressed at a high mesh number, by up to 50 % in terms of the root mean square amplitude. Meanwhile, the frequency increases with the increasing mesh number. The oscillation frequency and amplitude were insensitive to mesh number changes.

- The system would become more complex with more interruption of system state when applied the mesh. The system dynamical properties can be sensitive to both the changes in mesh number and position. The quasi-periodic oscillation could be triggered at specific mesh numbers and positions.

- The change in mesh number was found to have limited effects on the variation of T_{mesh}^{mean} but efficiently affect the $\bar{T}_{mesh}$. However, the degree of T_{mesh}^{mean} variation and $\bar{T}_{mesh}$ were sensitive to the mesh position changes. The agreements between the variation of T_{mesh}^{mean} and system dynamics were obtained.

- The schlieren images proved the effects of mesh on influencing the heat and flow conditions post to the mesh. A more complex pattern with greater contrast was obtained at a lower mesh number and without mesh. The formation of the planar shape pattern immediately after the mesh indicated the planar temperature profile caused by the mesh.

7.2 Suggested future works

The suggested future works are summarised as follows:

- For the current works conducted in this study, only the premixed laminar methane flame has been used to trigger the thermoacoustic oscillation in the Rijke tube burner. The results of this thesis show that the system responses and the dynamical properties are significantly related to the flame speed (via change in Φ) , flame front and total heat power (via change in fuel flowrate). Both the flame speed and total heat power can also strongly relate to the fuel type, as discussed in Section 2.1. Therefore, the response of the self-excited oscillation with different fuel types, including other hydrocarbons, hydrogen and ammonia, should be further investigated.

- The combustion process in the works is under fuel-rich conditions, which means an excess of methane beyond that required for complete combustion was supplied. Due to this, there would be unburned fuel and combustible species that were not completely consumed during the combustion process. Meanwhile, fresh air kept being drawn from the bottom end of the tube due to convection. The presence of fresh air with sufficient oxygen helps to consume the unburned methane and the combustible species which were produced due the incomplete combustion. As a result, secondary combustion can occur at the flame downstream. Thus, it is worth investigating the role of secondary combustion in

characterising the thermoacoustic system behaviour. The future study that changes the inlet gas drawn from the bottom end to the gases without oxygen, such as nitrogen, argon gases, is worth to be carried out.

- The filter for frequency decomposition, which is needed for the phase difference analysis, is challenging to apply in analysing instantaneous system response. Also, the phase difference analysis is difficult to achieve for the combustion with indirect combustion noise (noise of uniformly distributed intensity in the frequency domain). A more general method for applying this analysis to a system without limit-cycle characteristics should be developed.

- The studies in this thesis utilised a single microphone placed at the bottom of the tube to obtain the pressure fluctuations time series. The studies conducted by Zhao [144] and Sun et al. [145] applied multiple microphones and pressure transducers to investigate the acoustic properties of the system. According to the works conducted by Zhao [144], Sun et al. [145] and Seybert et al. [187], the two-microphone technique analysis is achieved by two microphones fixed perpendicular to the axial direction of the tube. The two-microphone technique can be effective for determining normal acoustic properties, such as the higher frequency resolution and the impedance of the system. Therefore, further investigations by applying multi-microphone techniques are suggested.

- During the studies, the interaction between flame dynamics and self-excited oscillation can be observed. Meanwhile, it was also aware of the relationship between the flame structures (flame mode) and the oscillation type (with significant differences in amplitude and stability). Therefore, the investigations of flame dynamics and the impact of the flame mode on the self-excited oscillation should be carried out in future studies.

- The heat release rate of the flame in this study was not measured. Rayleigh index, which was discussed in Section 2.2, demonstrates that the phase difference between the fluctuations of heat release rate and pressure fluctuations can be very crucial to the driving and intensity of the thermoacoustic oscillation. It is challenging to obtain the real-time and instantaneous heat release rate change

and its spatial distribution along the flame through the thermocouples. It has been verified that the heat release rate of the flame can be characterised by the chemiluminescence of the flame [188]. The time series of heat release rate fluctuation can be then obtained by using the chemiluminescence of OH* and CH*. Thus, as the two main system variables of the thermoacoustic system, it is also essential to investigate the system dynamics by constructing the phase space based on both the fluctuations of heat release rate and pressure.

- The current studies in this thesis mainly focus on experimental investigation. However, as a system that is dominated by the coupling of the flow field and acoustic field, numerical studies should be further conducted in the future to seek a way to predict the phenomenon observed in this study and the dynamical properties of the system.

Reference

[1] BP p.l.c., Statistical Review of World Energy 2022, 2022. https://www.bp.com/content/dam/bp/business-sites/en/global/corporate/pdfs/energy-economics/statistical-review/bp-stats-review-2022-full-report.pdf (accessed September 30, 2022).

[2] R.I. Sujith, S.A. Pawar, Thermoacoustic Instability, Springer International Publishing, Cham, 2021. https://doi.org/10.1007/978-3-030-81135-8.

[3] K.I. Matveev, F.E.C. Culick, A study of the transition to instability in a Rijke tube with axial temperature gradient, J Sound Vib. 264 (2003) 689–706. https://doi.org/10.1016/S0022-460X(02)01217-8.

[4] Monitoring Combustion Instabilities: E.On Uk's Experience, in: Combustion Instabilities In Gas Turbine Engines, American Institute of Aeronautics and Astronautics, Reston ,VA, 2006: pp. 163–175. https://doi.org/10.2514/5.9781600866807.0163.0175.

[5] J. Tyndall, Sound, 4th ed., Longmans, London, 1893.

[6] R.L. Raun, M.W. Beckstead, J.C. Finlinson, K.P. Brooks, A review of Rijke tubes, Rijke burners and related devices, Prog Energy Combust Sci. 19 (1993) 313–364. https://doi.org/10.1016/0360-1285(93)90007-2.

[7] P.L. Rijke, LXXI. *Notice of a new method of causing a vibration of the air contained in a tube open at both ends*, The London, Edinburgh, and Dublin Philosophical Magazine and Journal of Science. 17 (1859) 419–422. https://doi.org/10.1080/14786445908642701.

[8] D. Zhao, Z.H. Chow, Thermoacoustic instability of a laminar premixed flame in Rijke tube with a hydrodynamic region, J Sound Vib. 332 (2013) 3419–3437. https://doi.org/10.1016/j.jsv.2013.01.031.

[9] Rayleigh, The explanation of certain acoustical phenomena 1, Nature. 18 (1878) 319–321. https://doi.org/10.1038/018319a0.

[10] A.A. Putnam, W.R. Dennis, Burner Oscillations of the Gauze-Tone Type, J Acoust Soc Am. 26 (1954) 716–725. https://doi.org/10.1121/1.1907406.

[11] F.E.C. Culick, Nonlinear behavior of acoustic waves in combustion chambersml, Pergamon Press, 1976.

[12] Michigan Technological University, An Electric Rijke (a.k.a.hoot) Tube - How mine are made, (n.d.). https://pages.mtu.edu/~suits/electronics/ElecRijke.html (accessed February 10, 2023).

[13] N.M. Hariharan, P. Sivashanmugam, S. Kasthurirengan, Influence of stack geometry and resonator length on the performance of thermoacoustic engine, Applied Acoustics. 73 (2012) 1052–1058. https://doi.org/10.1016/j.apacoust.2012.05.003.

[14] M. Shaaban, Experimental investigations on a standing-wave thermoacoustic engine Development of a Thermo-Acoustic Power Converter Prototype View project Flow-sound and flow-structure interactions of arrangements of cylinders View project, (2013). https://doi.org/10.13140/RG.2.2.24827.67361.

[15] C.J. Lawn, G. Penelet, Common features in the thermoacoustics of flames and engines, International Journal of Spray and Combustion Dynamics. 10 (2018) 3–37. https://doi.org/10.1177/1756827717743911.

[16] G.W. Swift, Thermoacoustics, Springer International Publishing, Cham, 2017. https://doi.org/10.1007/978-3-319-66933-5.

[17] M.P. Juniper, R.I. Sujith, Sensitivity and Nonlinearity of Thermoacoustic Oscillations, Annu Rev Fluid Mech. 50 (2018) 661–689. https://doi.org/10.1146/annurev-fluid-122316-045125.

[18] K. Balasubramanian, R.I. Sujith, Thermoacoustic instability in a Rijke tube: Non-normality and nonlinearity, Physics of Fluids. 20 (2008) 044103. https://doi.org/10.1063/1.2895634.

[19] L. Kabiraj, A. Saurabh, P. Wahi, R.I. Sujith, Route to chaos for combustion instability in ducted laminar premixed flames, Chaos. 22 (2012). https://doi.org/10.1063/1.4718725.

[20] K.T. Kim, Nonlinear Interactions Between the Fundamental and Higher Harmonics of Self-Excited Combustion Instabilities, Combustion Science and Technology. 189 (2017) 1091–1106. https://doi.org/10.1080/00102202.2016.1275591.

[21] H. Kobayashi, H. Gotoda, S. Tachibana, Nonlinear determinism in degenerated combustion instability in a gas-turbine model combustor, Physica A: Statistical Mechanics and Its Applications. 510 (2018) 345–354. https://doi.org/10.1016/j.physa.2018.06.024.

[22] K. Kashinath, I.C. Waugh, M.P. Juniper, Nonlinear self-excited thermoacoustic oscillations of a ducted premixed flame: Bifurcations and routes to chaos, J Fluid Mech. 761 (2014) 399–430. https://doi.org/10.1017/jfm.2014.601.

[23] T. Braun, V.R. Unni, R.I. Sujith, J. Kurths, N. Marwan, Detection of dynamical regime transitions with lacunarity as a multiscale recurrence quantification measure, Nonlinear Dyn. 104 (2021) 3955–3973. https://doi.org/10.1007/s11071-021-06457-5.

[24] D. Zhao, Transient growth of flow disturbances in triggering a Rijke tube combustion instability, Combust Flame. 159 (2012) 2126–2137. https://doi.org/10.1016/j.combustflame.2012.02.002.

[25] C. Tao, H. Zhou, Effects of operating parameters on the combustion oscillation behaviour in a lean premixed CH4 combustor, Journal of Mechanical Science and Technology. 35 (2021) 3753–3762. https://doi.org/10.1007/s12206-021-0744-4.

[26] H. Zhao, G. Li, D. Zhao, Z. Zhang, D. Sun, W. Yang, S. Li, Z. Lu, Y. Zheng, Experimental study of equivalence ratio and fuel flow rate effects on nonlinear thermoacoustic instability in a swirl combustor, Appl Energy. 208 (2017) 123–131. https://doi.org/10.1016/j.apenergy.2017.10.061.

[27] M.A. Heckl, M.S. Howe, Stability analysis of the Rijke tube with a Green's function approach, J Sound Vib. 305 (2007) 672–688. https://doi.org/10.1016/j.jsv.2007.04.027.

[28] Y. Guan, D. Zhao, Enhancing ammonia combustion with minimum hydrogen blended in presence of self-excited intermittent pulsating oscillations, Physics of Fluids. 35 (2023). https://doi.org/10.1063/5.0147474.

[29] D. Zhao, X.Y. Li, A review of acoustic dampers applied to combustion chambers in aerospace industry, Progress in Aerospace Sciences. 74 (2015) 114–130. https://doi.org/10.1016/j.paerosci.2014.12.003.

[30] D. Zhao, Z. Lu, H. Zhao, X.Y. Li, B. Wang, P. Liu, A review of active control approaches in stabilizing combustion systems in aerospace industry, Progress in Aerospace Sciences. 97 (2018) 35–60. https://doi.org/10.1016/j.paerosci.2018.01.002.

[31] X. Liu, D. Zhao, D. Guan, S. Becker, D. Sun, X. Sun, Development and progress in aeroacoustic noise reduction on turbofan aeroengines, Progress in Aerospace Sciences. 130 (2022). https://doi.org/10.1016/j.paerosci.2021.100796.

[32] S.R. Turns, An Introduction to Combustion: Concepts and Applications, 3rd ed., McGraw-Hill, New York, 2011.

[33] Scion, What is fire? — Science Learning Hub, (2009). https://www.sciencelearn.org.nz/images/834-burning-showing-incomplete-combustion (accessed July 22, 2023).

[34] Heinz Pitsch, Laminar Premixed Flames: Kinematics and Burning Velocity, 2014.

[35] E.E. Arens, R.C. Youngquist, S.O. Starr, Intensity calibrated hydrogen flame spectrum, Int J Hydrogen Energy. 39 (2014) 9545–9551. https://doi.org/10.1016/j.ijhydene.2014.04.043.

[36] R.W. Schefer, W.D. Kulatilaka, B.D. Patterson, T.B. Settersten, Visible emission of hydrogen flames, Combust Flame. 156 (2009) 1234–1241. https://doi.org/10.1016/j.combustflame.2009.01.011.

[37] Combustion, Elsevier, 2015. https://doi.org/10.1016/C2011-0-05402-9.

[38] F.A. Williams, Combustion Theory, CRC Press, 2018. https://doi.org/10.1201/9780429494055.

[39] C.K. Law, Combustion Physics, Cambridge University Press, 2006. https://doi.org/10.1017/CBO9780511754517.

[40] T. Lieuwen, B.T. Zinn, The role of equivalence ratio oscillations in driving combustion instabilities in low NOx gas turbines, Symposium (International) on Combustion. 27 (1998) 1809–1816. https://doi.org/10.1016/S0082-0784(98)80022-2.

[41] M.M. Kamal, R.S. Barlow, S. Hochgreb, Conditional analysis of turbulent premixed and stratified flames on local equivalence ratio and progress of reaction, Combust Flame. 162 (2015) 3896–3913. https://doi.org/10.1016/j.combustflame.2015.07.026.

[42] T.S. Cheng, C.-Y. Wu, Y.-H. LI, Y.-C. Chao, Chemiluminescence measurements of local equivalence ratio in a partially premixed flame, Combustion Science and Technology. 178 (2006) 1821–1841. https://doi.org/10.1080/00102200600790755.

[43] M.S. Mansour, H. Imam, K.A. Elsayed, W. Abbass, Local equivalence ratio measurements in turbulent partially premixed flames using laser-induced breakdown spectroscopy, Spectrochim Acta Part B At Spectrosc. 64 (2009) 1079–1084. https://doi.org/10.1016/j.sab.2009.07.022.

[44] S. Tachibana, K. Kanai, S. Yoshida, K. Suzuki, T. Sato, Combined effect of spatial and temporal variations of equivalence ratio on combustion instability in a low-swirl combustor, Proceedings of the Combustion Institute. 35 (2015) 3299–3308. https://doi.org/10.1016/j.proci.2014.07.024.

[45] K.C. Smyth, J. Houston Miller, R.C. Dorfman, W. Gary Mallard, R.J. Santoro, Soot Inception in a Methane/Air Diffusion Flame as Characterized by Detailed Species Profiles, 1985.

[46] R.E. Mitchell, A.F. Sarofim, L.A. Clomburg, Experimental and numerical investigation of confined laminar diffusion flames, Combust Flame. 37 (1980) 227–244. https://doi.org/10.1016/0010-2180(80)90092-9.

[47] R. Friedman, E. Burke, Measurement of temperature distribution in a low-pressure flat flame, J Chem Phys. 22 (1954) 824–830. https://doi.org/10.1063/1.1740197.

[48] L.S. Tran, P.A. Glaude, F. Battin-Leclerc, Experimental study of the structure of laminar premixed flames of ethanol/methane/oxygen/argon, Combust Explos Shock Waves. 49 (2013) 11–18. https://doi.org/10.1134/S0010508213010024.

[49] C.K. Law, A. Makino, T.F. Lu, On the off-stoichiometric peaking of adiabatic flame temperature, Combust Flame. 145 (2006) 808–819. https://doi.org/10.1016/j.combustflame.2006.01.009.

[50] V. Nori, J. Seitzman, Chemiluminescence Measurements and Modeling in Syngas, Methane and Jet-A Fueled Combustors, in: 45th AIAA Aerospace Sciences Meeting and Exhibit, American Institute of Aeronautics and Astronautics, Reston, Virigina, 2007. https://doi.org/10.2514/6.2007-466.

[51] L. He, Q. Guo, Y. Gong, F. Wang, G. Yu, Investigation of OH* chemiluminescence and heat release in laminar methane–oxygen co-flow diffusion flames, Combust Flame. 201 (2019) 12–22. https://doi.org/10.1016/j.combustflame.2018.12.009.

[52] F. Weng, S. Li, D. Zhong, M. Zhu, Investigation of self-sustained beating oscillations in a Rijke burner, Combust Flame. 166 (2016) 181–191. https://doi.org/10.1016/j.combustflame.2016.01.016.

[53] H. Watanabe, S.J. Shanbhogue, S. Taamallah, N.W. Chakroun, A.F. Ghoniem, The structure of swirl-stabilized turbulent premixed CH4/air and CH4/O2/CO2 flames and mechanisms of intense burning of oxy-flames, Combust Flame. 174 (2016) 111–119. https://doi.org/10.1016/j.combustflame.2016.09.015.

[54] B. Zhou, C. Brackmann, Q. Li, Z. Wang, P. Petersson, Z. Li, M. Aldén, X. song Bai, Distributed reactions in highly turbulent premixed methane/air flames. Part I. Flame structure characterization, Combust Flame. 162 (2015) 2937–2953. https://doi.org/10.1016/j.combustflame.2014.12.021.

[55] T.C. Williams, C.R. Shaddix, R.W. Schefer, P. Desgroux, The response of buoyant laminar diffusion flames to low-frequency forcing, Combust Flame. 151 (2007) 676–684. https://doi.org/10.1016/j.combustflame.2007.07.023.

[56] V.N. Nori, J.M. Seitzman, CH* chemiluminescence modeling for combustion diagnostics, Proceedings of the Combustion Institute. 32 (2009) 895–903. https://doi.org/10.1016/j.proci.2008.05.050.

[57] T. Kathrotia, U. Riedel, A. Seipel, K. Moshammer, A. Brockhinke, Experimental and numerical study of chemiluminescent species in low-pressure flames, Applied Physics B. 107 (2012) 571–584. https://doi.org/10.1007/s00340-012-5002-0.

[58] K.R. McManus, T. Poinsot, S.M. Candel, A review of active control of combustion instabilities, Prog Energy Combust Sci. 19 (1993) 1–29. https://doi.org/10.1016/0360-1285(93)90020-F.

[59] A. Miglani, S. Basu, R. Kumar, Insight into instabilities in burning droplets, Physics of Fluids. 26 (2014). https://doi.org/10.1063/1.4866866.

[60] P. Clavin, Dynamic behavior of premixed flame fronts in laminar and turbulent flows, Prog Energy Combust Sci. 11 (1985) 1–59. https://doi.org/10.1016/0360-1285(85)90012-7.

[61] Y.K. Park, D.G. Vlachos, Isothermal Chain-Branching, Reaction Exothermicity, and Transport Interactions in the Stability of Methane/Air Mixtures*, Combust Flame. 114 (1998) 214–230. https://doi.org/10.1016/S0010-2180(97)00285-X.

[62] E.S. Oran, J.H. Gardner, Chemical-acoustic interactions in combustion systems, Prog Energy Combust Sci. 11 (1985) 253–276. https://doi.org/10.1016/0360-1285(85)90003-6.

[63] E. Shashi Menon, Fluid Flow in Pipes, in: Transmission Pipeline Calculations and Simulations Manual, Elsevier, 2015: pp. 149–234. https://doi.org/10.1016/B978-1-85617-830-3.00005-5.

[64] T.C. Lieuwen, Unsteady Combustor Physics, Cambridge University Press, Cambridge, 2012. https://doi.org/10.1017/CBO9781139059961.

[65] K.C. Schadow, E. Gutmark, Combustion instability related to vortex shedding in dump combustors and their passive control, Prog Energy Combust Sci. 18 (1992) 117–132. https://doi.org/10.1016/0360-1285(92)90020-2.

[66] J.J. Keenan, D. V. Makarov, V. V. Molkov, Rayleigh-Taylor instability: Modelling and effect on coherent deflagrations, in: Int J Hydrogen Energy, Elsevier Ltd, 2014: pp. 20467–20473. https://doi.org/10.1016/j.ijhydene.2014.03.230.

[67] Y. Leo, B. Zhang, Explosion behavior of methane-air mixtures and Rayleigh-Taylor instability in the explosion process near the flammability limits, Fuel. 324 (2022). https://doi.org/10.1016/j.fuel.2022.124730.

[68] J.P. Sykes, T.P. Gallagher, B.A. Rankin, Effects of Rayleigh-Taylor instabilities on turbulent premixed flames in a curved rectangular duct, Proceedings of the Combustion Institute. 38 (2021) 6059–6066. https://doi.org/10.1016/j.proci.2020.06.146.

[69] A. Prasad, C.H.K. Williamson, The instability of the shear layer separating from a bluff body, J Fluid Mech. 333 (1997) 375–402. https://doi.org/10.1017/S0022112096004326.

[70] A.E. Perry, M.S. Chong, T.T. Lim, The vortex-shedding process behind two-dimensional bluff bodies, J Fluid Mech. 116 (1982) 77–90. https://doi.org/10.1017/S0022112082000378.

[71] D. Hwang, C. Kang, K. Ahn, Effect of Mixing Section Acoustics on Combustion Instability in a Swirl-Stabilized Combustor, Energies (Basel). 15 (2022) 8492. https://doi.org/10.3390/en15228492.

[72] M. Bruneau, Fundamentals of Acoustics, ISTE, London, UK, 2006. https://doi.org/10.1002/9780470612439.

[73] L.E. Kinsler, A.R. Frey, Fundamentals of Acoustics, 4th ed., 2000.

[74] P. Novotný, T. Vít, M. Vestfálová, J. Lopes, Standing-wave thermoacoustic engines, EPJ Web Conf. 25 (2012) 01061. https://doi.org/10.1051/epjconf/20122501061.

[75] J.W. Strutt, The Theory of Sound, Cambridge University Press, 2011. https://doi.org/10.1017/CBO9781139058094.

[76] C. Sondhauss, Ueber die Schallschwingungen der Luft in erhitzten Glasröhren und in gedeckten Pfeifen von ungleicher Weite, Annalen Der Physik Und Chemie. 155 (1850) 1–34. https://doi.org/10.1002/andp.18501550102.

[77] S. Backhaus, G.W. Swift, A thermoacoustic-Stirling heat engine: Detailed study, J Acoust Soc Am. 107 (2000) 3148–3166. https://doi.org/10.1121/1.429343.

[78] Z. Yu, A.J. Jaworski, S. Backhaus, Travelling-wave thermoacoustic electricity generator using an ultra-compliant alternator for utilization of low-grade thermal energy, Appl Energy. 99 (2012) 135–145. https://doi.org/10.1016/j.apenergy.2012.04.046.

[79] P. Merkli, H. Thomann, Thermoacoustic effects in a resonance tube, J Fluid Mech. 70 (1975) 161–177. https://doi.org/10.1017/S0022112075001954.

[80] B. Higgins, On the sound produced by a current of hydrogen gas passing through a tube, Journal of Natural Philosophy, Chemistry and the Arts. (1802).

[81] K.T. Feldman, H. Hirsch, R.L. Carier, Experiments on the Sondhauss Thermoacoustical Phenomenon, J Acoust Soc Am. 39 (1966) 1236–1236. https://doi.org/10.1121/1.1942774.

[82] A.P. Dowling, Y. Mahmoudi, Combustion noise, Proceedings of the Combustion Institute. 35 (2015) 65–100. https://doi.org/10.1016/j.proci.2014.08.016.

[83] E.G. Richardson, The Theory of the Singing Flame, Proceedings of the Physical Society of London. 35 (1922) 47–54. https://doi.org/10.1088/1478-7814/35/1/308.

[84] A.A. PUTNAM, Experimental and Theoretical Studies of Combustion Oscillations, in: 1964: pp. 199–290. https://doi.org/10.1016/B978-1-4831-9659-6.50010-X.

[85] T. Lieuwen, Modeling Premixed Combustion-Acoustic Wave Interactions: A Review, J Propuls Power. 19 (2003) 765–781. https://doi.org/10.2514/2.6193.

[86] S. Candel, Combustion dynamics and control: Progress and challenges, Proceedings of the Combustion Institute. 29 (2002) 1–28. https://doi.org/10.1016/S1540-7489(02)80007-4.

[87] T. Lieuwen, H. Torres, C. Johnson, B.T. Zinn, A Mechanism of Combustion Instability in Lean Premixed Gas Turbine Combustors, J Eng Gas Turbine Power. 123 (2001) 182–189. https://doi.org/10.1115/1.1339002.

[88] M. Stöhr, Z. Yin, W. Meier, Interaction between velocity fluctuations and equivalence ratio fluctuations during thermoacoustic oscillations in a partially premixed swirl combustor, Proceedings of the Combustion Institute. 36 (2017) 3907–3915. https://doi.org/10.1016/j.proci.2016.06.084.

[89] C.O. Paschereit, E. Gutmark, W. Weisenstein, Coherent structures in swirling flows and their role in acoustic combustion control, Physics of Fluids. 11 (1999) 2667–2678. https://doi.org/10.1063/1.870128.

[90] F.E. Marble, S.M. Candel, Acoustic disturbance from gas non-uniformities convected through a nozzle, J Sound Vib. 55 (1977) 225–243. https://doi.org/10.1016/0022-460X(77)90596-X.

[91] A. Duvvur, C.H. Chiang, W.A. Sirignano, Oscillatory fuel droplet vaporization: Driving mechanism for combustion instability, J Propuls Power. 12 (1996) 358–365. https://doi.org/10.2514/3.24036.

[92] V. Jegadeesan, R.I. Sujith, Experimental investigation of noise induced triggering in thermoacoustic systems, Proceedings of the Combustion Institute. 34 (2013) 3175–3183. https://doi.org/10.1016/j.proci.2012.05.003.

[93] S.H. Strogatz, Nonlinear Dynamics and Chaos, CRC Press, 2018. https://doi.org/10.1201/9780429492563.

[94] A. Ghaffari, M. Tomizuka, R.A. Soltan, The stability of limit cycles in nonlinear systems, Nonlinear Dyn. 56 (2009) 269–275. https://doi.org/10.1007/s11071-008-9398-3.

[95] X. Liu, H. Zhou, Y. Lai, Y. Zhang, Equivalence ratio independence and dependence ranges of system responses for a nonlinear thermoacoustic oscillation in a Rijke tube, J Sound Vib. (2022) 117545. https://doi.org/10.1016/j.jsv.2022.117545.

[96] M. Haeringer, M. Merk, W. Polifke, Inclusion of higher harmonics in the flame describing function for predicting limit cycles of self-excited combustion instabilities, Proceedings of the Combustion Institute. 37 (2019) 5255–5262. https://doi.org/10.1016/j.proci.2018.06.150.

[97] X. Song, T. Zhu, D. Pan, Z. Wang, C. Ji, D. Zhao, Numerical investigations on the beating behavior of self-excited combustion instability in a hydrogen-fueled Rijke type combustor, Aerosp Sci Technol. 126 (2022). https://doi.org/10.1016/j.ast.2022.107624.

[98] J. Kim, M. Jang, K. Lee, A.R. Masri, Experimental study of the beating behavior of thermoacoustic self-excited instabilities in dual swirl combustors, Exp Therm Fluid Sci. 105 (2019) 1–10. https://doi.org/10.1016/j.expthermflusci.2019.03.007.

[99] X. Han, D. Laera, D. Yang, C. Zhang, J. Wang, X. Hui, Y. Lin, A.S. Morgans, C.J. Sung, Flame interactions in a stratified swirl burner: Flame stabilization, combustion instabilities and beating oscillations, Combust Flame. 212 (2020) 500–509. https://doi.org/10.1016/j.combustflame.2019.11.020.

[100] L.-W. Chen, Y. Zhang, Experimental observation of the nonlinear coupling of flame flow and acoustic wave, Flow Measurement and Instrumentation. 46 (2015) 12–17. https://doi.org/10.1016/j.flowmeasinst.2015.09.001.

[101] H.G. Schuster, W. Just, Deterministic Chaos, Wiley, 2005. https://doi.org/10.1002/3527604804.

[102] E.N. Lorenz, Deterministic Nonperiodic Flow, J Atmos Sci. 20 (1963) 130–141. https://doi.org/10.1175/1520-0469(1963)020<0130:DNF>2.0.CO;2.

[103] Y. Pomeau, P. Manneville, Intermittent transition to turbulence in dissipative dynamical systems, Commun Math Phys. 74 (1980) 189–197. https://doi.org/10.1007/BF01197757.

[104] Y. Guan, V. Gupta, L.K.B. Li, Intermittency route to self-excited chaotic thermoacoustic oscillations, J Fluid Mech. 894 (2020). https://doi.org/10.1017/jfm.2020.297.

[105] V. Nair, R.I. Sujith, Intermittency as a Transition State in Combustor Dynamics: An Explanation for Flame Dynamics Near Lean Blowout, Combustion Science and Technology. 187 (2015) 1821–1835. https://doi.org/10.1080/00102202.2015.1066339.

[106] V. Nair, G. Thampi, R.I. Sujith, Intermittency route to thermoacoustic instability in turbulent combustors, J Fluid Mech. 756 (2014) 470–487. https://doi.org/10.1017/jfm.2014.468.

[107] J.-C. Roux, R.H. Simoyi, H.L. Swinney, Observation of a strange attractor, Physica D. 8 (1983) 257–266. https://doi.org/10.1016/0167-2789(83)90323-8.

[108] N.H. Packard, J.P. Crutchfield, J.D. Farmer, R.S. Shaw, Geometry from a Time Series, Phys Rev Lett. 45 (1980) 712–716. https://doi.org/10.1103/PhysRevLett.45.712.

[109] F. Takens, Detecting strange attractors in turbulence, in: 1981: pp. 366–381. https://doi.org/10.1007/BFb0091924.

[110] H.D.I. Abarbanel, R. Brown, J.J. Sidorowich, L.Sh. Tsimring, The analysis of observed chaotic data in physical systems, Rev Mod Phys. 65 (1993) 1331–1392. https://doi.org/10.1103/RevModPhys.65.1331.

[111] M.B. Kennel, R. Brown, H.D.I. Abarbanel, Determining embedding dimension for phase-space reconstruction using a geometrical construction, Phys Rev A (Coll Park). 45 (1992) 3403–3411. https://doi.org/10.1103/PhysRevA.45.3403.

[112] R. Wayland, D. Bromley, D. Pickett, A. Passamante, Recognizing Determinism in a Time Series, 1993.

[113] Y. Hirata, S. Horai, H. Suzuki, K. Aihara, Testing serial dependence by Random-shuffle surrogates and the Wayland method, Physics Letters, Section A: General, Atomic and Solid State Physics. 370 (2007) 265–274. https://doi.org/10.1016/j.physleta.2007.05.061.

[114] H. Gotoda, H. Nikimoto, T. Miyano, S. Tachibana, Dynamic properties of combustion instability in a lean premixed gas-turbine combustor, Chaos. 21 (2011). https://doi.org/10.1063/1.3563577.

[115] N. Marwan, M. Carmenromano, M. Thiel, J. Kurths, Recurrence plots for the analysis of complex systems, Phys Rep. 438 (2007) 237–329. https://doi.org/10.1016/j.physrep.2006.11.001.

[116] J.-P. Eckmann, S.O. Kamphorst, D. Ruelle, Recurrence Plots of Dynamical Systems, Europhysics Letters (EPL). 4 (1987) 973–977. https://doi.org/10.1209/0295-5075/4/9/004.

[117] S. Schinkel, O. Dimigen, N. Marwan, Selection of recurrence threshold for signal detection, Eur Phys J Spec Top. 164 (2008) 45–53. https://doi.org/10.1140/epjst/e2008-00833-5.

[118] J.P. Zbilut, C.L. Webber, Embeddings and delays as derived from quantification of recurrence plots, Phys Lett A. 171 (1992) 199–203. https://doi.org/10.1016/0375-9601(92)90426-M.

[119] C.L. Webber, J.P. Zbilut, Dynamical assessment of physiological systems and states using recurrence plot strategies, J Appl Physiol. 76 (1994) 965–973. https://doi.org/10.1152/jappl.1994.76.2.965.

[120] N. Marwan, N. Wessel, U. Meyerfeldt, A. Schirdewan, J. Kurths, Recurrence-plot-based measures of complexity and their application to heart-rate-variability data, Phys Rev E. 66 (2002) 026702. https://doi.org/10.1103/PhysRevE.66.026702.

[121] L.L. Trulla, A. Giuliani, J.P. Zbilut, C.L. Webber, Recurrence quantification analysis of the logistic equation with transients, Phys Lett A. 223 (1996) 255–260. https://doi.org/10.1016/S0375-9601(96)00741-4.

[122] P. Horowitz, W. Hill, The Art of Electronics, 3rd ed., Cambridge University Press, 2015.

[123] H. Zan, W. Zhou, X. Xiao, L. Lin, J. Zhang, H. Li, Recurrence network analysis for uncovering dynamic transition of thermo-acoustic instability of supercritical hydrocarbon fuel flow, Aerosp Sci Technol. 85 (2019) 1–12. https://doi.org/10.1016/j.ast.2018.11.040.

[124] M. Murugesan, S. Balusamy, S. Hochgreb, L.K.B. Li, Recurrence analysis of forced synchronization in a self-excited thermoacoustic system, in: 24th International Congress on Sound and Vibration, ICSV 2017, 2017. https://doi.org/10.17863/CAM.33084.

[125] L.-P. Yang, S.-L. Ding, G. Litak, E.-Z. Song, X.-Z. Ma, Identification and quantification analysis of nonlinear dynamics properties of combustion instability in a diesel engine, Chaos: An Interdisciplinary Journal of Nonlinear Science. 25 (2015) 013105. https://doi.org/10.1063/1.4899056.

[126] Y. Guan, P. Liu, B. Jin, V. Gupta, L.K.B. Li, Nonlinear time-series analysis of thermoacoustic oscillations in a solid rocket motor, Exp Therm Fluid Sci. 98 (2018) 217–226. https://doi.org/10.1016/j.expthermflusci.2018.06.002.

[127] N. Marwan, How to avoid potential pitfalls in recurrence plot based data analysis, International Journal of Bifurcation and Chaos. 21 (2011) 1003–1017. https://doi.org/10.1142/S0218127411029008.

[128] A.P. Dowling, The calculation of thermoacoustic oscillations, J Sound Vib. 180 (1995) 557–581. https://doi.org/10.1006/JSVI.1995.0100.

[129] F.E.C. Culick, Short Communication A Note on Rayleigh's Criterion, Combustion Science and Technology. 56 (1987) 159–166. https://doi.org/10.1080/00102208708947087.

[130] F. Nicoud, T. Poinsot, Thermoacoustic instabilities: Should the Rayleigh criterion be extended to include entropy changes?, Combust Flame. 142 (2005) 153–159. https://doi.org/10.1016/j.combustflame.2005.02.013.

[131] L. Magri, M.P. Juniper, J.P. Moeck, Sensitivity of the Rayleigh criterion in thermoacoustics, J Fluid Mech. 882 (2020) R1. https://doi.org/10.1017/jfm.2019.860.

[132] P. Chatterjee, U. Vandsburger, W.R. Saunders, V.K. Khanna, W.T. Baumann, On the spectral characteristics of a self-excited Rijke tube combustor - Numerical simulation and experimental measurements, J Sound Vib. 283 (2005) 573–588. https://doi.org/10.1016/j.jsv.2004.04.019.

[133] J.A. Carvalho, M.A. Ferreira, C. Bressan, J.L.G. Ferreira, Definition of heater location to drive maximum amplitude acoustic oscillations in a Rijke tube, Combust Flame. 76 (1989) 17–27. https://doi.org/10.1016/0010-2180(89)90073-4.

[134] N.N. Deshmukh, S.D. Sharma, Suppression of thermo-acoustic instability using air injection in horizontal Rijke tube, Journal of the Energy Institute. 90 (2017) 485–495. https://doi.org/10.1016/j.joei.2016.03.001.

[135] U. Sen, T. Gangopadhyay, C. Bhattacharya, A. Mukhopadhyay, S. Sen, Dynamic Characterization of a Ducted Inverse Diffusion Flame Using Recurrence Analysis, Combustion Science and Technology. 190 (2018) 32–56. https://doi.org/10.1080/00102202.2017.1374952.

[136] X. Wu, M. Wang, P. Moin, N. Peters, Combustion instability due to the nonlinear interaction between sound and flame, J Fluid Mech. 497 (2003) S0022112003006554. https://doi.org/10.1017/S0022112003006554.

[137] B. Zhang, M. Shahsavari, Z. Rao, S. Yang, B. Wang, Thermoacoustic instability drivers and mode transitions in a lean premixed methane-air combustor at various swirl intensities, Proceedings of the Combustion Institute. 38 (2021) 6115–6124. https://doi.org/10.1016/j.proci.2020.06.226.

[138] J. Moeck, M. Bothien, S. Schimek, A. Lacarelle, C. Paschereit, Subcritical thermoacoustic instabilities in a premixed combustor, in: 14th AIAA/CEAS Aeroacoustics Conference (29th AIAA Aeroacoustics Conference), American Institute of Aeronautics and Astronautics, Reston, Virigina, 2008. https://doi.org/10.2514/6.2008-2946.

[139] D. Zhao, Y. Chew, Energy harvesting from a convection-driven Rijke-Zhao thermoacoustic engine, J Appl Phys. 112 (2012). https://doi.org/10.1063/1.4767914.

[140] Y. Sun, D. Zhao, C. Ji, T. Zhu, Z. Rao, B. Wang, Large-eddy simulations of self-excited thermoacoustic instability in a premixed swirling combustor with an outlet nozzle, Physics of Fluids. 34 (2022) 044112. https://doi.org/10.1063/5.0087055.

[141] S. Li, D. Zhao, C. Ji, J. Li, Combustion Instabilities in a Bifurcating Tube: Open- and Closed-Loop Measurements, AIAA Journal. 52 (2014) 2513–2523. https://doi.org/10.2514/1.J052758.

[142] C.O. Paschereit, W. Polifke, Investigation of the Thermoacoustic Characteristics of a Lean Premixed Gas Turbine Burner, in: Volume 3: Coal, Biomass and Alternative Fuels; Combustion and Fuels; Oil and Gas Applications; Cycle Innovations, American Society of Mechanical Engineers, 1998. https://doi.org/10.1115/98-GT-582.

[143] S. Mariappan, R.I. Sujith, P.J. Schmid, Experimental Investigation of Non-Normality of Thermoacoustic Interaction in an Electrically Heated Rijke Tube, International Journal of Spray and Combustion Dynamics. 7 (2015) 315–352. https://doi.org/10.1260/1756-8277.7.4.315.

[144] D. Zhao, A real-time plane-wave decomposition algorithm for characterizing perforated liners damping at multiple mode frequencies, J Acoust Soc Am. 129 (2011) 1184–1192. https://doi.org/10.1121/1.3533724.

[145] Y. Sun, Z. Rao, D. Zhao, B. Wang, D. Sun, X. Sun, Characterizing nonlinear dynamic features of self-sustained thermoacoustic oscillations in a premixed swirling combustor, Appl Energy. 264 (2020) 114698. https://doi.org/10.1016/j.apenergy.2020.114698.

[146] S. Tandon, R.I. Sujith, Condensation in the phase space and network topology during transition from chaos to order in turbulent thermoacoustic systems, Chaos: An Interdisciplinary Journal of Nonlinear Science. 31 (2021) 043126. https://doi.org/10.1063/5.0039229.

[147] A. Seshadri, V. Nair, R.I. Sujith, A reduced-order deterministic model describing an intermittency route to combustion instability, Combustion Theory and Modelling. 20 (2016) 441–456. https://doi.org/10.1080/13647830.2016.1143123.

[148] H. Gotoda, Y. Shinoda, M. Kobayashi, Y. Okuno, S. Tachibana, Detection and control of combustion instability based on the concept of dynamical system theory, Phys Rev E. 89 (2014) 022910. https://doi.org/10.1103/PhysRevE.89.022910.

[149] Y. Shinchi, N. Takeda, H. Gotoda, T. Shoji, S. Yoshida, Early Detection of Thermoacoustic Combustion Oscillations in Staged Multisector Combustor, AIAA Journal. 59 (2021) 4086–4093. https://doi.org/10.2514/1.J060268.

[150] H. Gotoda, Y. Okuno, K. Hayashi, S. Tachibana, Characterization of degeneration process in combustion instability based on dynamical systems theory, Phys Rev E. 92 (2015) 052906. https://doi.org/10.1103/PhysRevE.92.052906.

[151] M. Khosravy, Review of the New Combustion Technologies in Modern Gas Turbines, in: Progress in Gas Turbine Performance, InTech, 2013. https://doi.org/10.5772/54403.

[152] G.S. Samuelsen, J. Brouwer, M.A. Vardakas, J.D. Holdeman, Experimental and modeling investigation of the effect of air preheat on the formation of NOx in an RQL combustor, Heat and Mass Transfer. 49 (2013) 219–231. https://doi.org/10.1007/s00231-012-1080-0.

[153] F. Takens, Detecting strange attractors in turbulence, in: 1981: pp. 366–381. https://doi.org/10.1007/BFb0091924.

[154] Y. Huang, V. Yang, Bifurcation of flame structure in a lean-premixed swirl-stabilized combustor: transition from stable to unstable flame, Combust Flame. 136 (2004) 383–389. https://doi.org/10.1016/j.combustflame.2003.10.006.

[155] D. Ebi, A. Denisov, G. Bonciolini, E. Boujo, N. Noiray, Flame Dynamics Intermittency in the Bistable Region Near a Subcritical Hopf Bifurcation, J Eng Gas Turbine Power. 140 (2018). https://doi.org/10.1115/1.4038326.

[156] T.C. Lieuwen, Vigor. Yang, Combustion instabilities in gas turbine engines : operational experience, fundamental mechanisms and modeling, American Institute of Aeronautics and Astronautics, 2005.

[157] N. Swaminathan, G. Xu, A.P. Dowling, R. Balachandran, Heat release rate correlation and combustion noise in premixed flames, J Fluid Mech. 681 (2011) 80–115. https://doi.org/10.1017/jfm.2011.232.

[158] J. O'Connor, V. Acharya, T. Lieuwen, Transverse combustion instabilities: Acoustic, fluid mechanic, and flame processes, Prog Energy Combust Sci. 49 (2015) 1–39. https://doi.org/10.1016/j.pecs.2015.01.001.

[159] M.P. Juniper, Triggering in the horizontal Rijke tube: Non-normality, transient growth and bypass transition, J Fluid Mech. 667 (2011) 272–308. https://doi.org/10.1017/S0022112010004453.

[160] N.N. Deshmukh, S.D. Sharma, Experiments on heat content inside a Rijke tube with suppression of thermo-acoustics instability, International Journal of Spray and Combustion Dynamics. 9 (2017) 85–101. https://doi.org/10.1177/1756827716655007.

[161] M. Fleifil, Response of a laminar premixed flame to flow oscillations: A kinematic model and thermoacoustic instability results, Combust Flame. 106 (1996) 487–510. https://doi.org/10.1016/0010-2180(96)00049-1.

[162] X. Han, D. Laera, A.S. Morgans, C.J. Sung, X. Hui, Y.Z. Lin, Flame macrostructures and thermoacoustic instabilities in stratified swirling flames, Proceedings of the Combustion Institute. 37 (2019) 5377–5384. https://doi.org/10.1016/j.proci.2018.06.147.

[163] S.J. Shanbhogue, Y.S. Sanusi, S. Taamallah, M.A. Habib, E.M.A. Mokheimer, A.F. Ghoniem, Flame macrostructures, combustion instability and extinction strain scaling in swirl-stabilized premixed CH 4 /H 2 combustion, Combust Flame. 163 (2016) 494–507. https://doi.org/10.1016/j.combustflame.2015.10.026.

[164] D. You, Y. Huang, V. Yang, A generalized model of acoustic response of turbulent premixed flame and its application to gas-turbine combustion instability analysis, in: Combustion Science and Technology, 2005: pp. 1109–1150. https://doi.org/10.1080/00102200590927012.

[165] D. Zhao, Y. Guan, A. Reinecke, Characterizing hydrogen-fuelled pulsating combustion on thermodynamic properties of a combustor, Commun Phys. 2 (2019). https://doi.org/10.1038/s42005-019-0142-8.

[166] V. Godavarthi, P. Kasthuri, S. Mondal, R.I. Sujith, N. Marwan, J. Kurths, Synchronization transition from chaos to limit cycle oscillations when a locally coupled chaotic oscillator grid is coupled globally to another chaotic oscillator, Chaos. 30 (2020). https://doi.org/10.1063/1.5134821.

[167] H. Zhou, Z. Liu, C. Tao, M. Zhou, Mitigating self-excited thermoacoustic oscillations in a liquid fuel combustor using dual perforated plates, J Acoust Soc Am. 148 (2020) 1756–1766. https://doi.org/10.1121/10.0002007.

[168] Shreekrishna, S. Hemchandra, T. Lieuwen, Premixed flame response to equivalence ratio perturbations, Combustion Theory and Modelling. 14 (2010) 681–714. https://doi.org/10.1080/13647830.2010.502247.

[169] M. Han, X. Han, J. Wang, X. Gao, P. He, X. Feng, Y. Zhou, Experimental study of the effect of air split ratio on thermoacoustic instability in a centrally-staged swirl burner, Physics of Fluids. 34 (2022). https://doi.org/10.1063/5.0094071.

[170] H. Zhou, Z. Liu, H. Fang, C. Tao, M. Zhou, L. Hu, Attenuation effects of perforated plates with heterogeneously distributed holes on combustion instability in a spray

flame combustor, Journal of Mechanical Science and Technology. 34 (2020) 4865–4875. https://doi.org/10.1007/s12206-020-1042-2.

[171] N. Tran, S. Ducruix, T. Schuller, Passive control of the inlet acoustic boundary of a swirled burner at high amplitude combustion instabilities, J Eng Gas Turbine Power. 131 (2009). https://doi.org/10.1115/1.3078206.

[172] N. Tran, S. Ducruix, T. Schuller, Damping combustion instabilities with perforates at the premixer inlet of a swirled burner, Proceedings of the Combustion Institute. 32 II (2009) 2917–2924. https://doi.org/10.1016/j.proci.2008.06.123.

[173] C. Lawn, The acoustic impedance of perforated plates under various flow conditions relating to combustion chamber liners, Applied Acoustics. 106 (2016) 144–154. https://doi.org/10.1016/j.apacoust.2016.01.005.

[174] M.A. Temiz, J. Tournadre, I.L. Arteaga, A. Hirschberg, Non-linear acoustic transfer impedance of micro-perforated plates with circular orifices, J Sound Vib. 366 (2016) 418–428. https://doi.org/10.1016/j.jsv.2015.12.022.

[175] L. Xu, G. Zhang, G. Wang, Z. Feng, X. Tian, L. Li, F. Qi, Effects of acoustic liner on thermoacoustic instabilities in a premixed swirl combustor, Aerosp Sci Technol. 118 (2021). https://doi.org/10.1016/j.ast.2021.107070.

[176] D. Zhao, E. Gutmark, A. Reinecke, Mitigating self-excited flame pulsating and thermoacoustic oscillations using perforated liners, Sci Bull (Beijing). 64 (2019) 941–952. https://doi.org/10.1016/j.scib.2019.05.004.

[177] G. Zhang, X. Wang, L. Li, X. Sun, Effects of perforated liners on controlling combustion instabilities in annular combustors, AIAA Journal. 58 (2020) 3100–3114. https://doi.org/10.2514/1.J059099.

[178] X. Jing, X. Sun, Experimental investigations of perforated liners with bias flow, J Acoust Soc Am. 106 (1999) 2436–2441. https://doi.org/10.1121/1.428128.

[179] H. Kobayashi, H. Gotoda, S. Tachibana, S. Yoshida, Detection of frequency-mode-shift during thermoacoustic combustion oscillations in a staged aircraft engine model combustor, J Appl Phys. 122 (2017). https://doi.org/10.1063/1.5003912.

[180] C. Lawn, Acoustic pressure losses in woven screen regenerators, Applied Acoustics. 77 (2014) 42–48. https://doi.org/10.1016/j.apacoust.2013.09.019.

[181] Y. Lai, X. Wang, T.B.O. Rockett, J.R. Willmott, Y. Zhang, Investigation into wind effects on fire spread on inclined wooden rods by multi-spectrum and schlieren imaging, Fire Saf J. 127 (2022). https://doi.org/10.1016/j.firesaf.2021.103513.

[182] Y. Lai, A. Albadi, X. Liu, M. Davies, M. Hobbs, J. Willmott, Y. Zhang, Investigation of forced flow orientations on the burning behaviours of wooden rods using a synchronised multi-imaging system, Proceedings of the Combustion Institute. (2022). https://doi.org/10.1016/j.proci.2022.07.057.

[183] C. Zhu, M.J. Hobbs, J.R. Willmott, An accurate instrument for emissivity measurements by direct and indirect methods, Meas Sci Technol. 31 (2020). https://doi.org/10.1088/1361-6501/ab5e9b.

[184] American Society of Heating Refrigerating and Air-Conditioning Engineers, ASHRAE Handbook - Fundamentals (SI Edition), American Society of Heating, Refrigerating and Air-Conditioning Engineers, Atlanta, 2009.

[185] B. Entezam, W.K. Van Moorhem, J. Majdalani, Two-dimensional numerical verification of the unsteady thermoacoustic field inside a Rijke-type pulse combustor, Numeri Heat Transf A Appl. 41 (2002) 245–262. https://doi.org/10.1080/10407780252780153.

[186] Rayleigh, XXXVII. On the passage of waves through apertures in Plane screens, and allied problems, The London, Edinburgh, and Dublin Philosophical Magazine and Journal of Science. 43 (1897) 259–272. https://doi.org/10.1080/14786449708620990.

[187] A.F. Seybert, D.F. Ross, Experimental determination of acoustic properties using a two-microphone random-excitation technique, J Acoust Soc Am. 61 (1977) 1362–1370. https://doi.org/10.1121/1.381403.

[188] Y. Liu, J. Tan, H. Wang, L. Lv, Characterization of heat release rate by OH* and CH* chemiluminescence, Acta Astronaut. 154 (2019) 44–51. https://doi.org/10.1016/j.actaastro.2018.10.022.

Appendix

Dimension of tube and its holder base:

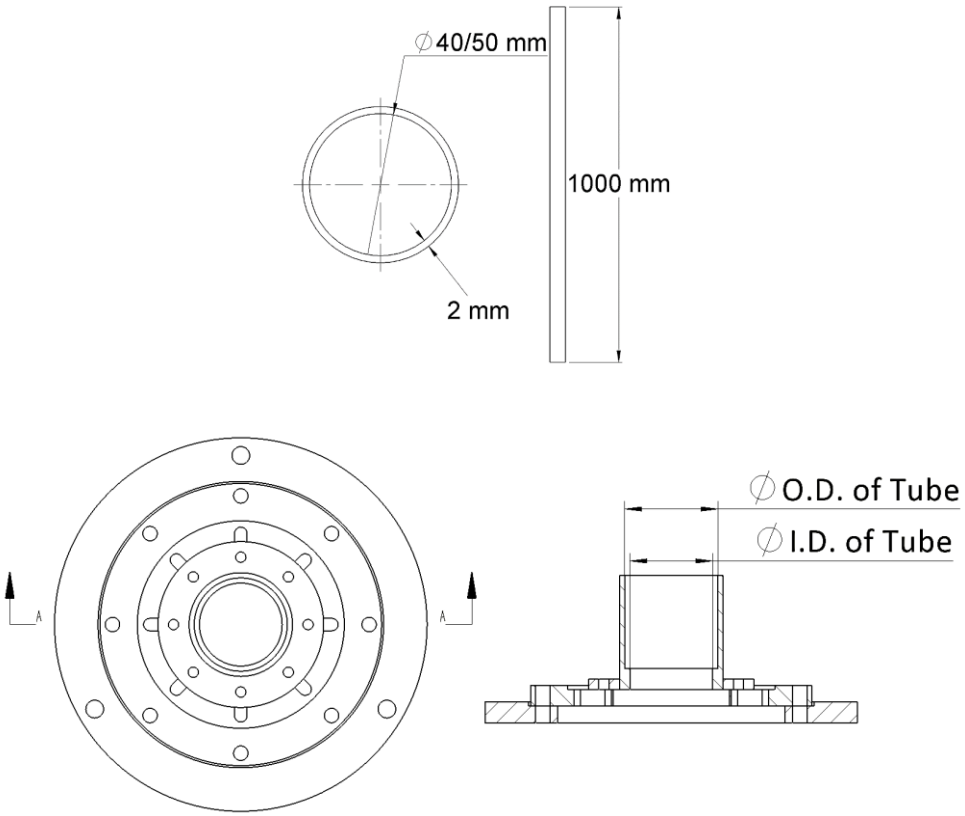

Microphone frequency response:

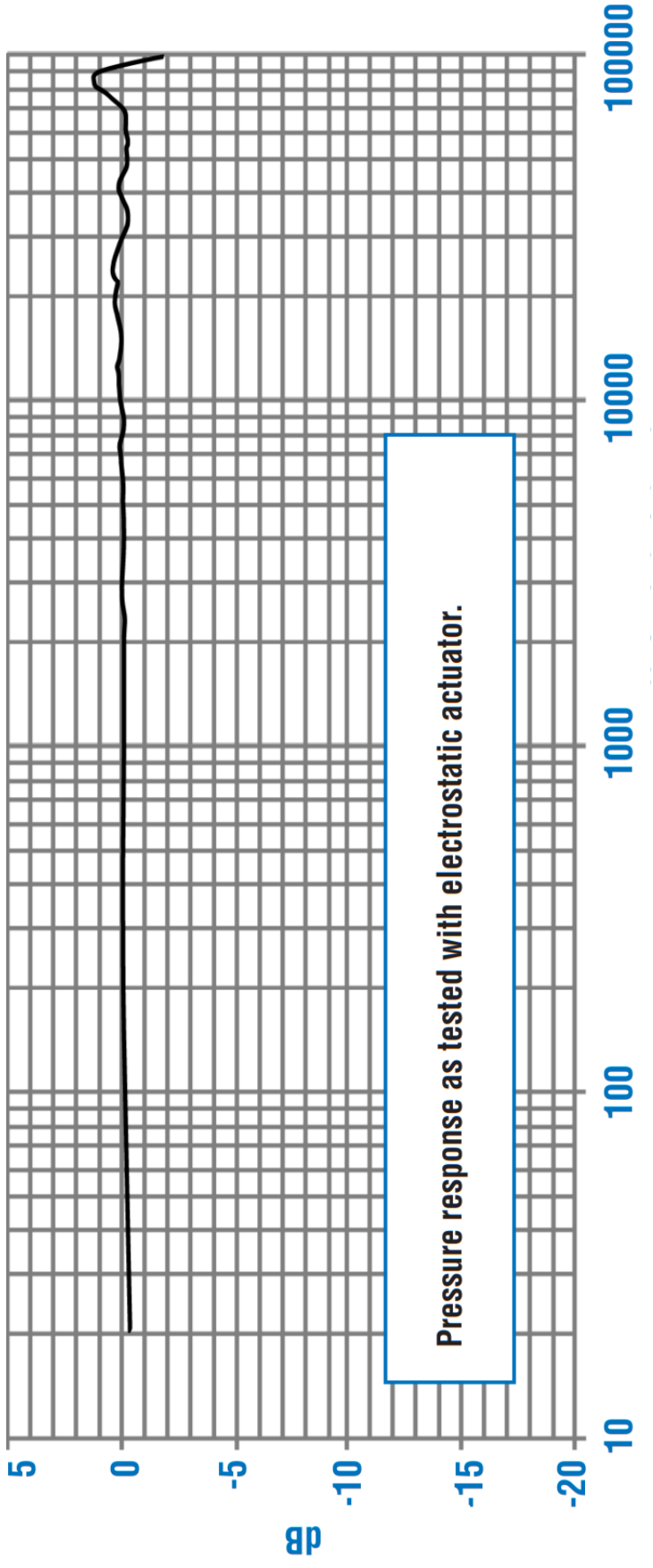

Investigation of flame root oscillations under the self-excited oscillation (preliminary results):

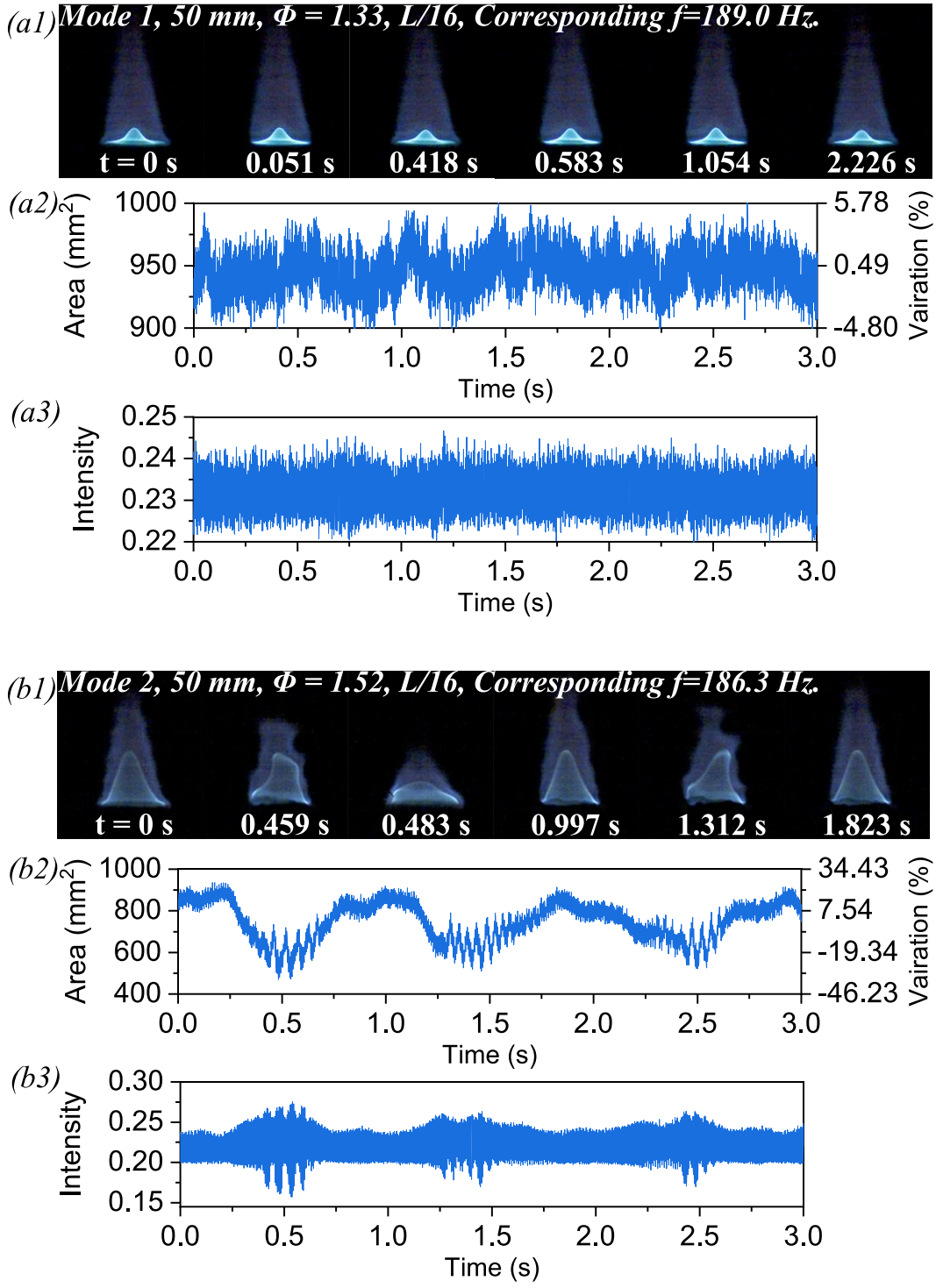

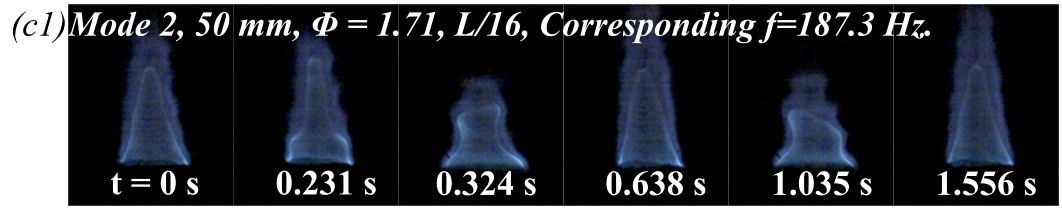
(c1) Mode 2, 50 mm, Φ = 1.71, L/16, Corresponding f=187.3 Hz.
t = 0 s
0.231 s
0.324 s
0.638 s
1.035 s
1.556 s

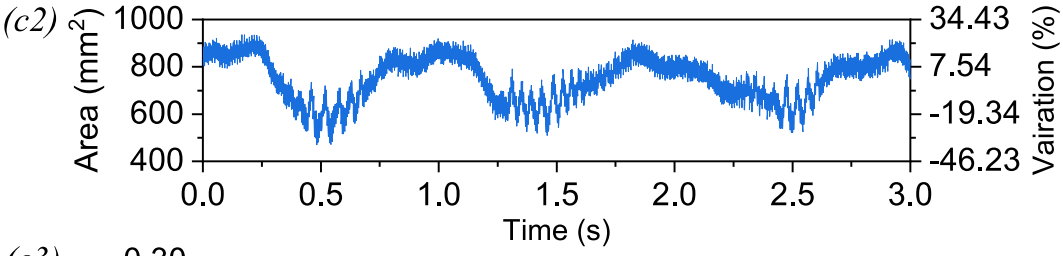
(c2)
Area (mm²)
1000
800
600
400
34.43
7.54
-19.34
-46.23
Vairation (%)
0.0
0.5
1.0
1.5
2.0
2.5
3.0
Time (s)

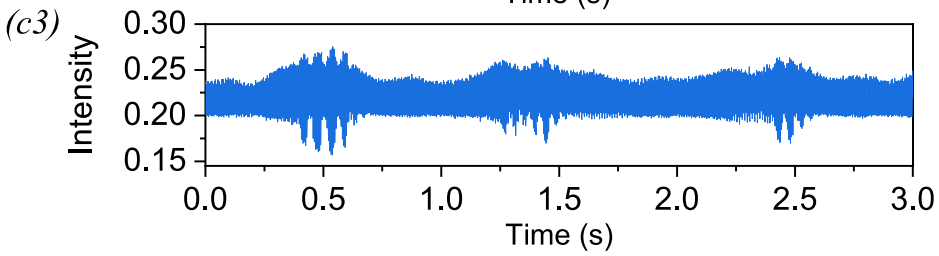
(c3)
Intensity
0.30
0.25
0.20
0.15
0.0
0.5
1.0
1.5
2.0
2.5
3.0
Time (s)

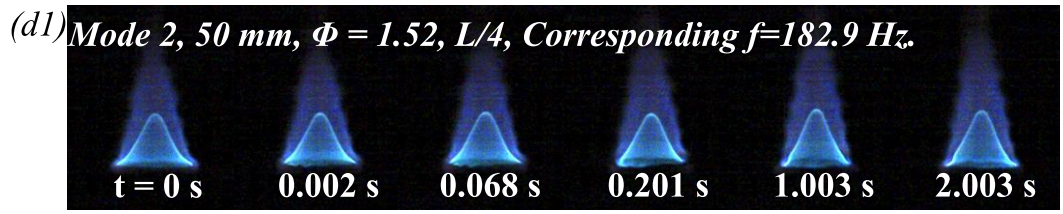
(d1) Mode 2, 50 mm, Φ = 1.52, L/4, Corresponding f=182.9 Hz.
t = 0 s
0.002 s
0.068 s
0.201 s
1.003 s
2.003 s

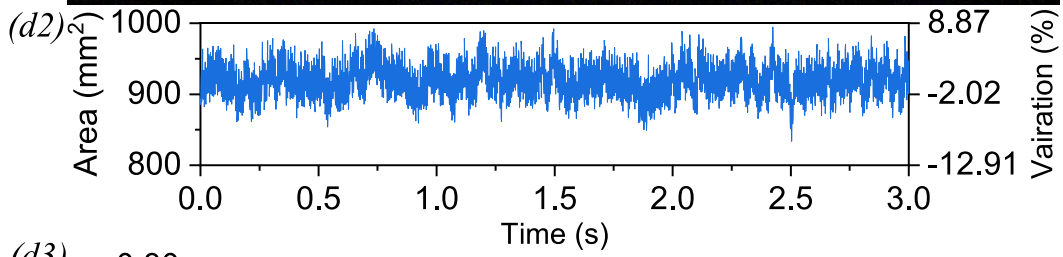
(d2)
Area (mm²)
1000
900
800
8.87
-2.02
-12.91
Vairation (%)
0.0
0.5
1.0
1.5
2.0
2.5
3.0
Time (s)

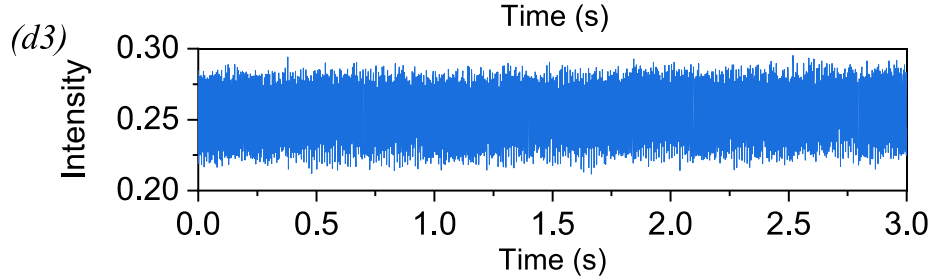
(d3)
Intensity
0.30
0.25
0.20
0.0
0.5
1.0
1.5
2.0
2.5
3.0
Time (s)

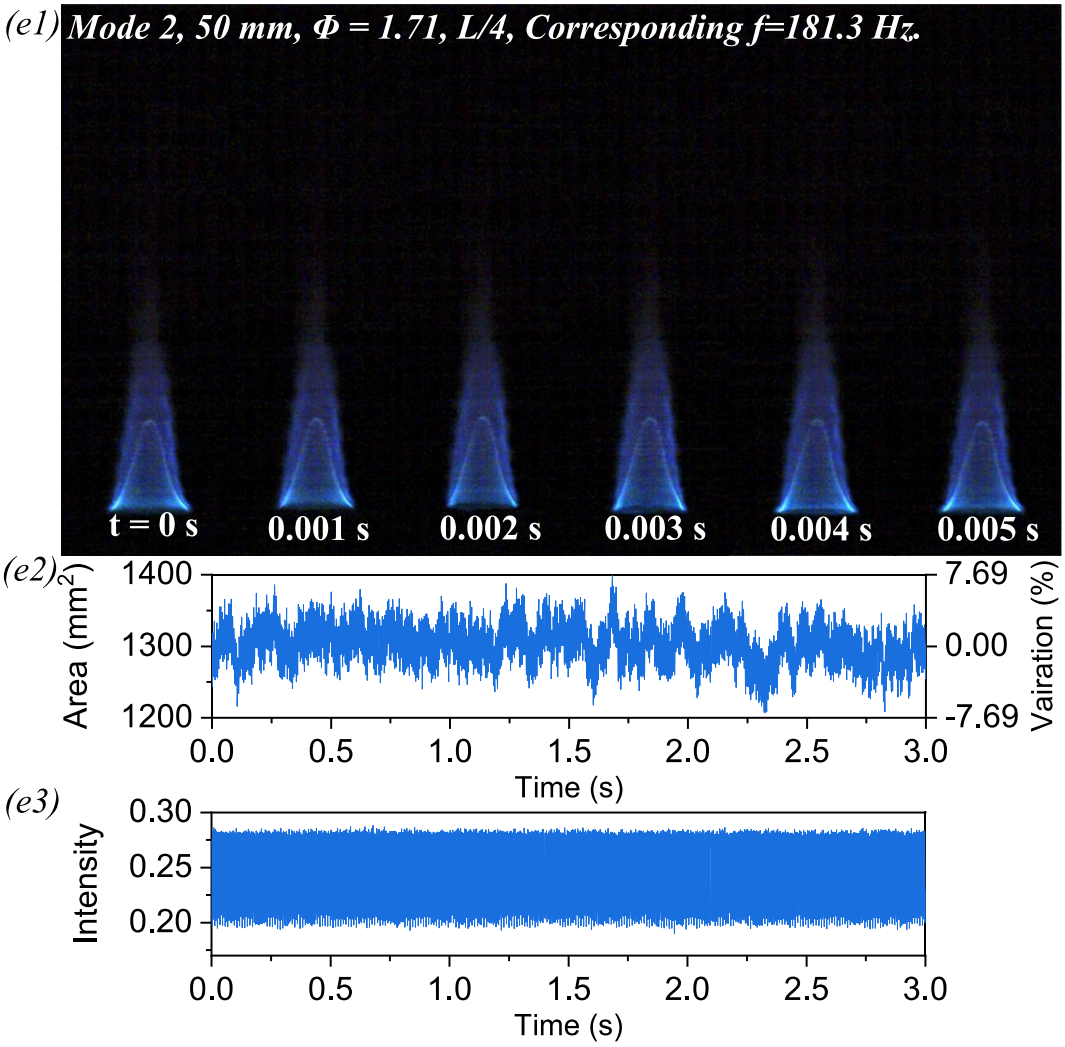
(e1)
Mode 2, 50 mm, Φ = 1.71, L/4, Corresponding f=181.3 Hz.
t = 0 s
0.001 s
0.002 s
0.003 s
0.004 s
0.005 s
(e2)
Area (mm²)
1400
1300
1200
7.69
0.00
-7.69
Vairation (%)
0.0
0.5
1.0
1.5
2.0
2.5
3.0
Time (s)
(e3)
Intensity
0.30
0.25
0.20
0.0
0.5
1.0
1.5
2.0
2.5
3.0
Time (s)

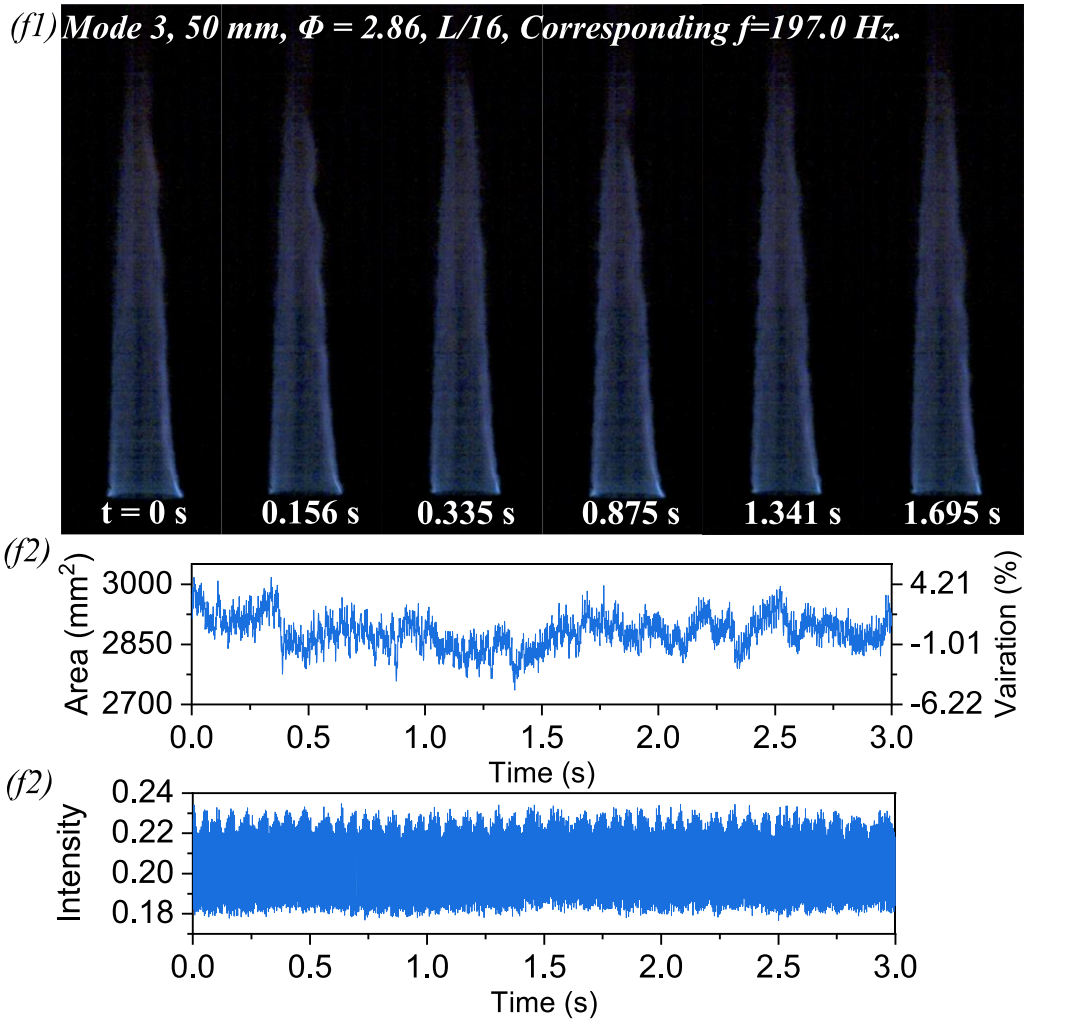

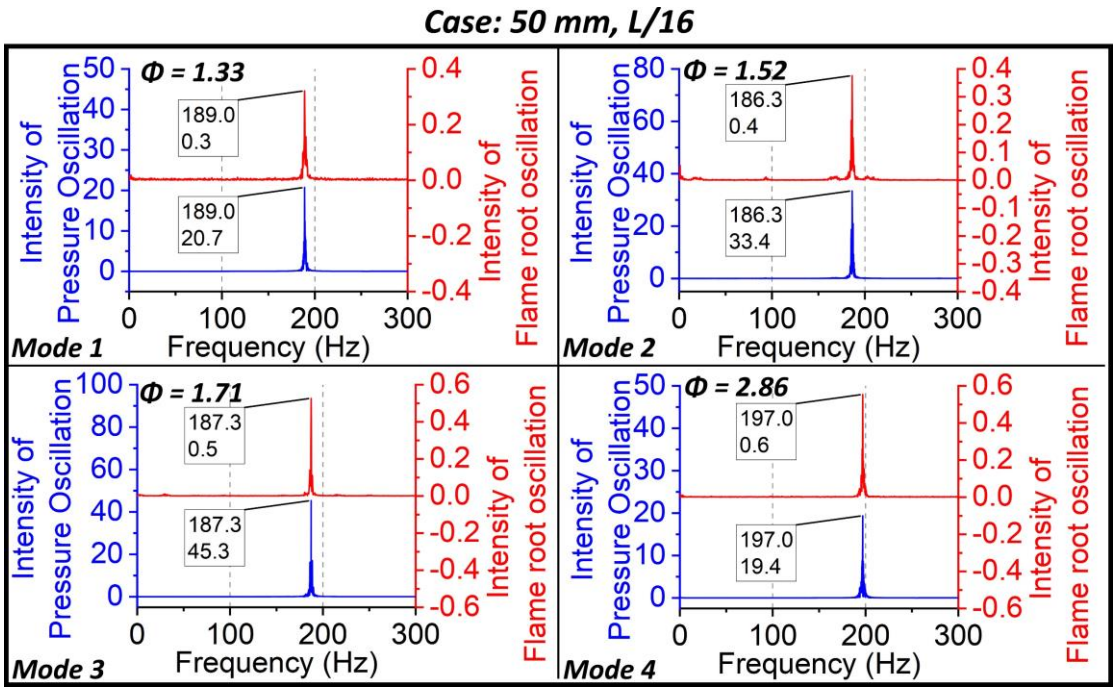

Flame under different oscillation conditions (Beating and limit-cycle oscillation)

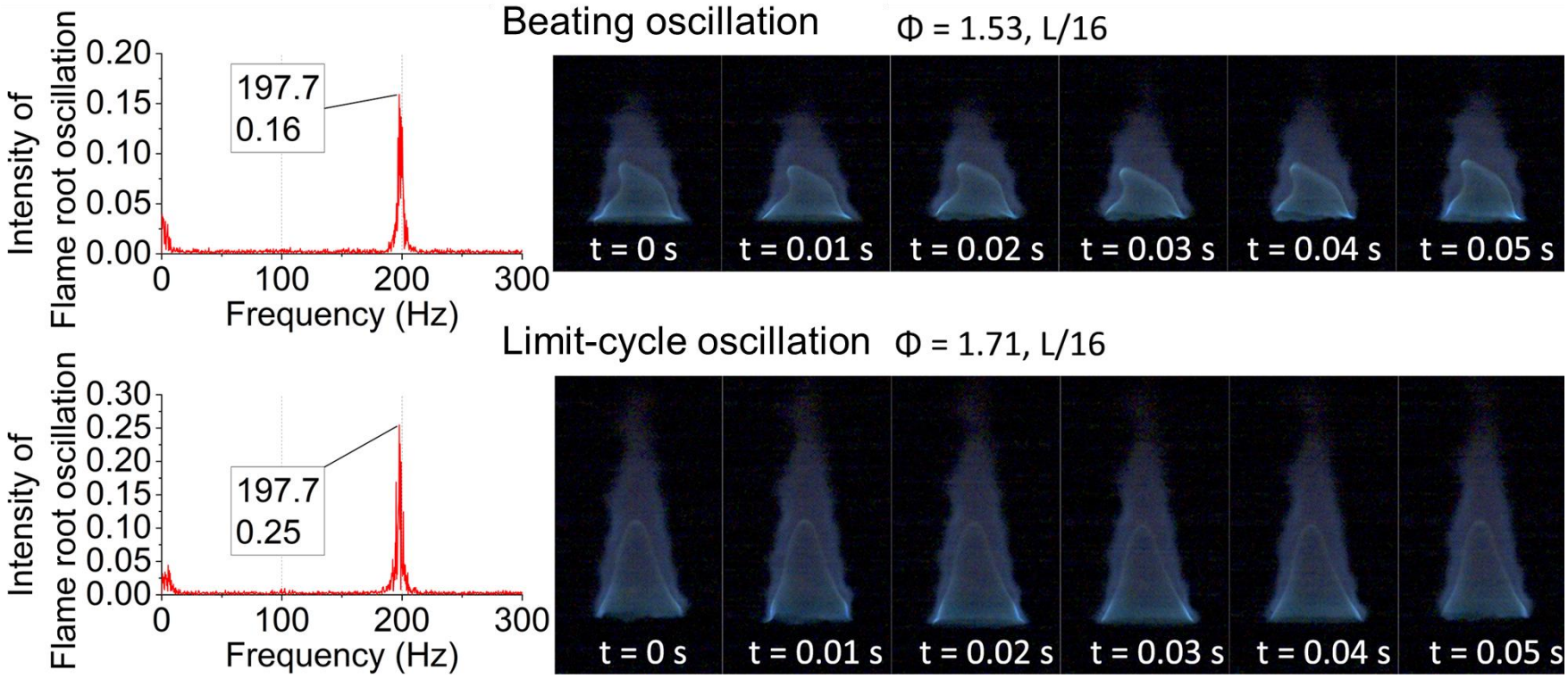
Beating oscillation
Φ = 1.53, L/16
Intensity of Flame root oscillation
0.20
0.15
0.10
0.05
0.00
197.7
0.16
0
100
200
300
Frequency (Hz)
t = 0 s
t = 0.01 s
t = 0.02 s
t = 0.03 s
t = 0.04 s
t = 0.05 s
Limit-cycle oscillation
Φ = 1.71, L/16
Intensity of Flame root oscillation
0.30
0.25
0.20
0.15
0.10
0.05
0.00
197.7
0.25
0
100
200
300
Frequency (Hz)
t = 0 s
t = 0.01 s
t = 0.02 s
t = 0.03 s
t = 0.04 s
t = 0.05 s